Improved Autogyro Flying Qualities Using Automatic Control Methods

Shahrul A. Shah, M.Sc

Submitted in fulfilment of the requirements
for the degree of
Doctor of Philosophy

School of Engineering
College of Science and Engineering
University of Glasgow

December 2018

Abstract

An autogyro or Autogiro is a unique type of rotary-wing aircraft that was successfully flown in the 1920s, many years before the first helicopter came to service. As far as the rotorcraft technology is concerned, the technical issues addressed by autogyros were eventually rectified and paved the way for the success of helicopter development. When helicopter became more popular and accepted in the civil aviation industry in the 1940s, autogyros were nearly forgotten and the popularity slowly diminished. The re-emergence of autogyros in the last two decades in hobby and sports flight activities, however, coincides with bad safety records due to stability issues.

At the time of this writing, there are no specific flying qualities standards to be employed as guidelines to design a light autogyro with good stability attributes. The only requirements available are addressed in the BCAR Section T airworthiness standard for light autogyros which only prescribes some basic dynamic stability requirements for the vehicle. For existing conventional light autogyros which mostly of 'home-built' type, complying with the airworthiness standards would be an issue as most of them were built beforehand. From these concerns, this Thesis aims to improve the flying qualities performance of existing light autogyros through automatic flight control methods, as one of the ways to practically achieve the required performance. Consequently, specific flying qualities requirements for light autogyros must first be proposed as preliminary guidelines for design and flying qualities improvement. A generic mathematical model of light autogyros named ARDiS is developed based on the 'multiblade' simulation approach which is computationally cost-effective. This model was successfully validated against real autogyro flight data and later implemented in the control enhancement of the vehicle.

The control enhancement was developed using classical approaches with limitation in size and simplicity of the vehicle as a light aircraft. Proper actuation control hardware was separately modelled and deployed into the autogyro to demonstrate a higher dynamics in the control mechanism so that a more realistic attitude behaviour of the vehicle is presented. This control enhancement was successfully evaluated with both, linear and nonlinear simulations according to the proposed autogyro flying qualities attributes. All presented results signify a higher possibility of improving the flying qualities of currently used and future built light autogyros through control enhancement.

Nomenclature

General

$\boldsymbol{a}$	Translational acceleration vector (m/s^2)
a_0	Lift-curve slope of rotor blade (1/rad)
a_1	Lift coefficient of rotor blade at zero angle-of-attack
a_x, a_z	Local acceleration components (m/s^2)
b	Number of blades
c	Chord length of a rotor blade (m)
d	Drag per unit span of a rotor blade (N/m)
dx, dz	Wind gust length in longitudinal mode (m)
$\boldsymbol{f}$	Local aerodynamic force vector at rotor blade (N/m)
f_y, f_z	Local aerodynamic force components per unit span of the blade (N/m)
g	Gravity acceleration (m/s^2)
$\boldsymbol{i}$, $\boldsymbol{j}$, $\boldsymbol{k}$	Unit vectors
k	Stiffness of spring (N/m)
l	Lift per unit span of rotor blade (N/m)
l_s	Spring length (m)
m	autogyro mass (kg)
m_0	Mass per unit span of rotor blade (kg/m)
n_β	Stiffness number of the rotor blade
n_{gear}	Motor gear ratio
n_p	Linear actuator leadscrew ratio
q	Pitch rate perturbation (rad/s)
q_c	Pitch-rate command signal
q_e	Pitch-rate error signal
$\boldsymbol{r}$	Position vector (m)
r_b	Distance of a specific point of a blade from the rotor hub (m)

$\boldsymbol{r}_{cg/ref}$	Position vector of the autogyro's centre of gravity relative to the reference point (m)
$r_{e/bl}$	Position vector of an element along the blade (m)
$\boldsymbol{r}_{hub/ref}$	Position vector of the rotor hub relative to the reference point (m)
$\boldsymbol{r}_{hub/pivot}$	Position vector of the rotor hub relative to the pivot point (m)
$\boldsymbol{r}_{P/CG}$	Position vector of the pivot point relative to the centre of gravity (m)
s	Rotor blade solidity
t_{lag}	Integral-lag in time response (s)
t_s	Settling time of a damped oscillation (s)
$\boldsymbol{u}$	Control matrix
u, w	Longitudinal velocities perturbation (m/s)
u_g, w_g	Wind gust in longitudinal mode (m/s)
$\boldsymbol{v}$	Translational velocity vector (m/s)
x, z	Longitudinal distance or position (m)
x_0	Linear position of actuator's leadscrew (m)
x_e, z_e	Longitudinal distance or position in earth-axes (m)
x_p	Linear extension of actuator's plunger (m)
$\boldsymbol{A}$, $\boldsymbol{B}$	System and control matrices
$\boldsymbol{A_{aug}}$	Augmented state matrix
B_m @ b_s	Rotor shaft viscous damping (Nm/rad/s)
C	Coefficient
E_b	Back-emf (Volts)
$\boldsymbol{F}$	Force vector (N)
F_{load}	Linear actuator load force (N)
$\boldsymbol{I}$	Identity matrix
I_β	Flapping moment of inertia (kg m^2)
I_R	Rotor blade moment of inertia (kg/m^2)
I_{yy}	Pitch moment of inertia of the autogyro (kg m^2)
$\boldsymbol{J}$	Jacobian matrix
J_m	Rotor inertia of a motor (kg m^2)
$\boldsymbol{K}$	State feedback gain matrix of controller
K_β	Spring stiffness of the rotor (Nm/rad)
K_e	Back-emf constant (V/rad/s)
K_{e_q}	Integral gain of RCAH control system
K_f	Feedforward gain of a linear actuator

K_m	Feedforward compensator gain of RCAH control
K_u, K_w, etc.	State feedback gains of autogyro
K_i	Integral gain
K_p	Proportional gain
K_t	Motor torque constant (Nm/A)
K_v	Velocity gain
L_a	Motor armature inductance (H)
M	External pitch moment (Nm)
$\boldsymbol{M}$	Moment vector (Nm)
M_β	Mass moment of rotor blade (kg/m)
$M_{\delta_{\theta_s}}$	Control derivative of pitch moment
M_{load}	Linear actuator load mass (kg)
M_u^*, M_w^*, etc.	State derivatives of the pitch moment
P_e	Power of motor electrical element (Watt)
P_{int}	Integral-pole of RCAH control system
P_m	Power of motor mechanical element (Nm/s)
$\boldsymbol{Q}$	Feedforward gain matrix of RCAH control
Q	Pitch rate (rad/s)
$\dot{Q}$	Angular acceleration in pitch (rad/s^2)
$Q_{\delta_{\theta_s}}$	Control derivative of rotor torque
Q_e	Engine torque (Nm)
Q_R	Rotor torque (Nm)
Q_T	Tail rotor torque (Nm)
$Q_{\theta_{pk}}$	Pitch attitude quickness (1/s)
Q_u, Q_w, etc.	State derivatives of the rotor torque
R	Rotor disc radius (m)
R_a	Motor armature resistance (ohm)
R_{lead}	Linear actuator Leadscrew radius (m)
S	Surface area (m^2)
S_{lead}	Screw-lead size of a linear actuator (mm/rev)
$\boldsymbol{T}$	Transformation matrix
T	Period of oscillation (s)
$T_{\frac{1}{2}}$	Time to halve amplitude (s)
T_2	Time to double amplitude (s)
T_m	Motor torque (Nm)
T_{prop}	Propeller thrust (N)
T_R	Rotor thrust (N)
U, W	Longitudinal velocity components of autogyro (m/s)

$\dot{U}$, $\dot{W}$	Longitudinal acceleration components of autogyro (m/s^2)
U_T, U_P	Tangential and normal velocity components of the rotor blade (m/s)
$\bar{U}_T$, $\bar{U}_P$	Tangential and normal velocity components in normalised form
V_f	Autogyro forward flight speed (m/s)
V_{L_a}	Motor's inductance voltage (Volts)
V_{R_a}	Motor's resistance voltage (Volts)
V_x, V_y, V_z	Local velocity components (m/s)
X, Y, Z	Autogyro external force components (N)
X_A, Y_A, Z_A	Aerodynamic force components
X_I, Y_I, Z_I	Inertial force components
$X_{\delta_{\theta_s}}$	Control derivative of X-force
X_u, X_w, etc.	State derivatives of X-force
$Z_{\delta_{\theta_s}}$	Control derivative of Z-force
Z_{int}	Integral-zero of RCAH control system
Z_u, Z_w, etc.	State derivatives of Z-force

Greek Symbols

$\boldsymbol{\alpha}$	Rotational acceleration vector (rad/s^2)
α_{1s}, α_{1c}	Normalised angular acceleration components of rotor blade
α_{bl}	Angle of incidence of the rotor blade (rad)
β	Flapping angle of rotor blade (rad)
δ	Profile drag coefficient of rotor blade
δ_{θ_s}	longitudinal control tilt of linearised autogyro model (rad)
ϵ_q	pitch-rate control error (rad/s)
η_z	Normalised rotor-disc acceleration in normal direction
$\mathcal{F}$	Evaluation points across the flight speed range
λ	Eigenvalue
λ_0, λ_{1_s}, λ_{1_c}	Normalised induced velocity components of the rotor disc
μ	Rotor hub plane resultant velocity in normalised form
μ_x, μ_y, μ_z	Rotor hub plane velocity components in normalised form
$\boldsymbol{\omega}$	Rotational velocity vector (rad/s^2)
Ω	Rotorspeed
ω_{BW}	frequency bandwidth (rad/s)
ω_{ls}	Leadscrew angular velocity (rad/s)

ω_n	Natural frequency of aircraft dynamic (rad/s)
ω_m	Motor shaft angular velocity (rad/s)
ϕ	Angle of attack of the rotor blade (rad)
Φ_M	Phase margin (deg)
ψ	Azimuth angle of the blade rotation (rad)
ρ	Air density (kg/m^3)
τ_p @ τ_θ	Phase delay (s)
τ_a	Actuator time constant (s)
Θ	Pitch attitude of autogyro (rad)
θ_{ls}	Leadscrew angular position (rad)
θ_r	Motor shaft angular position (rad)
θ_s	Longitudinal shaft tilt control angle of autogyro (rad)
ζ	Damping ratio

Subscripts

A	Aerodynamic
b	Body axes
bl	Rotor blade axes
cg	Centre of gravity
e	Earth axes
Fus	Fuselage
h	Rotor hub
I	Inertial
ph	Phugoid
pp	Pivot point
Prop	Propeller
pvt	Pivot axes
R	Rotor
ref	Reference
s	Shaft axes
sp	short-period
Tp	Tailplane

Superscripts

T	Transpose of a matrix
b	Body axes
bl	Blade axes
d	Disc axes
pvt	Pivot axes frame

Abbreviation

AAIB	Air Accident Investigation Bureau
ACAH	Attitude-Command Attitude Hold
AFCS	Automatic Flight Control System
APC	Aircraft-Pilot Coupling
ARDiS	Autogyro Rotor Disc Simulation
BCAR	British Civil Aviation Requirement
BLDC	Brushless-type DC motor
CAA	Civil Aviation Authority
CAD	Computer Aided Design
CAP	Control Anticipation Parameter
CG	Centre of Gravity
CP	Centre of Pressure
CPU	Central Processing Unit
DAE	Differential Algebraic Equation
EASA	European Aviation Safety Agency
EHA	Electro-Hydrostatic Actuator
EMA	Electro-Mechanical Actuator
PM	Phase Margin (deg)
RASCAL	Rotorcraft Aeromechanic Simulation for Control Analysis
RCAH	Rate-Command Attitude Hold
SAS	Stability Augmentation System
SML	Simscape Multibody Link
V/STOL	Vertical/Short Take-off and Landing
XML	Extensible Markup Language
FAA	Federal Aviation Administration
GM	Gain Margin

GSIM	Gyroplane Simulation Model
HGS	Helicopter Generic Simulation
HIBROM	Helicopter Individual-Blade Rotor Model
HQR	Handling Qualities Ratings
IAS	Indicated Air Speed
JAR	Joint Aviation Requirements
KVL	Kirchhoff's Voltage Law
MEA	More Electric Aircraft
MIMO	Multiple-Input, Multiple-Output
MTE	Mission Task Elements
NACA	National Advisory Committee for Aeronautics
NTSB	National Transportation Safety Board
ODE	Ordinary Differential Equation
PIO	Pilot-Induced Oscillation
PIV	Proportional-Integral-Velocity controller

Contents

List of Tables

List of Figures

Acknowledgements

Firstly, my sincere gratitude goes to my principal supervisor Dr Douglas Thomson, for his patience, motivation, and continuous support throughout these years in completing the research. His professional guidance and technical support helped me going through all challenging steps of my PhD journey. Also, my heartfelt thank goes to my second supervisor Dr David Anderson, for the advice and supports especially in the control field.

Also, a special thank goes to my respective viva convenor, Dr Ian Taylor, for assisting a smooth viva discussion. Not to forget, also special thanks to my thesis examiners, Dr Djamel Rezgui and Dr Kiran Ramesh, for their insightful comments, criticism, and encouragement throughout the viva.

Next, my sincere thanks also to Majlis Amanah Rakyat (MARA) and Universiti Kuala Lumpur (UniKL) for granting me the opportunity and funding for my doctorate study.

Finally, I would like to express my gratitude to my father, my mother-in-law, my siblings and friends for their support and prayers. Most importantly, a very special thank to my beloved wife, Nor Hamidah for being the 'angel on my shoulder'; my guide, my comforter, and my companion throughout these long 'spiritual' journey. I am also grateful to all my six boys; Syakir, Usamah, Ubaidah, Ramadhan, Amru, and Haneef, for brightening our lives in these difficult years. May Allah, the Almighty God grant all of us His mercy and blessings in all our future endeavours.

"*Education comes from within; you get it by struggle and effort and thought*". - Napoleon Hill

"*The climb might be tough and challenging, but the view is worth it. There is a purpose for that pain; you just can't always see it right away*". - Victoria Arlen

Chapter 1

Introduction

1.1 Research Motivation

An autogyro or gyroplane is a flying machine that flies according to a physical phenomenon called 'autorotation', which is defined as a self-sustained rotation of the main rotor without the application of shaft torque. Unlike helicopters, the rotor blade of an autogyro is unpowered, turning freely on a vertical shaft and generating the lift required to keep the vehicle airborne [1–4]. The forward propulsion of the vehicle is provided by a conventional propeller that is normally attached either at the front of the vehicle, known as tractor type, or at the rear, known as pusher type. Historically, the autogyro was trademarked as *Autogiro* by its inventor, Juan de la Cierva and firstly flown in 1923, which also pre-dating the first functional helicopter by 13 years [5]. In other words, the autogyro was the predecessor of powered helicopters, but slowly diminished as helicopters became more popular and successful until today.

Light autogyro has now become more popular, and the demand for this type of vehicle for sports and recreational flying has increased among hobbyist pilots. This popularity, without any doubt, is due to the underlying advantages an autogyro has over helicopters and fixed-wing aircraft. Light autogyro has low maintenance cost due to its simplicity in design and stall-proof capability, which makes it an enjoyable vehicle to be flown [4, 6].

Despite the increasing popularity on this type of vehicle, there has been a questionable safety track record which has drawn a serious concern amongst the aviation authorities regarding the safety of this type of vehicle. One of the main reasons for this is the fact

that the autogyro did not go through the formal design evolution throughout the years. Unlike autogyros, helicopters have gone through a thorough design evolution in many perspectives, from aerodynamics, propulsion, including stability and controllability. Many flying qualities standards and requirements for helicopters have been established to ensure their safety and practicality in all fields, which covers the commercial and also military sectors. For autogyros, the vehicle was traditionally designed and assembled in-house by hobbyists and used only for recreational flight. In recent years when the vehicle re-emerged back into the hobbyist community, the design was very much the same as it was in decades earlier, without significant design improvement. In fact, there was no specific design and airworthiness standards or flying qualities standards initially introduced for this type of vehicle, when it was re-introduced among the hobbyist communities.

The rapid re-emergence of autogyros have led to an increase in the number of reported accidents. The autogyro's poor safety concerns, however, were first addressed by the UK Civil Aviation Authority (CAA) prompted by a series of fatal accidents which involved the 'Air Command' light autogyros from 1989 to 1991 [7, p.1]. Due to these fatal incidents, an airworthiness review was commissioned by the UK's Air Accident Investigation Bureau (AAIB) which have led to the development of the first airworthiness standards for light autogyros in 1993. The new airworthiness standard was named the *British Civil Airworthiness Requirements, Section T (Light Gyroplane Design Requirements)* or known as the BCAR Section T, Issue 1. This airworthiness standard, however, was considered as the preliminary requirements, which was adapted from the light aeroplane's requirements, the BCAR Section S. Hence, more aerodynamics and stability studies on light autogyros have to be done to improvise the airworthiness standards, which have paved the way for more efforts in studying this type of vehicle.

The CAA had published its ten-year Aviation Safety Review of reportable incidents and accidents for all UK registered aircraft, known as the CAP735 and the CAP780 safety reviews [8, 9]. Since light autogyro is categorised under the 'Non-public Transport' category, comparisons can be made with other types of aircraft in the same category.

Table 1.1.1 summarises reported accidents that involved all aircraft in the 'Non-public Transport' category including light autogyros, extracted from the CAP780 report [9]. Note that, the number of UK-registered 'non-public' small aeroplanes was not reported in the CAP780. Hence, it is assumed that the number is many times larger than autogyros, of which was reported to have 2,513 actively registered for the same reportable duration [9, p.25]. As such, 25 reported accidents in ten years is considered relatively high for a small registered number of autogyros. More severely, eight of the reported accidents were fatal, which represents a 32% possibility for an accident to become fatal.

These number of accidents are then defined into accidents rate relative to the number of reported flying hours, so that comparison can be made with other types of aircraft of the same category.

Table 1.1.1: 'Non-public' Transport reported accidents (1998-2007) [9]

Aircraft type	Autogyros	Small Conventional Aeroplanes	Small Helicopters	Airships	Balloons	Gliders	Microlights
Total accident	25	1500	213	1	21	436	320
Fatal accident	8	96	24	0	0	36	23
Accident rate (per million flying hours)	1340.2	179.0	127.4	–	–	306.3	309.8
Fatal accident rate (per million flying hours)	428.9	11.7	14.4	–	–	24.6	22.3

The table revealed an average of 1340.2 accident rate with 428.9 fatal accidents per million flying hours for autogyros. These numbers demonstrate how severe the safety performance of a typical light autogyro is, considering the small number of registered autogyros than any other aircraft. For small conventional aeroplanes, 179 accidents with 11.7 fatality rates per million flying hours were reported, which is relatively much smaller (about 6%). Furthermore, 11% of fatalities were reported for small helicopters. Other types of 'non-public' light aircraft such as gliders and microlights were reported with 8% and 7% fatal accidents that are relatively small. For airships and balloons, no fatalities were reported, as the number of UK-registered airships and balloons were significantly small.

Since the flying principle of an autogyro is closer to fixed-wing aircraft and helicopters, it is worthwhile to compare the safety performance of light autogyros with those two aircraft. Table 1.1.1 also shows that the average fatal accidents per million flying hours for autogyros was about 36 times greater than the average rate of conventional aeroplanes, and about 30 times greater than small helicopters. Further investigations were made in a number of AAIB accident reports to find the root cause of the fatal accidents which pointed out at one particular problem, the longitudinal instability in forward flight. More detailed of this is discussed in Chapter 2 of the thesis.

There are still thousands of registered old-generation actively flown autogyros in the world, of which are still facing the longitudinal instability issues in forward flight. Piloting the older generation autogyro requires extensive training and experience to deal with the unexpected instability condition in manoeuvring the vehicle. This type of skill is crucial in preventing the vehicle from entering a severe pitch oscillation called

PIO (Pilot-Induced Oscillation). Even for an experienced autogyro pilot, handling this type of instability condition requires significant attention and work load levels.

Figure 1.1: VPM-M16 autogyro [10]

Figure 1.2: Montgomerie-Parsons (G-UNIV) research autogyro [11]

The safety concerns about light autogyros addressed by the CAA have paved the way for more detail studies being made on the vehicle. Proper understanding on the flight dynamics and stability of the vehicle is crucial in developing and improving its airworthiness standards. As such, the University of Glasgow was involved in research collaboration with the CAA between 1993 and 2010, to understand the aerodynamics of light autogyros in more detail [7, 12]. Two different types of light autogyros were used in Glasgow throughout the study, the VPM-M16 autogyro and the Montgomerie-Parsons (G-UNIV) research autogyro (as shown in Figure 1.1 and Figure 1.2).

Apart from the aerodynamic characteristics, the studies were also broadened into a bigger spectrum including the research on the stability, flight test and handling qualities [13–19]. The full report of the studies is also made available over the public domain under the CAA's Safety Regulation Group [7]. These results were eventually used to facilitate the improvement of the previous BCAR Section T to become an airworthiness requirement, the *BCAR Section T - Light Gyroplanes (Issue 3)* [20].

1.2 Main Goal and Objectives of the Research

The BCAR Section T [21] focuses on the airworthiness requirements and only includes minimum dynamic stability guidelines that must be complied by all light autogyros in the UK. These guidelines are applied to a production autogyro, and compliance is demonstrated through flight testing. The requirements, however, did not prescribe in detail the design criteria for an acceptable autogyro's flying qualities. Without formal flying qualities criteria, it is difficult for designers to build good flying qualities attributes into their designs. It is believed that the design of the new generation autogyros is totally depended on the individual understanding and capability of the designer. Consequently, it is also difficult for an old-generation unstable autogyro to be improved. From this point of view, it is then a strong necessity to have a specific flying qualities criteria for light autogyros, including the method of evaluating it. Whatever improvements are proposed, one must keep in mind the basic features of light autogyros that must be retained; the simplicity and the weight of the vehicle that has to be kept within the limit of a light autogyro according to the BCAR Section T standard. Hence, one possible way to improve the stability and controllability of these autogyros is to introduce a stability augmentation system through a simple automatic flight control hardware.

Therefore, the main goal of the research is,

> *To investigate if the flying qualities of light autogyros can be significantly improved using simple control techniques and actuator hardware, making them safer and an attractive vehicle to operators.*

To achieve the main goal of the research, several objectives have been achieved to serve the main goal and explained in the following.

1.2.1 Research Objectives

These are the objectives that have been carried out to achieve the main goal of the research.

(i) Propose Flying Qualities Requirements for Light Autogyros

It is well understood from the literature study that the longitudinal dynamic stability of the G-UNIV research autogyro used in the research resembles a mix of the stability characteristics of a conventional fixed-wing aircraft and helicopters. Due to these unique characteristics, the most suitable way to introduce a new flying qualities for an autogyro is by looking at the existing criteria of those two aircraft. Any suitable attributes of the existing criteria can be used for the light autogyro's flying qualities with proper comparison against the existing criteria. Since the longitudinal instability of lightly damped autogyros can cause severe pitch oscillation, the response of the vehicle must still be appropriate.

The proposed requirements focus on the time and bandwidth response of the vehicle to certain forms of pilot input. Additionally, the existing BCAR Section T requirements are used as underlying guidelines to ensure the new autogyro flying qualities standards are sensible. Specifically, for an autogyro, the flying qualities characteristics are divided according to the three different modes of flight; the short-period mode, the phugoid mode, and the rotorspeed degree of freedom. For the rotorspeed degree of freedom, due to the strong coupling with the pitch attitude, the G-force limit is introduced in the new autogyro flying qualities requirements to represent the rotorspeed degree of freedom. Evaluations of the flying qualities are also made according to the existing standards, whenever applicable.

(ii) Development of Nonlinear Mathematical Model Representing Light Autogyros

In this part of the thesis, the aim is to develop a nonlinear mathematical model of light autogyro in longitudinal flight. The development was based on the well-established *Helicopter Generic Simulation* package (HGS) [22] that features the 'multiblade' or 'rotor-disc' modelling approach which was originally meant for conventional helicopter modelling. The main reason for using this 'multiblade' modelling approach is because of its simplicity, which enables the model simulation to be performed in a simple machine with less computational run-time. This important features also enable the autogyro's mathematical model to be used in other applications such as flight controls and inverse simulations, without having computational run-time issues.

Since the autogyro mathematical model was developed from the existing HGS model, quite an extensive amount of modifications were made to meet the autogyro's flight dynamics attributes. One of the important features accounted for an autogyro is the rotorspeed degree of freedom as the vehicle flies in autorotating flight. Other important modifications have been considered for the modelling include the rotor kinematics, the aerofoil's lift and drag characteristics, the flapping dynamics and the rotor-disc dynamic inflow model. This significant amount of modifications accounted for an autogyro eventually contributed to the establishment of the *Autogyro Rotor-Disc Simulation* model or ARDiS.

(iii) Development of the Control Enhancement for Light Autogyros

The newly proposed flying qualities requirements are used as the basis for the study of stability augmentation systems for light autogyros. The real challenge in this stage is to find the most suitable feedback gains for the control enhancement to meet the attributes of good autogyro flying qualities. A linearised model of the autogyro is used to quantify and evaluate the vehicle's stability characteristics and later used to develop the controlled enhancement. At this stage, the control enhancement is considered as preliminary, since the hardware (servo-actuator and control linkages) are based on default values. The effectiveness of the control enhancement is evaluated by comparing the augmented and the basic aircraft responses against the proposed flying qualities criteria.

(iv) Development of Nonlinear Hardware Model for the Control Enhancement

This objective is required since there is no guarantee that the preliminary control enhancement will be successful when the real hardware is being deployed. The practicality of the flight controller has to be evaluated to ensure the control enhancement is realistic and achievable with the deployment of the real hardware. In any flight control system, the timely response of the vehicle's dynamic from the applied control input is very crucial. This response can be seen as quite related to the effectiveness of the servo-actuator and its control link mechanism. Hence, the most critical question to be asked is how long does it take for the actuator to move when the controller sends a command signal.

The real servo-actuator hardware model can be obtained, first by estimating the load requirement for the actuation system. Knowing the load requirement is essential so that the correct servo actuation size can be selected according to the size of the maximum estimated load. Estimation is done through rigid-body force and moment calculations of the mechanical linkages in trimmed flight, taking into account the aerodynamic forces applied at the rotor hub, which was obtained from the ARDiS model. The servo actuation system is then modelled

based on the given load estimation and a complete manufacturer's datasheet of the selected servo-actuator hardware. This actuation model includes its own actuation controller, which is then implemented in the autogyro configuration. The complete servo-actuator hardware model is assumed to represent the entire nonlinear dynamics of the servo-actuation, including the mechanical control linkages from the pilot input to the rotor hub. The deployment of this hardware model is done in both, linear and nonlinear form.

(v) Evaluations of the Light Autogyro Control Enhancement

At this stage, the aim is to implement the new servo-actuator model into the autogyro configuration, so that the same flying qualities evaluations can be done according to the proposed flying qualities requirements. As such, comparisons are made between the bare airframe model (unaugmented) and the one with the control enhancement in place (augmented). It is expected that the simulation results will be different with the new servo-actuator hardware model in place. This is due to the dynamics complexity of the new servo-actuation system, which could cause the performance of the control augmentation system to be degraded. Hence, it is expected that the controller to be fine-tuned to achieve the desired control performance. This fine-tuning, however, is an iteration process, which is quite cumbersome, but worthwhile. It is expected that the final result is improved flying qualities for the light autogyro.

Nevertheless, the results will not be perfect without the nonlinear simulation of the vehicle, with the fine-tuned nonlinear control enhancement in place. The complete nonlinear model will be tested against turbulence in the longitudinal flight mode, to have more confidence in the practicality of the control enhancement.

1.3 Thesis Outline

The thesis is outlined as follows. Chapter 2 presents a review of autogyro flying qualities. The chapter starts with an overview of flying qualities, and why the term 'flying qualities' is used in the study, rather than 'handling qualities'. A detailed overview of longitudinal stability and controllability issues being experienced by most old-generation autogyros is also discussed in the chapter, then followed by the survey on the main attributes of light autogyros, which differs from other aircraft. Since the flying qualities specification of light autogyros is not available, the flying qualities development in this chapter started with surveys of other flying qualities specifications, with more emphasise given on the existing BCAR Section T airworthiness require-

ments [20, 21]. The longitudinal flying qualities for light autogyros with the method of evaluation is then proposed as preliminary guidelines at the end of the chapter.

Chapter 3 describes the development of the Autogyro Rotor-Disc Simulation Model (ARDiS). The chapter started with an overview of different approaches being used in rotorcraft modelling and choosing the most appropriate one for the autogyro mathematical model. More emphasise were addressed on the development of the rotor model with many changes being composed on the blade mechanics, the rotor-disc inflow, and the blade flapping calculations. The development of other subsystems in longitudinal mode is also described in the chapter. Validations of the ARDiS nonlinear model are presented against the real flight data for the Montgomerie Parsons G-UNIV autogyro. Validations also include comparison with the established 'individual-blade' model (RASCAL), to gain more confidence in the newly developed ARDiS model. The ARDiS model is then linearised and defined as the basic airframe model, where it is then evaluated against the proposed flying qualities criteria at the end of the chapter.

The development of the control enhancement for light autogyros based on the linear longitudinal model is presented in Chapter 4. This longitudinal control enhancement is assumed to be a preliminary control enhancement, with a default actuator model being used. Evaluations are made for all longitudinal modes according to the proposed flying qualities criteria in Chapter 2. The control enhancement development in this chapter starts with the Stability Augmentation System (SAS) which is produced through conventional control feedback and pole placement method. This control enhancement is then compared with the basic airframe model according to the proposed flying qualities evaluation. The chapter then continues with another step in the development of the control enhancement strategy, in which Rate-Command Attitude Hold (RCAH) is introduced on top of the previously implemented augmentation system. Finally, the autogyro model is re-evaluated with the RCAH controller in place according to the proposed flying qualities criteria.

Chapter 5 presents the modelling of the control hardware of the autogyro, which is later used as part of the autogyro's hardware configuration. The initial part of the chapter describes the servo-actuator with its mechanical control linkages, which plays a significant role in determining the effectiveness of flight control implementation. The earlier section explains how the mechanical linkage forces are estimated through rigid-body calculations. The following section of the chapter describes the modelling of the G-UNIV mechanical linkages through physical modelling technique. This modelling also includes the servo-actuation control according to a specific servo bandwidth and damping ratio requirement. The succeeding section reveals the simulation results of the actuation model. This section also presents the complete nonlinear model of the

real servo-actuation dynamics, which includes the dynamics of the mechanical control linkages that physically connected with the servo-actuator unit. The linearised model of the servo-actuation is shown in the last part of the chapter, where it is employed into the autogyro configurations.

Chapter 6 describes the final flying qualities evaluation of the control enhancement with the actual servo-actuator model (obtained in Chapter 5) implemented into the G-UNIV configurations. The evaluations started with the unaugmented response of the vehicle, in which comparison is made between the new servo-actuator hardware model and the default (theoretical) actuator model. Evaluations are then carried out for the G-UNIV with SAS control enhancement and then followed by the model with the RCAH controller in place. Prior to this, the controllers were fine-tuned since the new servo-actuator model degrades the flying qualities of the augmented autogyro. The fine-tuning process eventually produces entirely different feedback gains which significantly improves the flying qualities of the augmented autogyro. The last part of the chapter describes the nonlinear simulation with the fine-tuned RCAH controller in place. Turbulence in terms of longitudinal discrete gust is also introduced into the simulation to gain a better confidence on the practicality of the control enhancement model.

Chapter 7 presents the conclusion of the research and some recommendations for future works.

Chapter 2

Review of Autogyro Flying Qualities

2.1 Introduction

The widespread application of fixed-wing aircraft and helicopters in military and commercial sectors contribute to their flying qualities establishment as early in the history of flight. Light autogyros, in contrast, started to emerge in the last twenty years, with an alarming number of incidents and accidents, as reported earlier in Chapter 1. These poor safety records have raised concerns amongst regulatory bodies around the world which were also discussed earlier. However, it is difficult for designers to improve this condition and to build an autogyro with good attributes into their design without formal flying qualities guidelines. Therefore, this chapter aims to study and propose flying qualities requirements for light autogyros. Hence, the chapter precedes with a review of existing fixed-wing and helicopters flying qualities requirements, and to identify those requirements that are directly applicable to light autogyros. A preliminary flying qualities requirements for light autogyros are then proposed at the end of the chapter, and used as the minimum guideline for the G-UNIV control enhancement in this thesis.

It is understood that to develop proper flying qualities requirements requires an iterative process with years of quantitative and qualitative investigations, including good assessment programme. Hence, it is important to note that, this chapter is not targeting in assessing the proposed flying qualities criteria, but to use it as a guideline for the control enhancement of the G-UNIV autogyro in this study.

2.2 Flying Qualities Versus Handling Qualities

In the early days during the establishment of the first aeroplane requirements, flying qualities were associated with the aeroplane's stability and control characteristics including flight safety as specified by Gilruth in 1943 [23]. In the requirements, Gilruth defines the aeroplane's flying qualities criteria that closely associated with flight dynamics and controls without involving pilots handling issues. Another study made by Phillips [24] in 1949 added the element of pilot impressions in achieving the flight safety of Gilruth's requirements. The concept highlighted by Phillips was that an aeroplane is quantitatively designed according to a specific goal or mission, but the adequacy of the flying is qualitatively based on the pilot opinion. Later, with new features on modern aircraft such as the stability augmentation system, the subtle differences between flying and handling qualities are more difficult to see. Since then, aircraft standards and specifications have evolved significantly with more research and findings that have led to more requirements, which complicates the definitions of flying qualities and handling qualities. The term 'flying qualities' is used by most aircraft standards and specifications to refer to the stability and control characteristics in achieving a particular pilot mission [25–28]. However, the specific levels of pilot opinions that reflect to specific stability characteristics in the earlier standards were not addressed in a standardised form. These stability characteristics were entirely based on subjective opinions of the pilot, which eventually led to the establishment of handling qualities requirements. The requirements include both, the flying qualities characteristics and specific standards which represent the pilot-aircraft interactions in achieving a particular flight mission as specified in [29, 30].

A clear distinction between flying and handling qualities has been reported by Andrews [31] and cited by Padfield [32], which defines flying qualities as anything related to the aircraft's stability, controllability and manoeuvring characteristics. Handling qualities, however, are defined as the combination of flying qualities and the capability of the vehicle to meet a specific mission task and visual cues, which is quite subjective. Additional factors that are affecting the mission task, such as the ergonomic design and environment of the cockpit are also considered as part of handling qualities. In fact, some references distinguish handling qualities as the external factors that influence the pilot's handling, even though the aircraft has excellent flying qualities attributes [33, p.4]. These external factors include the ergonomic design of the cockpit such as pilot seating, and the variety of instruments display in the cockpit that influences pilot workloads in achieving a particular flying mission.

Hence, it is now clear that flying qualities are regarded as internal within the aircraft,

which provide good stability and controllability. Handling qualities, however, are the quality of pilot-aircraft interactions to successfully achieve a particular mission task. Since the primary objective of this research is to improve the flight stability of a light autogyro through automatic control approach, it is then appropriate to use the term 'flying qualities' rather than 'handling qualities' throughout the thesis. In fact, flying qualities are measurable through computational simulation, but handling qualities require pilot opinions through flight test or piloted simulation which is beyond the scope of this study.

2.3 Stability and Controllability of Autogyros

In the early days when autogyros start to become popular, the flight dynamics of the vehicle were not fully understood. Failing to understand the correct ways to handle this type of aircraft have led to catastrophes as highlighted earlier. As such, early studies at the University of Glasgow were aimed at understanding the general aspects of the vehicle's aerodynamic stability by the effects of various design configurations. That was the first time where the higher fidelity, 'individual-blade' mathematical model was used to quantify the dynamic stability of the vehicle [13, 34–36]. It was discovered from the studies that typical autogyros have an oscillatory type short-term and phugoid dynamic response to perturbations. This behaviour also resembles the longitudinal dynamic stability of a conventional fixed-wing aircraft. Moreover, the phugoid oscillation was seen to be either lightly damped or unstable, depending on the vertical location of the propeller thrust line relative to the vehicle's *centre of gravity* (CG).

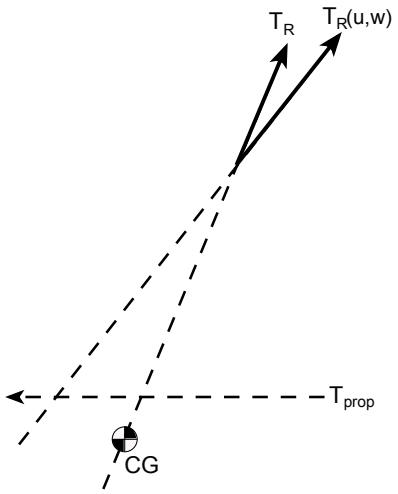

Figure 2.1: Illustration of the CG located below the propeller thrust line

The studies also suggested that the unstable phugoid mode contributes to handling difficulties, mainly if the CG is located lower than the propeller thrust line, as shown in Figure 2.1. The rotor thrust, $T_R(u, w)$ is supposed to balance the propeller thrust, T_{prop} in equilibrium flight. Moreover, in the event of high turbulence or abrupt manoeuvre, the possibility of having a negative rotor thrust is higher, which will cause the rotorspeed and lift to decay significantly. This condition also causes the propeller thrust to be dominant, thus causing a negative pitch moment (nose-down) and put the whole vehicle in a dangerous flying situation. This situation would lead to catastrophe if the unbalanced forces failed to be augmented by the pilot. Hence, the capability of the pilot to maintain a positive rotor thrust in autorotating flight is crucial in such an event.

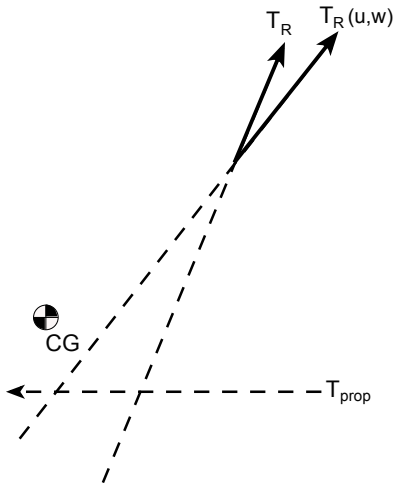

Figure 2.2: Illustration of the CG located above the propeller thrust line

On the contrary, an autogyro that is configured to have the CG located above the propeller thrust line will be more stable in most flight conditions, as shown in Figure 2.2. In steady-state flight, the propeller thrust contributes to a positive pitch moment (nose-up), which is balanced by the rotor thrust. In the event of abrupt manoeuvre that reduces the rotorspeed and lift, the autogyro will be pitched up and causes an aft tilt of the rotor disc. This condition will eventually trigger a positive rotor thrust and improve stability by increasing the rotorspeed and lift. It was also suggested that the stability of an autogyro is enhanced if the rotor thrust line falls further behind the CG. This configuration will promote better stability augmentation in any circumstances or flight conditions, as the rotor thrust line will not exceed the CG.

Further investigations on this unique configuration parameter were also done through flight trials, in which, the influence of external forces and moments relative to the vehicle's CG were quantified [14, 16, 37–39]. All results appeared from these studies

were found to be consistent, which pointed out the propeller-rotor thrust ($T_R - CG - T_{prop}$) relationship that mainly contributes to the longitudinal stability of an autogyro. Furthermore, the $T_R - CG - T_{prop}$ interaction was also seen to provide the angle-of-attack stability or pitch stiffness of the vehicle. For a typical aeroplane, the pitch stiffness is solely contributed by the CG-wing lift relationship.

Another important configuration parameter of light autogyros is the tailplane. The effectiveness of the tailplane for an autogyro was investigated and reported by Houston [40]. The tailplane or horizontal stabiliser was first introduced as the basic configuration for a conventional aeroplane to provide the primary pitch damping and static stability. Conversely, for typical helicopters, the tailplane provides the angle-of-attack stability rather than primary pitch damping. Since the lift, forward thrust and controls of a helicopter are all integrated through the main rotor, the flapping dynamic of the main rotor also contributed to the primary pitch damping of the helicopter. As for a traditional autogyro, the same principle also applies where the rotor provides the primary pitch damping, while the tailplane provides the pitch stiffness for the vehicle. However, the tailplane was reported to be less effective due to several factors that will be explained in the following paragraph.

There were at least three factors highlighted by Houston [40] that influenced the effectiveness of the tailplane and affecting the overall longitudinal stability of traditional light autogyros. Two light autogyros were used in the study, the VPM-M16 and the Montgomerie Parsons G-UNIV autogyro. The first factor was the horizontal location of the tailplane relative to the CG, which is related to the tailplane 'volume ratio'. The rule-of-thumb formula used for the horizontal stabiliser size was first established by Cierva [2], who proposed the tailplane volume ratio that should be around 12% to 15% of its rotor volume. Cierva defined the horizontal tailplane volume as the multiplication of the tailplane area with the arm length of the tailplane, of which was defined as the horizontal distance from the rotor hub to the 1/4−chord line of the tailplane. Consequently, the formula was effectively tested on Cierva's tractor-type propeller with a long fuselage configuration, similar to a typical tricycle aeroplane. However, Cierva's autogyro configuration was seen to be different as compared to today's pusher-propeller type autogyros, with shorter fuselage and empennage. Shorter empennage also means shorter moment arm to provide pitch damping in response to perturbation. The second factor was the tailplane surface area, which also corresponds to the angle-of-attack and the rotor downwash blockage. A bigger surface area directly increases the dynamic pressure of the tailplane surface that came into contact with the relative wind, thus, contributes to the pitch stability. Conversely, the bigger rotor downwash blockage reduces the dynamic pressure, thus the effectiveness of the tailplane. Similar study was also done by Laine [41] on a VPM M16 autogyro that have shown the effects of the

tailplane with different surface area in the vehicle's longitudinal stability. The third factor was the vertical location of the tailplane relative to the propeller slipstream. It was found that the highest tailplane effectiveness can be achieved if the tailplane is located just within the propeller arch. Off all these factors, the moment arm distance of the tailplane was seen to be the obvious factor that influences the pitch damping of the vehicle, thus affecting the short-period oscillation. This characteristic was also supported by Duda et al. [42] which indicated a significant relationship between the tailplane and the short-period pitch damping of the MTO-Sport autogyro used in their research.

Therefore, it can be presumed that the longitudinal dynamic stability of an autogyro largely depends on the dynamic behaviour of the rotor and propeller thrust relative to the CG in response to abrupt wind gust or disturbance in flight. The G-UNIV research autogyro, for example, besides having a less effective tailplane, the propeller hub was located about 3-inches above the CG, thus rendered a lightly damped short-period mode and slightly unstable phugoid oscillation [38, 39]. In contrast, the VPM-M16 autogyro was reported to have more stable short-period and phugoid mode, since the vehicle was designed with better tailplane effect and with propeller hub located just 1-inch above the CG. Managing a proper rotor thrust and rotorspeed, especially at higher airspeed is difficult for an inexperienced pilot and requires some form of augmentation system to maintain the autogyro in the safety margin. This safety margin will be discussed later in the following sections.

2.3.1 Autogyro Safety Track Record

The uprising popularity of autogyros in the past decades have raised many concerns among the aviation authorities, due to the increasing amount of incidents involving this type of vehicle. This matter was addressed earlier in Chapter 1, with regards to several ten-year safety review reports presented by the CAA, the the CAP735 (1992-2001) and CAP780 (1998-2007) [8,9]. According to the CAP735, 29 autogyro accidents were reported, in which 5 of the accidents were fatal. The later CAP780 reported 25 autogyro accidents, with 8 fatalities. Additionally, on the European counterpart, a five-year Annual Safety Review (2008-2012) produced by the European Aviation Safety Agency (EASA) reported an annual average of 18.6 accidents, with 4.4 average fatal incidents [43]. In the year 2013 alone, 17 accidents were reported from the same review with 6 fatalities. Table 2.3.1 shows some of the reported accidents which related to the autogyro's longitudinal stability in the UK and USA. All data are accessible from the UK "Air Accidents Investigation Branch" (AAIB) and the US "National Transportation

Safety Board" (NTSB).

These incidents were also perceived to be related to the so-called 'Aircraft-Pilot Coupling' or APC, following a longitudinal instability. An APC in this context is referring to an unintended or unexpected event that occurred between the aircraft and the pilot that leads to an unwanted flying condition, which jeopardises the safety level of the aircraft in flight. Unwanted APC events are mostly observed from aircraft with design deficiencies in the stability, which can lead to a form of an adverse coupling between the pilot and the aircraft [55–57]. The 'Pilot-Induced Oscillation' or PIO is one of it and discussed in the next section.

2.3.1.1 Pilot-Induced Oscillation (PIO)

There have been many definitions of PIO as it occurs at different flight states and phases. McRuer [56] defines Pilot-Induced Oscillation (PIO) as

"...an inadvertent, sustained aircraft oscillation which is the consequence of an abnormal joint enterprise between the aircraft and the pilot."

MIL-STD-1797A [28] defines PIO in its general stability requirement as

"...pilot-induced oscillations, that is, sustained or uncontrollable oscillations resulting from the efforts of the pilot to control the aircraft."

Not much work has been done to understand about PIO on a typical autogyro which is reported in the public domain, except a report that was made by Beaty [58]. Beaty highlighted about the so called 'buntover', 'porpoising' or 'negative-g' phenomena that happened in many autogyro incidents were actually identified as PIO. In his report, PIO is defined as a closed-loop interaction between pilot and the autogyro that turned into a divergent oscillation which can lead to a catastrophe. An autogyro that is marginally stable will have a higher tendency of getting into PIO due to at least one of these two factors. Firstly, if the autogyro involved in the situation where the pilot failed to maintain a positive rotor thrust, following a steep manoeuvre with an adverse 'g' condition. Secondly, if the vehicle involved in an unintended perturbation following an external event, of which the pilot failed to overcome. The external event in this instance can be caused by the atmospheric condition, such as turbulence and wind gust. In both cases, a prompt action by the pilot is crucial, as a slow corrective action will cause sequential delay in the vehicle's response time. This will eventually caused

Table 2.3.1: Fatal accidents involving autogyros in the UK and USA

Date	Autogyro Type	Accident Location	Accident Description	Remark
Dec 1993	Bensen	Dorset, UK [44]	Crashed during steep climb	Loss of positive disc loading due to steep manoeuvre, which causes a rapid decay of rotorspeed and lost of lift
Apr 1996	Air Command	Warwickshire, UK [45]	Tumble vertically to ground	Vehicle descended with decaying rotorspeed before tumbled inversely
Apr 2000	Bensen	Carlisle, UK [46]	Crashed during attempt to land	'Power pushover' following the loss of rotor lift at steep manouevre
June 2001	Cricket	Somerset, UK [47]	Crashed on approach	Lateral control being applied while rotor was unloaded condition following an induced oscillation
May 2002	RAF 2000	Essex, UK [48]	Started to break up and fell vertically	Rotor blade struck the vertical fin and rudder, due to pitch instability occurrence
June 2003	Bensen	Norfolk, UK [49]	Rudder struck by rotor blade	Pilot induced oscillation due to longitudinal instability
June 2006	RAF 2000	Cornwall, UK [50]	Vertical stabiliser, propeller and rudder struck by the rotor blade	Most probably a rapid positive pitch cyclic to overcome a 'power pushover' occurrence
Sept 2010	Rotorsport	Cumbria, UK [51]	Rotor blades struck the ground, causes damage to rotor, fuselage and propeller	Student pilot did not apply aft cyclic accordingly during takeoff, caused the rotor to decelerate and stall, before crashed
Dec 2012	Charland Vortex	Wellton, AZ [52]	Autogyro hit terrain following a loss of control	Pilot failed to maintain control at low altitude, caused the autogyro descending at 45° nose down and crashed
Apr 2013	Daniels Dominator	Valkaria, FL [53]	Loss of control in flight	Pilot failed to maintain adequate power and airspeed, caused abrupt pitched down and up before loss of lift and crashed
Mar 2016	Bensen	Bryant, AR [54]	Autogyro porpoising following loss of control in flight	Pilot failed to control in rough turbulence caused aircraft to 'porpoised', before entering a 'power push-over' condition and summersaulted to the ground

a pilot-in-the-loop oscillation as the pilot keep on applying the stick action without being noticed that the vehicle has already responded.

As explained previously in section 2.3, the longitudinal dynamic stability of a typical autogyro is lightly damped with the phugoid stability mode close to the unstable condition. In fact, since the vehicle's CG is located a certain vertical distance above or below the propeller thrust line, the pitch moment produced adds to the complexity in stabilising the aircraft in extreme dynamic event. Moreover, the rotorspeed degree of freedom added further to this complexity as it couples with the rigid-body mode of motion. The flight attitude must be managed properly in sustaining positive airflow through the rotor disc to maintain the rotorspeed and thrust, thus balancing the pitching moment from the propeller thrust.

Autogyros involved in the catastrophic events in Table 2.3.1 were seen manoeuvring with extreme pitch attitude when the rotor suddenly loses its rotational speed, and thus lift. In few cases, the pilot failed to recover the rotorspeed and lift, causing the propeller thrust to become dominant and creating a negative pitch moment and causing the autogyro to 'forward tumble' or 'buntover'. When this happens, it is too late for the pilot to correct the condition and often leads to a crash. In few other cases, pilots applied large inputs of longitudinal cyclic when they were trying to pitch up the rotor disc to gain control on the rotorspeed. Unfortunately, this large cyclic input causes the blade tip to strike the vertical fin or the propeller blade tip and leads to the crash. It is believed that a fast and correct action of the pilot might minimise such event, but this is only possible for pilots with extensive autogyro flying experience. Additionally, failing to take the corrective action promptly would also cause a phase lag and lead to an adverse reaction of the vehicle, rather than stabilising it. Since the pilot is the most 'unpredictable' element in this control event, enhancing the dynamic stability of the autogyro through an active control can be one of the solution.

2.4 Flying Qualities Specifications

It has been mentioned in the earlier chapter that having a formal flying qualities criteria for autogyros is now becoming a necessity so that proper improvement can be made for light autogyros that were designed with stability issues. It was also known from previous studies that the dynamic stability characteristics of light autogyros resembled a mix attributes between conventional aeroplanes and helicopters. Hence, it is then a necessity to look at the existing flying qualities requirements of those two aircraft,

before recommending the new requirements for autogyros according to the applicable criteria of the two aircraft. However, the existing autogyro's BCAR Section T airworthiness requirements will be used as the underlying guidelines to ensure a reasonable new flying qualities criteria.

2.4.1 BCAR Section T - Light Gyroplanes

The UK's BCAR Section T is a legislation that was established for light autogyros to ensure the minimum airworthiness requirements of an autogyro are complied with [21]. The requirements were first established as Issue 1 in 1995, adopting the airworthiness criteria for small rotorcraft from the JAR-27 requirements. Issue 2 followed in 2001 without any new technical changes, accept some restructuring according to JAR-EASA specifications. The only significant changes in the technical requirements for light autogyros were released as Issue 3 in 2005. In this issue, the changes in the BCAR Section S (fixed-wing light aircraft) were adopted and equally applicable to the BCAR Section T. The Issue 4 of Section T was then released in 2011, which incorporates a significant amount of technical changes, based on the studies made by the University of Glasgow on the aerodynamics and stability characteristics of autogyros. Consequently, more changes were made on the BCAR Section S which also reflect the changes in Section T. Issue 5 of the Section T was then released in 2013 with additional changes based on the Section S. Therefore, the BCAR section S specifications will not be included in the study, as most specifications of Section S that are applicable for light autogyros were adopted into Section T.

BCAR Section T specifies the fundamental airworthiness requirements to ensure the safety of all light autogyros operated in the UK. The standards, however, did not prescribe in detail the design criteria for autogyros flying qualities. It only provides the minimum requirements for dynamic stability that can be used as fundamental guidelines for safe flight, thus ensuring the autogyro is airworthy.

The general airworthiness standards in the BCAR Section T are divided into two major parts; Part 1 - *Requirements*, and Part 2 - *Acceptable Means of Compliance and Interpretative Material (AMC)*. Each part is then divided into subsections, and only one subsection addresses the requirements related to flying qualities, which is Subsection B - *Flight*. In Subsection B under Part 1, there are requirements that cover the elements of *controllability* and *manoeuvrability* (T143 to T155), the elements of *stability* (T171 until T181), and *ground handling* (T231 until T241). Detail descriptions of these requirements are explained in Part 2 of the standards. Dynamic stability requirements

are defined in Subsection T181 [21] as,

a) *Any oscillations occurring under any permissible flight condition must be damped both with the primary controls fixed and free for longitudinal and lateral controls but fixed for the yaw control.*

b) *The gyroplane, under smooth air conditions, must exhibit no dangerous behaviour at any speed between the speed for best rate of climb and never-exceed-speed, when all controls are fixed or free for a period of 5 seconds.*

Additionally, the AMC T181 in Part 2 Subsection B [21] explains the above dynamic stability requirements as

Longitudinal, lateral or directional oscillations with controls fixed or free for longitudinal and lateral controls (but fixed for the yaw control) and following a single disturbance in smooth air, should at least meet the following criteria:

(a) *Any oscillation having a period of less than 5 seconds should damp to one half amplitude in not more than one cycle. There should be no tendency for undamped small amplitude oscillations to persist.*

(b) *Any oscillation having a period between 5 and 10 seconds should damp to one half amplitude in not more than two cycles. There should be no tendency for undamped small oscillations to persist.*

(c) *Any oscillation having a period between 10 and 20 seconds should be damped, and in no circumstances should an oscillation having a period greater than 20 seconds achieve more than double amplitude in less than 20 seconds.*

Later in the same section also describes how the disturbance can be initiated and assessed for an autogyro, with in-flight adjustable trim control, and for the one which is not equipped with one [21]. The paragraphs state that

For gyroplane with an in flight adjustable variable trim control, where possible, the gyroplane should be trimmed at the required flight condition. The disturbance can then be introduced by moving one primary flight control to an out-of-trim position in one of axis sufficient to change the attitude of the gyroplane by approximately 5 degrees with the other primary flight control held and immediately returning it to its original trim position. If assessing stick (or yaw control) fixed rather than free, the stick (or yaw control) should be held with normal control force once returned to trim. Initially, a

small input should be employed, sufficient to generate an attitude rate of no more than approximately 3 - 5 deg/sec. The amplitude of the input can then be incrementally increased to generate an adequate pitch rate in the order of 5 - 10 deg/sec. Extreme caution must be exercised during this evaluation, particularly when considering the potential for rapidly reducing 'g', either as a direct result of an input, or as an indirect result during the ensuing phugoid response. Consideration should be given to some form of measurement of structural clearances for this testing, for example 'video camera'.

For those gyroplanes which do not have a variable trim control or which have a variable trim control with insufficient authority to trim at all conditions, the method of exciting the oscillation is the same and the control must be returned to its original position and then fixed if assessing "stick fixed" stability or held loosely without applying any force for "stick free". As it may not have been possible to establish a trim condition with zero control force, care must be taken to ensure that the control is returned to datum following the disturbance.

The above descriptions are seen to have been moved further from simple dynamic stability criteria in previous issues [20] to more comprehensive criteria, at least for the dynamic stability of the vehicle. The descriptions did not only emphasise on the short-period type of oscillation as in the previous issue, but also for all type of oscillations, especially the phugoid mode. The most probable reason for this is because of the T_R-CG-T_{prop} configuration of a typical autogyro, which affects both, the short-period and the phugoid oscillation. Although the short-period mode is lightly damped due to this configuration, the phugoid might resemble unstable oscillation that might slowly divert the vehicle and led to PIO. In fact, the FAA's "Rotorcraft Flying Handbook" mentions that the PIO in phugoid mode is more pronounced at the higher airspeed and difficult to be recognised by an inexperienced pilot that flies an autogyro with a limited flight instrument [59, p.21-2].

Special caution on the 'g' force rapid changes is also mentioned in the Section T and possibly considered as a unique requirement for a light autogyro to comply with. It can be observed from the list of fatal events in Table 2.3.1 that most accidents resulted from PIO in the short-period mode were caused by abrupt pitch manoeuvres, which triggers a 'zero' or 'negative g' condition. This situation eventually causes a reduction of positive airflow through the rotor disc, thus unloading the rotor. A study of rapid 'g' force manoeuvres of the G-UNIV autogyro was made by Gallup [60], which supports the concern about the pitch instability related to the 'g' force. Therefore, it is important to obligate this unique characteristic into the vehicle's flying qualities requirements, but how this can be quantified or implemented are discussed in Section 2.5.3.

2.4.2 Aeroplane Specifications

Since the longitudinal stability characteristic of a typical light autogyro resembles a mix between conventional fixed-wing aircraft and helicopters, the flying qualities standards of light autogyros can be quantified by reviewing the existing standards of both aircraft categories. Two significant and well established fixed-wing design specification were reviewed, the MIL-F-8785C and the MIL-STD-1797A [27, 28]. The MIL-F-8785C specification was first established as MIL-F-8785 in 1954 by the US Air Force with simple dynamic stability requirements in terms of damping and time domain response. This specification later went through stages of revisions, the MIL-F-8785A(USAF) in 1968 and MIL-F-8785B(ASG) in 1969. The later revision, the widely known MIL-F-8785C was consequently established in 1980, which was more of a flying qualities standard rather than handling qualities standard for fixed-wing aircraft [61]. The other specification, MIL-STD-1797A was established as a handling qualities standard for fixed-wing aircraft under the US Military. It was initially established as the MIL-STD-1797(USAF) in 1987 and later superseded by the MIL-STD-1797A in 1990 with more complete handling qualities requirements for piloted aircraft [61]. This standard was then turned into a handling qualities handbook, the MIL-HDBK-1797 in 1997, with all standards in the MIL-STD-1797A being preserved [28]. Later in 2004, the MIL-STD-1797A was reinstated back as a design standard and supersedes the MIL-HDBK-1797 handbook [62–64]. The two standards are described in more detail in Section 2.4.2.1 and Section 2.4.2.2.

2.4.2.1 MIL-F-8785C

The MIL-F-8785C [27] specifies all fixed-wing aircraft type under four general classifications, *Class* I - IV, based on the size and usage of the aircraft. Furthermore, the specification also categorises fixed-wing aircraft based on their operational objectives, either Category A, B or C *Flight Phases*. Since a light autogyro is restricted in the BCAR Section T [21] with a maximum weight 600 kg, obviously this vehicle is fallen under the Class I, Category B flight phase aircraft, according to the MIL-F-8785C.

MIL-F-8785C define Class I aircraft as,

"*Small light aircraft, such as light utility, primary trainer, and light observation craft (max. weight ≈5000kg)*",

while Category B flight phase is defined as

"*Those nonterminal Flight Phases that are normally accomplished using gradual maneuvers and without precision tracking, although accurate flight-path control may be required*".

Table 2.4.1: Flying Qualities level of acceptance (MIL-F-8785C) [27]

Flying Qualities Level	**Minimum condition requirement**
Level 1	Flying qualities clearly adequate for the mission flight phase
Level 2	Flying qualities adequate to accomplish the mission Flight Phase, but some increase in pilot workload or degradation in mission effectiveness, or both, exists
Level 3	Flying qualities such that the airplane can be controlled safely, but pilot workload is excessive or mission effectiveness is inadequate, or both. Category A Flight Phases can be terminated safely, and Category B and C Flight Phases can be completed

It is important to understand that the MIL-F-8785C flying qualities requirements were meant for an unaugmented pilot controlled aeroplane, in which the criteria were based on the capability of pilots to control and stabilise the aeroplane. The static and dynamic stability requirements in MIL-F-8785C are given in three different level of acceptance, *Level 1*, *Level 2* and *Level 3*, as described in Table 2.4.1. As such, it is important for a conventional aeroplane not equipped with stability augmentation system to have Level 1 flying qualities criteria.

The longitudinal stability requirements for this standard specifies a few qualities in longitudinal flight, such as the static stability relative to the speed, phugoid stability, flight-path stability, the short-period sensitivity with respect to the frequency and acceleration, the short-period damping, and the gradient of controls in manoeuvring flight. The stability requirements in this MIL-F-8785C standard are seen to be similar to the UK's DEF-STAN 00-970 standard [65].

Only suitable requirements will be discussed in this part with the consideration of the

normal flight phase of a light autogyro.

(A) Static stability relative to the airspeed

This requirement is specified for Level 1 and Level 2 flying qualities that there shall be no tendency for aperiodic divergence for the airspeed, following a small disturbance from trim, with the control stick fixed and free. For instance, a 'pull' position of the control stick will force the aircraft to nose-up, thus decreasing the airspeed due to changes of the angle-of-attack and put the aircraft in a convergent oscillation.

(B) Phugoid Stability

The requirements specify the long-period oscillation or phugoid mode, where the aircraft will stabilise its airspeed following a disturbance. The phugoid requirements are shown in Table 2.4.2. For the case of an unstable phugoid which produces a divergent oscillation, the "Time-to-double" amplitude can be obtained by

$$T_{2_{ph}} = \frac{-0.693}{\zeta_{ph}\,\omega_{n_{ph}}}$$

where $\omega_{n_{ph}}$ is the undamped natural frequency of the phugoid mode.

Table 2.4.2: Damping requirements for Phugoid Mode (MIL-F-8785C) [27]

Flying Qualities	Phugoid Damping, ζ_{ph}
Level 1	≥ 0.04
Level 2	0 (stable)
Level 3	"Time-to-double", $T_{2_{ph}} \geq 55$sec

(C) Short-Period Stability

The short-period mode requirements are more related to the changes of pitch attitude due to the changes of angle of attack of the aircraft, regarding its damping and natural frequency. The short-period oscillation in this standard is assumed to be produced by an abrupt pitch control input from the trim condition at a constant airspeed. The

short-period damping requirements for all flying qualities levels are shown in Table 2.4.3 [27].

Table 2.4.3: Damping requirements for short-period mode [27]

	Level 1		Level 2		Level 3
Flight Phase	ζ_{sp} min	ζ_{sp} max	ζ_{sp} min	ζ_{sp} max	ζ_{sp} min
Category A	0.35	1.30	0.25	2.00	0.15
Category B	0.30	2.00	0.20	2.00	0.15
Category C	0.50	1.30	0.35	2.00	0.15

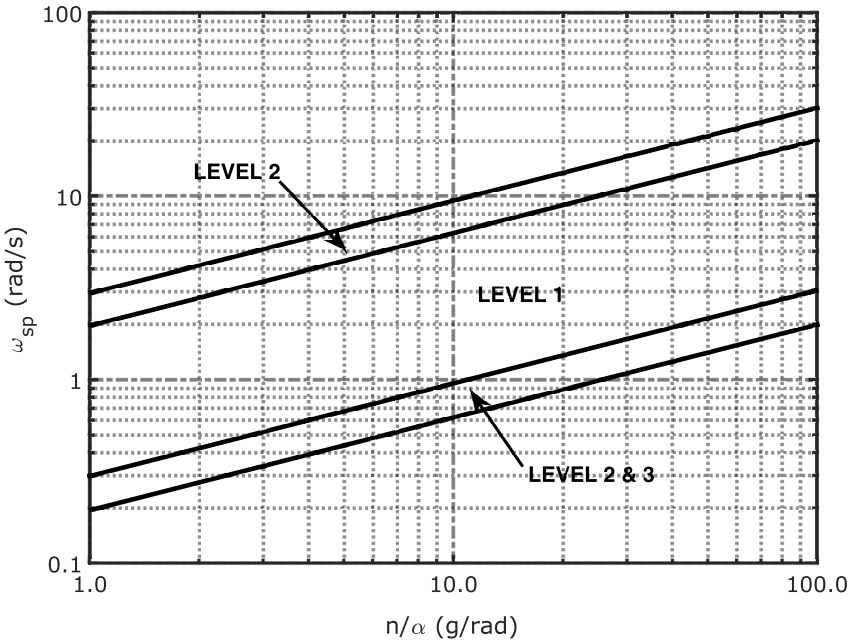

Figure 2.3: Short-period mode frequency requirements for Category B, all classes (MIL-F-8785C) [27]

Figure 2.3 shows frequency requirements of short-period mode Category B flight phase, which covers all types of aircraft. One of the important parameters included in the plot is the acceleration sensitivity (n_α), which is defined as the changes of normal acceleration per unit angle of attack changes due to the short-period oscillation. However, this standard does not quantify the acceleration sensitivity in detail. In fact, there are at least three important parameters within the short-period mode assessments; the acceleration sensitivity, the control anticipation parameter and the incidence lag. These parameters are also covered in the MIL-STD-1797A requirements [28] in Section 2.4.2.2.

It was earlier understood the fact that the short-period mode of light autogyros exhibits lightly damped with a higher frequency of oscillations, which is more akin to helicopters, rather than fixed-wing aircraft. Due to the concern about PIO excited from the short-term oscillation, the PIO prevention criteria for the short-period mode are then becoming crucial for autogyros. Generally, the frequency and acceleration sensitivity criteria of Figure 2.3 are relevant for the short-period mode evaluation of light autogyros, but might not be enough for the PIO evaluation. For the phugoid oscillation, it was also understood that the phugoid mode of typical autogyros resembles either lightly damped or unstable oscillation. Hence, the phugoid criteria of Table 2.4.2 are applicable and can be used as the basis of light autogyros flying qualities criteria.

2.4.2.2 MIL-STD-1797A

In general, the MIL-STD-1797A covers the same fundamental flying qualities criteria that were covered in the MIL-F-8785C, except with additional criteria that include qualitative requirements for handling qualities [28]. The longitudinal stability requirements in this standard also include the new bandwidth and time delay criteria, of which was not covered in the previous MIL-F-8785C.

The short-period pitch response criteria are commonly defined in terms of time and frequency. For the MIL-STD-1797A, the requirements for short-period dynamic stability is based on the Control Anticipation Parameter (CAP). The CAP in this document was defined based on the work reported by Bihrle [66] as, the ratio of initial pitching acceleration to the steady-state normal acceleration (the pseudo-steady state corresponding to the two-degree-of-freedom short-period approximation). Since the MIL-STD-1797A is meant for aeroplane's handling qualities criteria, the CAP evaluation can be done qualitatively through pilot opinion. When pilot applies a pitch control input, the aircraft will produce a pitching moment with a certain rotational pitch acceleration until a certain steady-state pitch angle is reached. Prior to this, the pilot must be able to anticipate the aircraft response to this control, based on the gradient of the control is being applied. For an aircraft with a good short-period pitch damping, the pilot will be able to precisely predict the longitudinal flight path of the aircraft, thus able to manoeuvre the aircraft correctly with less pilot workload. In contrast, a lightly damped or unstable aircraft will put the pilot in a difficult situation to predict the response of the aircraft prior to this pitch control input, thus unable to manoeuvre the aircraft correctly along the longitudinal flight path and increasing pilot workload.

The CAP can also be quantified analytically and given by

$$\text{CAP} = \frac{\dot{q}_o}{n_\alpha} \tag{2.4.1}$$

where $\dot{q}_o$ is the instantaneous pitch acceleration experienced by the aircraft due to the pitching moment produced by the control input, and n_α is the steady-state normal acceleration, also known as the acceleration sensitivity.

From Bihrle's definition, the CAP is analytically calculated based on the reduced order model of the short-period mode of the aircraft. In fact, this short-term oscillation is difficult to assess with a higher order model or full order, due to the phase lag associated with it. Hence, reducing it to the low order equivalent system is the solution, and this has been quantified by Cook [33, p.262]. Since the response of the aircraft to the short-period oscillation are mostly affected by the pitch damping and the natural frequency, the CAP is then written by

$$\text{CAP} = \frac{\omega_{sp}^2}{n_\alpha} \tag{2.4.2}$$

where ω_{sp} is the undamped natural frequency of the short-period mode of the aircraft. The CAP criteria guideline of Category B flight phase for all aircraft types has been shown previously in Figure 2.3. The diagonal lines in the figure indicate the suitable frequency and acceleration sensitivity in the short-period mode according to the satisfactory level. Additional CAP guidelines for the satisfactory level of flying qualities that reflect the short-period damping ratio criteria are also shown in Figure 2.4. All these were obtained from the derived reduced second order transfer function of the short-period mode.

In the real world of a dynamic system, the dynamic responses of the system always exist in a duality form, between the time response and frequency responses. As such, the flying qualities guideline in the MIL-STD-1797A requirement included both, the time-domain and the frequency-domain criteria. Figure 2.5 indicates the phase delay and the bandwidth criterion of Category B flight phase for the short-period mode, adapted from the MIL-STD-1797A requirement. This criterion actually indicates the pitch attitude response to the control input in bandwidth form. For a longitudinal pitch response, the basic time delay is referred to the time lag between the applied control input and the actual time when the aircraft attitude started to respond. This is also referred to the incidence lag (T_{θ_2}), which is derived from the reduced order short-period mode transfer function of an aircraft [33, p.243]. Since the time and phase delay is linearly related to the frequency, longer T_{θ_2} exhibits sluggish pitch response and more

substantial phase lag or delay on the bandwidth criterion which could lead to pitch instability. In contrast to that, a too fast or too small T_{θ_2} would exhibit a response that is too sensitive to control input.

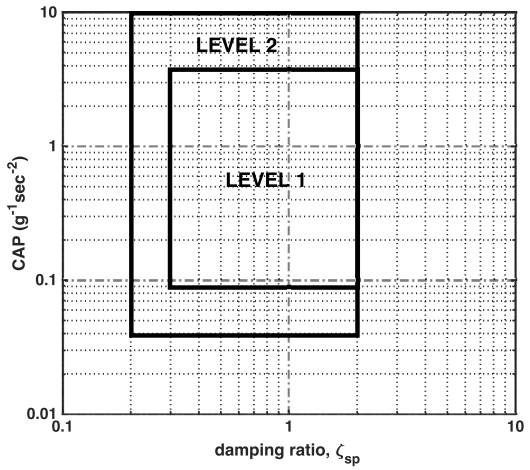

Figure 2.4: Category B Flight Phases - CAP to short-period damping requirements (MIL-STD-1797A) [28]

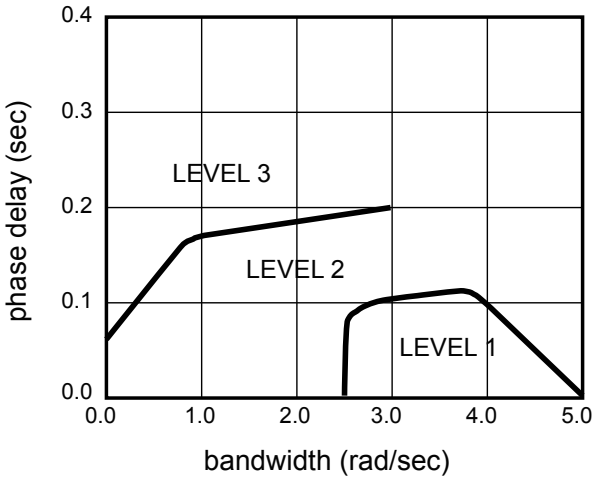

Figure 2.5: Category B Flight Phases - Bandwidth requirements (MIL-STD-1797A) [28]

In conclusion, the review has found that the MIL-F-8785C short-period criterion is generally applicable for light autogyros, but unable to quantify the phase delay parameter which closely related to the PIO. This criterion, however, is included in the MIL-STD-1797A and applicable for light autogyros, on tops of other criteria, such as the short-period damping ratio and the CAP. The phugoid criterion of both specifications is quite universal and obviously applicable for light autogyros.

2.4.3 V/STOL Specifications

The 'Vertical/Short Takeoff and Landing' (V/STOL) or conversion aircraft is considered as a unique type of aircraft that combines the characteristics of rotorcraft and fixed-wing aircraft. This type of aircraft behaved like a rotorcraft during take-off and landing but converted to a fixed-wing aircraft during normal or forward flight. The first V/STOL aircraft flew in 1954 before the first (V/STOL) specifications were introduced in 1962, which addressed the basic handling qualities requirements and design criteria for V/STOL aircraft [61]. The requirements were further established into airworthiness and design standard, MIL-F-83300 in 1970 [26]. The standard covered the basic handling qualities criteria and some basic stability and controllability requirements for V/STOL aircraft. On the European counterpart, requirements for V/STOL aircraft were established as AGARD-R-577-70 design standards in 1970 [25]. These two standards are briefly discussed in this section to consider any of the requirements that are relevant and applicable for light autogyros.

2.4.3.1 MIL-F-83300

The flying qualities classification of V/STOL aircraft in MIL-F-83300 involves both, the fixed-wing flying qualities requirements and the V/STOL requirements. General classification of flying qualities in this document corresponds to the fixed-wing MIL-F-8785C concerning the acceptance levels [26, 27]. However, the longitudinal flying attributes in the document were not defined in terms of short-period frequency and acceleration as being applied in the MIL-F-8785C, but in terms of short-period undamped natural frequency and damping ratio as shown in Figure 2.6. These requirements are seen to be suitable for implementation on light autogyros since the damping ratio, and the undamped natural frequency is within the same region as an autogyro. However, further investigation will be made to quantitatively assess the appropriateness of this requirement to autogyros.

2.4.3.2 AGARD-R-577-70

The longitudinal dynamic stability requirements stated in this document [25] are similar to those of MIL-F-83300 [26], except the root loci plot of the longitudinal dynamic stability criteria is in the form of damped natural oscillation ($2\pi/\omega_d$) versus ($-\zeta\omega_n$). This plot is shown in Figure 2.7. It is important to note that there are no bandwidth

criteria implemented in both standards, the MIL-F-83300 and AGARD-R-577-70.

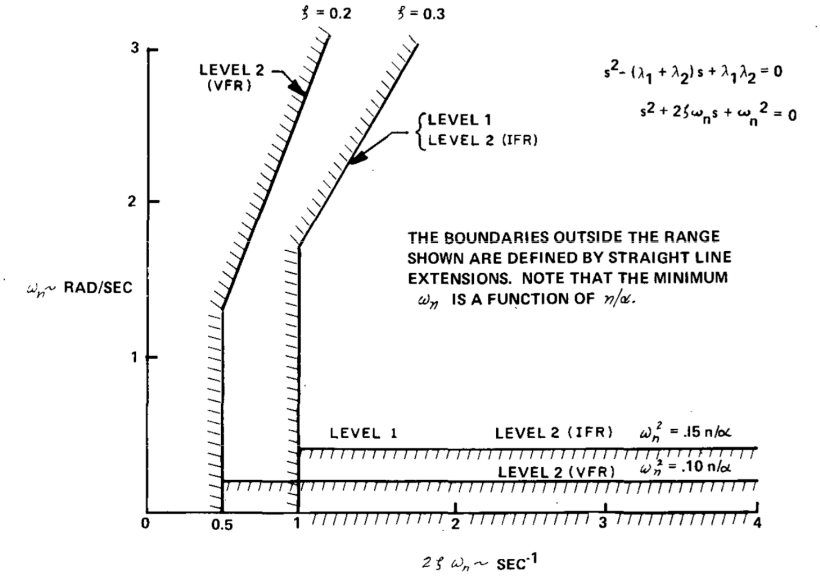

Figure 2.6: Short-period longitudinal response (MIL-F-83300) [26]

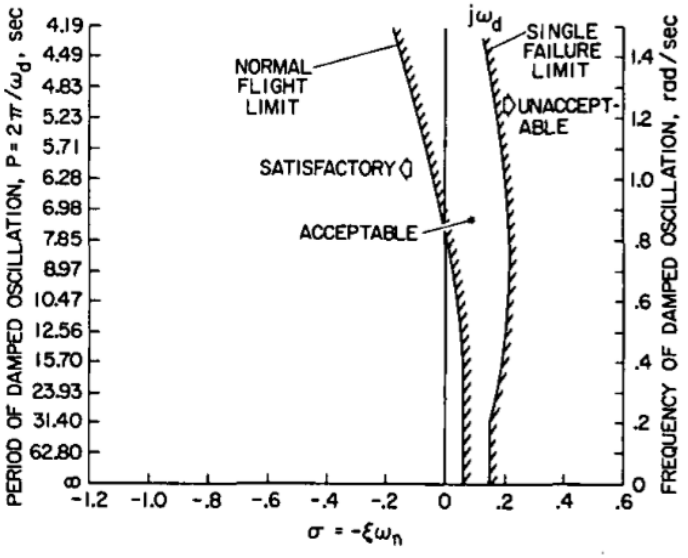

Figure 2.7: Longitudinal dynamic stability requirements (AGARD-R-577-70) [25]

2.4.4 Rotorcraft Specifications

The earliest rotorcraft specification, MIL-H-8501A was established in 1952, featuring a simple time domain flying qualities requirements for the first generation rotorcraft [67]. This establishment was made more than ten years after the earlier helicopter prototype VS-300 was flown by Igor Sikorsky in 1941 [32, 61]. The vast development in rotorcraft technology have seen more helicopters being built in the 1960s to 1970s, with more complicated stability and controllability criteria. In that time, the current military specification MIL-H-8501A were considered obsolete and incapable of being the standards to more sophisticated new generation helicopters. The specification was no longer being used and later cancelled in 1995 [68]. A more sophisticated specification, the Aeronautical Design Standard 33 or ADS-33 was established in 1985, which later supersedes the MIL-H-8501A, with new and advanced criteria for the US military helicopters. The ADS-33 specifies the flying and handling qualities criteria, featuring the time and frequency domain criteria and the newly introduced *Mission Task Elements* or MTEs. This was the first time that handling qualities requirements were addressed in the form of the *Cooper-Harper* Handling Qualities Ratings (HQRs) scale. The specifications later evolved from one revision to another, until reaching the latest and final version in the year 2000 as ADS-33E-PRF, also known as the military performance specification (PRF) [30].

For the UK counterpart, the Defence Standard's DEF STAN 00-970-Rotorcraft was first released as Issue 1 in 1984 [29]. The standard went through various revisions until the latest version, the DEF STAN 00-970-Rotorcraft, Part 7 Issue 6, that was mapped to the European CS-29 design standard [69]. These two rotorcraft standards, the ADS-33E-PRF and DEF STAN 00-970-Rotorcraft are discussed in this section to look for suitability with autogyros.

2.4.4.1 DEF-STAN 00-970 (Rotorcraft)

The main stability and controllability parameters of the latest version of the standard (Issue 5) remain the same as the first version (Issue 1) [29]. The stability criteria of this standard are mainly based on the time-domain criteria. In determining the flying qualities level of acceptance, the rotorcraft responses are defined within the three category of flight phases; The Active Flight Phase, the Attentive Flight Phase, and the Passive Flight Phase. 'Active Flight Phase' requires full pilot involvement in the flying, with good manoeuvrability and precise control of the flight path. This is considered as the basic flying criterion of rotorcraft with good controls. A rotorcraft with the 'Attentive

Flight Phase' is configured with medium intervention from the pilot, while a rotorcraft with 'Passive Flight Phase' is configured with low pilot intervention. These later two flight phases are meant for rotorcraft configured with a closed loop controller or automatic augmentation system. For a typical light autogyro with conventional mechanical control, the Active Flight Phase is suitable to be considered for the acceptance level, since full pilot involvement is required for this type of vehicle. If the light autogyro is configured with a stability control system, the Attentive Flight Phase might also be considered. Passive Flight Phase will not be considered for a light autogyro, due to the high workload usually experienced by autogyro pilots.

It is also mentioned in the specification that the pitch attitude and its derivatives relative to time are the essential parameters for longitudinal stability and control requirements [29]. There is no specific requirement of phugoid dynamic stability for the Active Flight Phase being set, as long as the phugoid oscillation be reasonably damped. For the Attentive flight phase, the requirements set for phugoid oscillations are defined in Table 2.4.4. These phugoid requirements were found suitable to be implemented on light autogyros, as the requirements are indeed similar to the BCAR Section T. The Section T is more of a basic airworthiness requirements, while the DEF-STAN is more of a flying qualities standard with complete acceptance levels for both, phugoid and short-period mode.

Table 2.4.4: Phugoid requirements for Attentive Flight Phase (DEF-STAN 00-970−Rotorcraft) [69]

Acceptance Level	Requirement
Level 1	20 seconds
Level 2	10 seconds
Level 3	→ Oscillation with period between 5 to 10 sec, should halve its amplitude in less than 2 cycles. → Oscillation with periods of up to 20 sec should not double the amplitude within the same time. → Any aperiodic mode should not double amplitude in less than 9 sec.

The short-period response criterion in the standard is dominated by the initial pitch response to the control input. This dynamic stability response is shown in Figure 2.8

and defined by Table 2.4.5. The initial response parameters are generalised in the terms of the control responsiveness, the initial delay and the sensitivity [29].

Responsiveness for level 1 flying qualities is characterised by the peak value that must be greater than a certain minimum value, but must not be greater than a specific maximum to prevent over-sensitivity. For level 2 and level 3 flying qualities, the peak values can be higher than level 1, but must still be within the maximum and minimum value limits. These characteristics depend on the type of manoeuvring requirements, whether an aggressive or moderate manoeuvre.

Initial Delay is defined in the document as "*the cumulative effect of the control system lags and delays*". The vehicle's initial response to the control input must reach a certain minimum percentage of peak value within the specified time limit, which is referred to the T_1 (sec) in Figure 2.8. The initial delay for level 1 flying qualities is a condition where the y_1 values at T_1 must be greater than 30% of the peak value. For level 2 and level 3, the minimum value of y_1 at T_1 can be lower than the level 1 requirement.

Sensitivity and *Responsiveness* of the rotorcraft to the control input have to be balanced with the control force induced by the pilot. This is important to avoid an unintentional control input from the pilot and resulting an adverse manoeuvre due to the cross coupled responses of the rotorcraft. The document also suggested that, "*to prevent an over-sensitivity of the initial response, the percentage value of y_1 at time T_1 must not exceed some percentage of the peak value, and at the end of the control input, the response parameter must not exceed more than y_2% of the peak value*".

In conclusion, it is important to note that the criteria stated in this document are just a guidelines as there are still 'grey area' in the numerical values within the criteria, as the term 'to be advised' (TBA) are being used. This can be understood as those TBA values are uncertain and subject to more interpretation. There is a suggestion in the same document to implement the bandwidth approach for future criteria and to give better guidance in preventing pilot-induced oscillation, especially for highly augmented rotorcraft [69, Leaflet 600/7, para 3.4.4]. Hence, implementing this specification on typical light autogyros will be difficult especially for the short-period mode, as the bandwidth criteria are known to be a better approach to define a PIO-prone condition. Moreover, the time-domain dynamic criteria used for the short-period oscillation are meant for precise manoeuvres and only useful for military helicopters that are designed for specific missions, say an attack helicopter. Hence, except the phugoid criteria, it is believed that the short-period mode criteria would not be relevant for typical light autogyros.

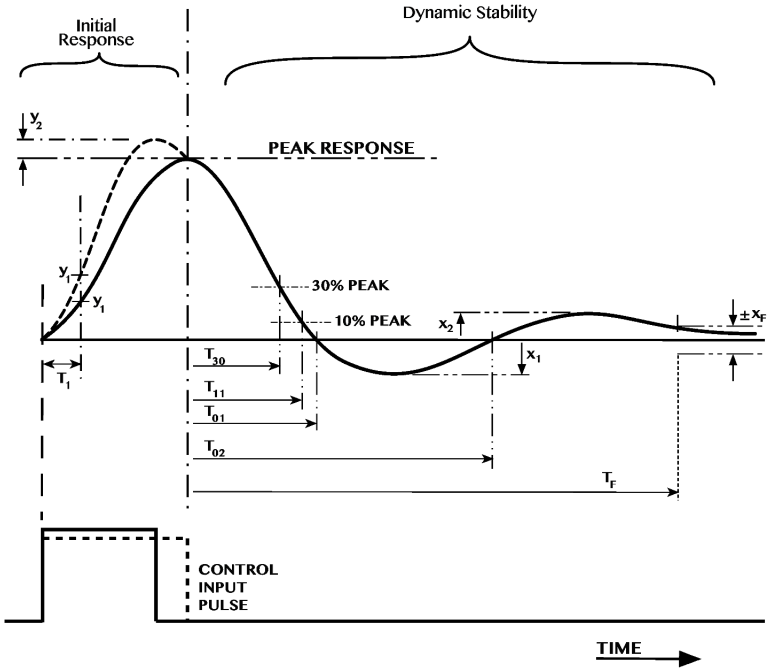

Figure 2.8: Short-period transient response (DEF STAN 00-970−Rotorcraft) [69]

Table 2.4.5: Transient response for Level 1 flying qualities (DEF STAN 00-970−Rotorcraft) [69]

Variable	Definition
T_{30}	Max. time to return within 30% peak disturbance from datum
T_{01}	Min. and max. limits on the time to first pass through datum
x_1	Max. percentage of peak distribution for first peak overshoot
T_{02}	Min. time for any second pass through datum (in same sense as inertial disturbance) form any overshoot x_1, greater than 5%
x_2	Max. percentage of peak distribution for any second peak (in same sense as inertial disturbance)
T_F	Max. time to return and remain within $\pm X_F$% of peak disturbance about datum

2.4.4.2 ADS-33E-PRF

The ADS-33E-PRF [30] standard outlines the desired handling qualities of military rotorcraft, based on the extensive frequency-domain criteria, compared to the conventional time-domain criteria implemented on other standards. This standard is more generic and applicable for all rotorcraft, as it does not categorise rotorcraft based on their sizes and weight.

Hence, it can be used as the basis of flying qualities for light rotorcraft, including autogyros. In fact, the standard is more advanced, in the sense that the criteria were developed for highly augmented rotorcraft with automatic control systems. There are two different methods used to establish the level of flying qualities in this requirements, the objective and the subjective approach. The objective approach is done based on the 'Predicted Levels' of the flying qualities, while the subjective approach is according to the 'Assigned Levels'.

Predictive Levels are obtained by comparing the rotorcraft's flying qualities parameters with the criteria limits for a certain defined operational requirements. These levels were defined in the form of three acceptance levels, either Level 1, Level 2 or level 3. The Assigned Levels are obtained by applying the Cooper-Harper's Handling Qualities Rating Scale (HQR) through flight trials. Pilots are required to perform certain tasks, based on the designated Mission Task Elements (MTEs) according to the rotorcraft operational requirements. The handling qualities Level 1, 2 or 3 will be obtained from the HQRs points through the pilot's subjective opinion. Since the objective of the research is to look for the flying qualities criteria, only Predictive Levels in the longitudinal mode were reviewed. In fact, autogyro flight test is not possible in the research.

In general, rotorcraft flying qualities requirements in this standard are evaluated in two operational flight speed ranges, the *Hover and Low-Speed Requirements* and the *Forward Flight Requirements*. Evaluations are based on the frequency domain approach, which specifies the requirements of the responses based on the frequency bandwidth, ω_{BW} (rad/sec) and the phase delay, τ_p (sec), as defined in Figure 2.9. The phase delay parameter is quantified by

$$\tau_p = \frac{\Delta\Phi_{2\omega_{180}}}{57.3(2\omega_{180})}(sec) \tag{2.4.3}$$

where ω_{180} is called *phase crossover frequency*, which is the frequency of neutral sta-

bility. At this frequency, the output response lags the input control by 180 deg. The $\Delta\Phi_{2\omega_{180}}$ is the change of phase at the double of the frequency ω_{180}.

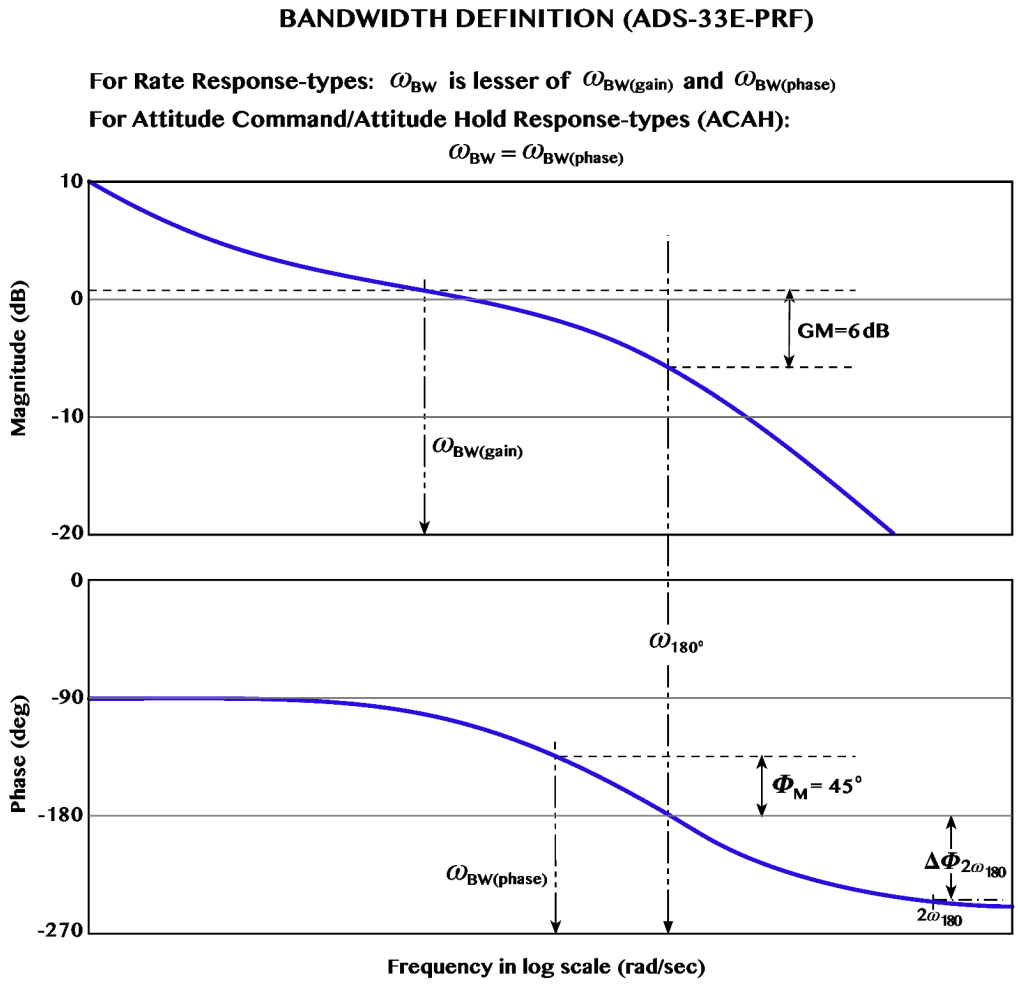

Figure 2.9: Bandwidth and phase delay definitions (ADS-33E-PRF) [30]

The bandwidth is defined in the ADS-33E-PRF [30] (see Figure 2.9) as the highest frequency at which the phase margin (Φ_M) is 45 deg at least, and the gain margin (GM) is at least 6dB. Phase margin (Φ_M) is the additional phase lag at the phase crossover frequency ω_{180} allowable before the system becomes unstable. Gain margin (GM), on the other hand, is the limit from the ω_{180} where the open loop gain can be increased before the system becomes unstable. It is important to note that, a high bandwidth rotorcraft is when the response to the control input is fast, which exhibits as sharp and agile response. In contrast, a slow and sluggish response is represented by a low bandwidth [70]. Descriptions of the two operational flight speeds in the criteria are discussed in the following.

(A) Hover and Low-Speed Requirements (0−45 knots / 0−52 mph)

In ADS-33E-PRF, hover and low-speed is defined as the applicable speed range from hover to 45 knots ground speed in the rotorcraft's Operational and Service Flight Envelopes. Since hover flight is impossible for a typical light autogyro, only the low-speed requirements are applicable for autogyros flying qualities consideration. Two longitudinal attitude response criteria to be assessed in this operational flight region; the *small-amplitude pitch attitude changes* and the *moderate-amplitude pitch attitude changes*.

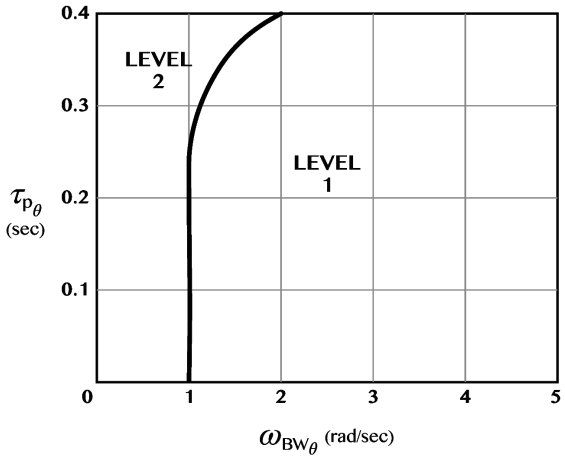

Figure 2.10: Bandwidth requirements for small-amplitude pitch attitude changes - Fully Attended operations (ADS-33E-PRF) [30]

Small-amplitude pitch attitude changes

Small amplitude response to the control input is defined in the form of two measurements, *short-term* and *mid-term* response.

a) *Short-term response to control input (Bandwidth)*
The limit of this short-term response criterion is specified in Figure 2.10. According to Figure 2.9, for a rotorcraft equipped with rate-response type augmentation, the frequency bandwidth ω_{BW} is the lesser of $\omega_{BW(gain)}$ and $\omega_{BW(phase)}$. For Attitude Command/Attitude Hold response type (ACAH), $\omega_{BW} = \omega_{BW(phase)}$, but if $\omega_{BW(gain)} < \omega_{BW(phase)}$ or $\omega_{BW(gain)}$ is undeterminate, the rotorcraft will be PIO prone.

b) *Mid-term response to control inputs (Fully Attended Operations)*
For a rotorcraft with Attitude-Hold stability augmentation, the damping ratio must effectively be at least $\zeta = 0.35$, following an abrupt control input. The mid-term response characteristic in this section is applicable for all frequencies less

than the bandwidth frequency from the previously obtained short-term response. The criteria limit for fully attended and divided attention operations of the mid-term response are shown in Figure 2.11.

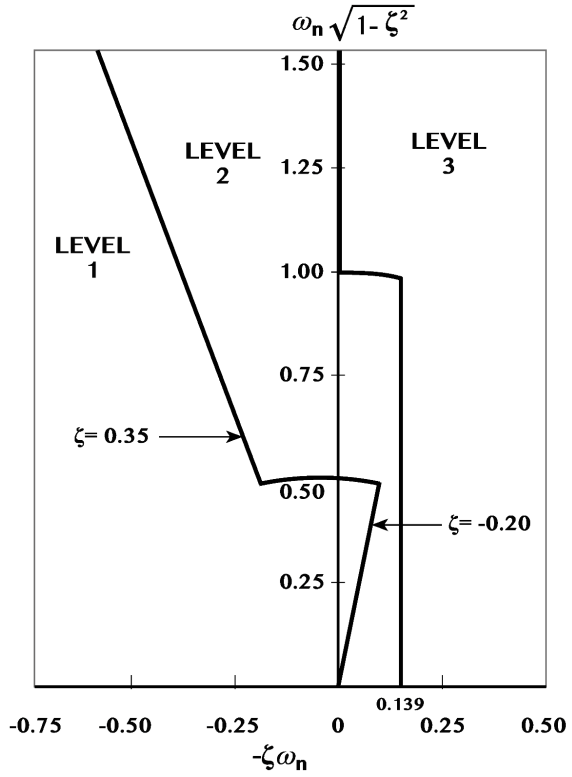

Figure 2.11: Damping requirements for small-amplitude pitch attitude changes (ADS-33E-PRF) [30]

Moderate-amplitude pitch attitude changes (Attitude Quickness)

Moderate-amplitude changes of the attitude required for the compliance with the pitch attitude requirement is mentioned in the document as, "*the excitation of pitch attitude between 5 deg minimum pitch to the limit of the Operational Flight Envelope or 30 deg in pitch, whichever is less*". The pitch attitude quickness is implemented in the time-domain as shown in Figure 2.12, and defined in the document as, *The ratio of peak pitch rate to the change in pitch attitude*,

$$\text{Attitude Quickness} = \frac{q_{pk}}{\Delta\theta_{pk}} \tag{2.4.4}$$

The function of $\Delta\theta_{min}$ in the attitude change is to prevent the control from being over-applied by the pilot and producing a high value of quickness [32].

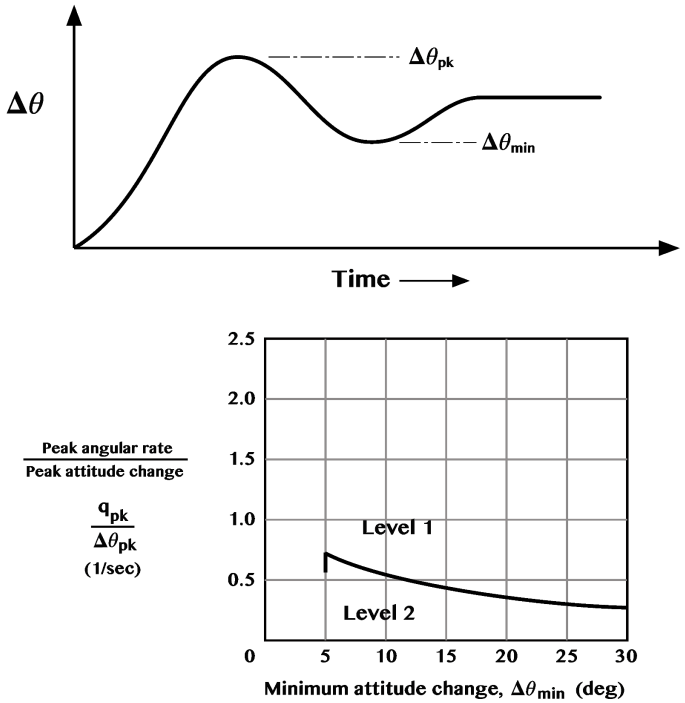

Figure 2.12: Attitude-Quickness requirements limit (ADS-33E-PRF) [30]

(B) Forward Flight Requirements (>45 knots @ 52 mph)

In the ADS-33E-PRF, forward flight speed is defined as the applicable speed range greater than 45 knots (52 mph) ground speed in the aircraft Operational and Service Flight Envelopes. There is at least one essential requirement involves the forward flight operation for the rotorcraft that is applicable for light autogyros, the Pitch attitude response to the longitudinal controller. For this requirement, the evaluation is divided into two, the short-term response (bandwidth), and the mid-term response to the control inputs. The evaluation methods are somehow similar to the earlier low-speed flight requirements.

2.5 Autogyro Flying Qualities Recommendation

Early attempts to assess the handling qualities of light autogyros have been done in Glasgow, but focusing on the subjective assessment through flight tests [10, 71, 72]. Moreover, according to the reviews that have been made in this chapter, the rotorcraft's ADS-33E-PRF specifications is found as the most sensible to be implemented on light

autogyros.

However, the underlying general definition from the MIL-F-8785C standards are still applicable for autogyros, which is defined as Class I aircraft, under the Category B flight phase. The recommendation of autogyros flying qualities will include the existing BCAR Section T airworthiness requirements. Most of the general requirements in the BCAR Section T were also seen to be in agreement with the MIL-STD-1797A as many requirements in Section T were previously adopted from the BCAR Section S (Light Aeroplane). The longitudinal flying qualities recommendation in this section are divided into two main sections, the Short-Period and the Phugoid requirements. Since the rotorspeed of a typical autogyro operates in its own degree of freedom during flight, the rotorspeed requirement is proposed separately.

2.5.1 The Short-Period Mode Requirements

The short-period mode criteria were featured in most conventional aircraft standards through time-domain evaluations, except a few, where the frequency-domain criteria were made as essential flying qualities requirements for modern aircraft that were designed with control enhancements. BCAR Section T [21] defines the short-period mode oscillation (in time-domain form) as an oscillation which has a period of fewer than 5 seconds, due to disturbance or small deflection of pilot input from the trim (Section 2.4.1). The dynamic stability of a typical light autogyro is considered as acceptable if the short-period oscillation is stable, with the amplitude should be halved in less than one cycle. Therefore, this definition of short-period mode will essentially be used in the recommendation of autogyro flying qualities.

The time-domain and frequency-domain criteria were covered in both, the fixed-wing MIL-STD-1797A and the rotorcraft ADS-33E-PRF requirements [28, 30]. In both requirements, the frequency-domain criteria are more crucial as it had been used to address the PIO prevention in short-period mode, which most existing traditional homebuilt autogyros are exposed with. Since these requirements were initially addressed for contemporary aircraft and rotorcraft equipped with stability augmentation system, they are also useful to be used on conventional aircraft with upgraded augmentation system. The criteria allow a room for improvement for any conventional aircraft to be upgraded with an appropriate guidance for better flying qualities.

Since typical light autogyros are designed with a lightly damped short-period oscillation, a pitch instability that leads to PIO may happen, in such circumstance where an

abrupt pilot input or a strong turbulence acted upon the vehicle. Again, Table 2.3.1 (Section 2.3) expose the list of incidents where this condition actually happened. Moreover, the PIO in the short-period mode, including all factors affecting the longitudinal stability of light autogyros have been discussed earlier in the same section. Therefore, it is essential that the frequency-domain criteria from the MIL-STD-1797A and ADS-33E-PRF be considered into the flying qualities requirements of light autogyros. However, since the PIO avoidance criteria are defined explicitly in the frequency-domain criteria of the ADS-33E-PRF (Figure 2.9), the same requirement can be adopted for light autogyros. This conclusion is also made due to the fact of the similarities between light autogyros and helicopters as mention in the points below;

- The short-period oscillation of both aircraft is lightly damped with less effective tailplane.
- The primary pitch damping of both aircraft is mainly contributed by the rotor disc.
- The primary manoeuvring controls of both aircraft are mainly contributed by the rotor disc.

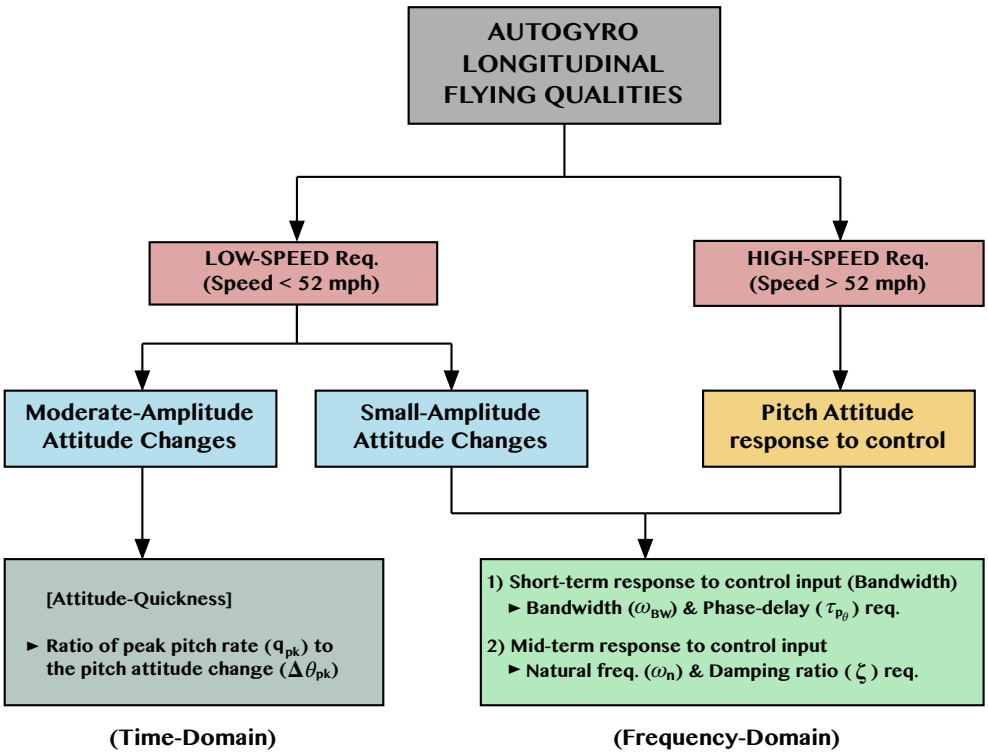

Figure 2.13: Autogyro Longitudinal Flying Qualities

Figure 2.13 features the summary of the proposed longitudinal flying qualities requirements of light autogyros in short-period mode, mainly adopted from the ADS-33E-PRF

requirements. Instead of using the 'Forward Flight Requirement' for the operational flight speed, 'High-Speed Requirement' is used in the proposed criteria for flight speeds of more than 40 knots (52 mph). The frequency-domain criteria are used across the whole speed region of the vehicle, due to the importance of preventing the vehicle from entering PIO in the short-period mode. In particular, two frequency-domain requirements are being used, the *Bandwidth and Phase-delay* requirement, and the *Natural-frequency and Damping-ratio* requirement.

a) Bandwidth and Phase-delay requirement

This criterion is used to evaluate the pitch attitude changes of the autogyro due to small-amplitude input in the low-speed flight, as well as to assess the pitch attitude response to control input in high-speed flight. Particularly for this type of criteria, the ADS-33E-PRF is the most suitable to be adopted for the autogyro. The bandwidth (BW) and phase delay (τ_θ) criteria of the ADS-33E-PRF are specified as (see Figure 2.9),

- For a *Rate-response* type stability system, the required bandwidth (BW) is the lesser between the phase-bandwidth $\omega_{BW(phase)}$ and the gain-bandwidth $\omega_{BW(gain)}$.
- For an *Attitude Command/Attitude Hold Response* type system (ACAH), the required bandwidth (BW) is the phase-bandwidth $\omega_{BW(phase)}$. Moreover, the rotorcraft maybe considered in PIO prone condition if the $\omega_{BW(gain)}$ is less than the $\omega_{BW(phase)}$.

As such, the bandwidth (ω_{BW}) and phase-delay (τ_{p_θ}) of the pitch attitude of the autogyro must first be quantified from the short-period linear model. These bandwidth parameters are then evaluated according to the above criteria. For an autogyro that is equipped with a closed loop augmentation control, it is important that the bandwidth parameter ω_{BW} meeting the condition where

$$\omega_{BW\,phase} < \omega_{BW\,gain} \ ,$$

so that the possibility of the autogyro to entering PIO can be prevented.

b) Natural-frequency and Damping-ratio requirement

This criterion is used to quantify the mid-term response to control input by assessing the pitch damping at frequencies lower than the previous bandwidth frequency found in a). The flying qualities limits for this requirement has been defined previously in Figure 2.11.

On the other hand, the 'time-domain' criteria is used to quantify the pitch attitude changes of the vehicle, due to moderate-amplitude control input applied in low-speed flight regime. This requirement is also known as *Attitude-Quickness* where the overshoot and undershoot of the attitude response is quantified properly. This measurement is also used to evaluate the rate response-type augmentation system, as the main purpose of this augmentation system is to improve the vehicle's agility. However, due to the trade-off between the vehicle's agility and stability, the Attitude-Quickness requirement is used to balance the two parameters, so that the autogyro will not be too stable and less agile in flight.

For an autogyro that is enhanced with an attitude-hold augmentation system, it is also recommended that the small-amplitude input be quantified in the time-domain form according to the BCAR Section T. The Section T requires the pitch attitude of the autogyro to be deflected approximately 5 degrees from the trim condition and return back to trim. The same control input must also be sufficient enough to produce an oscillation with the pitch rate of not more than $3 - 5$ deg/sec, and then incrementally increased up to $5 - 10$ deg/sec before being damped.

Therefore, for the longitudinal short-period mode flying qualities, the requirements are concluded in Table 2.5.1.

2.5.2 The Phugoid Mode Requirements

Phugoid is generally defined as a long-term lightly damped oscillation in longitudinal flight mode, which closely related to the airspeed and attitude. In MIL-F-8785C, MIL-STD-1797 and ADS-33E-PRF, the quantitative flying qualities requirement of the phugoid is given in the form of damping ratio. In contrary, for the DEF STAN 00-970 and BCAR Section T, the requirement is given in the form of time response. Moreover, it has been found from the earlier review that the quantitative guidelines of phugoid in BCAR Section T coincide with the DEF STAN 00-970 long-term oscillation requirements. The same coincidence was also found between the MIL-F-8785C and MIL-STD-1797 requirements.

Since phugoid is a long-term oscillation, an unstable or marginally stable phugoid might slowly divert the autogyro into PIO without being noticed by the pilot. Hence, it is important that the long-term oscillation is damped according to a specific standard of requirement for the flight safety, without degrading the manoeuvrability of the vehicle. For an unstable autogyro with a divergent phugoid oscillation, if the period of oscillation

is less than 10 seconds, a great amount of damping is required to stabilise and to prevent any unwanted event from occurring. According to the DEF STAN 00-970 and the BCAR Section T, this type of dynamic stability is suggested to be put under the level 3 flying qualities for light autogyros. In fact, the damping ratio for the phugoid oscillation can be added into the requirement for the proposed autogyros flying qualities. In conclusion, the proposed longitudinal flying qualities requirements for light autogyros are listed in Table 2.5.1, according to the suggested level of flying qualities as a reference.

2.5.3 The Rotorspeed Criteria

It was previously understood that one significant unique characteristic of autogyros compared to a helicopter is the rotorspeed degree of freedom that strongly coupled with the rigid-body attitudes of an autogyro [14, 39]. A similar relationship was also highlighted by Leishman [73], where a positive rotor thrust must be maintained during autorotation which also restricts the ability of an autogyro to perform extreme manoeuvres. Failing to maintain a positive rotor thrust will cause rotor disc unloading and rotorspeed decay, which eventually results to loss of lift. A rapid manoeuvre such as steep climb or dive is always associated with the load factor or the g-force. Unfortunately, there has been little study about the relationship between the g-force and rotorspeed loss, except one that was made by Gallup [60] based on the study done by Thomson [39] about the strong coupling between the autogyro's rigid-body dynamics and the rotorspeed. Simulation study made by Gallup using the inverse simulation of the G-UNIV autogyro found that the rotorspeed significantly decays in a rapid or high-g manoeuvre. Gallup also suggested a safety limit for the G-UNIV to only $1.2g$. This is because a rapid manoeuvre of more than $1.2g$ will cause a 20% rotorspeed loss. It is then proposed that the same g-factor of $1.2g$ be used in this autogyro flying qualities criteria. This criterion is also possible to be implemented since the existing 'g' meter of the autogyro's instrument can be used as an early indication of rotorspeed decay in manoeuvring flight.

Table 2.5.1: Autogyro Phugoid and Short-Period Flying Qualities recommendation

* **Short-Period Mode Oscillation** (Period $T < 5$ sec)			
Flight Regime	Response Type	Requirement	Reference**
Low-Speed (IAS < 52 mph)	Attitude changes to moderate-amp. input	Pitch Quickness	ADS-33E-PRF (Fig. 2.12)
	Attitude changes to small-amp. input	1) Short-term response to input (BW and τ_p) 2) Attitude-hold response to control input	ADS-33E-PRF (Fig. 2.9)
High-Speed (IAS > 52 mph)	Pitch Attitude response to control input		

Phugoid Mode Oscillation		
Acceptance level	Requirement	Reference**
Level 1	$\rightarrow \zeta_{ph} \geq 0.04$, or oscillation-period $T > 20$ sec.	MIL-STD-1797A & DEFSTAN 00970
Level 2	$\rightarrow 0 < \zeta_{ph} < 0.04$, with $T_{ph} > 20$ sec.	MIL-STD-1797A & BCAR Sec. T
	$\rightarrow$ Oscillation with period $10 < T < 20$ sec, should be damped.	BCAR Sec. T
Level 3	$\rightarrow$ Oscillation with $T < 10$ sec, amplitude must halve in less than 2 cycles.	DEFSTAN 00970 & BCAR Sec. T
	$\rightarrow$ For unstable phugoid with $T > 20$ sec, time-to-double amplitude $T_{2_{ph}} > 20$ sec.	DEFSTAN 00970 & BCAR Sec. T

* The max. period of the short-term oscillation complies with the BCAR Section T

** Reference to existing flying qualities criteria as specified

2.6 Chapter Summary

The main objective of this chapter is to propose a suitable flying qualities requirements for autogyros. This process requires a good understanding of dynamic stability characteristics and safety issues from various studies about this type of vehicle. The unique features of light autogyros were recognised between conventional fixed-wing aircraft and helicopters, which are summarised in the following;

a) The longitudinal dynamic stability of autogyros resembled the stability of a conventional aeroplane and helicopter with short-period and phugoid oscillations. However, the phugoid is either lightly damped or unstable, which manifest the phugoid mode of a typical helicopter.

b) The longitudinal stability characteristics are strongly influenced by the propeller thrust versus the rotor thrust vector with respect to the CG of the vehicle. The second parameter is the most crucial to be managed by the pilot, as the propeller thrust line is fixed during flight. In any circumstance, regardless of the default configuration of an autogyro, the relative horizontal safety position of the rotor thrust line from the CG must be kept to maintain a positive airflow through the rotor disc and keeping the vehicle in airborne.

c) The primary pitch damping of typical autogyro is contributed by the rotor disc, as the tailplane of the vehicle is less effective. This longitudinal damping is mostly influenced by the longitudinal shaft tilt control of the vehicle.

d) The rotorspeed degree of freedom contributes to an additional dynamic mode of the vehicle, as it strongly coupled with the vehicle's rigid-body attitude during flight. Abrupt pitch manoeuvres could cause decay in the rotorspeed, thus unloading the rotor which eventually leads to PIO.

Due to these unique characteristics, a suitable flying qualities requirements for light autogyros were proposed based on the existing criteria of conventional aeroplane and helicopter. Most importantly, to guarantee the practicality of the proposed flying qualities guidelines, the existing airworthiness requirements (BCAR Section T) were used as the basic requirements. The criteria from other specifications were then added on top of that, which include requirements from the ADS-33E-PRF, DEF-STAN 00-970 (Rotorcraft) and MIL-STD-1797A (see Table 2.5.1). However, since the longitudinal dynamic stability of light autogyros is generally close to rotorcraft's, the rotorcraft's flying qualities requirements consequently became dominant in the proposed flying qualities.

Finally, it can be concluded that the proposed longitudinal flying qualities requirements for light autogyros are divided into three sections, the short-period mode, the phugoid mode, and the rotorspeed requirements. Meeting all these requirements would ensure safe operation of the vehicle in any form of manoeuvres or atmospheric disturbances. Hence, this new proposal will be used to evaluate the flying qualities performance of the basic G-UNIV research autogyro model, where all necessary control enhancement of the vehicle will be developed accordingly in the next chapter.

Chapter 3

Autogyro Rotor-Disc Simulation Model - ARDiS

3.1 Introduction

A mathematical model of an autogyro can be considered as a mathematical representation of the vehicle's physical behaviour in response to external forces and moments acting upon it. The development of this model started with a consideration of an existing helicopter model, due to the similarities between the autogyro and helicopter, in which both vehicles generate lift through rotating blades. There are various rotorcraft simulation models available that differ from one to another in the sense of the approach used to calculate and predict the main rotor loads in various flight conditions. The ability to accurately simulate the behaviour of the main rotor during flight is essential for an effective rotorcraft mathematical model since the rotor behaviour is complex.

Padfield [74,75, p.90] defines rotor mathematical modelling according to three different levels of fidelity; Level 1, Level 2 and Level 3. Level 1 modelling is the most basic with the lowest fidelity where the aerodynamics of the rotor blade is defined based on a linear 2-dimensional aerofoil theory. The rotor dynamics are considered as quasi-steady relative to the fuselage modes with the rotor blade is assumed to be in the form of 'multiblade' or 'disc' representation, where the loads are calculated analytically as an average across the whole rotor disc. Analytical integration of rotor loads gives this method its advantage as the calculations require less computational effort. Level 2 modelling is more advanced where the aerodynamics of the rotor blade is calculated

based on a nonlinear and limited 3-dimensional aerofoil theory with more aerodynamic complexities. The blades are divided into elements, and the load calculations are done numerically. The advantage of this method is the higher fidelity simulation results that closer to the reality as compared to the Level 1 modelling. However, this method is computationally more expensive than the Level 1. Level 3 modelling is the most comprehensive mathematical model that focuses on the higher order rotor blade dynamics, which involves full 3-dimensional blade aerodynamics with more detail and complicated load calculations. Even though this approach has the highest fidelity than the other two, implementation in the flight dynamic and stability studies of the whole vehicle is complicated due to the calculation complexity which requires more calculation runtime and more powerful machines. As such, this Level 3 approach is mostly used for a more focused study on the blade dynamics, such as the study on the blade flapping and vibration, also study on the blade aerodynamics behaviour of a high-speed rotorcraft.

In general, there are many rotorcraft simulation codes used in helicopter modelling and simulations as reviewed by Johnson [76]. These simulation tools are used for comprehensive analysis tasks such as rotorcraft flight performance, aeroelastic stability, total vibration, noise, and blade loading and motion. 'Comprehensive' in this matter is referred as a complete computation to imitate the actual behaviour and performance of the rotorcraft, which is categorised under the Level 2 and Level 3 fidelity in the above context. Examples of rotorcraft computational tools discussed by Johnson include CAMRAD that was developed by NASA, COPTER by Bell Helicopter, CRFM by Westland, REXOR by Lockheed, and the commonly used FLIGHTLAB by Advanced Rotorcraft Technology. However, it was not known if any of these rotorcraft computational tools being used particularly for autogyro simulations, except the FLIGHTLAB. FLIGHTLAB was developed as a comprehensive real-time simulation tool that supports the simulation of both fixed-wing and rotorcraft models [77,78]. One of the applications of FLIGHTLAB in autogyro simulation was done by Robinson [79] at the University of Liverpool, which implements the 'individual-blade' rotor model for handling qualities simulations.

Rotorcraft simulation models developed at the University of Glasgow are based on two different mathematical approaches; the *Individual-Blade* model and the *Rotor-Disc (multiblade)* model [80, 81]. The Individual-Blade modelling approach can be categorised under the Padfield's Level 2 modelling approach, while the Rotor-Disc modelling approach is categorised under the Level 1.

For the *Individual-Blade* approach, each blade is divided into several segments, where the load are calculated numerically for each segment throughout the whole span of the blade. The aerodynamic characteristics of a single element of the blade, such as the

Mach number effects, the lift and drag coefficients for different angle of attack and the variable blade section geometry are captured. As such, numerical iterations of the rotor loads are performed in several loops before the total rotor loads are obtained. Consequently, more accurate predictions of rotor thrust and dynamic response of the rotor can be achieved.

There are several rotorcraft simulation packages developed at the University of Glasgow that incorporate the individual-blade approach; The *Helicopter Individual-Blade Rotor Model*, also known as HIBROM, and the *Rotorcraft Aeromechanic Simulation for Control Analysis*, also know as RASCAL. HIBROM is only generic for helicopter used and cannot be incorporated into autogyro simulations. Significant modifications have to be made to incorporate HIBROM into autogyro simulations. In contrary to HIBROM, the RASCAL model that was developed by Houston [82] was proven to be used for all types of rotorcraft simulations including autogyros. Several validation studies were done in Ref. [83–85] on the incorporation of RASCAL model in autogyro simulations, including the latest one as reported in the CAA technical report [7, p.2]. However, RASCAL was not the only rotorcraft model that has been used for autogyro simulations. The *Gyroplane Simulation Model* or GSIM, a HIBROM-based individual-blade model was developed by Bagiev [86, p.82] and used explicitly in autogyro inverse simulation studies.

In contrary to the Individual-Blade approach, the *Rotor-Disc* or *Multiblade* approach implements the traditional way of calculating loads acting on a rotor blade. The load of the blade elements are analytically integrated over the whole blade span and turned into the average loads for the entire blade rotation, This calculation also represents a complete blade rotation in the form of rotor 'disc'. Since the approach is to predict the average disc loading of the blade, it uses simplified aerodynamic properties for each blade element in the calculations. The drag coefficient is simplified with an average value across the span of the blade, regardless of the local angle of attack and the azimuth location of the blade as it rotates. It is expected that this simplification contributes to a small discrepancy in the rotor load calculation, due to the uncertainty reflected from the simplified drag coefficient. Ref. [22, 81, 86, 87] briefly explain the comparison between the individual-blade and the rotor-disc modelling approaches.

Helicopter Generic Simulation model or known as HGS was the only helicopter simulation package developed at the University of Glasgow by Thomson [22] that incorporates the Rotor-Disc modelling approach. As with HIBROM, HGS is generic only for helicopter simulations. Incorporating HGS in autogyro simulation would involve modifications especially on the rotor model kinematics and dynamics.

In traditional rotorcraft dynamic studies, a mathematical modelling approach that is capable to precisely predicts the dynamic behaviour of the rotorcraft is desirable. However, since the objective of the research is to implement an automatic flight control system for the autogyro, a suitable modelling approach to obtain a sensible rigid-body dynamics of the vehicle is acceptable. As such, the rotor-disc modelling approach is more suitable that the simplicity of this approach enables the autogyro simulation to be performed in Matlab environment on simple desktop PCs or laptops. The rotor-disc model also linearises more readily than a periodic individual-blade model.

Therefore, the HGS model is chosen to be the basis for the autogyro mathematical model. Since the HGS was meant only for helicopter simulations, modifications were made to incorporate this rotor-disc modelling approach for autogyro simulations. These modifications have led to the establishment of the *Autogyro Rotor-Disc Simulation* model or ARDiS which is described in the following section.

3.2 Overview of ARDiS Model

The HGS was defined as a nonlinear 7 degree-of-freedom dynamic model, with the common 6 rigid-body mode of motions and the additional rotorspeed mode [22, 81]. However, as previously understood in helicopter modelling, the rotorspeed mode is always referred to the rotorspeed of the main rotor, which is always associated with the rotor torque changes. For a helicopter, the rotor torque is actually governed by the engine power or throttle settings and essentially this rotorspeed changes is similar to the one given by Padfield [75, p.154], of which is written in the following;

$$\dot{\Omega} = \dot{R} + \frac{1}{I_R}(Q_e - Q_R - g_T Q_T) \tag{3.2.1}$$

From the equation (3.2.1) above, $\dot{\Omega}$ is the rate of change of the rotorspeed due to the applied rotor torque. The applied rotor torque corresponds to the helicopter yaw rate $\dot{R}$, and the differences between the torque produced by the engine Q_e, the rotor aerodynamic torque Q_R, and the tail rotor torque Q_T. For a given rotor moment of inertia I_R, the tail rotor torque is also associated to the gear reduction of the tail rotor g_T.

Since an autogyro operates based on the unpowered autorotative flight, equation (3.2.1)

is then simplified to be an unpowered rotorspeed as written in the following;

$$\dot{\Omega} = \dot{R} - \frac{Q_R}{I_R} \tag{3.2.2}$$

which clearly shows the rotorspeed state in autorotation mode is effected only by the fuselage yawing rate and the rotor aerodynamic torque. For an autogyro in equilibrium flight, the average rate of change of rotorspeed is zero, due to the fact that the rotor torque and the fuselage yawing rate are in equilibrium.

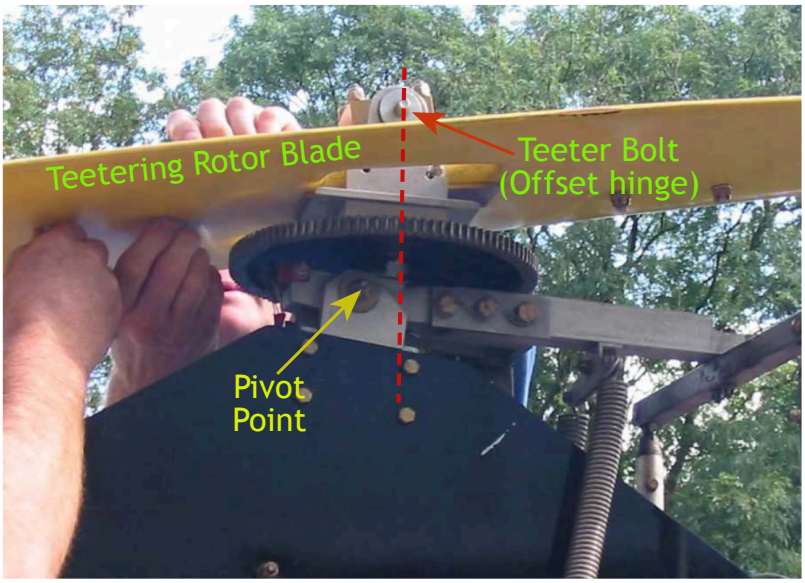

Figure 3.1: Autogyro Shaft Offset

Furthermore, due to differences between the autogyro and helicopters, as far as the flight mechanics are concerned, the ARDiS model differs from the existing HGS model in many aspects.

(a) In the HGS model, the rotor hub is fixed at a particular point on the helicopter's airframe with a fixed shaft tilt angle. The collective and cyclic control of the helicopter is applied by manipulating the pitch of the rotor blades (θ_0, θ_{1_c} and θ_{1_s}). Since the rotor disc plane of rotation is fixed, the kinematic transformations between the body to the hub, and later to the blade axes is straight forward and less complicated.

For the ARDiS model, the rotor hub is fixed to a pivot point on the vehicle's airframe through a small shaft offset, as shown in Figure 3.1 [7]. The cyclic control of the autogyro is applied by pivoting the rotor hub longitudinally (θ_s)

and laterally (ϕ_s) around the pivot point through a direct control linkage from the pilot to the rotor hub (see Figure 3.2 and Figure 3.4). Applying these control inputs around the pivot also changes the plane of rotation of the rotor disc. Therefore, the kinematic transformations from the body axes to the hub are more complicated as they involve the longitudinal and lateral control mechanism and the shaft offset. These kinematic transformation are detailed in the next section.

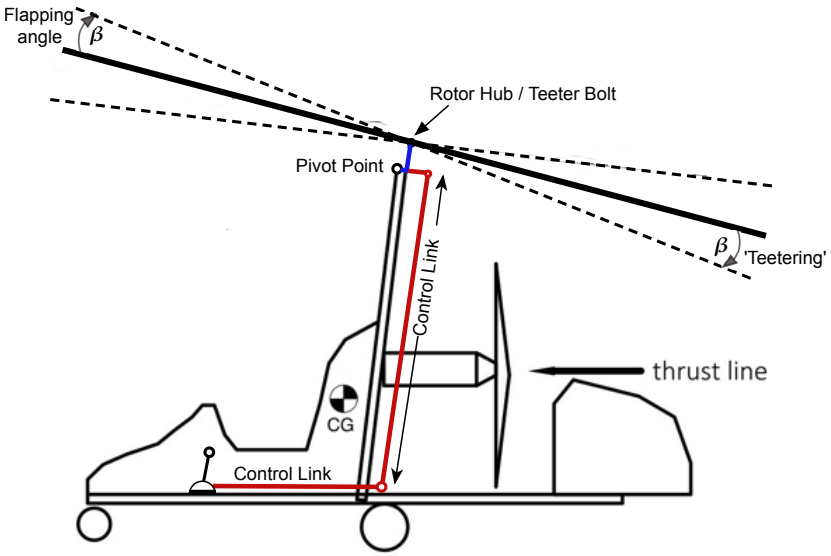

Figure 3.2: Illustration of Light Autogyro's 'teetering' rotor and control link

(b) In the HGS model, the rotor blade was assumed to be of a NACA0012 aerofoil, which is symmetrical in shape. Hence, the lift force coefficient per unit span of the blade is assumed to be linear in the form of $C_l = a_0\,\alpha_{bl}$, where a_0 is the lift curve slope of the aerofoil. As such, stall was not modelled to simplify the HGS package since the model was initially meant for inverse simulation studies on helicopters operating at normal operating speeds.

For the ARDiS model, the G-UNIV's rotor blade is known of using a NACA 8-H-12 aerofoil, which is not symmetrical in shape. Small modification is made to include the lift curve characteristic of the NACA 8-H-12 aerofoil where the lift force coefficient per unit span of the blade is in the form of $C_l = a_0\,\alpha_{bl} + a_1$, where a_1 is the zero angle-of-attack lift coefficient. This modification significantly contribute to the improvement in the rotorspeed behaviour of the ARDiS model, and the result is also shown in the trim simulations in the last part of this chapter.

(c) The flapping dynamics in the HGS main rotor is assumed to be quasi-steady, with suitable assumption to allow for multiblade representation to be used with the

main rotor. Most importantly in the HGS model, the main rotor is assumed to be centrally hinged with a specific stiffness in flapping that eventually turned into multiblade flapping angles, which consists of the coning (β_0), the longitudinal flapping (β_{1_c}) and the lateral flapping (β_{1_s}).

The flapping dynamics for the ARDiS are quite different, since the rotor of an autogyro is 'hingeless', with no root cut-out as mentioned in the above. The two-blade rotor of a typical light autogyro is not only hingeless, but also stiff, and assumed to act more likely as a single beam attached to the rotor hub with *teetering* effects like a 'see-saw' (Figure 3.1). Therefore, the flapping dynamics of an autogyro is modelled to manifest this teetering effect as the flapping angle (β).

It is understood that the flapping dynamics is a very high frequency dynamics compared to the rigid-body dynamics of the aircraft which is much slower. There is limited work available for the autogyro to proof this body-flapping dynamics relationship, except a few reports [7, 88]. However, for helicopters, it has been proved and understood that the rigid-body mode such as heave and phugoid mode are very much slower compared to the rotor mode. Padfield [74] for instance, implements a simplified rotor dynamics concept with the quasi-steady assumption of the rotor blade, as it should not effect the final results of the body dynamics computation. Therefore, it is worthwhile to note that capturing the complete rotor blade dynamics is not essential since the focus of the research is to obtain the rigid-body modes of the autogyro for flying qualities analysis.

(d) The rotor-disc inflow model implemented on the ARDiS rotor model is based on the basic momentum theory, which is similar to the one that was implemented on the HGS model. However, dynamics of the airflow across the rotor disc (induced airflow) for an autogyro is different as compared to a helicopter. In a normal forward flight of a helicopter, the airflow passes through the rotor disc in a way that the airflow is accelerated or induced downwards to produce rotor thrust in forward direction. In this flight condition, the rotor disc is pitched forward for the relative airflow to be accelerated downward in forward flight.

In contrast, the rotor disc of an autogyro in forward flight act like a wind-mill to produce aerodynamic lift, while the forward thrust is largely contributed by the pusher propeller. This wind-mill state flight condition causes the rotor disc of an autgoyro to flipped, or tilted backward in forward autorotation flight.

(e) Other than the rotor model as one of the subsystems in the HGS, the external forces and moments contribution of a helicopter also include the tail rotor subsystem, the fuselage subsystem, the horizontal tailplane subsystem and the vertical fin subsystem. These loads are calculated based on the aerodynamic

data of those subsystems in the form of look-up tables that were derived from wind-tunnel testing.

For the ARDiS model, these loads are contributed from different subsystems according to the flight principle of an autogyro. Other than the rotor model, the external loads are also contributed by the propeller thrust, the fuselage, the horizontal tailplane and the vertical fin subsystems. However, since the detail aerodynamic data of the G-UNIV autogyro were not available, the forces and moments calculation are based on the aerodynamic approximation as recommended from an approved publication [7].

3.2.1 Model Limitations - The Longitudinal Model

A significant amount of literature surveys were discussed in previous chapters regarding the flying qualities issues of light autogyros, which pointed out the concerns about stability in longitudinal flight mode. One important remark that was highlighted is the relationship between the vehicle's main rotor thrust and propeller thrust line relative to the CG [13, 35, 89, 90] (see Section 2.3). This unique characteristic was also recognised as fundamentally influences the vehicle's longitudinal stability. Nevertheless, studies on the effect of other subsystems such as the tailplane on its longitudinal stability were also highlighted in the same section. Since the primary objective of the research is to improve the flying qualities of typical autogyros through control enhancement, it is then essential to focus on the longitudinal flight mode of the vehicle. As such, the mathematical model developed in this chapter is limited to the longitudinal flight dynamics of the vehicle.

3.3 Rigid Body Dynamics of an Autogyro

The mathematical model of an aircraft normally starts with the implementation of the equations of motion of the fuselage as a rigid body, with the body axes set originated at the CG. For an autogyro, the resulting forces and moment of the rigid body of the vehicle are written in the form of Euler's equations of motion, with an additional state for the rotorspeed degree of freedom from equation (3.2.2). Figure 3.3 shows the rigid body forces and moments of an autogyro in the body axes orientation relative to the earth reference. The (x-y) plane in the figure is defined as the horizontal plane inline with the CG, while the (x-z) plane is the symmetrical plane perpendicular to

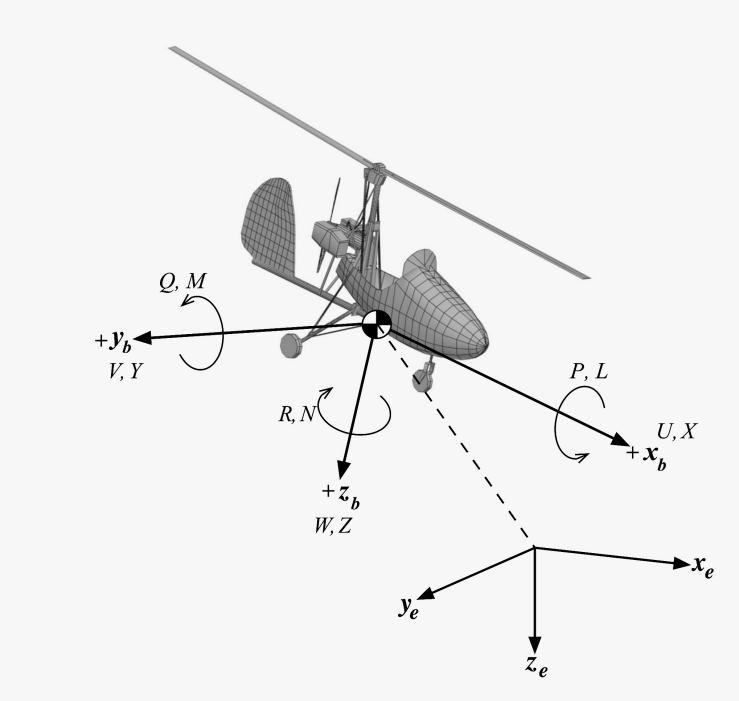

Figure 3.3: Autogyro rigid-body orientation in body and earth references

the horizontal plane. The resulting equations of motion in longitudinal mode can be written in the following:

$$m(\dot{U} + WQ) = \sum X - mg\sin\Theta \tag{3.3.1a}$$

$$m(\dot{W} - UQ) = \sum Z + mg\cos\Theta \tag{3.3.1b}$$

$$I_{yy}\dot{Q} = \sum M \tag{3.3.1c}$$

$$\dot{\Omega} = -\frac{Q_R}{I_R} \tag{3.3.1d}$$

From equations (3.3.1a) to (3.3.1d), U and W are translational velocity components of the aircraft in the body axes frame of motion, while Q is the angular velocity component of the aircraft around the lateral axis of rotation. The terms X and Z are external forces acting in the directions x_b and z_b of the body axes, while M is the external pitching moment acting about the autogyro's centre of gravity. These external forces and moment are composed of the propulsive and aerodynamic forces and moments. The term I_{yy} is the pitch moment of inertia of the autogyro. Θ is the pitch attitude of the aircraft, and the total mass of the aircraft is given by m (see Figure 3.4). Equation (3.3.1d) represents the rotorspeed state in autorotative flight, which was adapted from the rotor governor equation in [75]. Q_R is the rotor torque, while I_R is the rotor

moment of inertia at the centre of rotation.

The kinematic expressions for the rate of change of the autogyro attitude angle in longitudinal mode is given as

$$\dot{\Theta} = Q \tag{3.3.2}$$

The longitudinal orientation of the autogyro body axes in reference to the earth-fixed axes (x_e and z_e) in Figure 3.3 can be determined through the Euler transformation as

$$\begin{bmatrix} \dot{x}_e \\ \dot{z}_e \end{bmatrix} = \mathbf{T} \begin{bmatrix} U \\ W \end{bmatrix} \tag{3.3.3}$$

where the longitudinal mode transformation matrix $\mathbf{T}$ is given as

$$\mathbf{T} = \begin{bmatrix} \cos\Theta & \sin\Theta \\ -\sin\Theta & \cos\Theta \end{bmatrix} \tag{3.3.4}$$

In the autogyro longitudinal model, the contribution of external forces and moments on the rigid body from equation (3.3.1) are calculated by segregating the autogyro into four individual components or subsystems. These subsystems are named *Rotor subsystem (R)*, *Fuselage subsystem (fus)*, *Tailplane subsystem (tp)* and *Propeller subsystem (prop)*. The forces and moments are first calculated individually for each subsystem, and then combined in the form of total forces and moments contribution as expressed by

$$\sum X = X_R + X_{fus} + X_{tp} + X_{prop} \tag{3.3.5a}$$

$$\sum Z = Z_R + Z_{fus} + Z_{tp} + Z_{prop} \tag{3.3.5b}$$

$$\sum M = M_R + M_{fus} + M_{tp} + M_{prop} \tag{3.3.5c}$$

The external forces and moments in (3.3.5) also show the existence of a forward thrust component from a propeller effect, which similar to a fixed wing propeller. However, the main rotor disc forces and moments contribution are more of a helicopter than a fixed-wing.

The autogyro data used in the research is the University of Glasgow's Montgomerie-Parsons (G-UNIV) research autogyro (Figure 3.4), powered by a small ROTAX-618 two cylinder engine, with a 3-bladed fixed pitch propeller blade. All data were taken from the CAA report "The Aerodynamics of Gyroplane" [7, Appendix 2].

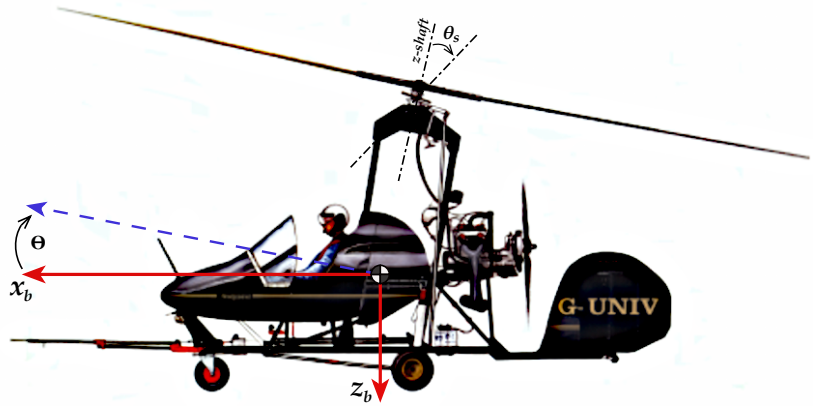

Figure 3.4: Montgomerie-Parsons G-UNIV autogyro in longitudinal mode [7] (angles exaggerated for clarity)

3.4 The Rotor Model

In a rotorcraft model, the main rotor model is the most critical subsystem and mainly contributes to the dynamic behaviour of the vehicle during flight. The primary purpose of the rotor model is to calculate the external load contributions of the rotor that eventually reflects to the rigid body of the vehicle. These external loads are determined by first, calculating the absolute velocities and accelerations of the blade through a sequence of kinematic transformations from the body axes frame to the blade axes. These sequence of kinematic transformations are summarised through a simple flow chart in Figure 3.5. The velocities and accelerations include both *translational* and *rotational* (*angular*) components. The external loads contribution of the rotor at the blade axes can then be determined from the calculated velocities and accelerations. These loads are then transformed and translated back into the load contributions relative to the CG of the autogyro. The kinematics of the blade and derivations of the rotor subsystem are briefly explained in the following subsections.

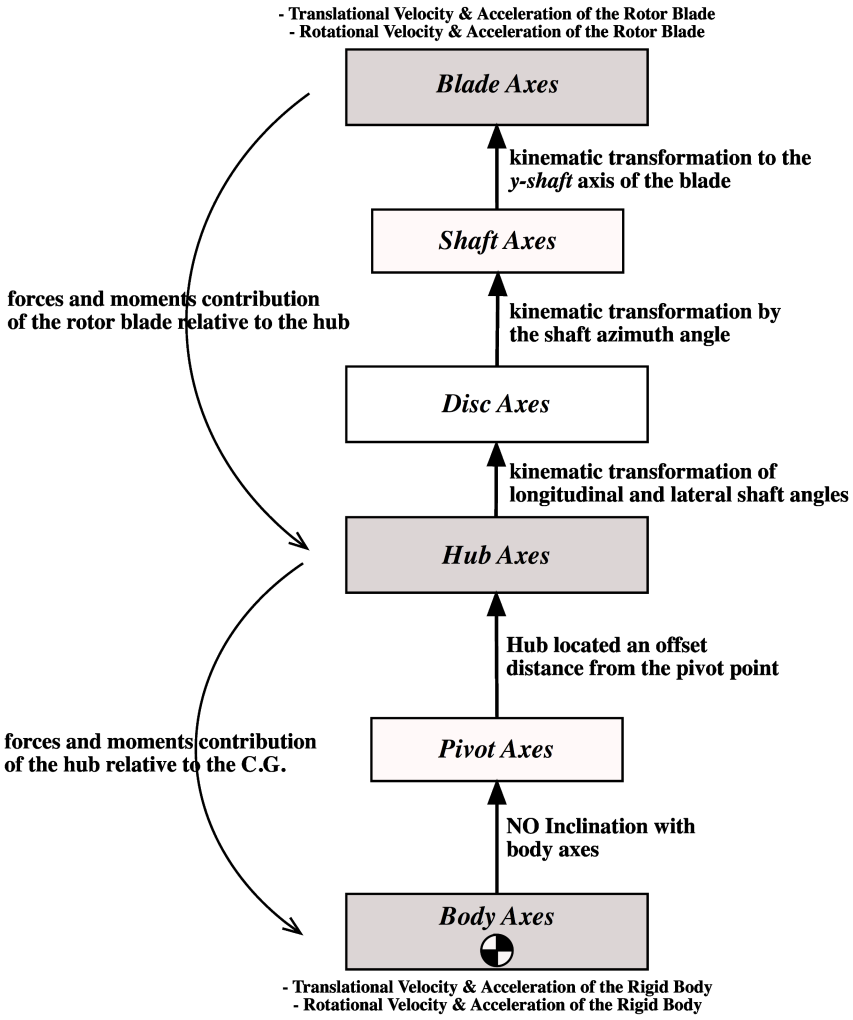

Figure 3.5: Kinematic transformations between the body axes and the blade axes orientations

3.4.1 Kinematics of the Rotor Blade

The translation along the (x_b, y_b, z_b) axes of the body axes set shown in Figure 3.3 is also defined by the unit vector $(\boldsymbol{i_b}, \boldsymbol{j_b}, \boldsymbol{k_b})$ respectively. Hence, the longitudinal translational and angular velocity of the autogyro's centre of gravity (CG) in the body-fixed axes set is defined as

$$\boldsymbol{v}_{cg}^{b} = \begin{bmatrix} U & 0 & W \end{bmatrix}^T \tag{3.4.1}$$

$$\boldsymbol{\omega}_b = \begin{bmatrix} 0 & Q & 0 \end{bmatrix}^T \tag{3.4.2}$$

while, the longitudinal translational and angular accelerations of the CG in the body axes as referring to equations ((3.3.1a)) through ((3.3.1d)) are defined as

$$\boldsymbol{a}_{cg}^{b} = \begin{bmatrix} (\dot{U} + WQ) & 0 & (\dot{W} - UQ) \end{bmatrix}^{T} \tag{3.4.3}$$

$$\boldsymbol{\alpha}_{b} = \begin{bmatrix} 0 & \dot{Q} & 0 \end{bmatrix}^{T} \tag{3.4.4}$$

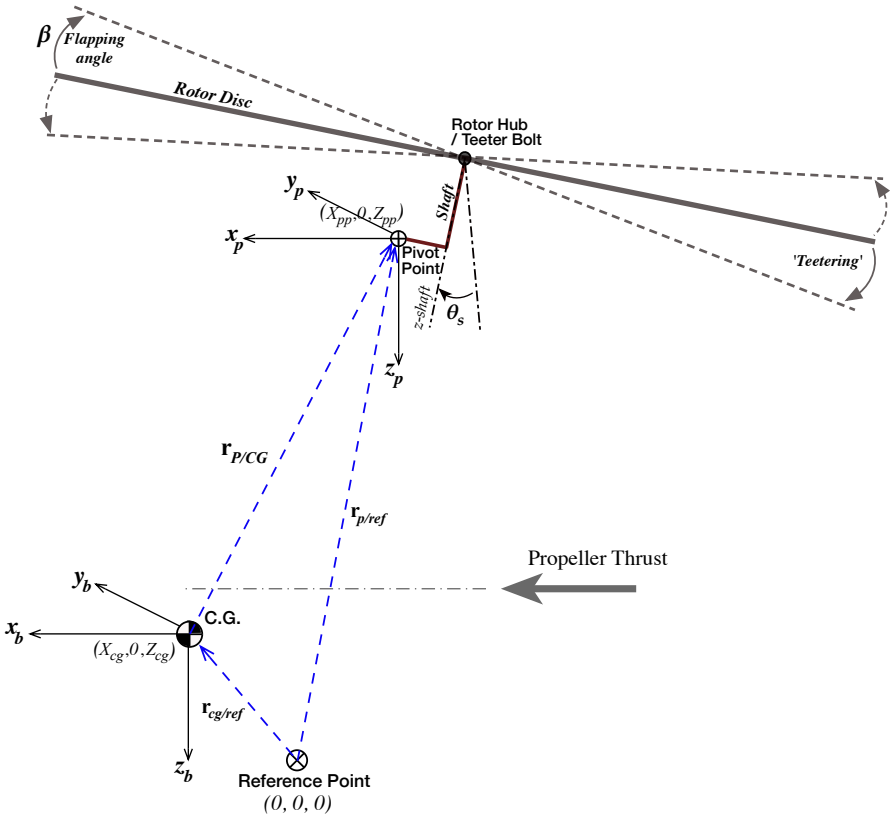

Figure 3.6: Transformation from the body axes to the hub axes (angles exaggerated for clarity)

3.4.1.1 Velocity and Acceleration of the Pivot Axes

Figure 3.6 shows different axes orientations from the body axes, pivot axes and the rotor hub axes system. It is important to note that all vector locations presented are defined in relation to the reference point. From the same CAA report [7], the reference point is defined at a particular bolt on the keel of the aircraft to ease of measurement. Therefore, based on the same figure, the vector location of the autogyro's CG relative to the reference point is written as

$$\boldsymbol{r}_{cg/ref} = \begin{bmatrix} x_{cg} & 0 & z_{cg} \end{bmatrix}^T \tag{3.4.5}$$

while the relative vector location of the pivot point from the CG is defined in the same manner as,

$$\boldsymbol{r}_{p/ref} = \begin{bmatrix} x_{pp} & 0 & z_{pp} \end{bmatrix}^T \tag{3.4.6}$$

Hence, the vector position of the pivot point relative to the CG is determined as

$$\boldsymbol{r}_{P/CG} = \begin{bmatrix} x_{pcg} & 0 & z_{pcg} \end{bmatrix}^T \tag{3.4.7}$$

where x_{pcg} and z_{pcg} are given by $(\boldsymbol{r}_{p/ref} - \boldsymbol{r}_{cg/ref})$.

The kinematic transformations begin with calculating the velocity and acceleration of the pivot point relative to the CG through consideration of the equations (3.4.1) to (3.4.4), and expressed by

$$\boldsymbol{v}_{pp}^b = \boldsymbol{v}_{cg}^b + \boldsymbol{\omega}_b \times \boldsymbol{r}_{P/CG} \tag{3.4.8}$$

$$\boldsymbol{a}_{pp}^b = \boldsymbol{a}_{cg}^b + \boldsymbol{\alpha}_b \times \boldsymbol{r}_{P/CG} + \boldsymbol{\omega}_b \times (\boldsymbol{\omega}_b \times \boldsymbol{r}_{P/CG}) \tag{3.4.9}$$

The pivot axes is fixed and aligned with the body axes frame of the autogyro and act as a reference axes that distinguish the motion of the autogyro's airframe and its rotor-disc. Although there is no inclination between the pivot axes and the body axes, the pivot axes is needed in the autogyro's kinematic calculation for two reasons; Firstly, the location of the pivot with respect to the CG ($\boldsymbol{r}_{P/CG}$) provides the external moment contribution of the rotor blade, thus affecting calculations in the rotor model. Secondly, the rotor hub is shifted by a longitudinal and vertical *offset* distance from the pivot. Since the shaft tilt is controlled through a direct link from pilot to the pivot point (as seen in Figure 3.2), the rotor shaft will be seen pivoting around the pivot point. Hence, pivot axes is needed as the reference frame for the rotor-disc orientation in the autogyro kinematics.

Without any inclination from the body axes, the pivot axes frame is defined with translational velocities and accelerations equal to those of the body axes frame in

equation (3.4.8) and (3.4.9), and written as

$$\boldsymbol{v}_{pp}^{pvt} = \boldsymbol{v}_{pp}^{b} \quad \text{and} \quad \boldsymbol{a}_{pp}^{pvt} = \boldsymbol{a}_{pp}^{b}$$

Similarly, the angular velocity and acceleration of the pivot axes can be written as

$$\boldsymbol{\omega}_{pvt} = \boldsymbol{\omega}_{b} \quad \text{and} \quad \boldsymbol{\alpha}_{pvt} = \boldsymbol{\alpha}_{b}$$

It is important to note that the *shaft offset* between the rotor hub and the longitudinal pivot hinge plays an important role in autogyro's handling (see Figure 3.1). The shaft offset acts as a 'lever arm' that provides a small moment that helps in damping the airframe of the autogyro in the presence of disturbances or perturbations. When a disturbance acts on the rotor-disc, the equilibrium teetering motion will be disturbed and causes the rotor blade to dynamically change its teetering motion. This condition also creates an extra moment due to the shaft offset that feeds through to the whole mechanical linkages causes them to vibrate. In this scenario, the extra force and moment of the gust is said to be 'absorbed' by the mechanical linkages, also causing the pilot control stick to vibrates or shaken according to the magnitude of the gust. There has been a study made by Trchalik [91] on autogyro's rotor blade dynamics that indicates the changes of the blade axis position relative to the azimuth in autorotation which is due to the shaft offset. These blade axis position changes can be understood as being translated into a form of 'vibration' that eventually transmitted from the rotor hub to the pilot control stick. In fact, Trchalik also proves that the shaft offset relative to the longitudinal hinge (pivot point) of an autogyro does not affect the stability of the rotor disc in autorotation [91, p.166]. Hence, the control stick 'shaking' is considered to act as a natural indicator for the pilot to acknowledge the existence of gust during flight. Without the shaft offset, the full disturbance force or effect will be transferred from the rotor-disc to the whole airframe of the autogyro. This disturbance also causing the whole airframe of the vehicle to be shaken according to the magnitude of the disturbance [92].

3.4.1.2 Velocity and Acceleration of the Hub Axes

The next step is to look into the kinematics of the hub axes as translated from the pivot axes. The rotor hub of the G-UNIV autogyro is located an *offset* distance from the pivot point, also known as the *shaft offset* as shown in Figure 3.7. The vector position of the hub relative to the reference point is given by

$$\boldsymbol{r}_{hub/ref} = \begin{bmatrix} x_{hub} & 0 & z_{hub} \end{bmatrix}^T \tag{3.4.10}$$

while the location vector of the CG relative to the reference has been defined previously in (3.4.5). The location vector of the hub relative to the pivot point is then calculated by $(\boldsymbol{r}_{hub/ref} - \boldsymbol{r}_{cg/ref})$ and written as

$$\boldsymbol{r}_{hub/pivot} = \begin{bmatrix} x_{hpp} & 0 & z_{hpp} \end{bmatrix}^T \tag{3.4.11}$$

Hence, the translational velocity and acceleration of the hub in the pivot axes can be determined by

$$\boldsymbol{v}_h^{pvt} = \boldsymbol{v}_{pp}^{pvt} + \boldsymbol{\omega}_{pvt} \times \boldsymbol{r}_{hub/pivot} \tag{3.4.12}$$

$$\boldsymbol{a}_h^{pvt} = \boldsymbol{a}_{pp}^{pvt} + \boldsymbol{\alpha}_{pvt} \times \boldsymbol{r}_{hub/pivot} + \boldsymbol{\omega}_{pvt} \times (\boldsymbol{\omega}_{pvt} \times \boldsymbol{r}_{hub/pivot}) \tag{3.4.13}$$

The shaft is actually connected to the pilot control stick directly through mechanical linkages and this offset distance would give a small mechanical advantage of forces for the pilot in manoeuvring the aircraft.

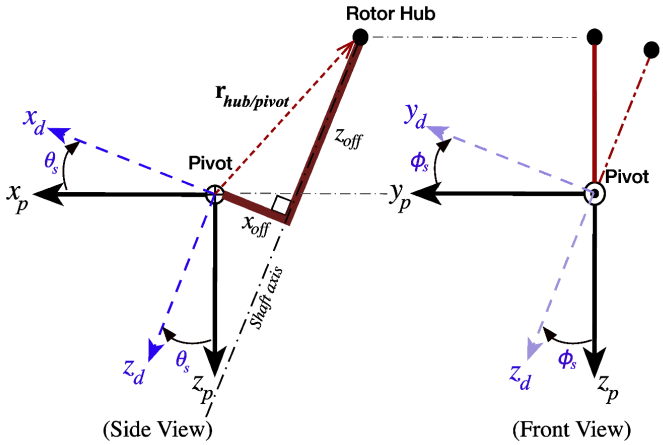

Figure 3.7: Transformations from the pivot axes to the hub axes

3.4.1.3 Velocity and Acceleration of the Disc Axes

The *rotor disc* axes frame is associated with the control of the autogyro through the longitudinal shaft tilt angle θ_s and the lateral shaft tilt angle ϕ_s about the pivot point as shown in Figure 3.7.

The translational velocity and acceleration vectors from equation (3.4.12) and (3.4.13) are then transformed into the disc axes orientation. Hence, the longitudinal translational and angular velocities of the hub in the disc axes set are now expressed by

$$\boldsymbol{v}_h^d = \boldsymbol{T}_{pivot \to disc}\, \boldsymbol{v}_h^{pvt} = \begin{bmatrix} U_h^d & 0 & W_h^d \end{bmatrix}^T \tag{3.4.14}$$

$$\boldsymbol{\omega}_d = \boldsymbol{T}_{pivot \to disc}\, \boldsymbol{\omega}_{pvt} = \begin{bmatrix} 0 & Q_h^d & 0 \end{bmatrix}^T \tag{3.4.15}$$

where $\boldsymbol{T}_{pivot \to disc}$ is the transformation matrix from the pivot axes to the disc axes in Figure 3.7. Assuming that the lateral shaft tilt $\phi_s = 0$, the longitudinal control tilt θ_s would involve the transformation of

$$\boldsymbol{T}_{pivot \to disc} = \begin{bmatrix} \cos\theta_s & 0 & -\sin\theta_s \\ 0 & 1 & 0 \\ \sin\theta_s & 0 & \cos\theta_s \end{bmatrix} \tag{3.4.16}$$

Similarly, the translational and angular accelerations of the hub in the disc axes set are given by

$$\boldsymbol{a}_h^d = \boldsymbol{T}_{pivot \to disc}\, \boldsymbol{a}_h^{pvt} = \begin{bmatrix} a_x^d & 0 & a_z^d \end{bmatrix}^T \tag{3.4.17}$$

$$\boldsymbol{\alpha}_d = \boldsymbol{T}_{pivot \to disc}\, \boldsymbol{\alpha}_{pvt} = \begin{bmatrix} 0 & \dot{Q}_h^d & 0 \end{bmatrix}^T \tag{3.4.18}$$

3.4.1.4 Velocity and Acceleration of the Shaft Axes

The next step is to transform the velocities and accelerations in the disc axes set from equations (3.4.14) through (3.4.18) into the *shaft* axes orientation. The shaft axes are defined as a reference frame with the origin at the rotor hub, but the axis of rotation pointing down through the *z-shaft* axis as shown in Figures 3.8 and 3.9. The shaft

and blade rotation is given by the azimuth angle ψ_s. The translational velocity and acceleration of the hub in the shaft axes can be determined through the transformation:

$$\boldsymbol{v}_h^s = \boldsymbol{T}_{disc \to shaft}\ \boldsymbol{v}_h^d \tag{3.4.19}$$

$$\boldsymbol{a}_h^s = \boldsymbol{T}_{disc \to shaft}\ \boldsymbol{a}_h^d \tag{3.4.20}$$

where $\boldsymbol{T}_{disc \to shaft}$ is the transformation matrix from the disc to the shaft axes which is given by

$$\boldsymbol{T}_{disc \to shaft} = \begin{bmatrix} -\cos\psi_s & \sin\psi_s & 0 \\ -\sin\psi_s & -\cos\psi_s & 0 \\ 0 & 0 & 1 \end{bmatrix} \tag{3.4.21}$$

The angular velocity and acceleration of the hub in the shaft axes are determined through the same transformation, with an additional rotorspeed Ω term as part of the shaft's angular function and expressed by

$$\boldsymbol{\omega}_s = \boldsymbol{T}_{disc \to shaft}\ \boldsymbol{\omega}_d + \begin{bmatrix} 0 & 0 & -\Omega \end{bmatrix}^T \tag{3.4.22}$$

$$\boldsymbol{\alpha}_s = \boldsymbol{T}_{disc \to shaft}\ \boldsymbol{\alpha}_d + \begin{bmatrix} 0 & 0 & -\dot{\Omega} \end{bmatrix}^T \tag{3.4.23}$$

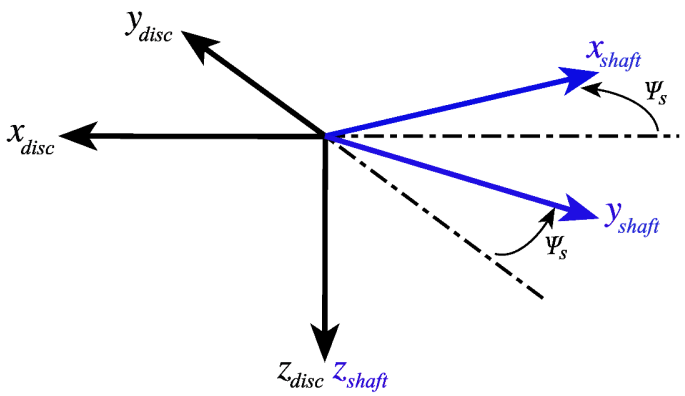

Figure 3.8: Transformation from the Disc axes to the Shaft axes

Note that the rotor blade of the G-UNIV autogyro rotates in a counter-clockwise direction as seen from the above. Hence, the negative sign $(-\Omega)$ is to show the opposites

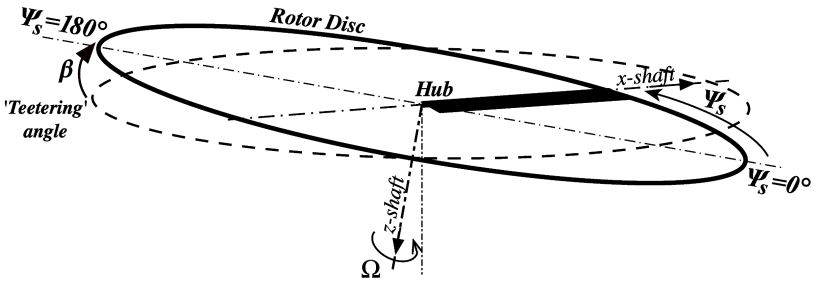

Figure 3.9: Blade rotation with respect to the azimuth position

between the direction of the blade rotation with respect to the standard convention of the body orientations shown in Figure 3.3.

3.4.1.5 Velocity and Acceleration of the Blade Axes

The final step is the transformation from the shaft axes to the blade axes of orientation. It is important to emphasise that for most light autogyros, the rotor blade is usually a 'teetering' type. This is actually a two-bladed rotor that acts as a single rigid blade pivoting around the hub like a 'see-saw', with the blade being held tightly by a teetering bolt as shown in Figure 3.1. Therefore, flapping on one side of the blade tip causes the other side of the tip to flap in the opposite direction with the same flapping angle β as shown in Figure 3.9. Hence, this flapping angle is now considered as the 'teetering angle' of the rotor disc, of which is unique for an autogyro case. During a flight, the rotor disc is rotating and teetering freely in its degree of freedom in sustaining the aerodynamic lift. Therefore, it is important to note that the control angles (θ_s and ϕ_s) indicate only the shaft tilt angles that are directly linked mechanically with the pilot control stick. These control angles are not representing the actual rotor disc angle, for which is given by the additional function of flapping (teetering). The flapping equation is shown in the later subsection of this chapter.

Since the rotor blade is attached to the hub without hinge offset, and referring to equations (3.4.19) and (3.4.20), the translational velocity and acceleration of the hub in the blade axes can be written as

$$\boldsymbol{v}_h^{bl} = \boldsymbol{T}_{shaft \rightarrow blade}\ \boldsymbol{v}_h^s \tag{3.4.24}$$

$$\boldsymbol{a}_h^{bl} = \boldsymbol{T}_{shaft \rightarrow blade}\ \boldsymbol{a}_h^s \tag{3.4.25}$$

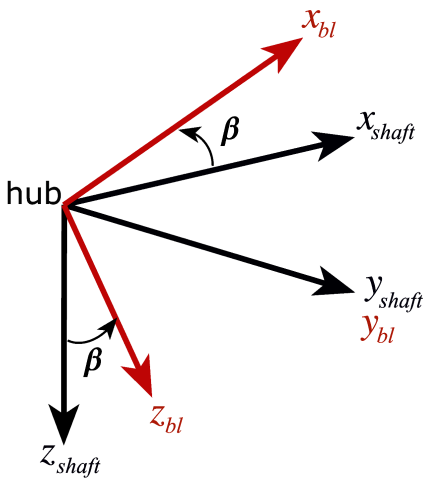

Figure 3.10: Shaft to blade axes transformation

$\boldsymbol{T}_{shaft\rightarrow blade}$ is the transformation matrix from the shaft to the blade axes of orientation as shown in Figure 3.10, where the blade flaps around the *y-shaft* axis with small flapping angle β and expressed by

$$\boldsymbol{T}_{shaft\rightarrow blade} = \begin{bmatrix} \cos\beta & 0 & -\sin\beta \\ 0 & 1 & 0 \\ \sin\beta & 0 & \cos\beta \end{bmatrix} \approx \begin{bmatrix} 1 & 0 & -\beta \\ 0 & 1 & 0 \\ \beta & 0 & 1 \end{bmatrix} \tag{3.4.26}$$

With the consideration of the flapping rate ($\dot{\beta}$) around the *y-shaft* axis, the angular velocity and acceleration of the hub in the blade axes are then determined by

$$\boldsymbol{\omega}_{bl} = \boldsymbol{T}_{shaft\rightarrow blade}\ \boldsymbol{\omega}_s + \begin{bmatrix} 0 & \dot{\beta} & 0 \end{bmatrix}^T \tag{3.4.27}$$

$$\boldsymbol{\alpha}_{bl} = \boldsymbol{T}_{shaft\rightarrow blade}\ \boldsymbol{\alpha}_s + \begin{bmatrix} 0 & \ddot{\beta} & 0 \end{bmatrix}^T \tag{3.4.28}$$

Finally, within the same blade axes orientation, the translational velocity and acceleration of an element of mass (denoted by a subscript 'e') with a distance r_b along the blade span can be obtained and expressed by

$$\boldsymbol{v}_e^{bl} = \boldsymbol{v}_h^{bl} + \boldsymbol{\omega}_{bl} \times \boldsymbol{r}_{e/bl} \tag{3.4.29}$$

$$\boldsymbol{a}_e^{bl} = \boldsymbol{a}_h^{bl} + \boldsymbol{\alpha}_{bl} \times \boldsymbol{r}_{e/bl} + \boldsymbol{\omega}_{bl} \times (\boldsymbol{\omega}_{bl} \times \boldsymbol{r}_{e/bl}) \tag{3.4.30}$$

where $\boldsymbol{r}_{e/bl}$ is the position vector of the element, e along the *x-blade* axis as shown in Figure 3.11, and denoted as

$$\boldsymbol{r}_{e/bl} = \begin{bmatrix} r_b & 0 & 0 \end{bmatrix}^T \tag{3.4.31}$$

The velocity and acceleration in equations (3.4.29) and (3.4.30) are then expressed in vector form as

$$\boldsymbol{v}_e^{bl} = \begin{bmatrix} v_x^{bl} & v_y^{bl} & v_z^{bl} \end{bmatrix}^T \tag{3.4.32}$$

$$\boldsymbol{a}_e^{bl} = \begin{bmatrix} a_x^{bl} & a_y^{bl} & a_z^{bl} \end{bmatrix}^T \tag{3.4.33}$$

From these kinematic vectors, the contribution of forces and moments of the blade element can then be determined according to the local equations of motion at the blade element, which are explained in the following section.

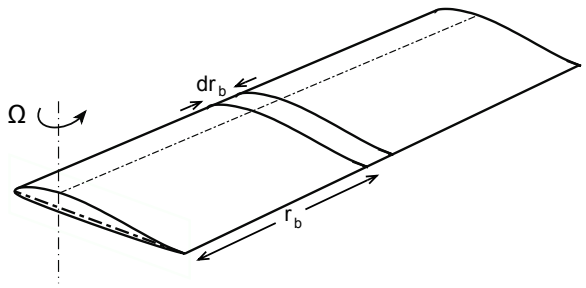

Figure 3.11: Illustration of a single rotor blade

3.4.2 Rotor Forces and Moments

The external forces contribution of the blade element can be obtained by considering the local aerodynamic and inertial forces as shown in Figure 3.12. These forces are determined by considering the equilibrium between the two forces and written in the form of elemental force vector

$$\boldsymbol{f}_e^{bl} = \begin{bmatrix} -m_0 a_x^{bl} \\ \left(f_y^{bl} - m_0 a_y^{bl}\right) \\ \left(f_z^{bl} - m_0 a_z^{bl}\right) \end{bmatrix} \tag{3.4.34}$$

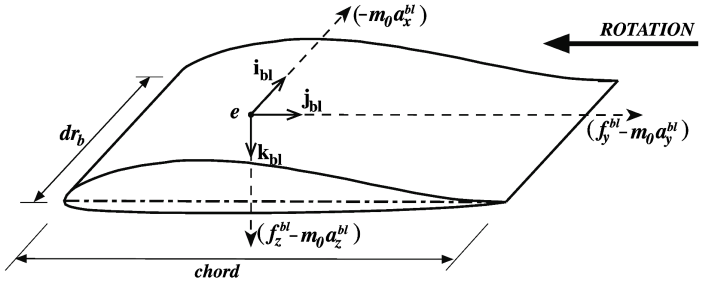

Figure 3.12: Forces orientation on a Blade Element

where f_y^{bl} and f_z^{bl} are the local aerodynamic forces in the *y-blade* and *z-blade* direction of the element e and m_0 is the mass per unit span of the blade element. The elemental force f_x^{bl} is neglected as the blade is assumed to be rigid and fixed to the root of the rotor hub and rotating in the direction perpendicular to the *x-blade* axis.

It is important to note that the inertial force in *y-blade* is always much more smaller than the aerodynamic forces that it can be disregarded in the rotor moment calculations. This assumption was proven in the HGS model [22], where the inertial forces contribute the least to the rigid-body moment calculations, which can be neglected. In fact, Padfield [74] disregarded the inertial force in the helicopter's moment calculations due to the same reason. Therefore, the inertial force will not be included in the rotor moment calculations.

3.4.2.1 Aerodynamic Forces of the Blade

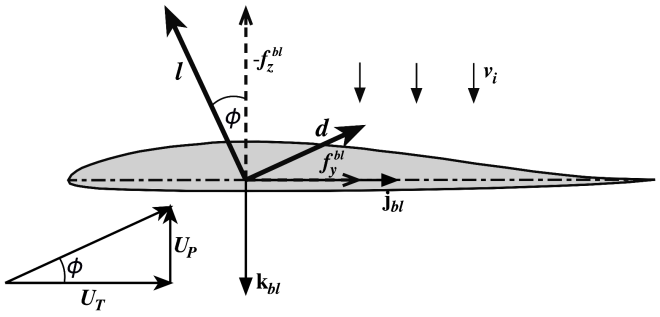

Figure 3.13: The blade element's normal and tangential velocity components

The *aerodynamic forces* of the blade are always associated with the local lift and drag forces created due to the local blade angle of attack as shown in Figure 3.13. For modelling simplification, the *tangential* velocity airflow, U_T is assumed to be much

greater than the *normal* velocity airflow, U_P, where ($U_T \gg U_P$). Furthermore, the local angle of attack is assumed to be small, where $l\cos\phi \gg d\sin\phi$.

Hence, the aerodynamic force components can then be simplified as

$$f_y^{bl} = (d\cos\phi - l\sin\phi) \approx d - l\phi \tag{3.4.35}$$

$$f_z^{bl} = (-l\cos\phi - d\sin\phi) \approx -l \tag{3.4.36}$$

Since ϕ is assumed as a small incidence, the tangential and normal airflows can be written as

$$U_T = -v_y^{bl} \tag{3.4.37}$$

$$U_P = v_z^{bl} - v_i \tag{3.4.38}$$

$$\phi = \tan^{-1}\left(\frac{U_P}{U_T}\right) \approx \frac{U_P}{U_T} \tag{3.4.39}$$

v_y^{bl} and v_z^{bl} of equations (3.4.37) and (3.4.38) are the velocity components of the blade element from equation (3.4.32). Furthermore, the velocity of the induced airflow (v_i) that passes through the rotor disc is given by

$$v_i = v_0 + \frac{r_b}{R}(v_{1_s}\sin\psi + v_{1_c}\cos\psi) \tag{3.4.40}$$

where v_0 is the uniform airflow through the rotor disc, v_{1_s} and v_{1_c} are the longitudinal and lateral airflow components in the function of the rotating azimuth angle ψ.

A higher fidelity rotorcraft model with highly accurate prediction usually employs higher fidelity dynamic inflow model like the one being used on the individual-blade approach. The RASCAL model, for instance, employed the Peters and HaQuang dynamic inflow model, in which the non-uniform induced velocity of airflow through the rotor blade is calculated numerically with the function of radial and azimuthal position of the blade element [19, 34, 93]. This sophisticated approach is very useful, but the rotor blade complexity is less significant for a rigid-body dynamics and flight control study.

For the ARDiS model that employs a rotor-disc modelling approach, a more simple inflow model is used, which was typically used in conventional rotorcraft model. The

approach is based on the fundamental Glauert's inflow model as mentioned in equation (3.4.40), and explained in Appendix A [1]. Implementing this simple rotor inflow model in an autogyro involved some changes, due to the nature of the induced air velocity that passes through the rotor disc. Comparison between helicopter and autogyro induced airflow are illustrated in Figure 3.14 and 3.15. For a helicopter in forward flight, the relative air is induced and passes through the rotor disc with a negative pitch angle (Figure 3.14). In this condition, the wake angle (χ_w) is less than 90° relative to the induced inflow. In contrast to helicopters, autogyros fly in a way that the rotor disc or the rotor hub is positively pitch (aft pitch). This is also known as a wind-mill flight state where the lift is created based on the amount of air induced or accelerated to the opposite direction like a wind brake (Figure 3.15). To have a positive airflow through the rotor disc and creating lift, the wake angle (χ_w) of an autogyro must always be greater than 90° relative to the induced inflow.

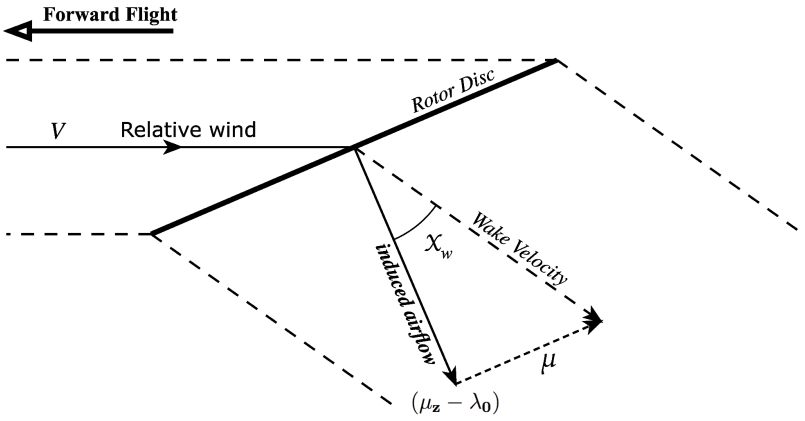

Figure 3.14: Illustration of induced airflow of a helicopter

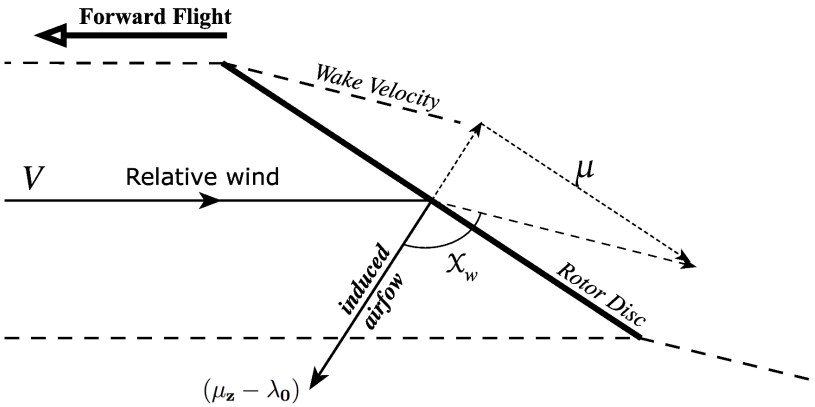

Figure 3.15: Illustration of induced airflow of an autogyro

Another important point to note that in ARDiS model, aerodynamic details of the blade's aerofoil such as the lift and drag coefficients for different points along the blade span (including the Mach number) are not modelled. This aerofoil is expressed in a simple 2-dimensional aerofoil (thin aerofoil theory) that the lift and drag forces per unit span of the blade element are written as

$$l(r_b, \psi) = \frac{1}{2}\,\rho\, c\left(U_P^2 + U_T^2\right) C_l \tag{3.4.41}$$

$$d(r_b, \psi) = \frac{1}{2}\,\rho\, c\, U_T^2\, C_d \tag{3.4.42}$$

where C_l and C_d are the lift and drag coefficients given as the average values for the whole span of the blade. Furthermore, the G-UNIV autogyro is equipped with a two-blade teetering rotor with NACA 8-H-12 aerofoil that has a lift coefficient according to Ref. [94];

$$C_l = a_0\ \alpha_{bl} + a_1 \tag{3.4.43}$$

Since the blades of light autogyros are mostly untwisted with zero pitch angle ($\theta = 0$), the angle of incidence is then similar to the blade's angle of attack in equation (3.4.39) and expressed by

$$\alpha_{bl} = \theta + \phi \approx \frac{U_P}{U_T} \tag{3.4.44}$$

Also in this ARDiS model, the elemental drag coefficient C_d is assumed to have a constant mean value denoted as δ. Correspondingly, the elemental lift and drag forces of the blade in equations (3.4.41) and (3.4.42) are now written as

$$l\,(r_b, \psi) = \frac{1}{2}\,\rho c\left(U_P^2 + U_T^2\right)(a_0\alpha_{bl} + a_1) \tag{3.4.45}$$

$$d\,(r_b, \psi) = \frac{1}{2}\,\rho c\, U_T^2\,\delta \tag{3.4.46}$$

These lift and drag forces are then incorporated into equations (3.4.35) and (3.4.36) to determine the *aerodynamic force* components in the *y-blade* and *z-blade* direction along the elemental length (dr_b) of the blade. The total aerodynamic forces are then determined by analytically integrate these elemental forces over the whole blade span (R), and expressed by

$$\boldsymbol{F}_A^{bl} = \begin{bmatrix} X_A^{bl} \\ Y_A^{bl} \\ Z_A^{bl} \end{bmatrix} = \frac{1}{2}\,\rho c \begin{bmatrix} 0 \\ \int_0^R \left(\delta U_T^2 - a_1 U_P U_T - a_0 U_P^2\right) dr_b \\ -\int_0^R \left(a_0 U_P U_T + a_1 U_T^2\right) dr_b \end{bmatrix} \tag{3.4.47}$$

These aerodynamic forces are normalised by the term $\rho(\Omega R)^2 \pi R^2$ and re-written in a dimensionless form as

$$\boldsymbol{C}_{F_A}^{bl} = \begin{bmatrix} \boldsymbol{C}_{X_A}^{bl} \\ \boldsymbol{C}_{Y_A}^{bl} \\ \boldsymbol{C}_{Z_A}^{bl} \end{bmatrix} = \frac{1}{2}\,s \begin{bmatrix} 0 \\ \int_0^1 \left(\delta \bar{U}_T^2 - a_1 \bar{U}_P \bar{U}_T - a_0 \bar{U}_P^2\right) d\bar{r}_b \\ -\int_0^1 \left(a_0 \bar{U}_P \bar{U}_T + a_1 \bar{U}_T^2\right) d\bar{r}_b \end{bmatrix} \tag{3.4.48}$$

where, s is the blade solidity for the total number of blades b, given by

$$s = \frac{b\,c}{\pi R}$$

while the normalised velocity components and distance are given by

$$\bar{U}_T = \frac{U_T}{\Omega R}, \quad \bar{U}_P = \frac{U_P}{\Omega R}, \quad \bar{r}_b = \frac{r_b}{R}$$

It will be shown later in Section 3.4.2.3 that the teetering angle β variation is expressed as the function of azimuth angle ψ in the first harmonic forms ($\cos\psi$ and $\sin\psi$). On the other hand, analytical integration of rotor blade aerodynamic forces is quite complex that the calculations are checked using symbolic algebra package *Mathematica*® [95,96]. The blade aerodynamic forces calculation results from the Mathematica were actually expressed up to the fourth harmonic terms. However, it was decided that the force coefficients to be addressed in the same degree of accuracy with the teetering angle β for consistency. Hence, only the first harmonic form of the blade aerodynamic force coefficients are considered in this modelling approach, which is written as

$$\begin{bmatrix} \boldsymbol{C}^{bl}_{X_A} \\ \boldsymbol{C}^{bl}_{Y_A} \\ \boldsymbol{C}^{bl}_{Z_A} \end{bmatrix} = \frac{1}{2}\, s \begin{bmatrix} 0 \\ C^{bl}_{Y_{A_0}} + C^{bl}_{Y_{A_{1c}}} \cos\psi + C^{bl}_{Y_{A_{1s}}} \sin\psi \\ -\big(C^{bl}_{Z_{A_0}} + C^{bl}_{Z_{A_{1c}}} \cos\psi + C^{bl}_{Z_{A_{1s}}} \sin\psi\big) \end{bmatrix} \tag{3.4.49}$$

3.4.2.2 Total Forces and Moments Contribution of the Rotor

In general the force acted on the rotor can be determined by calculating the rotor hub forces in the blade axes orientation. From the aerodynamic and initial force components in (3.4.34), the total rotor hub forces in the blade axes can be generalised and given as

$$\boldsymbol{F}^{bl}_h = \int_0^R \big(\boldsymbol{f}^{bl}_a - \boldsymbol{f}^{bl}_i\big) dr_b \tag{3.4.50}$$

Since the inertial force is neglected as discussed in Section 3.4.2.1, and considering the evaluated coefficients in (3.4.49), the total forces acting at the hub in the blade axes set can be written in coefficient form as

$$\boldsymbol{C}^{bl}_h = \begin{bmatrix} C^{bl}_X \\ C^{bl}_Y \\ C^{bl}_Z \end{bmatrix} = \begin{bmatrix} C^{bl}_{X_0} + C^{bl}_{X_{1s}} \sin\psi + C^{bl}_{X_{1c}} \cos\psi \\ C^{bl}_{Y_0} + C^{bl}_{Y_{1s}} \sin\psi + C^{bl}_{Y_{1c}} \cos\psi \\ C^{bl}_{Z_0} + C^{bl}_{Z_{1s}} \sin\psi + C^{bl}_{Z_{1c}} \cos\psi \end{bmatrix} \tag{3.4.51}$$

On the other hand, the blade moment acting on the rotor hub is contributed by the elemental force of an element 'e' with a distance $r_{e/hub}$ from the hub, which is given by

$$\boldsymbol{M}^{bl}_h = \int_0^R \boldsymbol{r}_{e/hub} \times \boldsymbol{f}^{bl}_e dr_b = \begin{bmatrix} 0 \\ \int_0^R -r_b\big(f^{bl}_z - m_0\, a^{bl}_z\big) \\ \int_0^R r_b\big(f^{bl}_y - m_0\, a^{bl}_y\big) \end{bmatrix} = \begin{bmatrix} 0 \\ K_\beta \beta \\ Q^{bl}_h \end{bmatrix} \tag{3.4.52}$$

Equation (3.4.52) clearly shows that the total hub moment is contributed by two elemental moment of the blade element. These are the moment about the *y-blade* axis, known as the *flapping* moment, and the moment acted about the *z-blade* axis, known

as the *torque* moment. The contribution to the torque moment of equation (3.4.52) is solved individually in normalised form through analytical integration and yields its uniform and harmonic terms as

$$C^{bl}_{Q_h} = \frac{1}{2}\rho c \left(C^{bl}_{Q_0} + C^{bl}_{Q_{1_c}} \cos\psi + C^{bl}_{Q_{1_s}} \sin\psi\right) \tag{3.4.53}$$

The effective torque of the hub is assumed to be primarily affected by the uniform or average values of equation (3.4.53), and therefore, the hub torque of the blades can be simplified to be

$$C^{bl}_{Q_h} = \frac{1}{2}\rho c\, C^{bl}_{Q_0} \tag{3.4.54}$$

which finally gives the hub moment vector in the blade axes as

$$\boldsymbol{C}^{bl}_{M_h} = \begin{bmatrix} 0 & 0 & C^{bl}_{Q_h} \end{bmatrix}^T \tag{3.4.55}$$

The forces and moments contribution of the blade must be transformed back to the body axes orientation since the autogyro's rigid body equations of motion are expressed in the body axes. This reverse transformation represents the load contribution of the rotor blade to the vehicle's dynamic motions about its CG. First, the forces and moments of the blade axes in equations (3.4.51) and (3.4.55) are transformed to the disc axes orientation, given by

$$\boldsymbol{C}^{d}_{F_h} = (\boldsymbol{T}_{disc\to shaft})^T (\boldsymbol{T}_{shaft\to blade})^T\, \boldsymbol{C}^{bl}_{h} = \begin{bmatrix} C^{d}_{X_h} & C^{d}_{Y_h} & C^{d}_{Z_h} \end{bmatrix}^T \tag{3.4.56}$$

and

$$\boldsymbol{C}^{d}_{M_h} = (\boldsymbol{T}_{disc\to shaft})^T (\boldsymbol{T}_{shaft\to blade})^T\, \boldsymbol{C}^{bl}_{M_h} = \begin{bmatrix} C^{d}_{l_h} & C^{d}_{m_h} & C^{d}_{n_h} \end{bmatrix}^T \tag{3.4.57}$$

where the transformation matrices $(\boldsymbol{T}_{disc\to shaft})^T$ and $(\boldsymbol{T}_{shaft\to blade})^T$ were transposed from equations (3.4.21) and (3.4.26), which also represent the reverse transformation from the blade to the disc axes.

Next, the force and moment coefficients in (3.4.56) and (3.4.57) are transformed to the pivot axes through the transposed of matrix (3.4.16) and given by

$$\boldsymbol{C}^{pvt}_{F_{pp}} = (\boldsymbol{T}_{pivot\to disc})^T\, \boldsymbol{C}^{d}_{F_h} \tag{3.4.58}$$

and

$$\boldsymbol{C}^{pvt}_{M_{pp}} = (\boldsymbol{T}_{pivot\rightarrow disc})^T \, \boldsymbol{C}^{d}_{M_h} + (\boldsymbol{r}_{hub/pivot} \times \boldsymbol{C}^{pvt}_{F_{pp}}) \tag{3.4.59}$$

Note that the shaft offset between the hub and pivot ($\boldsymbol{r}_{hub/pivot}$) was also accounted for the moment transformation in equation (3.4.59).

Finally, the force and moment coefficients in the body axes is determined through the transformation from the pivot axes. Since the pivot axes and the body axes are in the same orientation (no inclination), the force and moment coefficients about the vehicle's CG are expressed by

$$\boldsymbol{C}^{b}_{F_{cg}} = \boldsymbol{C}^{pvt}_{F_{pp}} \tag{3.4.60}$$

and

$$\boldsymbol{C}^{b}_{M_{cg}} = \boldsymbol{C}^{pvt}_{M_{pp}} + (\boldsymbol{r}_{P/CG} \times \boldsymbol{C}^{b}_{F_{cg}}) \tag{3.4.61}$$

These coefficients are then de-normalised and written as the following external force and moment contributions of the rotor relative to the CG to be included in the equations of motion.

$$\boldsymbol{F}^{b}_{cg} = \begin{bmatrix} X_R & 0 & Z_R \end{bmatrix}^T \tag{3.4.62}$$

$$\boldsymbol{M}^{b}_{cg} = \begin{bmatrix} 0 & M_R & 0 \end{bmatrix}^T \tag{3.4.63}$$

3.4.2.3 Flapping (Teetering) Dynamics

Rotorcraft blade flapping is generically defined as the movement of the blade about the *y-blade* ($\boldsymbol{j}_{bl}$) axis. Correspondingly, the flapping moment contribution of the blade element from equation (3.4.52) is referred to in explaining the blade flapping dynamics. On a typical helicopter that used an articulated type rotor blade, the blade flapping through the angle β is always resisted by the rotor hub stiffness denoted by K_β. This phenomena is expressed through the flapping moment vector in the following

$$\boldsymbol{M}^{bl}_{Flap} = \begin{bmatrix} 0 & K_\beta \beta & 0 \end{bmatrix}^T \tag{3.4.64}$$

Thus, the flapping equation of the helicopter rotor blade in (3.4.52) can be written as

$$-\int_0^R \left(f^{bl}_z - m_0 \, a^{bl}_z\right) r_b \, dr_b = K_\beta \beta \tag{3.4.65}$$

However, an autogyro usually used hingeless teetering rotor with two blades connected and free to rotate at the teetering bolt. The rotor hub stiffness effect is negligible due to the teetering effect, where flapping on one side of the blade causes the other side to also flaps in the opposite direction (see Figure 3.9). Consequently, the $K_\beta\beta$ is neglected and the equilibrium flapping moment can be obtained with the centre hinge of the hub is defined as the axis of rotation. Hence, equation (3.4.65) becomes

$$\int_0^R \left(f_z^{bl} - m_0\, a_z^{bl}\right) r_b\, dr_b = 0 \tag{3.4.66}$$

Solving equation (3.4.66) using *Mathematica*® revealed the flapping angle β, including the second order dynamics of the flapping, denoted as $\ddot{\beta}$. Note that the a_z^{bl} and f_z^{bl} were substituted from equations (3.4.33) and (3.4.47) respectively. The revealed flapping equation is a second order with a nonlinear dynamics and written as

$$\ddot{\beta} + \left[\Omega^2 + \frac{M_\beta}{I_\beta}\left(a_x^d \cos\psi - a_y^d \sin\psi\right)\right]\beta = \frac{1}{2}\frac{\rho\, c}{I_\beta}\int_0^R \left(a_0 U_p U_T + a_1 U_T^2\right) r_b\, dr_b + ... \\ \frac{M_\beta}{I_\beta} a_z^d + \left(\dot{Q}_d + 2\Omega P_d\right)\cos\psi + \left(\dot{P}_d + 2\Omega Q_d\right)\sin\psi \tag{3.4.67}$$

where M_β and I_β are the moment of mass and the moment of inertia of the blade, and given by

$$M_\beta = \int_0^R m_0\, r_b\, dr_b \ , \text{ and } \quad I_\beta = \int_0^R m_0\, r_b^2\, dr_b$$

Equation (3.4.67) is further evaluated where two assumptions have been made for the flapping angle β. First, the flapping rate is assumed to be constant with a small flapping angle, thus, the higher order of β can be neglected. Second, since there is no significant deformation of the blade during flapping (due to teetering), the harmonic terms of the flapping equation can also be neglected. Hence, the flapping angle β can best be called the 'teetering' angle. Equation (3.4.67) is normalised and re-evaluated to reveal the teetering angle β at equilibrium blade moment in autorotation that gives

$$\beta = 4n_\beta \left\{ a_0 \left[\frac{1}{3}(\mu_z - \lambda_0) + \frac{1}{6}(\alpha_{1s}\mu_x + \alpha_{1c}\mu_y)\right] + \frac{1}{4} a_1 \left[1 + \mu_x^2 + \mu_y^2\right]\right\} + \frac{M_\beta}{I_\beta}\eta_z \tag{3.4.68}$$

3.5 Modelling of Other Subsystems

The mathematical modelling of these subsystems are discussed in the following.

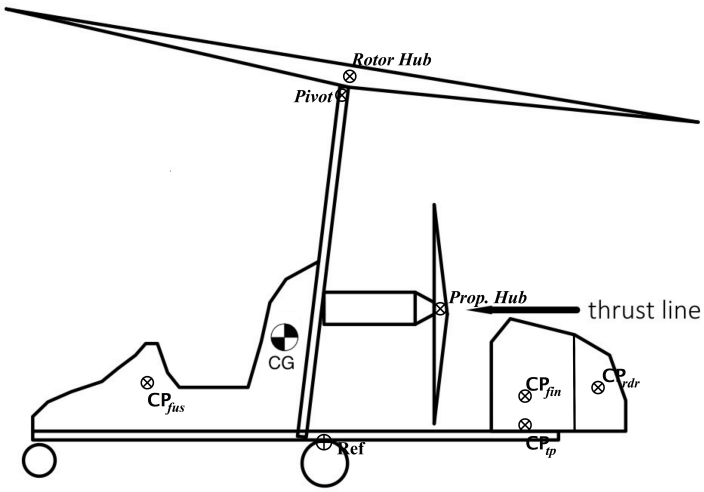

Figure 3.16: Autogyro subsystems CP location

The final step in the autogyro modelling is to obtain the external forces and moments contributed by other subsystems relative to the vehicle's CG (as shown in Figure 2.16). These mechanic values are then included in the equations of motion (3.3.5) so that the whole dynamics behaviour of the vehicle can be simulated. This evaluation can only be done with the inclusion of the aerodynamic lift and drag coefficients of those subsystems. In most practices, the polynomial representations of the lift and drag coefficients from the wind tunnel testing are used. These data are stored in the form of a look-up table with the function of the vehicle's angle of incidence.

For the G-UNIV autogyro, since the wind-tunnel data of the vehicle is not available, the approximation method is used. In this method, the aerodynamic loads of the subsystems are approximated based on the kinematic relationships between the surface areas and the angle of incidence. Other than this, recommendations from other related references are also used to obtain these data. All configuration data of the G-UNIV subsystems were taken from Ref. [7].

Fundamentally, the translational velocity of the autogyro's CG in the longitudinal body-fixed axes set had been defined earlier (refer to Section 3.4.1), where

$$\boldsymbol{v}_{\text{cg}}^{b} = \begin{bmatrix} U & 0 & W \end{bmatrix}^{T} \tag{3.5.1}$$

3.5.1 Fuselage Subsystem

To determine the force and moment contribution of the fuselage, the location vector of the fuselage Centre of Pressure (CP) relative to the CG must be known (see Figure 3.16). The location vector of the autogyro's CG with respect to its reference point had been defined previously in equation (3.4.5) of the rotor model, and re-written again as

$$\boldsymbol{r}_{\text{cg/ref}} = \begin{bmatrix} x_{cg} & 0 & z_{cg} \end{bmatrix}^{T} \tag{3.5.2}$$

while the vector location of the fuselage CP with respect to the reference point is defined as

$$\boldsymbol{r}_{\text{fus/ref}} = \begin{bmatrix} x_{fus} & 0 & z_{fus} \end{bmatrix}^{T} \tag{3.5.3}$$

Since the CP of the fuselage is located at the lower front of the vehicle's CG, the vector location of the fuselage's CP relative to the CG is determined as

$$\boldsymbol{r}_{\text{fus/cg}} = (\boldsymbol{r}_{\text{fus/ref}} - \boldsymbol{r}_{\text{cg/ref}}) = \begin{bmatrix} x_{fus/cg} & 0 & z_{fus/cg} \end{bmatrix} \tag{3.5.4}$$

The translational velocity of the fuselage in the longitudinal body axes is obtained with the function of the velocity from (3.5.1) and can be written as

$$\boldsymbol{v}_{\text{fus}}^{b} = \boldsymbol{v}_{cg}^{b} + (\omega_b \times \boldsymbol{r}_{\text{fus/cg}}) \tag{3.5.5}$$

Equation (3.5.5) is evaluated and written as

$$\boldsymbol{v}_{\text{fus}}^{b} = \begin{bmatrix} U_{fus} & 0 & W_{fus} \end{bmatrix}^{T} \tag{3.5.6}$$

Hence, the fuselage angle of incidence is then given by

$$\alpha_{\text{fus}} = \tan^{-1}\left(\frac{W_{fus}}{U_{fus}}\right) \tag{3.5.7}$$

and the magnitude of the fuselage longitudinal velocity component from (3.5.6) is given by

$$V_f = \sqrt{U_{fus}^2 + W_{fus}^2} \tag{3.5.8}$$

3.5.1.1 Fuselage Aerodynamic Forces and Moments

The fuselage aerodynamic forces and moments depend on its surface areas that come into contact with the air during flight. The axial and normal forces are the components of forces acting on the fuselage CP in the longitudinal body axes, written by

$$\boldsymbol{F}_{\text{fus}}^b = \begin{bmatrix} X_{fus}^b & 0 & Z_{fus}^b \end{bmatrix}^T \tag{3.5.9}$$

where the two forces are then determined according to the fuselage velocity from (3.5.8) as

$$X_{fus}^b = \frac{1}{2}\rho\, V_f^2\, S_{F_{fus}} C_{x_{fus}} \tag{3.5.10a}$$

$$Z_{fus}^b = \frac{1}{2}\rho\, V_f^2\, S_{P_{fus}} C_{z_{fus}} \tag{3.5.10b}$$

From equation (3.5.10), $S_{F_{fus}}$ and $S_{P_{fus}}$ are the frontal surface area and the plan surface area of the fuselage. Furthermore, the force coefficients are defined as

$$C_{x_{fus}} = -C_D \tag{3.5.11a}$$

$$C_{z_{fus}} = 2\,\alpha_{fus} \tag{3.5.11b}$$

C_D is the induced drag coefficient associated with the frontal area of the fuselage, which is assumed to have a constant value of -1 relative to the wind. $C_{z_{fus}}$ is the normal force coefficient associated with the fuselage incidence angle with a slope of $+2$. These approximations were implemented on the VPM-M16 acquired from Ref. [7] and can be recommended for other light autogyros.

Finally, the contribution of the fuselage moment in the longitudinal body axes orientation can be obtained. The moment is contributed by the amount of forces acting on the fuselage CP and its distance relative to the CG, as given by

$$\boldsymbol{M}^b_{\text{fus}} = \boldsymbol{r}_{\text{fus/cg}} \times \boldsymbol{F}^b_{\text{fus}} \tag{3.5.12}$$

which is then evaluated as

$$M^b_{fus} = X^b_{fus}(z_{fus} - z_{cg}) - Z^b_{fus}(x_{fus} - x_{cg}) \tag{3.5.13}$$

3.5.2 Tailplane Subsystem

The tailplane CP is located at $(x_{tp}, 0, z_{tp})$ relative to the reference point. Similar to the fuselage, the vector location of the tailplane with respect to the CG is determined as

$$\boldsymbol{r}_{\text{tp/cg}} = \begin{bmatrix} (x_{tp} - x_{cg}) & 0 & (z_{tp} - z_{cg}) \end{bmatrix}^T \tag{3.5.14}$$

The local velocity of tailplane in the body axes is given as

$$\boldsymbol{v}^b_{\text{tp}} = \boldsymbol{v}^b_{cg} + (\boldsymbol{\omega}_b \times \boldsymbol{r}_{\text{tp/cg}}) \tag{3.5.15}$$

which is then evaluated for the longitudinal mode and written by

$$\boldsymbol{v}^b_{\text{tp}} = \begin{bmatrix} U_{tp} & 0 & W_{tp} \end{bmatrix}^T \tag{3.5.16}$$

3.5.2.1 Tailplane Forces and Moments

The angle of incidence of the tailplane is determined by

$$\alpha_{tp} = \alpha_{0_{tp}} + \tan^{-1}\left(\frac{W_{tp}}{U_{tp}}\right) \tag{3.5.17}$$

where $\alpha_{0_{tp}}$ is the tailplane angle relative to the fuselage horizontal centreline, of which is zero for the G-UNIV autogyro. Since the tailplane of the G-UNIV is actually a

thin flat plate fixed to the fuselage, there will be only one force acting on the surface area of the tailplane, which is the z_{tp}-*force*. The z-force coefficient of the tailplane also corresponds to the lift coefficient of the tailplane and given as

$$C_{Z_{tp}} = -a_{0_{tp}}\,\alpha_{tp} \tag{3.5.18}$$

where, $a_{0_{tp}}$ is the lift-curve slope of the tailplane. The tailplane is designed to produce lift at positive angle of attack, which represented by the negative sign. From (3.5.18), the contributions of the tailplane to the external forces of the autogyro are therefore given as

$$\boldsymbol{F}^b_{\text{tp}} = \begin{bmatrix} X_{tp} \\ Y_{tp} \\ Z_{tp} \end{bmatrix} = \begin{bmatrix} 0 \\ 0 \\ \frac{1}{2}\rho\, V^2_{tp}\, S_{tp} C_{Z_{tp}} \end{bmatrix} \tag{3.5.19}$$

where S_{tp} is the surface area of the tailplane.

Therefore, the external moment contributions of the tailplane relative to the CG can be obtained by

$$\boldsymbol{M}^b_{\text{tp}} = \boldsymbol{r}_{\text{tp/cg}} \times \boldsymbol{F}^b_{\text{tp}} \tag{3.5.20}$$

which is evaluated and written as

$$M^b_{tp} = -Z_{tp}(x_{tp} - x_{cg}) \tag{3.5.21}$$

3.5.3 Propeller Thrust Subsystem

One of the most important parameters about the propeller thrust of an autogyro is the location and orientation of the thrust line relative to the autogyro's CG. The vector location of the G-UNIV propeller hub relative to the CG is obtained in a similar way of other subsystems and given by

$$\boldsymbol{r}_{\text{prop/cg}} = \begin{bmatrix} (x_{prop} - x_{cg}) & 0 & (z_{prop} - z_{cg}) \end{bmatrix}^T \tag{3.5.22}$$

Due to the lack of engine data, the throttle-thrust subsystem is modelled with an assumption of a simple linear relationship between the thrust produced according to the airspeed. As one of the control inputs, the thrust is iteratively estimated according to the forward airspeed of the vehicle. Hence, the longitudinal propeller force contribution relative to the CG can be calculated by

$$\boldsymbol{F}^{b}_{\text{prop}} = \begin{bmatrix} X_{prop} \\ Y_{prop} \\ Z_{prop} \end{bmatrix} = \begin{bmatrix} T_{prop}\cos(\alpha_{prop}) \\ 0 \\ T_{prop}\sin(\alpha_{prop}) \end{bmatrix} \tag{3.5.23}$$

where, T_{prop} is the amount of propeller thrust in Newton, and α_{prop} is the orientation angle of the propeller thrust line relative to the autogyro's horizontal centreline (in degrees). Finally, the longitudinal moment contributions of the propeller thrust relative to the CG can be obtained by

$$\boldsymbol{M}^{b}_{\text{prop}} = \boldsymbol{r}_{\text{prop/cg}} \times \boldsymbol{F}^{b}_{\text{prop}} \tag{3.5.24}$$

that yields

$$M^{b}_{prop} = X_{prop}(z_{prop} - z_{cg}) - Z_{prop}(x_{prop} - x_{cg}) \tag{3.5.25}$$

3.6 Discussion on Model Validation

In any mathematical modelling of an existing dynamic system, validation is important to prove the reliability and accuracy of the model according to the real system. For the G-UNIV research autogyro, having the real flight data is an advantage that a straight comparison can be made for the ARDiS model. The flight data of the G-UNIV had been produced in earlier flight dynamic studies, which involved a number of flight tests [7, 16, 19, 89]. As such, the configuration parameters of the vehicle had changed a lot according to the objective of the research. Hence, to ensure the consistency of the validation, the configuration parameters and the flight data of the autogyro must also be consistent. Therefore, for the G-UNIV autogyro in this research, the final version of the flight data and configuration parameters reported in Ref [7] were used for the simulation. Some of the basic configuration data of the G-UNIV are presented in Table 3.6.1.

Table 3.6.1: Montgomerie-Parsons GUNIV Autogyro Basic Configurations [7]

Parameter	Value
Gross Mass (m)	355 kg
Moments of Inertia:	
I_{xx}	72.96 $kg\,m^2$
I_{yy}	297.21 $kg\,m^2$
I_{zz}	224.25 $kg\,m^2$
I_{xz}	0 $kg\,m^2$
Rotor Parameters:	
Radius (R)	3.81 m
Chord (c)	0.197 m
Rotor Mass (m_r)	17.255 kg
Lift Curve Slope (a_0)	5.75/rad

The initial step to evaluate a newly developed autogyro model is to obtain the trim condition of the autogyro. Having the trim condition of a nonlinear aircraft model is essential to evaluate the dynamic behaviour and to assess the stability and performance of the aircraft. For the longitudinal mode of an autogyro, the trim condition is obtained by assuming that the autogyro flies in steady flight state, with all forces and moments, including the rotorspeed, are in equilibrium. The trim calculation of the ARDiS model is described in Appendix B, and the comparison between the ARDiS trim results and the flight data of the G-UNIV in the longitudinal flight mode are shown in Figure 3.17. Additionally, for a better confidence in the simulation results, the numerical modelling results of RASCAL are also included in the comparison, so that the differences between the two simulation packages can be evaluated. The simulation results of the RASCAL were acquired from same CAA report [7].

In general, the results show a good agreement between the model and the flight data for most parameters across the speed range. These correlations are seen to be sound regarding the trend. The simulation involved two longitudinal flight attitudes and one control parameter of the G-UNIV according to different airspeed settings. The two flight attitudes are the fuselage pitch angle (Θ) and the rotorspeed (Ω), and the control parameter is the longitudinal shaft tilt (θ_s) which also represents the rotor-disc pitch angle of the vehicle. Additionally, the rotor dynamic parameter, the teetering angle (β) is also calculated for the trim condition and plotted in the same plot. From the simulation results, the pitch attitude and longitudinal shaft tilt decrease with the forward velocities. This behaviour is recognised as the combination of a few factors; the fuselage aerodynamics, the propeller thrust and the rotor-disc angle of attack.

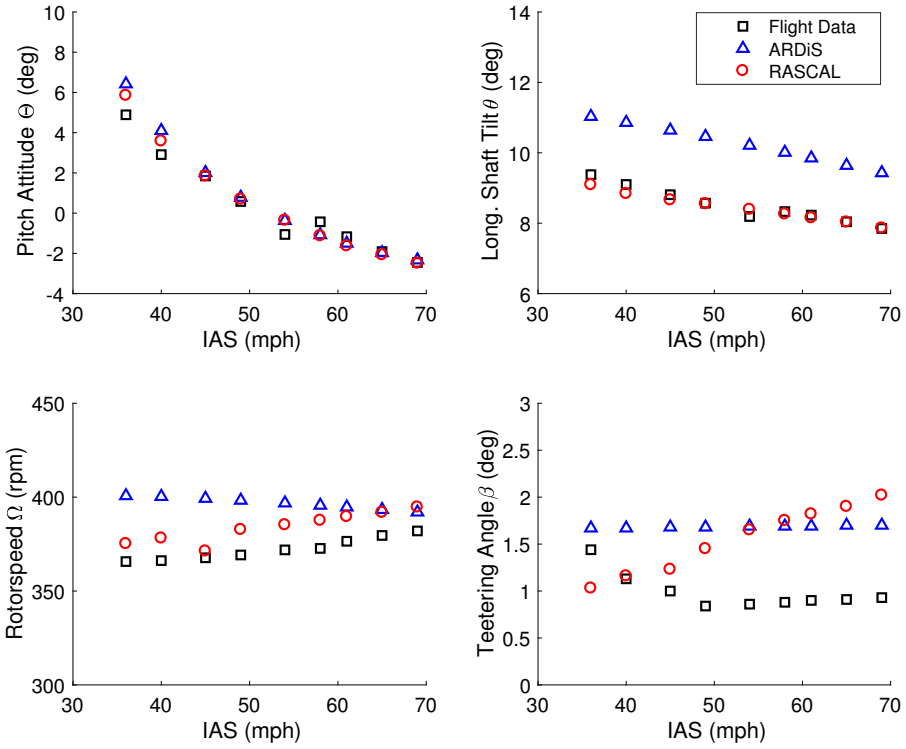

Figure 3.17: Trim comparison against the G-UNIV flight data

At the lower flight regime, the pitch attitude is more influenced by the rotor-disc angle of attack, where the fuselage aerodynamics are less influential in this region. The rotor disc angle-of-attack is high (i.e. tilted aft) causing a large nose-up moment. It is also important to note that the propeller thrust line is located about 3.8 cm (1.5 inches) above the autogyro CG and causing a nose down pitching moment. This relationship was previously shown in Figure 2.1. In this operating region, the propeller thrust is high, which also contributes to a higher rotor disc angle-of-attack to maintain the vehicle in level flight. Since the drag coefficient of the rotor blade is taken as an average value regardless of the blade angle-of-attack, the pitch attitude is then predicted with a small deviation from the flight data. At higher airspeed regime, the aerodynamics of the autogyro is more influenced by the fuselage, which results in a smaller rotor disc angle-of-attack, thus smaller lift and drag forces produced by the rotor disc. Hence, a smaller pitch attitude is predicted by the trim simulation in this flight region.

The pitch moment contributed by the rotor-disc thrust line relative to the CG also plays a significant role in autogyros longitudinal flight dynamics. In steady-state flight as a default condition, the rotor-disc thrust line of the G-UNIV is located at a normal distance in front of the CG, as shown in Figure 2.1. The two thrust parameters (the rotor-disc thrust and the propeller thrust) compensate and balance each other in

equilibrium flight across the speed range. These two pitching moments is unique for autogyros and played a significant role in the vehicle's longitudinal flying qualities, and a number of studies about these two parameters were done and published [19,35,39,90]. Initial discussions about these relationships were previously done in Chapter 2.

It is also worth to mention that, the good correlation in pitch attitude between ARDiS against RASCAL and the flight data is actually expected, even though the rotorspeed and longitudinal control were deviated. This good correlation shows that the higher frequency rotor dynamics are giving less effect on the external force and moment of the rigid-body dynamics which is much slower. This rotor-body relationship has been discussed earlier in Section 3.2 of this chapter.

The rotorspeed trim plot of the ARDiS model in Figure 3.17 shows a discrepancy with the flight data, with an approximately 10% deviation at the lower airspeed, but improves at the higher airspeed. This is expected with the multiblade approach where the rotor loads are calculated as the average contribution of the blade elements throughout the rotor disc. The deviation also resembles the uncertainty in the rotor load estimation, as the detail lift and drag coefficients at different angle of attack and Mach numbers are not modelled. Hence, a more uniform pattern of almost constant rotorspeed for the ARDiS model is observed across the speed range in Figure 3.17. On the other hand, the RASCAL results are seen to have smaller deviation with the flight data, consistently across the speed regime. This type of correlation are also expected for the RASCAL as a higher fidelity model, where the aerodynamic details of the rotor blade are captured in the model.

It is also worth to mention that the good correlation between the ARDiS and the flight data of the G-UNIV were contributed through the modifications of the rotor model. These modifications have been detailed in the earlier section (see Section 3.4.2.1).

The lift coefficient was denoted in the HGS rotor model (default) as

$$C_l = a_0 \, \alpha_{bl}$$

which indicates that there is no lift at zero angle-of-attack ($C_{L_0} = 0$). Since the rotor blade of the G-UNIV is known for using the NACA 8-H-12, the lift coefficient yields

$$C_l = a_0 \, \alpha_{bl} + a_1$$

where a_1 is the lift coefficient at zero angle-of-attack, which is not zero due to the shape of the aerofoil. Hence, a comparison has been made to verify the difference in

the trim simulation results between the two configurations, as shown in Figure 3.18. The results also verified the practicality of the newly modified rotor model implemented in the ARDiS compared to the default HGS based rotor model.

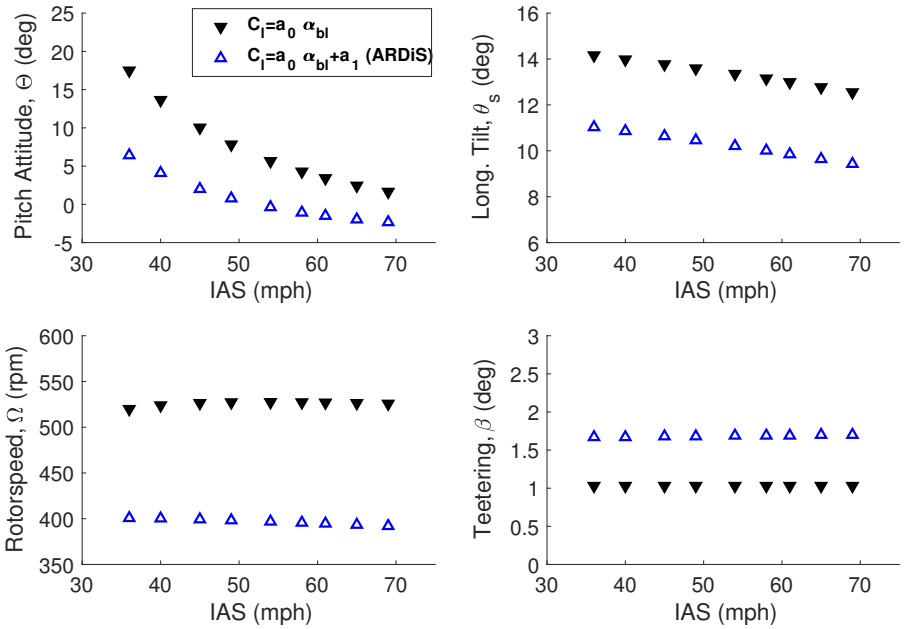

Figure 3.18: Trim comparison against the default (HGS) rotor model

As the value of a_1 of the ARDiS rotor blade is not zero, the amount of lift created by this type of aerofoil is greater, which results in a higher induced drag for every blade rotation. The drag also contributes to a slower rotorspeed for the same amount of lift compared to the default rotor model as shown in the Figure 3.18. This rotorspeed difference between the two rotor models is seen to be consistent across the whole speed range of the vehicle. The higher rotorspeed prediction in the default model also exhibits an insufficient amount of lift produced by the rotor that requires higher speed of rotation. This condition also contributes to more rotor disc aft tilt, a higher pitch attitude, but lower teetering angle presented by the default simulation model.

For the control parameter in Figure 3.17, the longitudinal shaft tilt of the ARDiS model is observed with an average 20% deviation from the flight data across the speed regime. One possible reason is due to the uncertainty in the calculated moment that associated with errors in the lever arm measurement of the vehicle since the deviation was seen consistently across the speed range. One important parameter that reflects the control margin of an aircraft is the longitudinal CG position as reported in the CAA report [7]. A 20% overprediction in the simulation result manifest a small error, where the longitudinal CG was positioned in certain centimetres in front of the actual CG position of the real G-UNIV. This error in measurement is possible to happen, as

the G-UNIV autogyro has gone through some flight tests, which involved many changes of onboard sensors and measurement equipment with different objectives. Hence, the longitudinal CG position keep on changes along with those modifications and contribute to a small deviation in the measurement during the weighing processes. The effects of longitudinal CG shifting are clearly shown in Figure 3.19, in which the longitudinal changes of the CG are demonstrated with the 3 inches forward and aft changes of the X_{cg}. The 6-inch variation in the longitudinal CG position caused an average deviation of 1.25° in pitch attitude and 1.3° in the longitudinal tilt. The rotorspeed and teetering angle, however, are not significantly affected by the longitudinal CG variation.

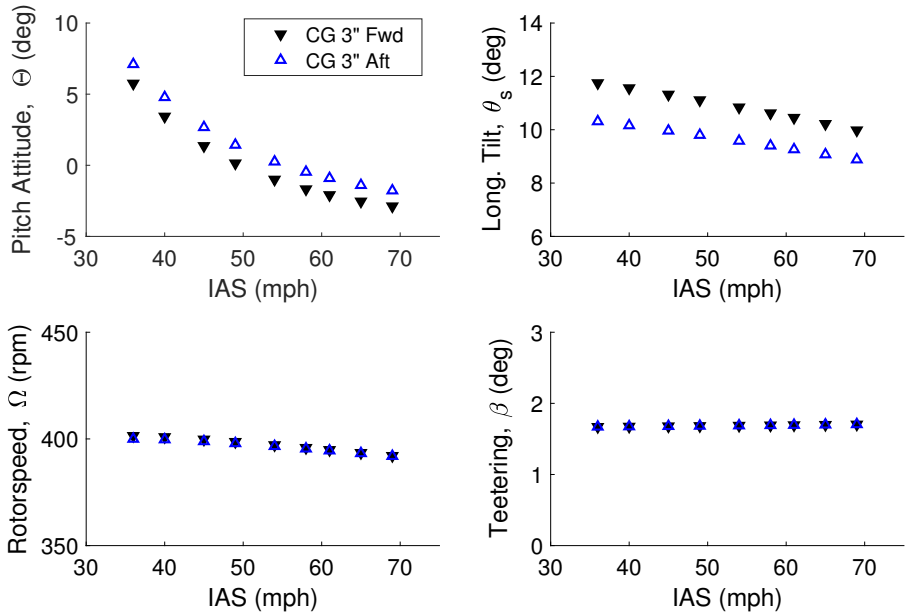

Figure 3.19: Longitudinal CG variations of ARDiS in trim condition

3.7 Dynamic Response to Control Inputs

The verification of the nonlinear ARDiS model can be done by looking at the autogyro's dynamic response to control inputs. For the longitudinal mode of the ARDiS model, the steady-state point in a specific flight condition was chosen and used as the initial conditions for the simulation. In this particular example, the trim airspeed of 55 mph was chosen for a simple reason that this flight speed is located in between the lower and the higher speed region of the G-UNIV. The nonlinear simulation is done for both longitudinal control inputs, the shaft tilt (θ_s) and the propeller thrust (T_{prop}). In order to correctly verify the effect of control input to the dynamic behaviour of the vehicle,

only one control input is used, while the other one must be held constant. However, there are no standard requirements specified regarding the type and magnitude of control inputs to be applied to the simulation model. As such, the control input must be appropriate to achieve the purpose of the verification exercise, that is to look at how the model responded to at least a small perturbation from a steady state condition. The nonlinear simulation results of the ARDiS for the respective flight state are shown in Figure 3.20 and 3.21. Four longitudinal flight state responses were recorded; the forward velocity (IAS), the pitch-rate (q), the pitch attitude angle (Θ), and the rotorspeed (Ω).

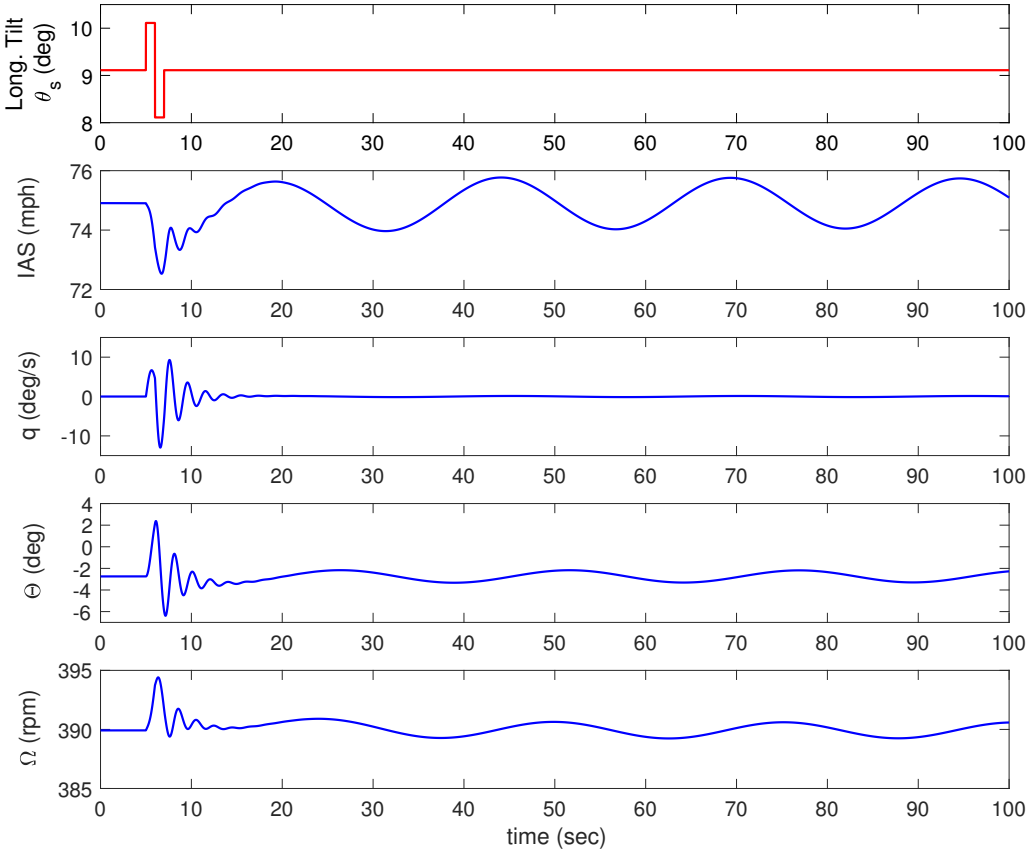

Figure 3.20: Nonlinear response to shaft tilt from the trim condition at 75 mph

Simulation of the dynamic response to the longitudinal hub tilt of the ARDiS was done by applying a doublet input signal with a $\pm 1^\circ$ tilt for 2 seconds into the model in steady-state condition, as shown in Figure 3.20. This input signal represents an aft pull of the control stick for 1 second and followed by an abrupt forward push for another 1 second, before being fixed back in the neutral position for the rest of the simulation. The response can be seen as a fast oscillation as soon as the control is being applied, and then followed by a slower oscillation for the rest of the time history. The

overall response of the model revealed a short-term oscillation for a period (T_{sp}) of 2 seconds and followed by a phugoid mode with a period (T_{ph}) of 24 seconds. Generally, the simulation of the model shows a sensible result, where pulling the control stick backwards causes the autogyro to nose up and also the vice versa when the control stick is pushed forward.

Since the propeller thrust is held constant, the nose up condition and the aft tilt of the control actually increases the induced drag of the vehicle that mainly contributed by the aft tilt of the rotor disc, thus significantly reduces the forward airspeed. In this control condition, more induced airflow produced by the rotor disc, thus increases the rotorspeed and creates more lift to compensate the lost of lift associated with the aft tilting of the rotor hub at constant propeller thrust. It is presumed that a prolong aft tilt of the control without changing the propeller thrust will destabilise and deviate the vehicle from the trim condition.

Abruptly pushing forward the control stick causes the opposite response and followed with the short term mode, then the phugoid oscillation. Overall results also revealed the phugoid mode is dynamically close to a marginal stability in this flight region, as the amplitude of the phugoid response is very lightly damped throughout the rest of the simulation. The simulation results also show that the short period and the phugoid oscillations in overall are directly triggered by the longitudinal hub tilt.

On the other hand, to verify the dynamic response to the propeller thrust input, the longitudinal hub tilt control must be held constant at its trim position. Figure 3.21 shows the dynamic response of the model to an impulse input signal for 2 seconds. This also represents a +10% abrupt push of the engine throttle level from the trim setting, before being pulled back to the trim position for the rest of the simulation. Since the propeller thrust line of the G-UNIV is located a few inches above the CG, the abrupt increase of thrust causes a negative pitch moment to the aircraft, thus contribute to a little nose-down pitch attitude as soon as the additional thrust is applied.

The slight increase in the forward airspeed was also seen to be the direct effect of the increased throttle. The short-term response is hardly noticed from this effect, but the phugoid oscillation was apparent and indicates another lightly damped oscillation with the same period of 24 seconds. This clearly indicates a strong coupling between the autogyro's forward speed and the phugoid oscillation. However, the overall response to this type of input was seen to be small and less significant to the dynamic stability of the vehicle, except that the phugoid mode was seen directly affected by the changes of airspeed.

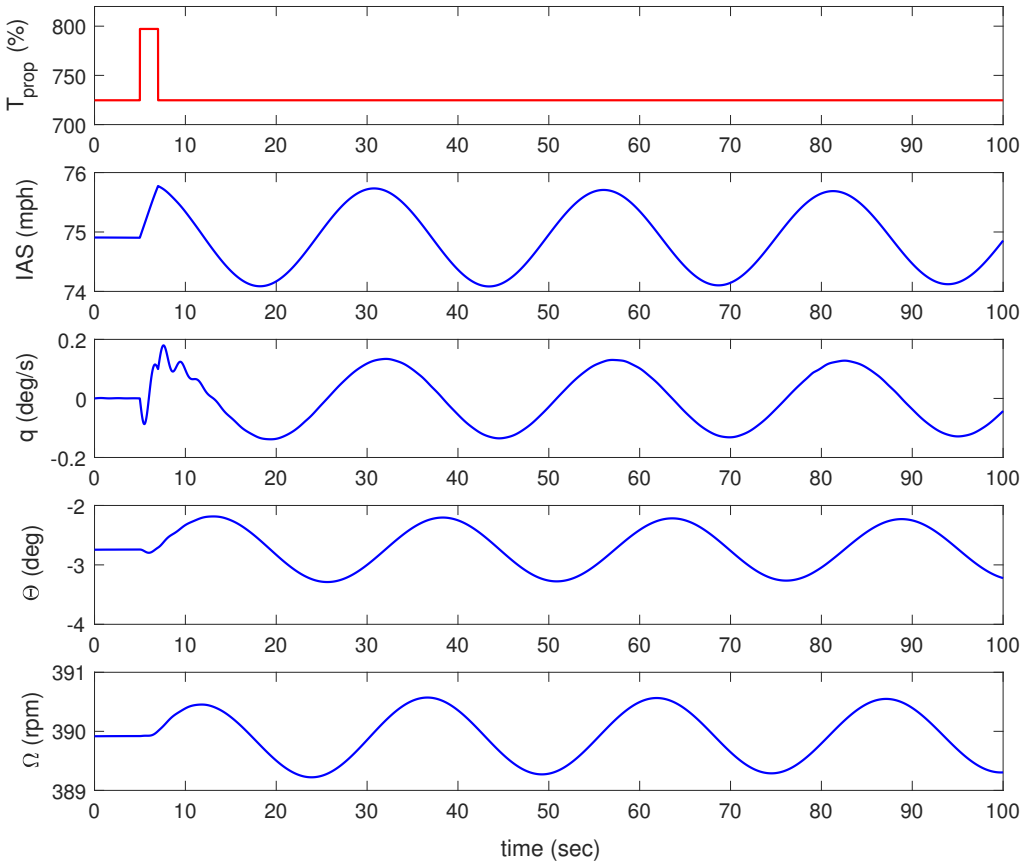

Figure 3.21: Nonlinear response to thrust input from trim condition at 75 mph

Therefore, several concluding remarks can be made for the nonlinear dynamic response of the G-UNIV. The time response of the rigid body for each control input was seen to be slower, which indicates a sluggish manoeuvre. The response time, however, can explicitly be quantified through linearisation of the G-UNIV longitudinal model. Furthermore, the response of the rotorspeed in both figures clearly indicate the strong coupling between the rotorspeed degree of freedom and the pitch attitude. The strong coupling also resembles the strong relationship between the rotorspeed degree of freedom and the attitude of the rigid body of the vehicle. Finally, it was found that the dynamic stability of the G-UNIV autogyro is more affected by the longitudinal hub tilt, compared to the control input of the propeller thrust.

3.8 Evaluation of ARDiS Basic Model

It is important to evaluate the flying qualities of the basic G-UNIV model against the proposed criteria in Chapter 2. The existing nonlinear ARDiS model is first linearised so that the dynamic stability characteristics can be quantified and later evaluated.

The nonlinear longitudinal model of ARDiS from Section 3.3 can be linearised using the 'small disturbance theory' [97, 98]. This was done by restraining the equations of motion of the autogyro to small disturbance around its steady-state condition (trim). Those nonlinear equations of motion can be written in a generic form of state vector $\mathbf{x}$, and control vector $\mathbf{u}$, which written as

$$\dot{\mathbf{x}} = \mathbf{F}(\mathbf{x}, \mathbf{u}) \tag{3.8.1}$$

The equations are solved for small perturbation from the trim condition in translational states and controls. The nonlinear equation (3.8.1) was then reduced to a state and control vector in a linear form and written as

$$\dot{\mathbf{x}}(\mathrm{t}) = \mathbf{A}\,\mathbf{x}(\mathrm{t}) + \mathbf{B}\,\mathbf{u}(\mathrm{t}) \tag{3.8.2}$$

where $\mathbf{A}$ is the system matrix, which consist of the state derivatives, and $\mathbf{B}$ is the control matrix, which consist of the control derivatives.

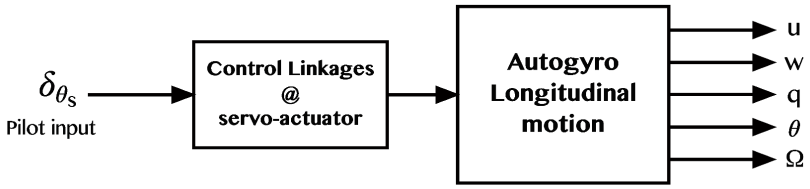

Figure 3.22: G-UNIV open loop model schematic

Linearising the nonlinear model will enable the dynamic characteristics of the vehicle to be studied and manipulated quantitatively in developing the flight controller. In the case of an autogyro, the general form of its longitudinal full order state-space equation (without engine control) in (3.8.2) is written as

$$\begin{bmatrix} \dot{u} \\ \dot{w} \\ \dot{q} \\ \dot{\theta} \\ \dot{\Omega} \end{bmatrix} = \begin{bmatrix} X_u & X_w & X_q & X_\Theta & X_\Omega \\ Z_u & Z_w & (Z_q + U_e) & Z_\Theta & Z_\Omega \\ M_u^* & M_w^* & M_q^* & M_\Theta^* & M_\Omega^* \\ 0 & 0 & 1 & 0 & 0 \\ Q_u & Q_w & Q_q & Q_\Theta & Q_\Omega \end{bmatrix} \begin{bmatrix} u \\ w \\ q \\ \theta \\ \Omega \end{bmatrix} + \begin{bmatrix} X_{\delta_{\theta_s}} \\ Z_{\delta_{\theta_s}} \\ M_{\delta_{\theta_s}}^* \\ 0 \\ Q_{\delta_{\theta_s}} \end{bmatrix} \left[\delta_{\theta_s}\right] \tag{3.8.3}$$

The general schematic of the G-UNIV basic model for the longitudinal motion is shown in Figure 3.22. Note that the dynamics of the mechanical control linkages for the bare airframe can be neglected in the evaluation of the G-UNIV basic model.

An example of the state-space equation for the G-UNIV autogyro at the trim airspeed of 75 mph according to equation (3.8.3) is written as

$$\begin{bmatrix} \dot{u} \\ \dot{w} \\ \dot{q} \\ \dot{\theta} \\ \dot{\Omega} \end{bmatrix} = \begin{bmatrix} -0.0943 & -0.1797 & 1.7800 & -9.8010 & -0.0583 \\ -0.2374 & -1.0230 & 33.3300 & 0.5042 & -0.3163 \\ -0.0077 & -0.3227 & 0.0565 & -0.0005 & -0.0049 \\ 0 & 0 & 1 & 0 & 0 \\ 0.0605 & 0.3034 & -0.1388 & -0.0003 & -0.0352 \end{bmatrix} \begin{bmatrix} u \\ w \\ q \\ \theta \\ \Omega \end{bmatrix} + \begin{bmatrix} -15.97 \\ -33.99 \\ 13.39 \\ 0 \\ 10.26 \end{bmatrix} \left[\delta_{\theta_s}\right] \tag{3.8.4}$$

Equation (3.8.4) is then solved for its characteristic equation where the open loop system transfer functions are calculated and written as

$$\begin{aligned} \frac{u(s)}{\delta_{\theta_s}(s)} &= \frac{-15.97(s+0.6111)(s+0.1454)(s^2-1.592s+22.35)}{(s+0.1084)(s^2+0.0127s+0.0676)(s^2+0.975s+10.71)} \\ \frac{w(s)}{\delta_{\theta_s}(s)} &= \frac{-33.99(s-13.22)(s+0.1105)(s^2+0.0331s+0.0800)}{(s+0.1084)(s^2+0.0127s+0.0676)(s^2+0.975s+10.71)} \\ \frac{q(s)}{\delta_{\theta_s}(s)} &= \frac{13.39s(s+1.818)(s+0.1308)(s+0.0278)}{(s+0.1084)(s^2+0.0127s+0.0676)(s^2+0.975s+10.71)} \\ \frac{\Theta(s)}{\delta_{\theta_s}(s)} &= \frac{13.39(s+1.818)(s+0.1308)(s+0.0278)}{(s+0.1084)(s^2+0.0127s+0.0676)(s^2+0.975s+10.71)} \\ \frac{\Omega(s)}{\delta_{\theta_s}(s)} &= \frac{10.26(s^2+0.0130s+0.0109)(s^2-0.2326s+23.76)}{(s+0.1084)(s^2+0.0127s+0.0676)(s^2+0.975s+10.71)} \end{aligned} \tag{3.8.5}$$

The open loop transfer functions provide the response in each longitudinal flight state

for the longitudinal shaft tilt δ_{θ_s} of the autogyro. The eigenvalues and eigenvectors are calculated and written as

$$\begin{aligned} \lambda_{1,2} &= -0.4874 \pm 3.236\, i \\ \lambda_{3,4} &= -0.0063 \pm 0.260\, i \\ \lambda_5 &= -0.1084 \end{aligned} \tag{3.8.6}$$

The $\lambda_{1,2}$ in equation (3.8.6) clearly show the eigenvalues that correspond to the short period mode, while the $\lambda_{3,4}$ are the phugoid mode eigenvalues of the open loop G-UNIV at 75 mph.

Table 3.8.1: G-UNIV full order dynamic modes at 75 mph

Dynamic mode	**Damping**	ω **(rad/s)**	**Period (sec)**	$t_{\frac{1}{2}}$ **(sec)**
Short-period	$\zeta_{sp} = 0.1490$	$\omega_{sp} = 3.27$	1.94	1.42
Phugoid	$\zeta_{ph} = 0.0244$	$\omega_{ph} = 0.26$	24.2	109.31
Rotorspeed, Ω	1.0	n/a	n/a	n/a

Moreover, the eigenvalue λ_5 in (3.8.6) represents a subsidence in rotorspeed that consists of a negative real number, which resembles an aperiodic oscillation.

The damping ratio and the natural frequency of each mode are given in Table 3.8.1. Note that the $t_{\frac{1}{2}}$ in the table is the time-to-halve amplitude for the oscillations. The table also indicates a lightly damped short period mode and a marginally stable phugoid oscillation, of which are correlated with the dynamic stability characteristics of a typical helicopter as reported in the previous chapters. The low pitch damping might cause instability that will lead the vehicle to PIO in short period oscillation, following a steep manoeuvre or strong disturbance.

Figure 3.23 shows the comparison between the nonlinear and the linearised model of the vehicle's open loop response to a small longitudinal control input (δ_{θ_s}). The comparison also indicates that the linearisation to be working quite well, with a small lagging in the velocity and rotorspeed of the nonlinear plot. It is quite evident that the lightly damped short period oscillation lasts for about 10 seconds from the time where the perturbation was taken place. A huge perturbation might also lead the vehicle to instability if the necessary action is not promptly taken. Therefore, having a closed loop control is desirable in this situation.

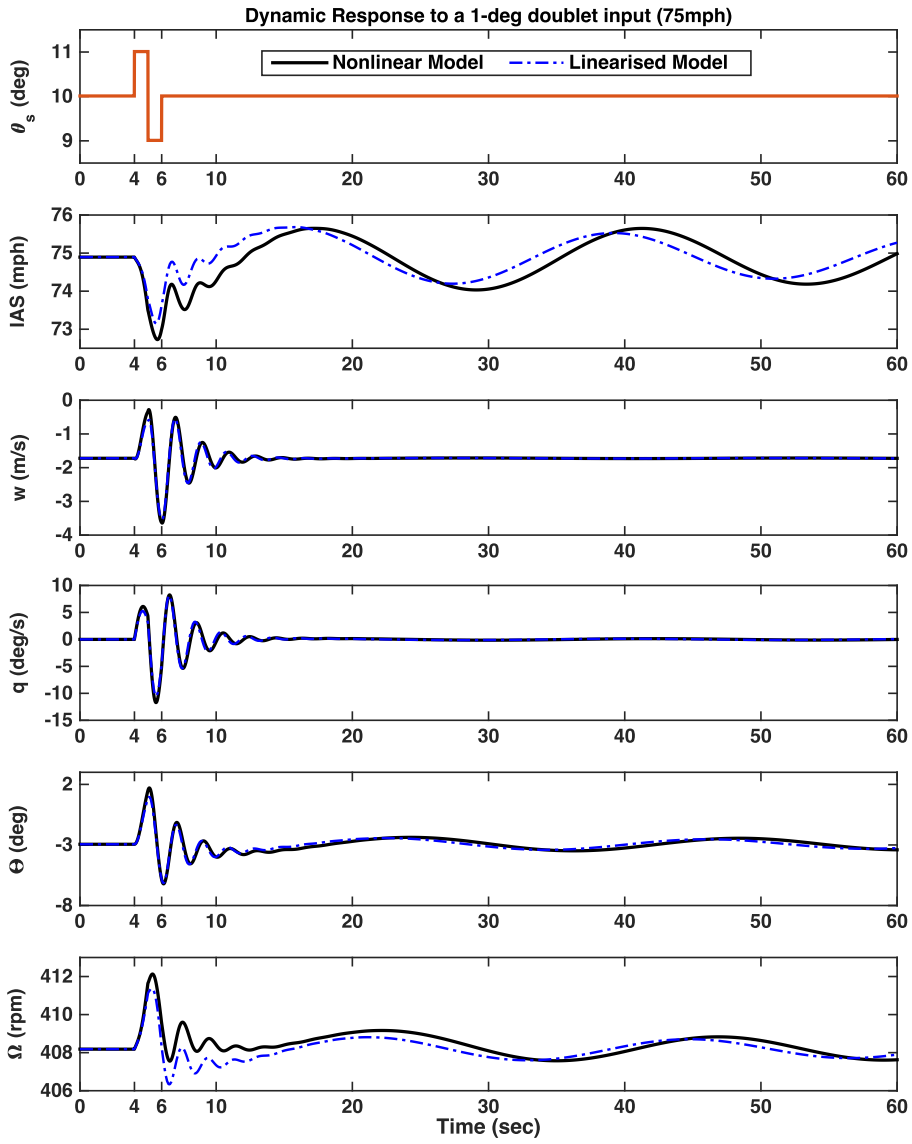

Figure 3.23: G-UNIV Nonlinear Vs Linearised Model

Figure 3.24 shows the open loop eigenvalues of the G-UNIV in the s-plane for five different flight conditions across the speed range. The eigenvalues of the phugoid mode indicate undamped oscillations in lower flight speed regime but increase in damping at higher flight speeds. Note that this type of phugoid characteristic is similar to typical helicopters. Conversely, for the short period mode, the damping increases with flight speed. The subsidence in rotorspeed is more consistent with a stable aperiodic oscillation throughout the speed regime.

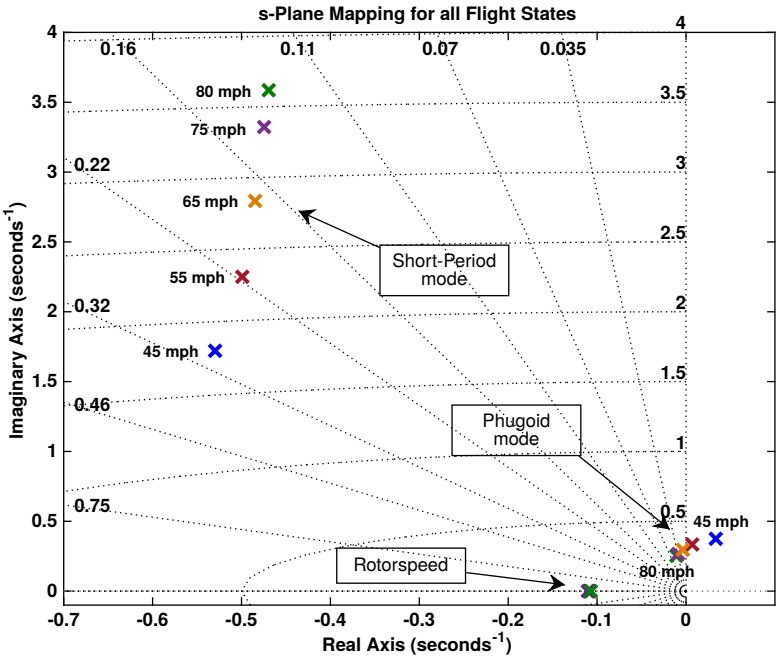

Figure 3.24: G-UNIV open loop eigenvalues variation with flight speed

3.8.1 The Reduced Order Model

To further evaluate the short-period mode, the lower order model of the autogyro is used, so that the phase lag associated with the higher order model will not be interfering. The effect of higher order dynamics is more significant on aircraft that is equipped with sophisticated control and augmentation systems. Hence, the short-period mode is separated from the full order model for further evaluations and analysis. In fact, the short-period mode is more crucial to be considered first in the evaluation of longitudinal flying qualities of autogyros. According to Cook [33], the short-period and phugoid mode can be decoupled by suppressing the phugoid mode and producing a reduced order equation that is equivalent to the short-period mode. For an autogyro, the reduced order short-period approximation is obtained by assuming that there is no changes in the forward velocity (U_e) during the short-period oscillation, thus neglecting the X-force component. The term $(Z_q + U_e)$ in equation (3.8.3) then became Z_q. In the same instance, it is assumed that there is no changes in the pitch attitude (Θ_e) of the vehicle during the short-period oscillation. For instance, the reduced order short-period approximation of the G-UNIV at the flight speed of 75 mph from equation (3.8.4) is obtained and written as

$$\begin{bmatrix} \dot{w} \\ \dot{q} \end{bmatrix} = \begin{bmatrix} -1.0230 & 33.33 \\ -0.3227 & 0.0565 \end{bmatrix} \begin{bmatrix} w \\ q \end{bmatrix} + \begin{bmatrix} -33.99 \\ 13.39 \end{bmatrix} \begin{bmatrix} \delta_{\theta_s} \end{bmatrix} \tag{3.8.7}$$

In this model, the subsidence in rotorspeed (Ω) of the autogyro is suppressed or omitted, as it is closely coupled with the rigid-body attitude, particularly the pitch attitude (Θ). Hence, it is assumed that there is no change in rotorspeed in short-term oscillation of the vehicle ($\dot{\Omega} = 0$). Hence, taking the same 75 mph flight state of the G-UNIV as an example, the transfer functions of the short-period dynamics for the G-UNIV basic configuration is obtained as

$$\frac{w(s)}{\delta_{\theta_s}(s)} = \frac{-33.99(s - 12.74)}{(s^2 + 0.9416s + 11.25)} \tag{3.8.8a}$$

$$\frac{q(s)}{\delta_{\theta_s}(s)} = \frac{12.85(s + 1.91)}{(s^2 + 0.9416s + 11.25)} \tag{3.8.8b}$$

which reveals the short period eigenvalues $\lambda_{sp} = -0.483 \pm 3.23i$. This also implies the stability characteristics for the reduced mode approximation with a damping ratio of $\zeta_{sp} = 0.148$ and undamped natural frequency of $\omega_{sp} = 3.27$ rad/s.

Table 3.8.2: G-UNIV short-period mode comparison

Speed (IAS)	**Short-period Mode**	
	Full Order	Reduced Order
45 mph	$\zeta = 0.290$ $\omega_n = 1.80\,\text{rad/s}$ $T = 3.65\,\text{sec}$	$\zeta = 0.270$ $\omega_n = 1.80\,\text{rad/s}$ $T = 3.61\,\text{sec}$
55 mph	$\zeta = 0.242$ $\omega_n = 2.31\,\text{rad/s}$ $T = 2.10\,\text{sec}$	$\zeta = 0.232$ $\omega_n = 2.31\,\text{rad/s}$ $T = 2.12\,\text{sec}$
65 mph	$\zeta = 0.185$ $\omega_n = 2.83\,\text{rad/s}$ $T = 2.63\,\text{sec}$	$\zeta = 0.184$ $\omega_n = 2.48\,\text{rad/s}$ $T = 2.64\,\text{sec}$
75 mph	$\zeta = 0.149$ $\omega_n = 3.27\,\text{rad/s}$ $T = 1.94\,\text{sec}$	$\zeta = 0.148$ $\omega_n = 3.27\,\text{rad/s}$ $T = 1.95\,\text{sec}$
80 mph	$\zeta = 0.130$ $\omega_n = 3.62\,\text{rad/s}$ $T = 1.75\,\text{sec}$	$\zeta = 0.120$ $\omega_n = 3.61\,\text{rad/s}$ $T = 1.76\,\text{sec}$

For verification of the reduced order approximation, it is clear that the stability characteristics of the reduced order are closely correlated with the full order of Table 3.8.1. In fact, a complete comparison with the full-order dynamics is also made for the whole flight regimes as shown in Table 3.8.2. Since the reduced order short period mode closely approximates the full order model, the control enhancement of short period mode can be done through this without being interfered by the higher order dynamics of the full order model. It is also noticed that the simplified model (reduced order) does not affect the rotorspeed, as it is coupled with the phugoid. This condition is verified in the full order time history simulation in Figure 3.23 where the pitch attitude of the vehicle directly influences the changes in rotorspeed.

3.8.2 The Short-Period Mode Evaluation

The longitudinal flying qualities evaluations of the G-UNIV autogyro are made according to the proposed requirements in Chapter 2 (see Table 2.5.1). For the short-period mode, the dynamic response of the vehicle is quantified and evaluated according to the commonly used criteria, the time-domain and frequency-domain criteria. Evaluations include all flight conditions for the whole speed regime, particularly the low-speed and high-speed, as defined in the proposal. Since the objective of the research is to enhance the stability and controllability of the autogyro through automatic control method, it is more realistic to include the dynamic of the vehicle's control actuation linkages in the model, as shown in Figure 3.22. In this part, an assumption has been made for the basic configuration, where the actuation dynamics are assumed to contribute to a time lag of 0.05 seconds behind the applied input, as suggested in Ref [98–100]. The reduced model of the G-UNIV from the state-space equation (3.8.7) is used to quantify the flying qualities performance in the short-period mode of the G-UNIV.

In general, the recommended evaluations of autogyro longitudinal flying qualities are made according to the typical longitudinal stability characteristics, the short-period mode and the phugoid mode, plus the additional rotorspeed criterion. Since the short-period mode requirements were mainly adopted from the ADS-33E-PRF, the assessments were also made according to the same structure. As such, the evaluated flight conditions were divided into two different flight regimes, the *Low-Speed* regime and the *High-Speed* regime (see Figure 2.13). Two steady-state flight speeds were chosen to be evaluated in the Low-Speed regime, 40 mph and 50 mph. Another three flight speeds were chosen for the High-Speed regime, 55 mph, 65 mph and 75 mph. These evaluations are presented in the following.

3.8.2.1 Pitch attitude changes to small-amplitude input

The pitch attitude effect due to a small-amplitude input in the proposed criteria is quantified and evaluated in the frequency domain environment through the Bode-plot representation according to Figure 2.9. Bode plot represents the spectrum of frequency response created from the dynamic equations of a system. This frequency response representation enables the behaviour of the system to be analysed and quantified in the form of gain magnitude (in decibels) and phase delays (in degrees) along the frequency spectrum of the system.

With the reference from Cook [33], the transfer function of the pitch attitude response from the longitudinal shaft tilt in short-period mode can be written in a generic form as

$$H(s) = \frac{\Theta(s)}{\delta_{\theta_s}(s)} = \frac{k_\theta(s + (1/T_\theta))}{s(s^2 + 2\zeta_{sp}\omega_{sp}s + \omega_{sp}^2)} \tag{3.8.9}$$

where k_θ is the pitch attitude gain, T_θ is the numerator zero of the pitch attitude. The steady-state frequency response can then be transformed from the transfer function by setting $s = j\omega$, where the $H(j\omega) = \text{real} + j(\text{imaginary})$. The magnitude is then written as $\mid H(j\omega) \mid = \sqrt{(\text{re})^2 + (im)^2}$, and the phase is the angle between the two values, given by $atan2(\text{im}, \text{re})$. In a bode plot, the magnitude or gain is given in decibels (dB), where magnitude (dB)$= 20 \log_{10} \mid H(j\omega) \mid$.

The transfer function of the G-UNIV in equation (3.8.9) has one integrator pole, two complex poles and one zero, which reflects to the bode plot in Figure 3.25. The bode plot shows the open loop gain and phase response across the frequency spectrum for the G-UNIV in the short period mode. Note that, the Matlab control toolbox function *bode* was used to plot the bode plot from the open loop transfer function in equation (3.8.9).

From the plot (Figure 3.25), the -20 dB/decade slope at the lower frequency region reflects to the integrator pole $1/s$ of the transfer function, which also causes a constant phase delay of -90 deg. The effect of the zero can be seen at higher frequency region as it produces a +20 dB/decade slope which compensates the previous -20 dB/decade, which also results in a small phase leading from -90 deg. However, the two complex pole with a -20 dB/decade each causing an approximate -40 dB/decade with another -90 deg phase delay. The -40 dB/decade can be seen manifests by the 45-deg slope in the figure. The same trend can be seen on the bode plot across the speed region as shown in Figure 3.26, where the short-period damping ratio changes across the speed range.

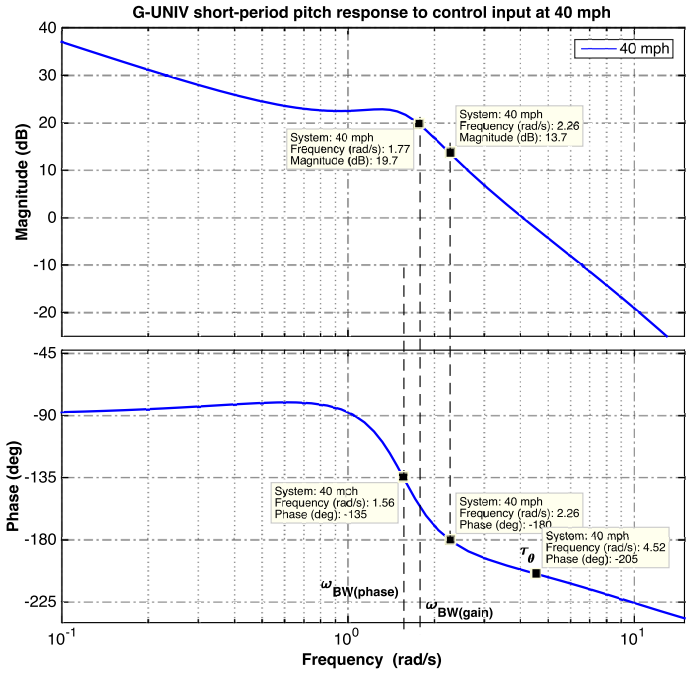

Figure 3.25: Bandwidth plot of the G-UNIV basic airframe at 40 mph

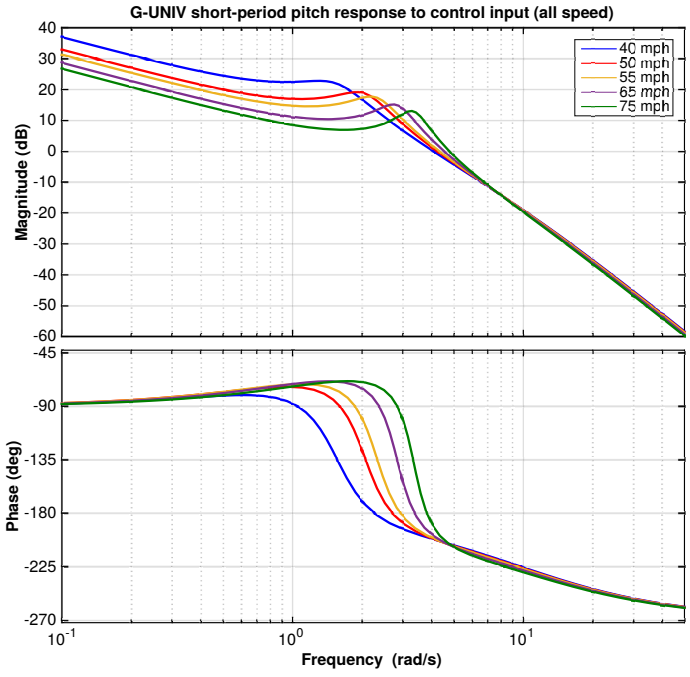

Figure 3.26: Bandwidth plot of the G-UNIV basic airframe - all speeds

Table 3.8.3 shows the gain bandwidth, phase bandwidth, and the phase delay which associated with the time-lag for the G-UNIV basic model according to the proposed flight speeds. The phase delay representation in this short-period oscillation is a direct contribution of the additional dynamic complexity within the G-UNIV basic model, particularly the control linkages. In this case, the phase delay τ_θ is calculated in terms of time-lag with the value of 0.0965 sec (96.5 msec).

Table 3.8.3: Bandwidth assessment of short-period mode of G-UNIV (basic model)

Flight Speed	Phase Bandwidth, $\omega_{BW(phase)}$ (rad/s)	Gain Bandwidth, $\omega_{BW(gain)}$ (rad/s)	Phase Delay, τ_θ (msec)
40 mph	1.560	1.770	96.5
50 mph	2.070	2.170	97.0
55 mph	2.330	2.360	95.0
65 mph	2.840	0.464	98.1
75 mph	3.330	0.419	98.2

Note that, the ADS-33E-PRF [30] criteria is adopted for the bandwidth (BW) and phase delay (τ_θ) requirements in the proposed autogyro criteria. Details of this criteria have been discussed in Section 2.5.1 of Chapter 2 (see also Table 2.5.1).

The bandwidth values in Table 3.8.3 indicate two different trends of bandwidth relationships. For the low-speed flight conditions (40 mph and 50 mph), the phase bandwidths $\omega_{BW(phase)}$ are less than the gain bandwidths $\omega_{BW(gain)}$, but with very small frequency margin between the two bandwidths.

These bandwidth conditions, although complying with the recommended bandwidth requirement, the small frequency margin also implicates a near PIO condition as the $\omega_{BW(phase)}$ is marginally close with the $\omega_{BW(gain)}$. This problem will probably become a reality if the controller is designed for an attitude-hold control system, as mentioned in the requirement. However, if the controller is designed for a rate-response augmentation system, the issue would be different, as the bandwidth ω_{BW} requirement for rate-response is defined as whichever the less between the $\omega_{BW(phase)}$ and the $\omega_{BW(gain)}$.

For the high-speed regime, the $\omega_{BW(phase)}$ shows an increase with the increasing airspeed, which is opposite to the $\omega_{BW(gain)}$ where the frequency reduces (see Table 3.8.3). In Figure 3.26, as the flight speed increases, the phase bandwidth curves are seen moving to the right with a steeper phase lag.

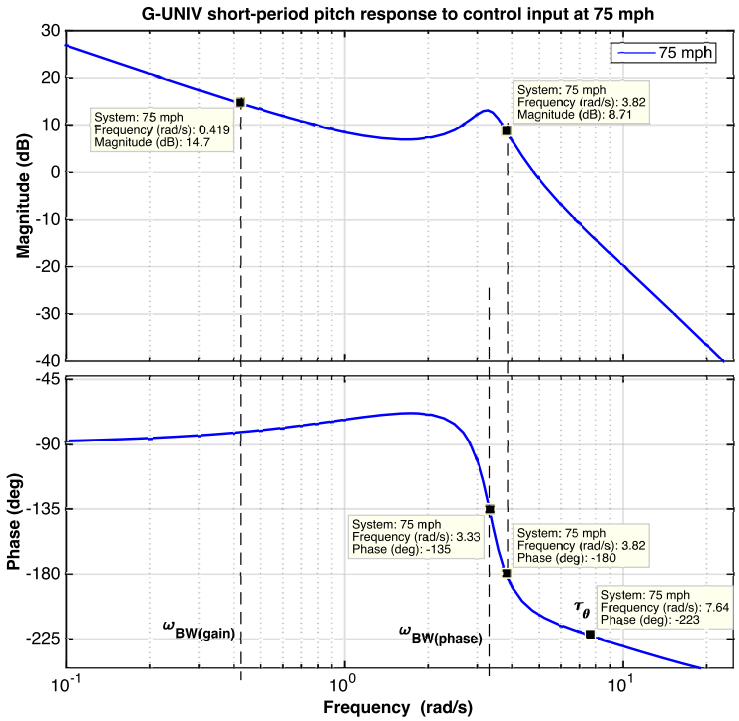

Figure 3.27: Bandwidth plot of the G-UNIV basic airframe at 75 mph

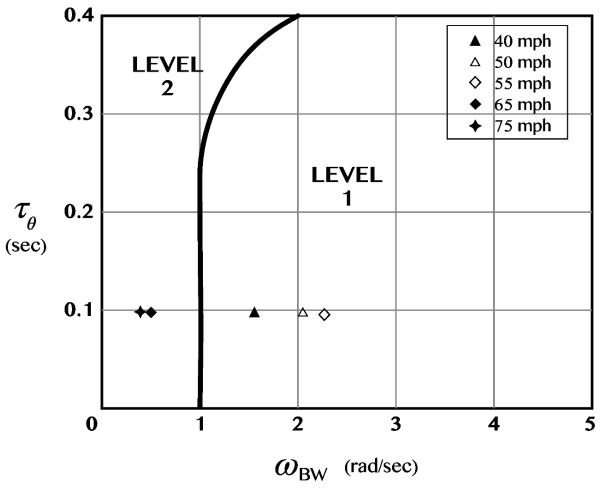

Figure 3.28: Short-term response to small-amplitude input limits - all speed

In the same instance, the gain bandwidth curves are seen to reduce, but having sharper or steeper peak with the increase in flight speed. At flight conditions where the gain curves are having the higher peak (at higher speed regime), the 6 dB gain margin are also seen to deflect the gain bandwidth further to the left and settled at much more lower frequencies, compared to the phase bandwidth. Hence, at these flight

conditions, the vehicle is said to be flying in a PIO prone conditions for an attitude-hold augmentation system. Figure 3.27 shows an example of bandwidth relationships for the G-UNIV flying at 75 mph where the $\omega_{BW(gain)}$ is lesser than the $\omega_{BW(phase)}$. The bandwidth (ω_{BW}) and phase delay (τ_θ) for the whole flight speed of the G-UNIV basic model are then mapped into the proposed limits in Figure 3.28, which revealed a Level 2 flying qualities at higher speed regime (65 mph and 75 mph).

3.8.2.2 Pitch attitude changes to moderate-amplitude input

This requirement is also referred to the so-called 'Attitude Quickness' as proposed in Chapter 2. To comply with this time-domain requirement, a step input that excites a minimum 5° pitch response is applied, of which is considered as a moderate amplitude change. The pitch attitude quickness in the requirement is defined as the ratio of the maximum pitch rate q_{pk} to the change of pitch angle $\Delta\theta_{pk}$ due to the input excitation, and written as

$$\text{Pitch-Quickness} = Q_{\theta_{pk}} = \frac{q_{pk}}{\Delta\theta_{pk}} \tag{3.8.10}$$

Table 3.8.4: Pitch-Quickness evaluation of G-UNIV basic configuration

	q_{pk} (deg/s)	$\Delta\theta_{pk}$ (deg)	$\Delta\theta_{min}$ (deg)	$q_{pk}/\Delta\theta_{pk}$ (s^{-1})
40 mph	14.2	12.4	5.10	1.15
50 mph	13.5	9.1	2.24	1.48

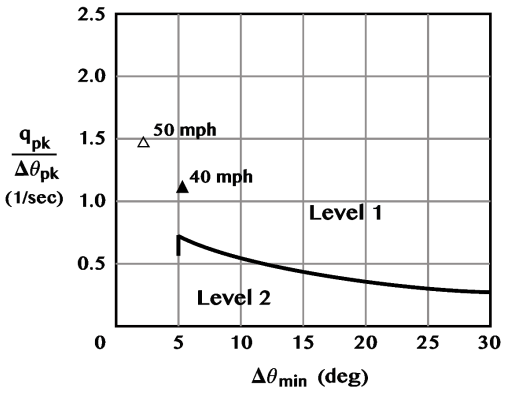

Figure 3.29: Pitch-Quickness limits for the G-UNIV basic airframe

This requirement is only applicable for the low-speed flying region, as it requires the vehicle to excite high pitch rates within a short time. The vehicle must be able to achieve a high ratio of pitch quickness according to the recommended flying qualities

levels. The ratio of pitch quickness for the basic configuration of G-UNIV autogyro are quantified and shown in Table 3.8.4, and also mapped according to the level of flying qualities as shown in Figure 3.29. The result shows that the pitch-quickness of the G-UNIV basic configuration falls well within the Level 1 flying qualities for the quickness ratio. However, the pitch attitude behaviour is too agile and less damping that the pitch attitude changes ($\Delta\theta_{min}$) for the G-UNIV fell below the 5-deg limit.

3.8.3 The Phugoid Mode Evaluation

The phugoid evaluation of the G-UNIV basic configuration is carried out through simulation of the full order state-space equation (3.8.3), according to the previously defined flight categories, the low-speed and the high-speed. There is one requirement that is used in the proposed flying qualities to evaluate the phugoid mode, which is the mid-term response for small-amplitude change as mentioned in Table 2.5.1.

Table 3.8.5: Phugoid mode evaluation of G-UNIV basic configuration

Flight Speed	Damping, ζ_{ph}	Period, T_{ph}	* $T_{1/2}$ @ $T_{2_{ph}}$
40 mph	-0.155	16.0 sec	$T_{2_{ph}} = 11.2$ sec
50 mph	-0.048	17.7 sec	$T_{2_{ph}} = 40.8$ sec
55 mph	-0.021	18.9 sec	$T_{2_{ph}} = 100.7$ sec
65 mph	0.012	21.2 sec	$T_{1/2} = 196.3$ sec
75 mph	0.034	23.5 sec	$T_{1/2} = 77.5$ sec

* $T_{1/2}$ is time to halve amplitude, $T_{2_{ph}}$ is time to double amplitude of phugoid mode

3.8.3.1 Mid-term response for small-amplitude pitch changes

The mid-term response is considered as phugoid oscillation for the new flying qualities recommendation where the damping ratio at frequencies below the bandwidth frequency ω_{BW} is the main concern in this requirement. Figure 3.30 shows the stability roots of the phugoid mode for the G-UNIV basic configuration in all flight conditions, which revealed the damping ratio of less than 0.04 in all flight conditions. It was also found that the phugoid mode is unstable in the lower flight regime (40 mph to 55 mph), but marginally stable and lightly damped in high-speed flight conditions. These evaluations are summarised in Table 3.8.5 for the whole flight conditions. Additionally, the unstable phugoid mode at 40 mph also revealed a below Level 3 acceptance, as the

period of oscillation and the time-to-double amplitude are both less than 20 seconds. This condition is obviously unacceptable and could lead to catastrophe. Consequently, the stability improves gradually with the increased in airspeed. At higher airspeeds (55 mph to 75 mph), these phugoid oscillations are marginally stable with Level 2 flying qualities. Hence, an augmentation system for the phugoid mode is then a necessity for the G-UNIV autogyro, so that the Level 1 flying qualities can be achieved.

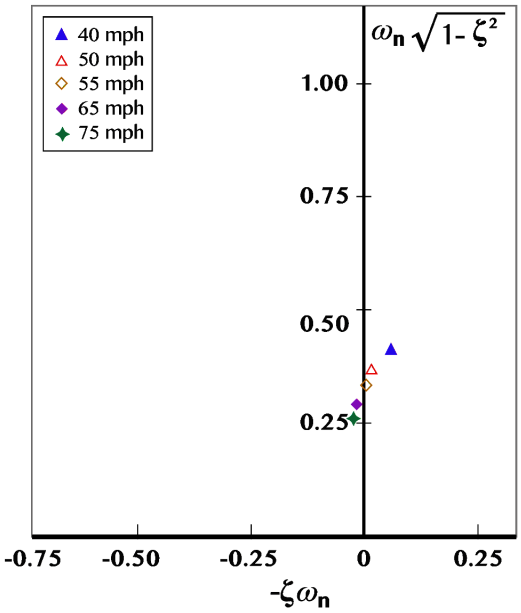

Figure 3.30: Mid-term response to small-amplitude input - all speeds

3.8.4 The Rotorspeed Evaluation

Figure 3.31 shows the g-force dynamic condition which approximates the load factor exerted from a steep impulse input manoeuvre at 75 mph. The g-force approximation shows a positive 'g' condition as the autogyro gained a pitch with less than 10% changes in rotorspeed at the positive control input. The manoeuvre is then followed with an abrupt forward push of the control input that causes a steep nose-down pitch attitude, which also contributes to a negative g-force. This condition can be seen to cause a rotorspeed decay which also implies the reduction of positive airflow through the rotor disc during the steep negative pitch manoeuvre. It can be seen that nothing much can be done to actively control the rotorspeed as it has its own degree of freedom in dynamic flight. Since the rotorspeed is coupled with the rigid body attitude of the autogyro, proper control enhancement on the pitch attitude will directly improve the rotorspeed degree of freedom respectively.

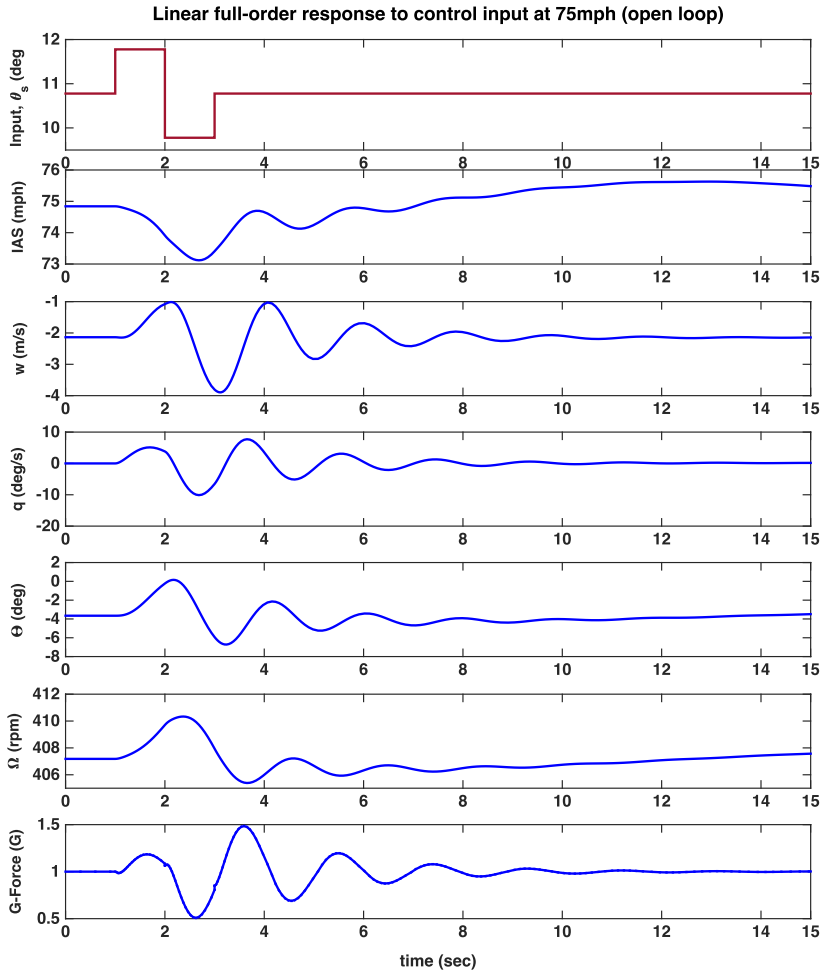

Figure 3.31: G-UNIV linear full-order open loop simulation

3.9 Chapter Summary

The main purpose of this chapter is to explain the development of an autogyro's mathematical model that later will be used to improve its flying qualities. The chapter started with highlighting the two existing modelling approaches implemented in rotorcraft simulations, the higher fidelity individual-blade approach and the conventional rotor-disc or multiblade approach. The Autogyro Rotor-Disc Simulation model (ARDiS) was then developed from the conventional multiblade Helicopter Generic Simulation model (HGS), due to the different flying characteristics the autogyro has, compared to helicopters. The modifications, mainly on the rotor model were successfully made with several aspects of achievements.

(i) The kinematics of the rotor model were modified to suit for more complex axes transformations, which successfully includes the important shaft offset of the

rotor hub that directly connected to the control mechanism. In fact, the model is considered as generic and can suit for most light autogyros, as long as the basic configurations of the particular autogyro are known.

(ii) The new lift curve characteristics based on the NACA 8-H-12 aerofoil that was commonly used for light autogyros were successfully embedded into the rotor blade's force and moment calculations. The combination between the new lift coefficient and the average profile drag of the rotor blade also contributed to acceptable correlations in the simulation against the flight data. Although the simplification in this rotor-disc approach also contributed to the less accuracy in other trim parameters such as the rotorspeed, the overall results are still acceptable to be used on autogyros. Since autogyros are operated in lower speed region, the accuracy of prediction has become less critical, compared to helicopters.

(iii) The modification of the flapping dynamics is considered as the most significant achievement for the autogyro model. The 'teetering' effects of the flapping dynamics was successfully included in the rotor model with the assumption that the rotor blade is hingeless and stiff, and contributed to the teetering effect in autorotating flight.

(iv) The modification of the rotor disc inflow model that represents the autorotating disc of an autogyro was also implemented, based on the unique attributes an autogyro flight has, compared to a helicopter. The calculation of the induced velocity of airflow through the rotor disc was modified in such a way that the rotor blade rotates in the wind-mill state in forward flight.

(v) The modification also successfully included other autogyro subsystems that contributed to the external forces and moments of the rigid body equations of motion, which also contains the rotorspeed degree of freedom for autorotating flight.

(vi) Lastly, the validation and verification of the ARDiS model were successfully made for the steady-state flight and nonlinear simulations.

Moreover, the chapter had also discussed the limitation of the study, where the longitudinal mode of the flight dynamics of the autogyro was focused. This limitation was due to the reason that the critical dynamic stability and controllability issues of autogyros were mostly associated with the longitudinal mode. The unique and important attributes highlighted in the discussion was the rotor-disc and propeller thrust relationship relative to the CG, including the strong coupling between rotorspeed and the pitch attitude. All these were supported through the trim results validations of the model against the G-UNIV flight data. Nonetheless, the nonlinear ARDiS model was also verified through the dynamic response of the model to the control inputs.

Finally, the flying qualities performance evaluations of the basic linear model of G-UNIV autogyro were done according to the new flying qualities requirements developed in Chapter 2. It was found that the G-UNIV basic model (known as the open loop model) indicated a non-compliance with the proposed flying qualities requirements. The flying qualities performance of the open loop model can be summarised in the following;

a) The short-period mode revealed a non-compliance according to the proposed time-domain and the frequency-domain evaluation. According to the performance evaluation, the open loop model exhibits a stable, but yet, a lightly damped short-period oscillation across the flight speeds. On the other hand, the frequency bandwidth of the open loop model exhibits a non-compliance, in which the analytical interaction between the phase-bandwidth and the gain-bandwidth indicated a PIO-prone condition, especially at higher airspeeds.

b) The phugoid mode of the open loop G-UNIV model revealed the worse condition. According to the performance evaluation, the open loop phugoid mode yields unstable oscillations, especially at lower flight regime, and a marginally stable at higher flight regime. In general, the open loop phugoid mode exhibits a Level 3 flying qualities.

Due to these poor longitudinal flying qualities performance, necessary steps to implement the control enhancement for the vehicle must be done accordingly. The control enhancement will be implemented in the following chapter.

Chapter 4

Autogyro Control Enhancement

4.1 Introduction

In Chapter 2, flying qualities requirements for light autogyros have been proposed with the BCAR Section T airworthiness requirements being used as the basis for the requirements [21]. The rationale is that the stability guidelines in the BCAR Section T were based on years of studies on the flight dynamics of the vehicle [7]. Since BCAR Section T only prescribes simple requirements for light autogyros dynamics stability, a certain amount of adjustments were made to form a better flying qualities requirements. As such, other requirements from fixed wing aircraft and helicopters were highlighted with some elements were included in the proposal. The requirements are structured according to the characteristics of the typical longitudinal stability modes, the short-period mode and the phugoid mode. An additional dynamic requirement, which is the rotorspeed was also included in the proposal. The proposed evaluation criteria were based on the two commonly used quantitative approaches, the time-based and the frequency-based approach.

The flying qualities of the G-UNIV basic airframe model were evaluated in Chapter 3, and it shows a non-compliance with the proposed requirements. With this condition, control design strategies are carried out as the main aim of this chapter, to improve the flying qualities of the vehicle according to the requirements. As such, the proposed flying qualities criteria are used as the design requirements for the control system. In this particular process, it is essential to ensure that the designed controller will not complicate the control hardware implementation, and the simple configurations the

vehicle has as a 'light autogyro' will not be violated [21, Part 1, Sub-Section A].

4.2 The Stability Augmentation System

It was previously understood that the short period and phugoid oscillations of the G-UNIV autogyro are lightly damped, with unstable phugoid in some flight conditions. The *Stability Augmentation System* (SAS) for the G-UNIV is then a necessity to improve its longitudinal flying qualities. The development of the SAS for the G-UNIV is done in two stages. First, the SAS is introduced to the autogyro model as a 'pitch damper' with negative feedback through a pitch-rate gyro within the feedback loop. The pitch damper provides proper damping for the short-period oscillation beyond pilot control, as it is installed within the inner-loop of the feedback system. Secondly, the 'phugoid damper' is also introduced which provides the required damping for the phugoid oscillation. For the phugoid augmentation, the speed sensor is used as the outer loop of the feedback system as it measures the forward velocity of the vehicle and provides the feedback gain for the phugoid damper controller. However, the strategy to implement the phugoid damper is subject to how complicated the controller hardware would be, thus affecting the physical complexity of the whole vehicle. In this matter, one important requirement is the complexity of the controller has to be kept as simple as possible to maintain the status of the vehicle as a 'light autogyro'. As such, the new hardware introduced in the control system should not jeopardise the simplicity of the autogyro. Therefore, maintaining the simplicity of the Automatic Flight Control System (AFCS), and improving the dynamic stability of the vehicle with the same simplistic autogyro configuration is an advantage. In this situation, the propeller or the engine thrust parameter is continued to be held fixed at trim values in each flight condition, and the controller is used to manipulate the longitudinal shaft tilt control (δ_{θ_s}) for the pitch augmentation.

4.2.1 The Pitch Damper

From the previous G-UNIV open loop short-period evaluations, there were some issues with the bandwidth margins that affecting the short-period stability of the vehicle (see Table 3.8.3 in Section 3.8.2). At lower flight speeds, the $\omega_{BW(phase)}$ is less than the $\omega_{BW(gain)}$, but the frequency difference between the two are comparatively closed. Conversely, at higher flight speeds, the $\omega_{BW(gain)}$ are smaller which caused a PIO-prone conditions. Assuming that the controller is targeted to be an attitude-hold system, the

margin of difference between the two bandwidths must be significant enough to prevent the possibility of getting into PIO. In this case, the larger the difference between the two bandwidth, the more room available for the closed-loop augmentation to be implemented to meet the flying qualities requirements. The more controller hardware implemented, the more will be the dynamic complexity of the vehicle, thus, contributes to the phase delay of the pitch response. Hence, the pitch damper must be designed with a proper feedback gain to provide a better margin bandwidth and better damping. In the research, two approaches have been implemented for the pitch damper of the G-UNIV, the pitch-rate feedback loop, and the blended feedback loop.

4.2.1.1 Pitch-rate Feedback Loop

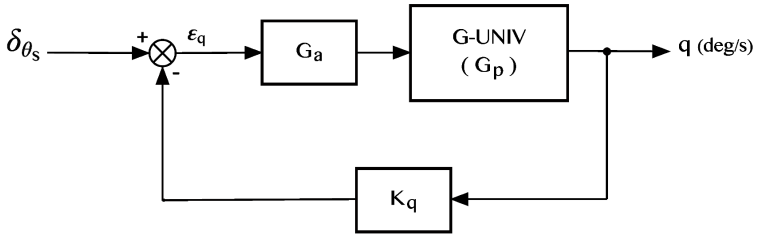

Figure 4.1: Reduced order schematic with pitch-rate feedback

The general form of classical design of aircraft control systems is a loop closure to provide inner feedback around the basic reduced-order aircraft model for damping improvement. Figure 4.1 shows the pitch-rate feedback system with the pitch-rate feedback gain (K_q), and G_a as the linear actuator dynamics. A simple control law for the closed loop system yields

$$\epsilon_q = \delta_{\theta_s} - q \tag{4.2.1}$$

Considering a Linear and Time Invariant (LTI) system where the general feedback equation is written by

$$\frac{q}{\delta_{\theta_s}} = \frac{G_a(s)\, G_p(s)}{1 + K_q\, G_a(s)\, G_p(s)} \tag{4.2.2}$$

Taking an example at the airspeed of 40 mph, the open loop transfer functions of the G-UNIV short-period mode yield

$$\frac{w(s)}{\delta_{\theta_s}(s)} = \frac{-149.8(s - 18.37)}{(s + 10)(s^2 + 0.957s + 2.414)} \tag{4.2.3a}$$

$$\frac{q(s)}{\delta_{\theta_s}(s)} = \frac{153.8(s + 1.106)}{(s + 10)(s^2 + 0.957s + 2.414)} \tag{4.2.3b}$$

$$\frac{\theta(s)}{\delta_{\theta_s}(s)} = \frac{153.8(s + 1.106)}{s(s + 10)(s^2 + 0.957s + 2.414)} \tag{4.2.3c}$$

The characteristic equation from (4.2.3) then yields the unaugmented short-period stability characteristics, with the damping ratio, natural frequency and poles given as

$$\zeta_{sp} = 0.308 \ , \quad \omega_{n_{sp}} = 1.55\,\text{rad/s} \quad \text{and} \quad s = -0.479 \pm 1.478\,i$$

The time-domain requirement for the short period-mode of an autogyro was not specified in the proposed flying qualities, as the bandwidth requirement is more crucial for this type of vehicle. As such, the time-domain criteria for the fixed wing aircraft can be used as general guidelines to choose the pitch damper feedback gain. Level 1 short-period mode criteria from the fixed-wing aircraft is used, where the short-period damping margins are specified from 0.35 to 1.35 [27, 28]. However, the damping ratio should be carefully chosen so that the control mechanism will not be physically overstressed with the amount of force applied by the servo actuator to achieve a particular amount of damping. An overdamped control system could also cause a rigid and less agile manoeuvre. The closed loop feedback gain was chosen through the *Root-locus* technique, as one of the fundamental techniques in classical control theory [101, 102]. This technique was proven to be successful and still widely being used for simple SISO systems until today [103–106].

For the 40 mph flight condition, the closed-loop feedback gain $K_q = 0.0156$ was chosen through the root-locus technique that gives the damping of $\zeta_{sp} = 0.36$, which is slightly above the minimum. This value, however, does not significantly improve the bandwidth of the augmented SAS compared to the open loop system. A 'try and error' technique is then implemented to find the most suitable damping for the SAS, which significantly makes a difference in the bandwidth and phase delay. Consequently, the pitch-rate gain is increased to $K_q = 0.132$ which reveals the damping, natural frequency and poles of the closed-loop system as

$$\zeta_{sp} = 0.7 \ , \quad \omega_{n_{sp}} = 2.50\,\text{rad/s} \quad \text{and} \quad s = -1.74 \pm 1.79\,i$$

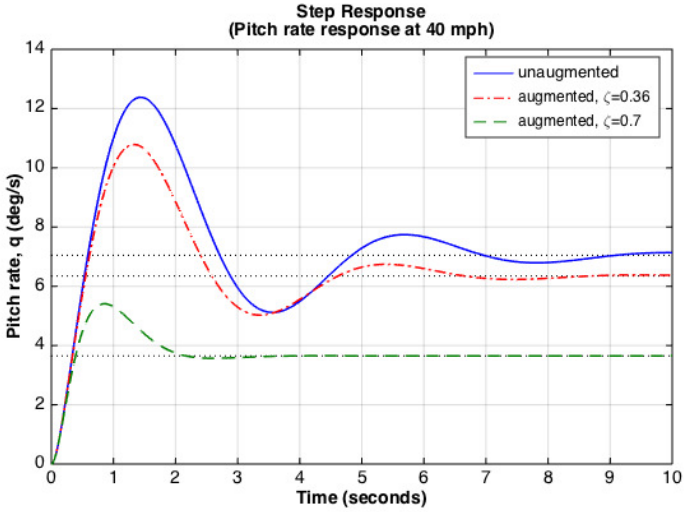

Figure 4.2: Pitch rate responses for different K_q values at 40 mph

Figure 4.2 shows the improvement of the pitch rate damping for different pitch-rate gain K_q selected through the root locus technique. The figure reveals the settling time at 2.8 sec for the $\zeta_{sp} = 0.7$, of which is 67% improved or faster than the open loop system. The rise time shows an improvement of about 35% from the open loop system. Even though the overshoot improved about 36% from the open loop system, the overshoot appeared to be still high for a normal pitch damper system.

The bode plots in Figure 4.3 and 4.4 show the bandwidth features of the G-UNIV short-period pitch response for the two different damping in the same flight condition (40 mph). Figure 4.3 indicates a slight change in gain and bandwidth when the first feedback loop ($K_q = 0.0156$) is applied. The phase bandwidth curve was slightly shifted to the right, which also represents a slight increased in damping. In Figure 4.4, however, the phase cut-off ($-180°$) frequency of the $\zeta_{sp} = 0.7$ was seen shifted to the right or increased twice the value of the open loop frequency. The gain plot also showed a slight decrease about 5 dB at the lower frequency region, but remain the same slope position with the open loop gain for higher frequency region. Although the phase bandwidth frequency remains less than the gain bandwidth (for the $\zeta_{sp} = 0.7$), the margin different between the two bandwidths did not improve, compared to the margin different of the open loop system. This condition reveals the ineffectiveness of the pitch-rate feedback in improving the bandwidth of the closed-loop system. Increasing the pitch-rate feedback gain alone only increases the damping ratio, but does not improve the bandwidth margin according to the proposed requirement.

The same evaluation was also done for the higher flight speed condition (at 75 mph)

where the bandwidth issue is more significant as mentioned previously (see Figure 3.27).

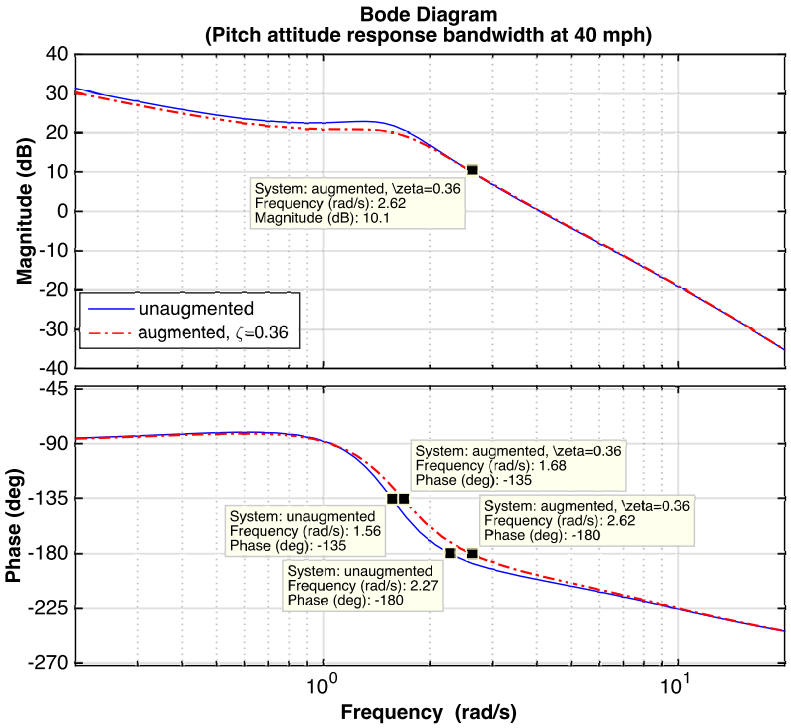

Figure 4.3: Bandwidth of pitch response for $K_q = 0.0156$ at 40 mph

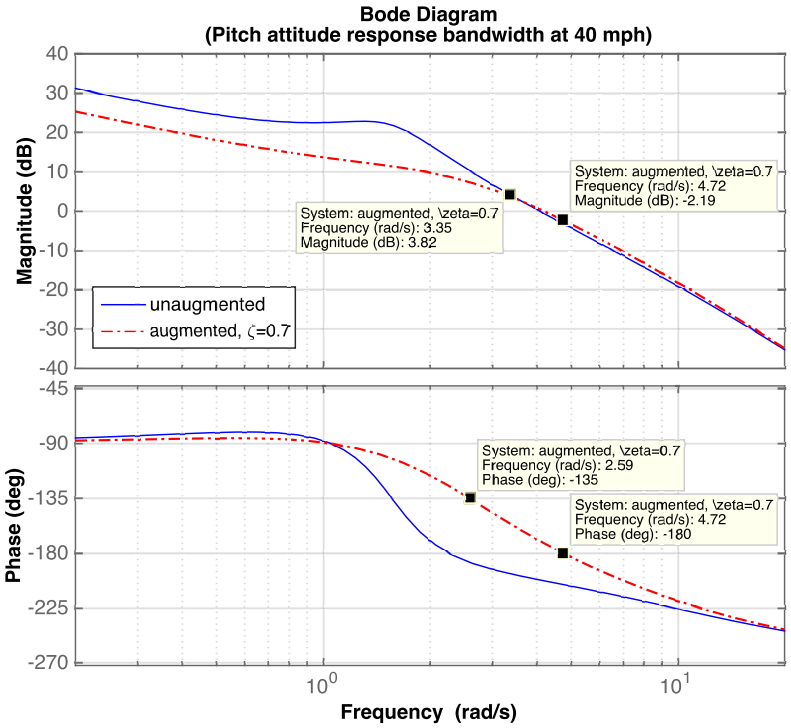

Figure 4.4: Bandwidth of pitch response for $K_q = 0.132$ at 40 mph

Figure 4.5, however, shows the time response of the G-UNIV short-period oscillations with different pitch-rate feedback gains. The feedback gain of $K_q = 0.202$ gives the minimum damping of $\zeta_{sp} = 0.36$, which reveals a 66% reduction in settling time, with the steady-state value settled at 1.51 deg/s. The feedback gain $K_q = 0.403$ is the maximum gain that is possible for the closed-loop system according to the root-locus technique, which produces the damping of $\zeta_{sp} = 0.459$. With this amount of feedback and damping, the settling time was reduced to more than 80%, with the augmented steady-state settled at 1.16 deg/s.

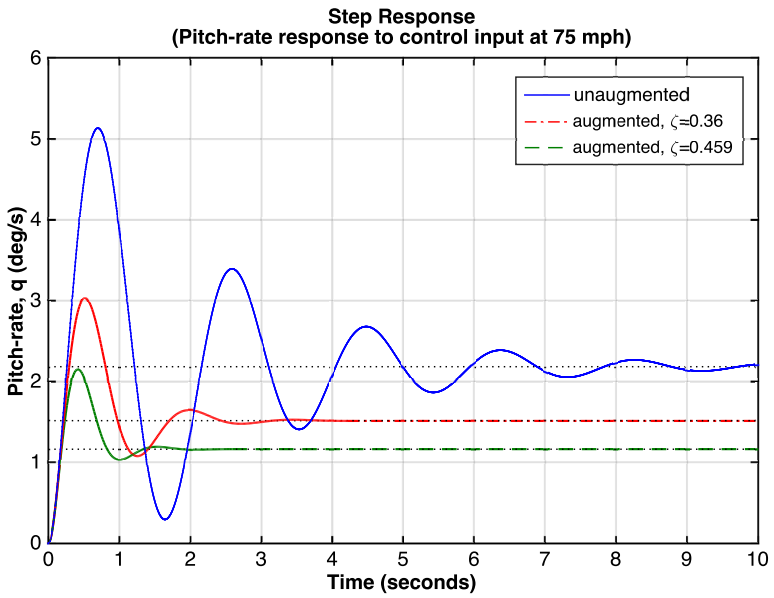

Figure 4.5: Pitch-rate step response with K_q feedback at 75 mph

The same feedback gains were presented in the bandwidth evaluation as shown in Figure 4.6. The maximum feedback gain $K_q = 0.403$ contributes to a smoother gain curve where the gain peak that appeared in the open loop bandwidth response was significantly eliminated. In this case, there is no more rapid phase lag of pitch response at higher frequency oscillations as the phase-lag curve is seen to gradually reduced until it passed the $-180°$ lag behind the control input. The phase bandwidth, $\omega_{BW(gain)}$ of the closed-loop system is also seen to be improved due to the damping as it was shifted to the right, compared to the open loop system. However, this was not good enough to prevent the vehicle from getting into PIO as the $\omega_{BW(gain)}$ and $\omega_{BW(phase)}$ are still marginally closed together. The bode plot also shows that the $\omega_{BW(gain)}$ is less than the $\omega_{BW(phase)}$ for the damping $\zeta_{sp} = 0.459$, with 0.97 rad/s margin difference.

It can be concluded that implementing the pitch-rate feedback technique does improve damping, but also contributes to the phase-lag at the higher frequency. This technique,

however, does not comply with the proposed bandwidth requirement.

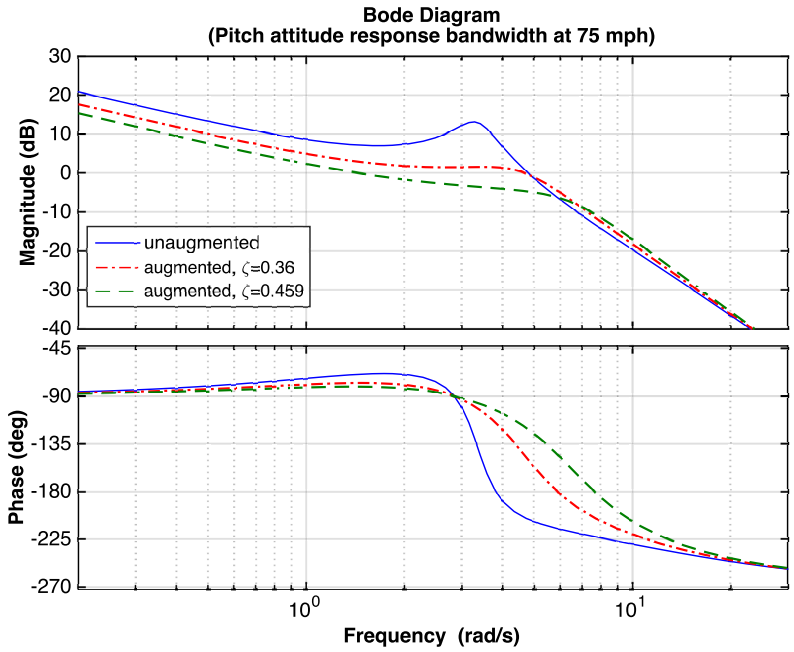

Figure 4.6: Pitch response bandwidth with K_q feedback at 75 mph

4.2.1.2 Blended Feedback Loop

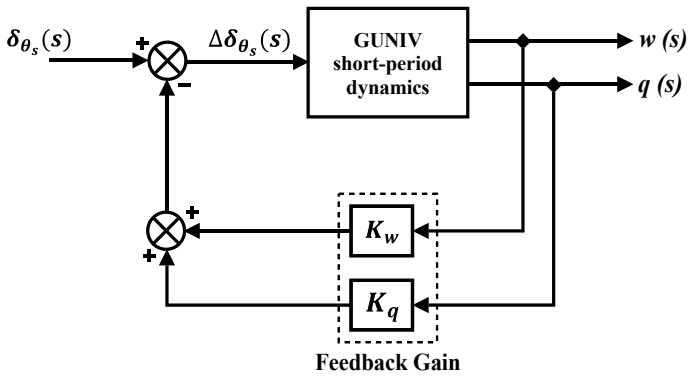

Figure 4.7: Reduced order SAS with blended feedback gain

It is now clear that the pitch-rate feedback alone cannot satisfy the bandwidth margin requirements for autogyros flying qualities. For the reduced order short-period dynamics, the state parameter outputs comprise of the vertical speed (w) and the pitch-rate (q) as shown in Figure 4.7. These state parameters can be manipulated to possibly change the phase and gain bandwidth, as well as the damping. This is possible if the closed-loop poles of the short-period mode can be relocated or reassigned to produce

a desired closed-loop response. The new eigenvalue assignment can be achieved by having a 'blended feedback' of the two-state parameters and then applying the 'pole-placement' technique for both parameters.

The pole-placement technique for linear systems was first reported by Davison [107] and is used for finding the state feedback gain matrix **K** that will give the desired response based on the eigenvalues assignment approach [108]. Until today, this technique has proven to be successful in the tuning of many linear control system applications [109–113], including on linear flight control systems [114–117].

From Figure 4.7, the general control law can be written as

$$\mathbf{u} = \mathbf{v} + \mathbf{K}\,\mathbf{x} \tag{4.2.4}$$

where **K** is the feedback gain matrix, **x** is the state feedback vector and **v** is the input command variable vector.

Substituting equation (4.2.4) into (3.8.2), the closed-loop state vectors of the augmented system can be written as

$$\begin{aligned} \dot{\mathbf{x}} &= [\mathbf{A} - \mathbf{BK}]\,\mathbf{x} + \mathbf{Bv} \\ \mathbf{y} &= [\mathbf{C} - \mathbf{DK}]\,\mathbf{x} + \mathbf{Dv} \end{aligned} \tag{4.2.5}$$

The closed-loop equation (4.2.5) is then turned into a new set of equations with the augmented state equation and state feedback matrix given by

$$\mathbf{A_{aug}} = \mathbf{A} - \mathbf{BK} \tag{4.2.6a}$$

$$\mathbf{K} = \begin{bmatrix} K_w & K_q \end{bmatrix} \tag{4.2.6b}$$

From here, the pole-placement technique is used to find the value of **K** matrix for specified pole locations. The process starts from the root locus plot of the closed-loop $(A - BK)$ system. However, choosing the best pole location is not a straightforward process. As such, the most suitable **K** matrix for each flight condition is determined based on analytical iteration. The iteration starts with choosing several pole locations and calculating the **K** matrix through the pole-placement technique. The phase and gain bandwidth, including the damping, can then be quantified from the calculated **K** matrix. The iterations continue with different **K** matrices based on different pole

locations that have been chosen, and the **K** matrix that gives the best result according to the requirement will be used as the final result for the augmentation system. The theoretical concept of the pole-placement technique is explained in Appendix C.

As an aid for the calculation and to avoid errors, the MATLAB's Control Toolbox function called *place* is used to obtain the new state feedback gain matrix **K** from the desired closed-loop poles of a state-space matrix [118]. For the G-UNIV autogyro, the short-period eigenvalues with the damping and frequency for the 75 mph flight condition are

$$p_{1,2} = -1.8 \pm 3.10\,i \;; \quad \zeta = 0.148 \;; \quad \omega_n = 3.27\,\text{rad/s} \tag{4.2.7}$$

which gives the state feedback gain matrix of

$$\mathbf{K} = \begin{bmatrix} K_w & K_q \end{bmatrix} = \begin{bmatrix} -0.0093 & 0.1514 \end{bmatrix} \tag{4.2.8}$$

The new characteristic polynomial for the closed-loop system is then given by

$$\delta_{\theta_s}(s) = (s + 17.33)(s^2 + 3.613s + 12.66) \tag{4.2.9}$$

that gives a new damping and frequency of $\zeta_{sp} = 0.51$ and $\omega_{sp} = 3.56$ rad/s. The bandwidth comparison between the open loop and the augmented pitch response of the G-UNIV at 75 mph are shown in Table 4.2.1 and Figure 4.8.

Table 4.2.1: Stability characteristics in short period mode at 75 mph

Parameters	Open-loop	Augmented
Damping, ζ_{sp}	0.141	0.51
Natural Frequency, ω_{sp} (rad/s)	3.36	3.56
Gain Bandwidth, $\omega_{BW_{gain}}$ (rad/s)	3.45	4.94
Phase Bandwidth, $\omega_{BW_{phase}}$ (rad/s)	3.41	3.75
Phase delay, τ_p (sec)	0.058	0.039

The bandwidth evaluation reveals a significant improvement on the phase and gain bandwidth in the particular flight condition. The bandwidth of the augmented system shows compliance with the bandwidth requirement of the proposed autogyro flying qualities, of which $\omega_{BW(phase)} < \omega_{BW(gain)}$ with a margin different of 1.19 rad/s (0.19

Hz). The short-period damping also reveals an improvement from 0.14 for the open loop to 0.51 for the augmented system. Moreover, the time response of the pitch-rate in the same flight condition is shown in Figure 4.9, which indicate an improvement in the settling time from 8 seconds to only 2.3 seconds for the augmented system.

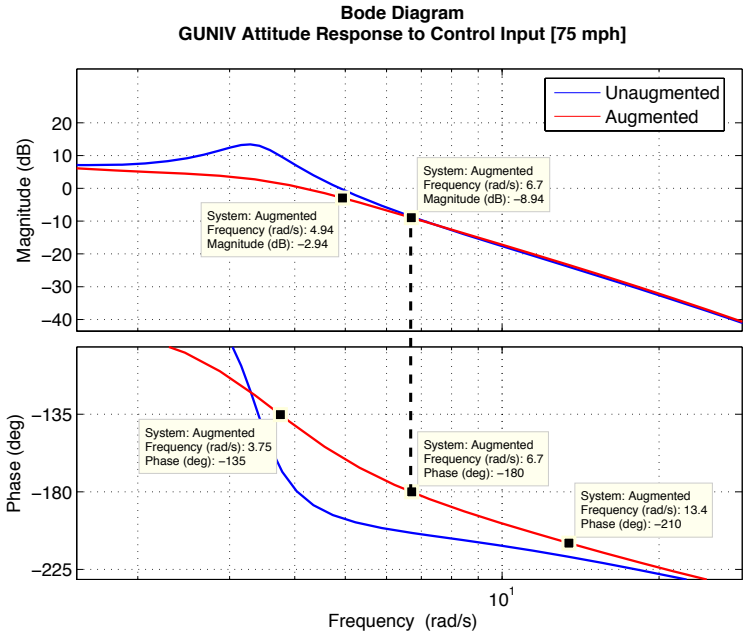

Figure 4.8: Bandwidth and Phase Delay of the short-period mode at 75 mph

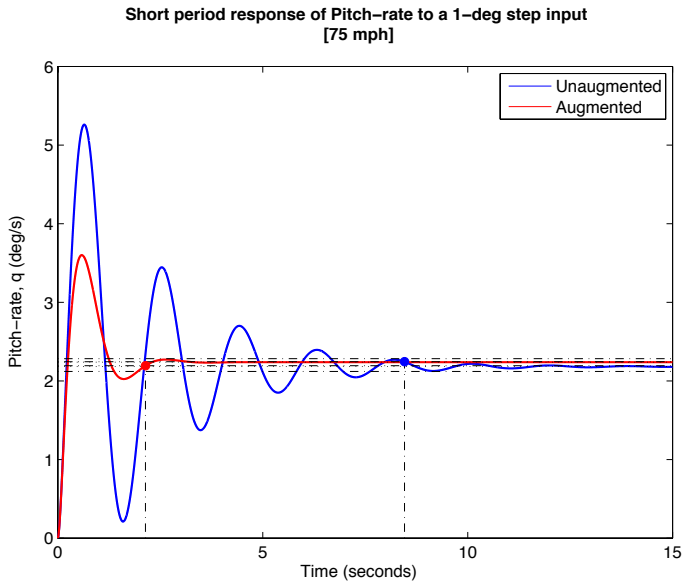

Figure 4.9: Pitch rate response to a 1-deg step input at 75 mph

The same pole-placement procedures were then carried out for other flight conditions according to the recommended flying qualities evaluation, and the results are revealed

in Table 4.2.2.

Table 4.2.2: Pole-placement feedback gain of short period mode

Evaluation Point	Pole Location	Feedback Gain, $\boldsymbol{K}_{\text{aug}} = [K_w \quad K_q]$	ω_{BW} margin
40 mph	$-0.800 \pm 1.40i$	$[-0.0018 \quad 0.0401]$	1.16 rad/s
50 mph	$-1.000 \pm 1.80i$	$[-0.0036 \quad 0.0648]$	1.23 rad/s
55 mph	$-1.125 \pm 2.05i$	$[-0.0041 \quad 0.0818]$	1.27 rad/s
65 mph	$-1.380 \pm 2.35i$	$[-0.0062 \quad 0.1183]$	1.26 rad/s
75 mph	$-1.800 \pm 3.11i$	$[-0.0093 \quad 0.1514]$	1.19 rad/s

The next step of the SAS development is to evaluate the effect of these short period state feedback gain to the full order model of the autogyro, particularly the phugoid mode. In doing so, the newly obtained short period feedback gain **K** will be applied to the full order state feedback gain matrix, which is explained in the following section.

4.2.1.3 Effect on the Linear Full Order Model

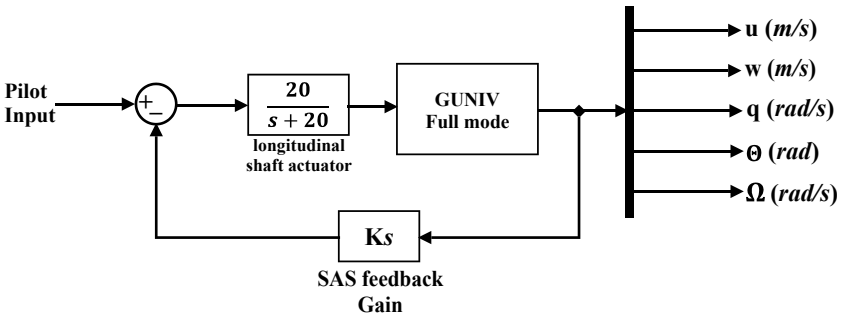

Figure 4.10: Schematic of rate-response SAS on a full order G-UNIV model

Figure 4.10 shows the schematic of the linear full order model with the state feedback gain of SAS given by

$$K_s = \begin{bmatrix} K_u & K_w & K_q & K_\Theta & K_\Omega \end{bmatrix} \tag{4.2.10}$$

To evaluate the effect of the short-period mode, $K = [K_w \; K_q]$ on the linear full order G-UNIV model, the state feedback gain is redefined to comply with the 5^{th} order state-

space equation of the autogyro model. Hence, the full order state feedback gain of the G-UNIV at the trim speed of 75 mph is redefined according to (4.2.10) as

$$K_s = \begin{bmatrix} 0 & -0.0093 & 0.1514 & 0 & 0 \end{bmatrix} \tag{4.2.11}$$

which gives a new characteristic polynomial of the full order augmented system as

$$\delta_{\theta_s}(s) = (s + 17.33)(s + 0.1084)(s^2 + 0.0168s + 0.041)(s^2 + 3.62s + 12.73) \tag{4.2.12}$$

Note that the short-period augmentation does not significantly affect the dynamics of the rotorspeed as the eigenvalue remains unchanged.

$$\begin{aligned} \lambda_{1,2} &= -1.81 \pm 3.075i \quad \text{(short-period)} \\ \lambda_{3,4} &= -0.0084 \pm 0.202i \quad \text{(phugoid)} \\ \lambda_5 &= -0.1084 \quad \text{(rotorspeed)} \\ \lambda_6 &= -17.3296 \quad \text{(actuator)} \end{aligned} \tag{4.2.13}$$

Other than the short-period mode damping, the phugoid eigenvalues also revealed a small change in the phugoid damping which increased from 0.034 to 0.042 with the short-period SAS. Correspondingly, the oscillation period of the phugoid also increased from 21.5 seconds to 31 seconds. Figure 4.11 shows the time response plot of the linear full order dynamics of the G-UNIV with the short-period augmentation at the flight speed of 75 mph. However, evaluations across the speed range indicate that the improvement of the phugoid was not significant with the short-period augmentation. This matter was confirmed by the results listed in Table 4.2.3, which revealed a non-compliance to the phugoid requirement of the proposed flying qualities.

Since the phugoid mode is known as a speed dependent oscillation in the longitudinal flight dynamics, another way to improve the phugoid damping is to introduce a speed damper. However, to implement a speed damping feedback loop would also involve the engine throttle and thrust dynamics that would promote a more complicated SAS due to the new MIMO control system. A more complicated flight control systems would also complicate the hardware configurations, thus, shifts the vehicle further away from being a light autogyro. Therefore, it is assumed that the pilot manually controls the engine throttle but the short-period dynamic of the autogyro is automatically solved through the flight control system.

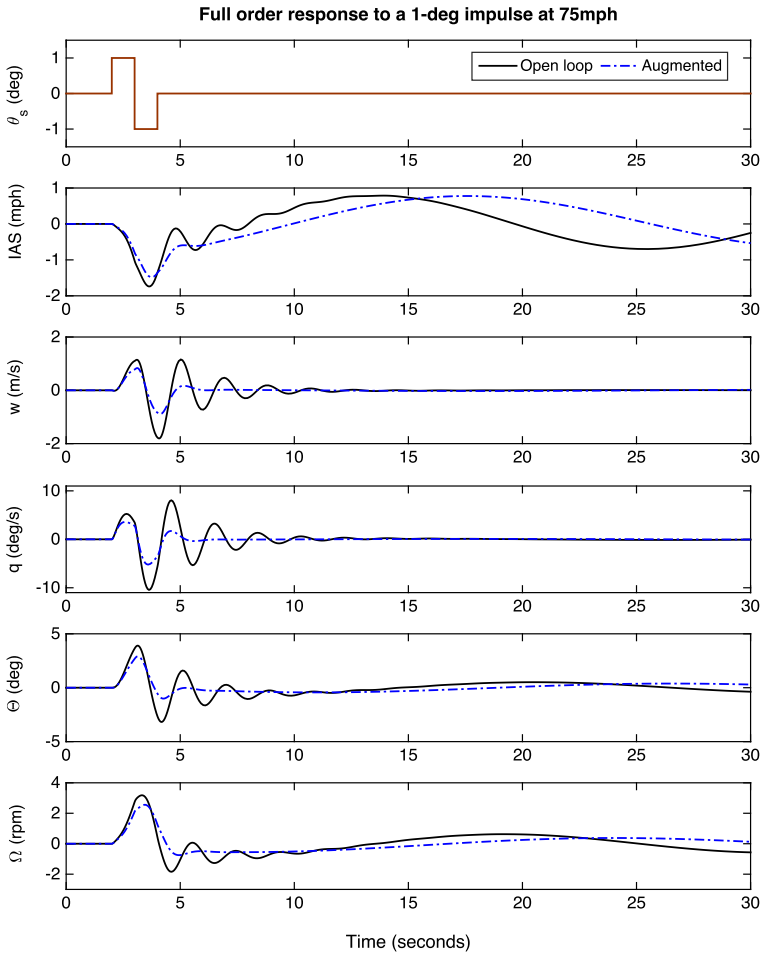

Figure 4.11: Linear full order response with SAS at 75 mph

Table 4.2.3: Stability characteristic of linear full order with SAS

Evaluation Point	Feedback Gain $\boldsymbol{K}_{\text{aug}}$, $[K_u\ K_w\ K_q\ K_\theta\ K_\Omega]$	Open loop Damping	Closed-loop Damping
40 mph	[0 -0.0018 0.0401 0 0]	$\zeta_{ph} = (0.155)$ $\zeta_{sp} = 0.360$	$\zeta_{ph} = (0.163)$ $\zeta_{sp} = 0.531$
50 mph	[0 -0.0036 0.0648 0 0]	$\zeta_{ph} = (0.048)$ $\zeta_{sp} = 0.250$	$\zeta_{ph} = (0.072)$ $\zeta_{sp} = 0.509$
55 mph	[0 -0.0041 0.0818 0 0]	$\zeta_{ph} = (0.021)$ $\zeta_{sp} = 0.217$	$\zeta_{ph} = (0.040)$ $\zeta_{sp} = 0.500$
65 mph	[0 -0.0062 0.1183 0 0]	$\zeta_{ph} = 0.012$ $\zeta_{sp} = 0.171$	$\zeta_{ph} = 0.0036$ $\zeta_{sp} = 0.502$
75 mph	[0 -0.0093 0.1514 0 0]	$\zeta_{ph} = 0.034$ $\zeta_{sp} = 0.141$	$\zeta_{ph} = 0.042$ $\zeta_{sp} = 0.507$

4.3 Rate-Command Attitude Hold Controller

It is well understood that the stability augmentation system of an aircraft is generally built for only one reason, to improve the basic dynamic stability of the aircraft, particularly the damping. For an aircraft that was designed with a statically stable characteristic, the SAS system is only useful in certain flight mission. Thus the SAS can be switch ON and OFF. For an aircraft that has issues with static stability, or the static stability was removed for a special reason (fighter aircraft for instance), the SAS is very useful to safely maintain the stability in flight. This type of automatic system is considered of having a full authority as it works independently and cannot be overridden by the pilot. This can also be understood that when the SAS is working, the pilot can still freely control the aircraft through the control stick without interfering with the SAS. A typical light autogyro might be put into this second category, where the SAS is expected to continuously function to provide basic stability and safety in flight. This is also true, especially for those home-built autogyros and early generation models that often have a tendency to enter a PIO condition during flight. Incidents and fatalities statistics mentioned in Chapter 2 can be referred to regarding this.

On top of having the SAS, the quality of controllability and manoeuvrability provided by the controller are still questionable from the pilot's point of view (in the sense of handling qualities). This is because, there is no guarantee that for every degree of stick deflection, the aircraft will respond precisely, regardless of the time lag between the response and the control input is applied. For a typical light autogyro, for example, fast and precise control of pitch-rate is desirable, especially when dealing with abrupt wind gusts that tend to de-stabilise the vehicle. In this particular case, the ability of the control system to precisely respond to pilot inputs is also crucial as the SAS is only used for damping and not for precision manoeuvring. Therefore, it is desirable to have a Rate-Command Attitude Hold (RCAH) controller for the autogyro, once the stability augmentation system is already in place. This type of automatic control is generally known as Control Stability Augmentation System (CSAS), which is not just a SAS, but a controlled SAS.

4.3.1 Implementing PI Controller for the RCAH

For a number of flight control text such as Schmidt [97], Cook [33] and Lewis [119], linear control for RCAH is commonly implemented through (P+I) compensator that is generally explained in a simple schematic in Figure 4.12. There have been a number

of studies and implementation of the PI controller-based RCAH similar to the one in the figure [115, 116, 120].

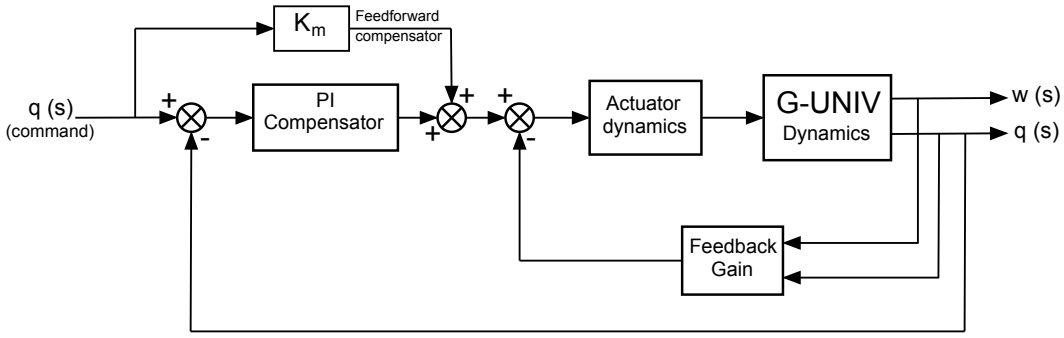

Figure 4.12: General schematic of pitch rate RCAH

The RCAH was initially meant for fast and agile response of statically unstable military combat aircraft. The implementations were then expanded for broader applications in other types of aircraft that were designed with marginally stable bare airframe but requiring a precision response to pilot's command. Rahman et al. [115] for instance, implemented RCAH on a Blended Wing Body aircraft where the aircraft itself was designed without a tail. The handling qualities of the aircraft were proven to be upgraded to level 1 according to the appropriate handling qualities requirements. Perera [120] implemented RCAH on the Aerosonde Unmanned Vehicle, an aircraft that was found to have poor stability characteristics. A flying qualities improvement was successfully made for the aircraft, measured by testing against the flying qualities requirements of a piloted aircraft, the MIL-F-8785C. Mansor et al. [116] have also proved the same for RCAH on a canard controlled aircraft.

The following RCAH design is targeted to be implemented particularly on the G-UNIV autogyro model used in this research. It is important to note that the underlying concept of the following RCAH design was adapted from the previous work made by Rahman et al. [115] and Guo [121] for fixed-wing aircraft, but yet to be implemented on any rotorcraft including autogyros. The challenge that put forward in this section is whether the same design concept can be applied on an autogyro, particularly the G-UNIV light autogyro.

The pitch-rate RCAH design started with the reduced order approximation of the short period state-space equations, as the pitch-rate (q) and the normal speed (w) are to be manipulated for the augmentation system. For the G-UNIV autogyro, the reduced order approximation for the short-period mode similar to equation (3.8.7) is used. An additional state parameter that is contributed by the PI compensator of the short-

period equation is introduced, as shown in Figure 4.12. It is actually a 'lag integrator' that contributes to the augmentation of the pitch-rate parameter as shown in Figure 4.13.

Thus, the additional state variable in terms of time domain can be written by

$$q_e(t) = \int \big[q(t) - q_c(t)\big]dt \tag{4.3.1}$$

that yields the additional state equation

$$\dot{q_e}(t) = q(t) - q_c(t) \tag{4.3.2}$$

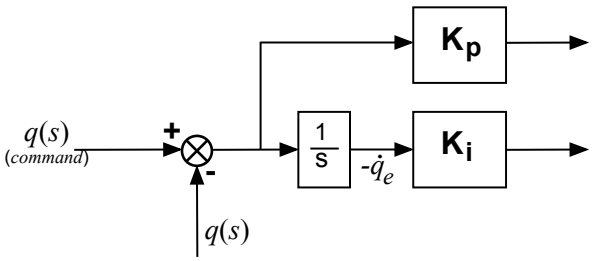

Figure 4.13: Additional state for pitch-rate command

The integral state equation can then be augmented into the original reduced order state-space equation in (3.8.7), and written back as follows

$$\begin{bmatrix} \dot{w} \\ \dot{q} \\ \dot{q_e} \end{bmatrix} = \begin{bmatrix} Z_w & Z_q & 0 \\ M_w & M_q & 0 \\ 0 & 1 & 0 \end{bmatrix} \begin{bmatrix} w \\ q \\ q_e \end{bmatrix} + \begin{bmatrix} Z_{\delta_{\theta_s}} \\ M_{\delta_{\theta_s}} \\ 0 \end{bmatrix} \begin{bmatrix} \delta_{\theta_s} \end{bmatrix} + \begin{bmatrix} 0 \\ 0 \\ -1 \end{bmatrix} \begin{bmatrix} q_c \end{bmatrix} \tag{4.3.3}$$

As such, the general term of the open loop equation in (4.3.3) and its feedback control law can then be written as

$$\begin{aligned} \dot{x}(t) &= \mathbf{A}x(t) + \mathbf{B}u(t) + \mathbf{P}v(t) \\ u(t) &= -\mathbf{K}x(t) + \mathbf{Q}v(t) \end{aligned} \tag{4.3.4}$$

where $\mathbf{K}$ is the state feedback gain and $\mathbf{Q}$ is the state feed-forward gain. Solving for (4.3.4) then produces a new state-space equation that represents the full augmented

RCAH model and presented as

$$\dot{x}(t) = [\mathbf{A} - \mathbf{BK}]\, x(t) + [\mathbf{BQ} + \mathbf{P}]\, v(t) \tag{4.3.5}$$

4.3.2 Finding the Gain Matrices, K and Q

To find the suitable selection of the gain **K** and **Q** in (4.3.5) that comply with the autogyro flying qualities requirements mentioned in the last section, the following steps are made:

a) The feedback gain matrix **K** has to be determined first by placing the closed-loop poles at the desired location to comply with the bandwidth and phase delay requirement of the proposed criteria. Again, the pole-placement technique is implemented at the flight speed of 75 mph as an example. In this particular case, the desired location of the poles is already known, as they have been located when implementing the SAS in the previous section. The targeted closed-loop short-period mode eigenvalues and its stability characteristics are shown in Table 4.3.1.

b) The feedforward gain **Q** is then to be determined once the feedback gain **K** values are known. Feedforward compensator is commonly used to enhance the controller so that changes in the control input can be anticipated for better total control. For aircraft control, the feedforward compensator in commonly applied for control input tracking purposes and to improve the settling time of the steady-state response. On the other hand, the PI controller is used to improve the steady-state gain, which also contributed to the performance of the transient response of the RCAH.

Table 4.3.1: RCAH short period requirements for feedback gain **K** (75 mph)

Desired poles location	$\lambda_{sp} = -1.8 \pm 3.11i$
Desired damping and frequency	$\zeta_{sp} = 0.5$, $\omega_{sp} = 3.6$ (rad/s)
Desired characteristic polynomial	$(s^2 + 3.6s + 12.91)$

It is important to note that, in this development stage, the dynamic of the actuator including the control linkages are not included to simplify the design of the RCAH controller. The actuator model will be included later with some gain adjustments according to the changes of the vehicle's dynamic.

4.3.2.1 The Feedback Gain K

It can be seen in (4.3.3) that the system is of 3^{rd} order, which requires three poles to be solved for the closed-loop equation. The three poles consist of the two complex poles of the short-period oscillation as suggested in Table 4.3.1, and one real pole which represents the lag integrator state parameter, denoted as P_{int}. Rahman et al. [115] suggested that the lag time of the P_{int} should be close to the frequency of the desired short-period mode ω_{sp}. For that matter, the pole location of $P_{int} = 3.11$ is chosen, which gives the desired closed-loop characteristic polynomial which is written as

$$(s + 3.11)(s^2 + 3.6s + 12.91) \tag{4.3.6}$$

Applying the same pole-placement technique as mentioned in the previous section, the state feedback gain **K** is found to be

$$\mathbf{K} = \begin{bmatrix} K_w & K_q & K_{q_e} \end{bmatrix} = \begin{bmatrix} -0.0388 & 0.3469 & 1.6352 \end{bmatrix} \tag{4.3.7}$$

Therefore, the new augmented state-space equation with the feedback gain **K** can be obtained and written as

$$\begin{bmatrix} \dot{w} \\ \dot{q} \\ \dot{q_e} \end{bmatrix} = \begin{bmatrix} -2.326 & 44.94 & 55.16 \\ 0.158 & -4.384 & -21.01 \\ 0 & 1 & 0 \end{bmatrix} \begin{bmatrix} w \\ q \\ q_e \end{bmatrix} + \begin{bmatrix} -33.73 \\ 12.85 \\ 0 \end{bmatrix} \begin{bmatrix} \delta_{\theta_s} \end{bmatrix} + \begin{bmatrix} 0 \\ 0 \\ -1 \end{bmatrix} \begin{bmatrix} q_c \end{bmatrix} \tag{4.3.8}$$

which yields the augmented transfer functions of

$$\begin{aligned} \frac{w(s)}{q_c(s)} &= \frac{-33.73s(s - 12.74)}{(s + 3.11)(s^2 + 3.6s + 12.91)} \\ \frac{q(s)}{q_c(s)} &= \frac{12.85s(s + 1.911)}{(s + 3.11)(s^2 + 3.6s + 12.91)} \\ \frac{q_e(s)}{q_c(s)} &= \frac{12.85(s + 1.911)}{(s + 3.11)(s^2 + 3.6s + 12.91)} \end{aligned} \tag{4.3.9}$$

From equation 4.3.9 the integral-lag pole is located at the desired location of ($s = -3.11$), which also represents an additional time lag of 0.322 seconds for the aircraft to response to the command input of the pilot. As previously understood that an increase in the controller dynamics would also affect the bandwidth of the augmented system. As such, maintaining a sufficient margin between the particular bandwidth is crucial for an autogyro. Therefore, it is important to find the correct value of feedforward gain **Q** so that the additional feedback time lag can be reduced more.

4.3.2.2 The Feed-forward Gain Q

Referring back to the augmentation state and control equation in (4.3.5), since there is only one input signal for the RCAH, then the feedforward matrix **Q** will comprise of only one parameter, denoted as 'm'. Since the feedforward compensator is used for the controller to anticipate the changes of the control input, the state-space equation in (4.3.8) is then written as

$$\begin{bmatrix} \dot{w} \\ \dot{q} \\ \dot{q_e} \end{bmatrix} = \begin{bmatrix} -2.326 & 44.94 & 55.16 \\ 0.158 & -4.384 & -21.01 \\ 0 & 1 & 0 \end{bmatrix} \begin{bmatrix} w \\ q \\ q_e \end{bmatrix} + \begin{bmatrix} -33.73m \\ 12.85m \\ -1 \end{bmatrix} \begin{bmatrix} q_c \end{bmatrix} \tag{4.3.10}$$

One of the important features of this design concept is that, the value of m also reflects the integral-lag pole of the system. As such, the m can be set in a way that the feedforward gain will diminish the integrator lag time giving a faster response time and better zero steady-state response for the RCAH. Thus, it can be seen that the *integral-zero* of the transfer functions in (4.3.9) would have the same value with the *integral-pole*, which is $s = -3.11$. Since the feedback gain **K** was previously known and the closed-loop state equation is given in (4.3.10), the integral-zero can then be written as

$$Z_{int} = \frac{K_{q_e}}{m} \tag{4.3.11}$$

where the integral gain K_{q_e} is already known from (4.3.7) as 1.6352 and the integral-pole was set to 3.11. Therefore, according to (4.3.11), the feedforward gain m is found to be

$$m = 0.5258 \tag{4.3.12}$$

so that the integrator-pole P_{int} can be ruled out by the Z_{int} and yield faster response time for the RCAH system.

4.3.3 RCAH Control Applied to the Reduced Order Model

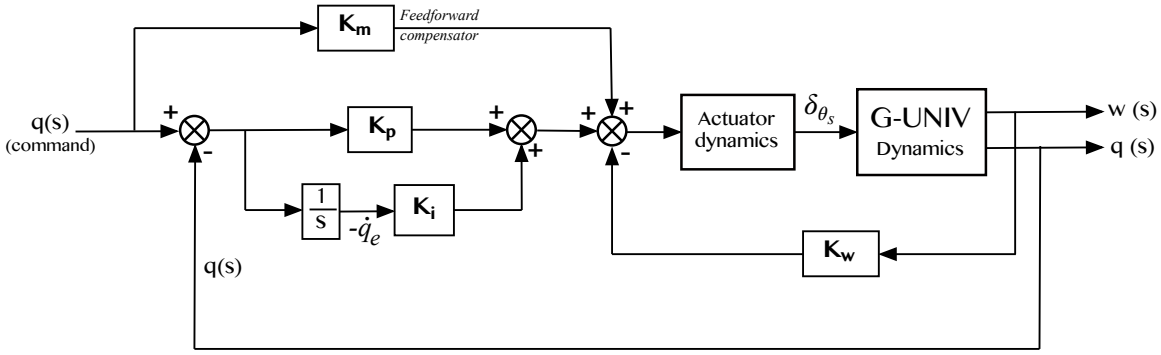

Figure 4.14: Pitch-rate RCAH system schematic

Knowing the values of **K** and **Q**, the controller output in the form of longitudinal shaft tilt δ_{θ_s} can be written according to the control law in (4.3.4) as

$$\delta_{\theta_s} = -\begin{bmatrix} -0.0388 & 0.3469 & 1.6352 \end{bmatrix} \begin{bmatrix} w \\ q \\ q_e \end{bmatrix} + 0.5258\, q_c \tag{4.3.13}$$

Hence, the new augmented system for both, feedback gain **K** and feedforward gain **Q** can be written as a new closed-loop state-space equation in the following

$$\begin{bmatrix} \dot{w} \\ \dot{q} \\ \dot{q_e} \end{bmatrix} = \begin{bmatrix} -2.326 & 44.94 & 55.16 \\ 0.158 & -4.384 & -21.01 \\ 0 & 1 & 0 \end{bmatrix} \begin{bmatrix} w \\ q \\ q_e \end{bmatrix} + \begin{bmatrix} -17.73 \\ 6.756 \\ -1 \end{bmatrix} \begin{bmatrix} q_c \end{bmatrix} \tag{4.3.14}$$

which yields the new closed-loop transfer functions

$$\begin{aligned} \frac{w(s)}{q_c(s)} &= \frac{-17.735(s - 12.74)}{(s^2 + 3.6s + 12.91)} \\ \frac{q(s)}{q_c(s)} &= \frac{6.756(s + 1.911)}{(s^2 + 3.6s + 12.91)} \end{aligned} \tag{4.3.15}$$

Comparing the new transfer functions in (4.3.15) with the previous one in (4.3.9) obviously reveals the removal of the integral-pole, or simply called the 'zero-pole cancellation'.

The complete RCAH system schematic can be seen in Figure 4.14, where the integral gain $K_i = K_{q_e}$, the proportional gain $K_p = K_q$, and the feedforward gain K_m is represented by $(m - K_q)$ respectively. Figure 4.15 shows the short-period response of the autogyro to a 1-deg/s step input q_c, with and without the RCAH system engaged. Figure 4.16 shows another short-period response of the same RCAH to a 1-deg/s pulse input q_c.

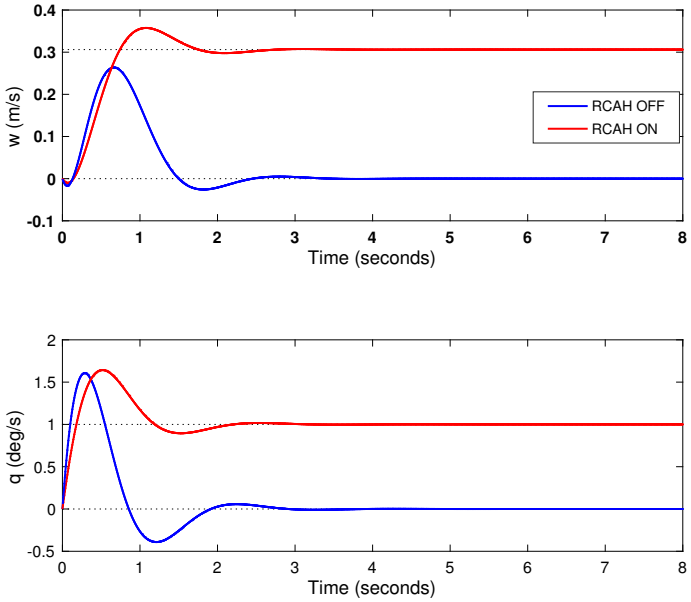

Figure 4.15: Short-period RCAH response to a step input q_c

It can be observed from the two figures that the pitch-rate response of the vehicle is well damped and almost perfectly tracked to the desired command pitch-rate signal. When a command pitch-rate, q_c of 1-deg/s is held for a duration of 6 seconds, the pitch attitude angle θ ramps up at 1-deg/s for 6 seconds and then settles at the new pitch attitude ($\theta = 6°$). This is when the pilot releases the stick back to its origin. The autogyro continues flying in the attitude-hold condition, at the new settled pitch attitude angle until the next stick displacement.

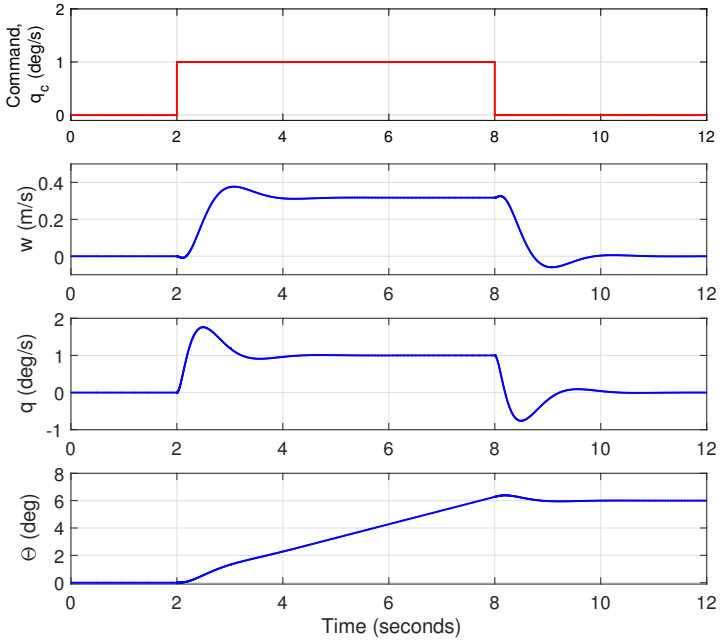

Figure 4.16: Short-period RCAH response to a pitch-rate command q_c

4.3.4 Implementing the RCAH in the Linear Full Order Model

The same way of placing the additional integrator state in (4.3.3) is carried out for the full order state-space equation (3.8.3), that yields

$$\begin{bmatrix} \dot{u} \\ \dot{w} \\ \dot{q} \\ \dot{\theta} \\ \dot{\Omega} \\ \dot{q}_e \end{bmatrix} = \begin{bmatrix} X_u & X_w & X_q & X_\Theta & X_\Omega & 0 \\ Z_u & Z_w & U_e & Z_\Theta & Z_\Omega & 0 \\ M_u^* & M_w^* & M_q^* & M_\Theta^* & M_\Omega^* & 0 \\ 0 & 0 & 1 & 0 & 0 & 0 \\ Q_u & Q_w & Q_q & Q_\Theta & Q_\Omega & 0 \\ 0 & 0 & 1 & 0 & 0 & 0 \end{bmatrix} \begin{bmatrix} u \\ w \\ p \\ \theta \\ \Omega \\ q_e \end{bmatrix} + \begin{bmatrix} X_{\delta_{\theta_s}} \\ Z_{\delta_{\theta_s}} \\ M_{\delta_{\theta_s}}^* \\ 0 \\ Q_{\delta_{\theta_s}} \\ 0 \end{bmatrix} \begin{bmatrix} \delta_{\theta_s} \end{bmatrix} + \begin{bmatrix} 0 \\ 0 \\ 0 \\ 0 \\ 0 \\ -1 \end{bmatrix} q_c \quad (4.3.16)$$

Similarly, the control law in (4.3.13) is then written for the full order as

$$\delta_{\theta_s} = -\begin{bmatrix} K_u & K_w & K_q & K_\Theta & K_\Omega \end{bmatrix} \begin{bmatrix} u \\ w \\ q \\ \Theta \\ \Omega \\ q_e \end{bmatrix} + m\, q_c \tag{4.3.17}$$

Inserting the short-period feedback matrix $\mathbf{K} = \begin{bmatrix} -0.0388 & 0.3469 & 1.6352 \end{bmatrix}$ and $m = 0.5258$ from the previous reduced order section into the full order augmentation in (4.3.17) would give

$$\delta_{\theta_s} = -\begin{bmatrix} 0 & -0.0388 & 0.3469 & 0 & 0 & 1.6352 \end{bmatrix} \begin{bmatrix} u \\ w \\ q \\ \Theta \\ \Omega \\ q_e \end{bmatrix} + 0.5258\,[q_c] \tag{4.3.18}$$

Table 4.3.2: RCAH Stability characteristics comparison of G-UNIV

Mode	**Unaugmented Aircraft**	**Reduced order RCAH**	**Full order RCAH**
Short period	$\zeta_{sp} = 0.141$ $\omega_{sp} = 3.36$ rad/s	$\zeta_{sp} = 0.5$ $\omega_{sp} = 3.35$ rad/s	$\zeta_{sp} = 0.5$ $\omega_{sp} = 3.6$ rad/s
Phugoid	$\zeta_{ph} = 0.0335$ $\omega_{ph} = 0.27$ rad/s	N/A	$T_1 = 1/0 = \infty$ $T_2 = 1/0.1264 = 7.91$s
Integral-lag	N/A	$t_{lag} = 1/3.11 = 0.321$s	$t_{lag} = 1/3.1 = 0.323$s

The stability characteristics of the RCAH between the short-period and phugoid mode of the G-UNIV are compared and shown in Table 4.3.2. The table reveals that the damping of the short-period mode does not change when the RCAH is implemented in the full order mode. In this particular case, the frequency of the full order short-period oscillation is slightly increased. The phugoid mode acted conversely between the augmented and the bare airframe, which is believed to be the effect of the integral

feedback. The integral feedback of the pitch-rate q modifies the closed-loop phugoid mode where a non-oscillatory mode replaces the phugoid. The dynamics of the phugoid are represented by a stable pole T1 and another T2 pole with a time constant 7.91 sec.

Moreover, Figure 4.17 shows the full order state response of the G-UNIV to a 1-deg/s pulse input q_c for a duration of 6 seconds. The figure also shows how the command pitch-rate q_c is tracked by the pitch-rate response of the vehicle and settles in an approximate 1.6 seconds, which conforms to the common approximation that the settling time is given by

$$t_s = \frac{3}{\zeta \omega_n} \tag{4.3.19}$$

The pitch attitude angle Θ in the same figure can be seen rises at the rate 1-deg/s for the duration of 6 seconds before settling at an angle of slightly above 6-degrees with a small overshoot.

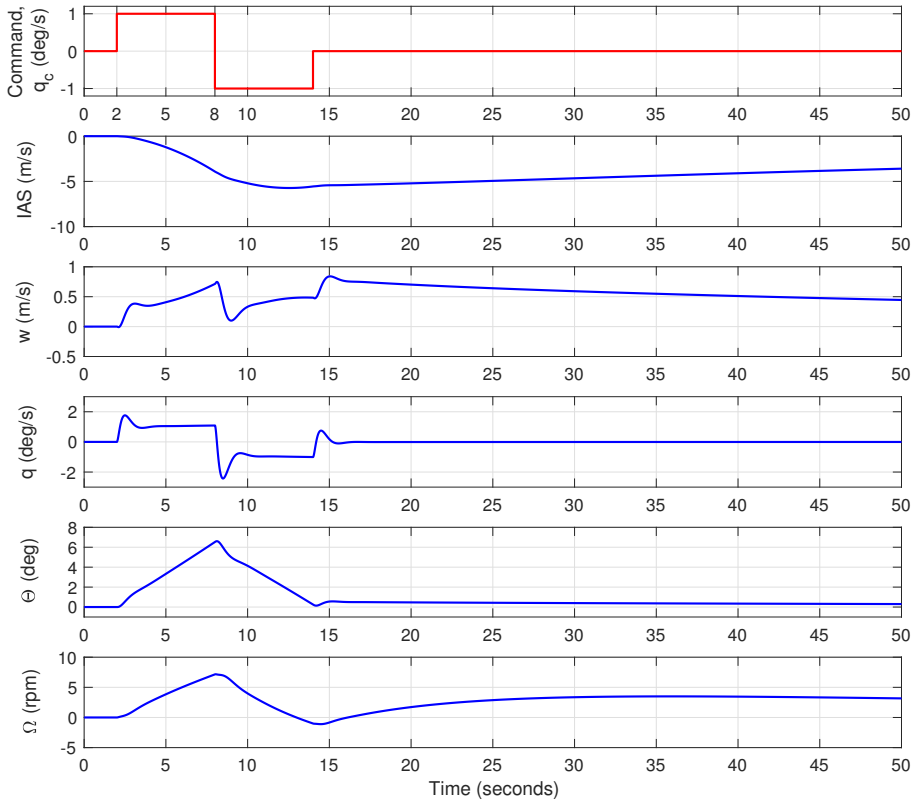

Figure 4.17: Full order RCAH response to a doublet input q_c for 12 seconds

As far as autogyros flying qualities are concerned, Table 4.3.2 also show a good flying qualities compliances of the short-term dynamics, which is the most crucial in ensuring the autogyro is safe from pitch instability. In fact, the bandwidth and the phase delay of the augmented RCAH in Figure 4.18 exhibits a good compliance to the autogyro bandwidth requirement of the proposed flying qualities criteria, compared to the unaugmented condition shown in Figure 3.27. It can be seen in Figure 4.18 that the phase-bandwidth $\omega_{BW(phase)}$ is lesser than the gain-bandwidth $\omega_{BW(gain)}$ with a margin different of about 1.45 rad/s.

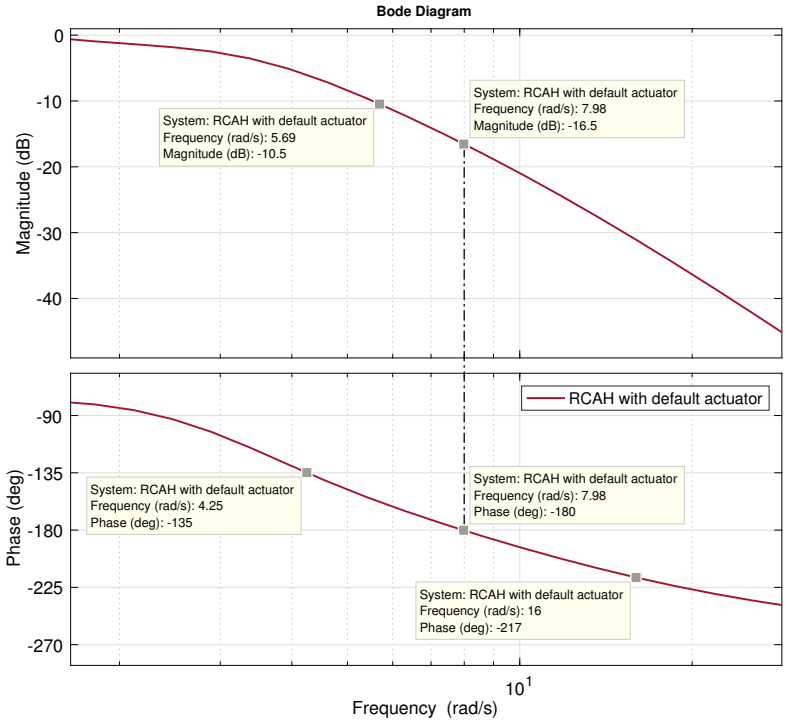

Figure 4.18: RCAH bandwidth plot in short-period mode at 75 mph (close-in view)

4.3.5 Implementing the Controller over All Flight Speeds

To guarantee the desired controllability and robustness with the designed controller, the controller is tested with different evaluation points (trim flight speeds) along the whole flight range and named $\mathcal{F}_1$ to $\mathcal{F}_5$. These evaluation points are set according to the flight speeds proposed in the autogyro flying qualities requirements in Chapter 2. The new feedback gain $\mathbf{K}$ and feedforward gain $\mathbf{Q}$ for each design point of the RCAH is determined with the same approach presented in the previous section. These include

the damping ratio, the bandwidth, and other related criteria, same as the one that has been obtained from the previous evaluation point of 75 mph. The gain values obtained for the design points across the flight speed are listed in Table 4.3.3 and illustrated in Figure 4.19.

Table 4.3.3: RCAH controller gains for the whole flight range

Evaluation points (mph)	$\mathbf{K} = \begin{bmatrix} K_w & K_q & K_{q_e} & Q \end{bmatrix}$	**Damping ratio, ζ**	**Frequency, ω (rad/s)**
$\mathcal{F}_1 = 40$	$K_1 = \begin{bmatrix} -0.0107 & 0.1224 & 0.2140 & 0.1529 \end{bmatrix}$	0.513	1.62
$\mathcal{F}_2 = 50$	$K_2 = \begin{bmatrix} -0.0168 & 0.1671 & 0.4078 & 0.2266 \end{bmatrix}$	0.517	2.06
$\mathcal{F}_3 = 55$	$K_3 = \begin{bmatrix} -0.0207 & 0.1957 & 0.5691 & 0.2776 \end{bmatrix}$	0.521	2.36
$\mathcal{F}_4 = 65$	$K_4 = \begin{bmatrix} -0.0306 & 0.2557 & 0.8301 & 0.3320 \end{bmatrix}$	0.500	2.35
$\mathcal{F}_5 = 75$	$K_5 = \begin{bmatrix} -0.0388 & 0.3469 & 1.6352 & 0.5258 \end{bmatrix}$	0.593	3.66

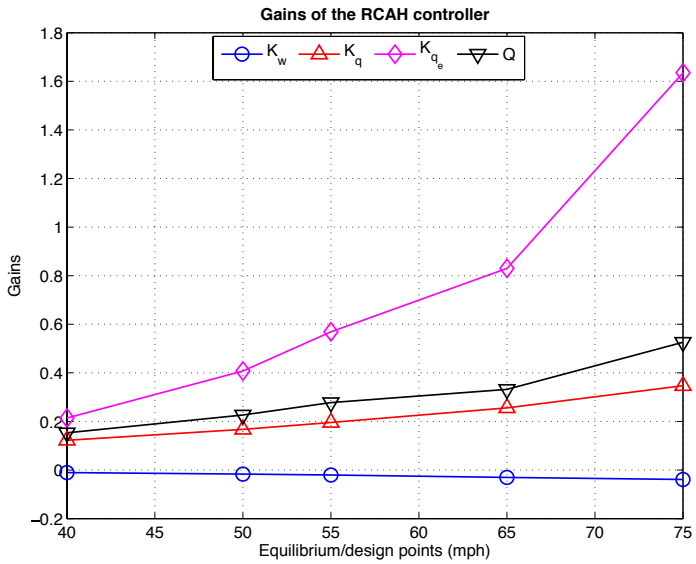

Figure 4.19: G-UNIV RCAH gain obtained for the selected evaluation points

It can be seen from the table and figure that these gains and natural frequencies of the short-period oscillations increased gradually with the increase of airspeeds. Moreover, the RCAH controller consistently achieved short-period damping of around 0.5 across the speed range. It is assumed that the zero-pole cancellation strategy was successfully put in place in order to reduce or deminish the integrator-lag time that was introduced in the feedforward compensator.

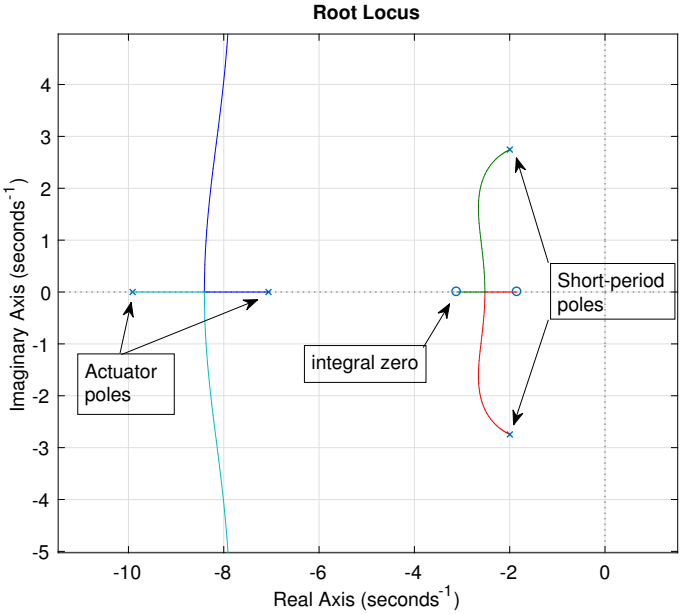

Figure 4.20: Root-locus plot of RCAH with the actuator at flight speed 75 mph

However, in reality, when the actuator dynamics are put in place, the transfer function of the aircraft is totally changed, even though the effect of the actuator dynamics is negligible due to fact that the dynamic of the actuator is faster than the aircraft dynamics. For the G-UNIV example, a first-order linear actuator is used with a time constant, $\tau_a = 0.05$ seconds, which gives $G_a = \frac{20}{s+20}$ rad/s. Figure 4.20 shows the root-locus plot of the closed-loop system at the flight speed 75 mph, which also represents the RCAH system with the actuator included. The closed-loop transfer functions for this RCAH system are given by

$$\begin{aligned}
\frac{w(s)}{q_c(s)} &= \frac{-6.2383(s-13.19)(s+3.11)}{(s+9.911)(s+7.061)(s^2+3.995s+11.53)} \\
\frac{q(s)}{q_c(s)} &= \frac{140.81(s+3.11)(s+1.842)}{(s+9.911)(s+7.061)(s^2+3.995s+11.53)} \\
\frac{\Theta(s)}{q_c(s)} &= \frac{140.81(s+3.11)(s+1.842)}{s(s+9.911)(s+7.061)(s^2+3.995s+11.53)}
\end{aligned} \tag{4.3.20}$$

Note that, the pole-zero cancellation that was placed previously in equation (4.3.9) does not happen once the actuator is in place. The change in pole locations as shown in Figure 4.20 is due to the actuator dynamics employed in the model that affecting

the closed-loop pole locations of the aircraft's dynamics.

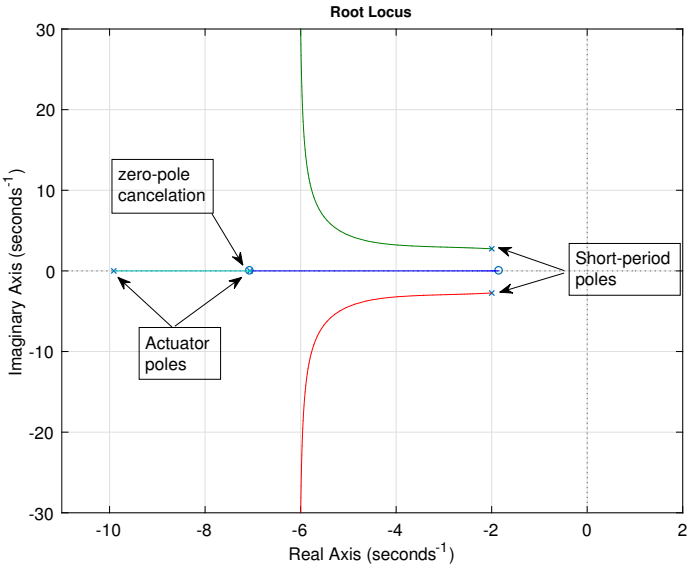

Figure 4.21: Root locus of the short-period RCAH with zero-pole cancellation

The alternative way to minimise the actuator effect, as suggested by Stevens et al. [119], is by placing the compensator zero close to the pole at $s = -5.323$, for the zero-pole cancellation to take place. The result of the pole-zero cancellation is shown in the root-locus plot in Figure 4.21, where all poles and zeros are located on the real axis, except the short-period poles. The zero-pole elimination causes the poles and zeros of the feedforward gain and actuator to be connected or overlapped, thus eliminate the integral-lag time. Fortunately, all these changes did not affect the short-period poles, thus, the short-period flying qualities performance which has been set previously. Therefore, the new transfer functions of the corrected short-period mode RCAH for the design point of 75 mph can then be written as

$$\begin{aligned}
\frac{w(s)}{q_c(s)} &= \frac{-2.7477(s-13.19)(s+7.061)}{(s+9.911)(s+7.061)(s^2+3.995s+11.53)} \\
\frac{q(s)}{q_c(s)} &= \frac{62.018(s+7.061)(s+1.842)}{(s+9.911)(s+7.061)(s^2+3.995s+11.53)} \\
\frac{\Theta(s)}{q_c(s)} &= \frac{62.018(s+7.061)(s+1.842)}{s(s+9.911)(s+7.061)(s^2+3.995s+11.53)}
\end{aligned} \tag{4.3.21}$$

Note that the new placement of the compensator's zero to the new location also directly

affecting the feedforward gain matrix **Q** of the RCAH, which is then given by

$$m = \frac{K_{q_e}}{P_{int}} = \frac{1.6352}{5.323} = 0.3072 \tag{4.3.22}$$

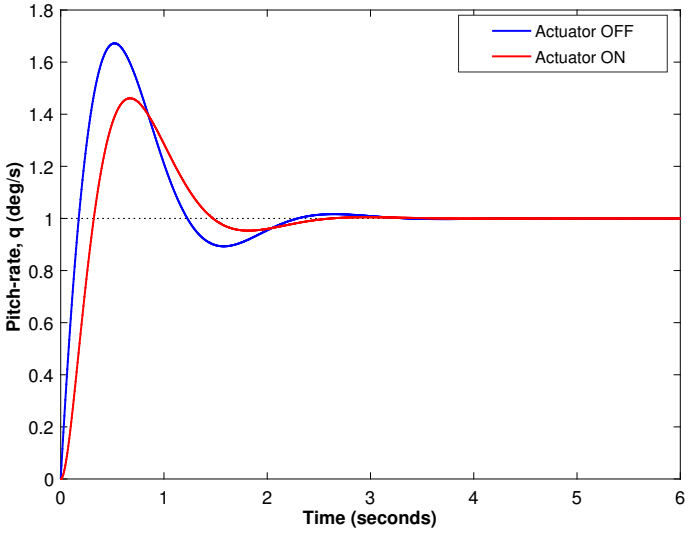

Figure 4.22: New RCAH pitch-rate response to a step input at 75 mph

The short-period response of the new RCAH pitch-rate to a 1-deg step input is shown in Figure 4.22. The figure shows that the new feedforward gain also improves the overshoot of the pitch-rate response, but maintaining the settling time close to the previous RCAH setting. Hence, considering the new changes of the feedforward gain **Q** for all selected design points, the new gain scheduling matrices for all flight conditions can be written as

$$\begin{aligned}
K_1 &= \begin{bmatrix} -0.0107 & 0.1224 & 0.2140 & 0.1372 \end{bmatrix} \\
K_2 &= \begin{bmatrix} -0.0168 & 0.1671 & 0.4078 & 0.1897 \end{bmatrix} \\
K_3 &= \begin{bmatrix} -0.0207 & 0.1957 & 0.5691 & 0.2249 \end{bmatrix} \\
K_4 &= \begin{bmatrix} -0.0306 & 0.2557 & 0.8301 & 0.2650 \end{bmatrix} \\
K_5 &= \begin{bmatrix} -0.0388 & 0.3469 & 1.6352 & 0.3072 \end{bmatrix}
\end{aligned} \tag{4.3.23}$$

These finally give a new gain plot for the new RCAH adjustment for the whole flight regime, as shown in Figure 4.23.

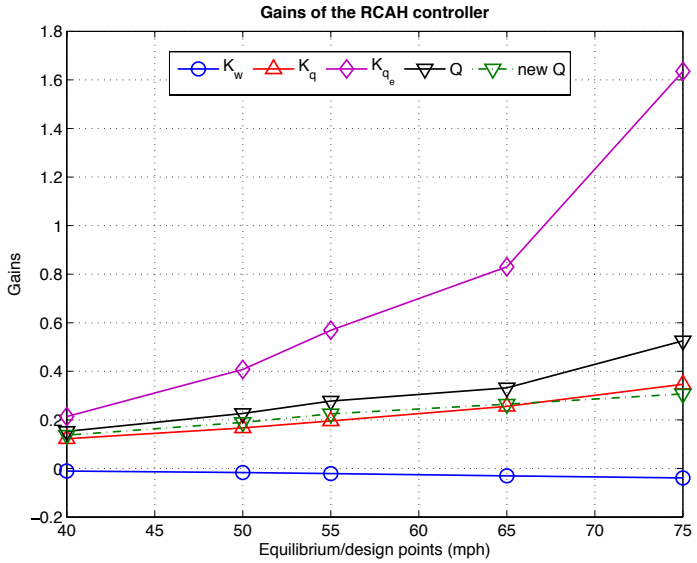

Figure 4.23: New RCAH gain plots for all flight regime (with default actuator)

4.4 Chapter Summary

The flying qualities performance evaluations of the linear model G-UNIV autogyro have been done according to the new flying qualities requirements developed in Chapter 2. It was found that the bare airframe model (or the open loop model) of the G-UNIV autogyro indicates a non-compliance with the proposed flying qualities requirements. The flying qualities performance of the open loop model can be summarised in the following;

a) The short-period mode revealed a non-compliance according to the time-domain and the frequency-domain criteria of the evaluation. According to the performance evaluation, the open loop model of the G-UNIV exhibits a stable, but yet, a lightly damped short-period oscillation across the flight speeds. On the other hand, the frequency bandwidth of the open loop model exhibits a non-compliance in which the analytical interaction between the phase-bandwidth and the gain-bandwidth indicate a PIO-prone condition, especially at higher airspeeds.

b) The phugoid mode of the open loop G-UNIV model revealed the worse case scenario. According to the performance evaluation, the open loop phugoid mode

yields unstable oscillations, especially at lower airspeed regime, and a marginally stable at higher airspeed regime. In general, the open loop phugoid mode exhibits a Level 3 flying qualities performance.

Due to these poor longitudinal flying qualities performance, the necessary steps to implement the control enhancement for the vehicle have been made accordingly. The implementation of the control enhancement started with the implementation of the Stability Augmentation System (SAS) for the G-UNIV, which can be summarised in the following;

a) The first control strategy was to apply pitch-rate feedback for the augmentation system, which is considered as the most simple and straight forward technique used for SAS. This pitch-rate feedback only resulted in the improvement of the pitch damping, but with unsolved bandwidth issues.

b) The second strategy was to apply the 'blended feedback' where both short-period mode state output variables were fed back as the closed-loop augmentation. The pole-placement technique was applied in this case which resulted in the value of blended feedback gain obtained. This technique is shown to be able to improve the pitch damping and the bandwidth response according to the respective requirements.

c) Executing the state feedback matrices obtained from (b) into the full order model did not significantly improve the phugoid mode, which requires for another control strategy to be performed. Implementing the speed damping through engine throttle control was not feasible as an additional input would cause the whole system to become MIMO, which could violate the simplicity of a 'light autogyro' configurations.

Hence, the Rate-Command Attitude Hold system was introduced to give a higher priority for the pilot to have better control of the aircraft manoeuvre. For the autogyro case, the pitch-rate RCAH was implemented, and the same pole-placement technique was used to find the respective state feedback gain matrix that will comply with the desired flying qualities characteristics. In this particular pitch-rate RCAH, the PI controller with an additional feedforward gain was introduced. The simulation results generated through this control strategy were also promising. The simulation results show not only good pitch-rate tracking response to the pilot pitch-rate command but also improved the short-period and phugoid damping respectively.

It can be concluded that theoretically, the automatic control enhancements developed

in this chapter have met the objective of the chapter. The flying qualities performance of the G-UNIV autogyro used in this research was quantified and evaluated according to the proposed flying qualities criteria in Chapter 2. It has also been proven in this chapter that the flying qualities performance of a typical light autogyro managed to be improved using flight control enhancement. However, the flight control enhancement developed in this chapter is considered as a preliminary as the control enhancement model being developed does not include the actual hardware configuration. The actuator, by default, was represented by a simple first-order dynamics with a frequency of 20 Hz throughout the chapter. Therefore, it is important to find an actual hardware to be implemented in the control enhancement, so that the augmentation system would be more reliable and producing more realistic flying qualities improvement. The investigation on the control hardware requirements will be carried out in the following chapter.

Chapter 5

Control Hardware Requirements

5.1 Introduction

Initial flying qualities evaluation was performed on the longitudinal dynamic stability of the bare airframe G-UNIV autogyro, which also led to the development of the control enhancement of the vehicle in Chapter 4. Even though the flight control strategies were proven to be theoretically successful, there is no guarantee that the implemented control strategy will also be successful when it comes to the practicality of the implementation on the real aircraft. Several issues were raised including whether the assumptions that had been made earlier are practical, such as the dynamic response of the servo-actuation and the dynamic of the sensors to be used. Since the ultimate goal of this research is to improve the flying qualities of the said vehicle through control enhancement, it is then a necessity to look into the practical issues of implementing the control enhancement.

One important issue to put into the perspective of a controller is how long does it take for the actuator to actually move when a command signal is sent from the controller. If the exact dynamics of the actuator and its control link mechanism are known, the control strategies of the controller can then be adjusted accordingly, and good flying qualities can be achieved. Therefore, the strategy of this chapter is to look into the hardware requirements for the controller to be implemented on the G-UNIV autogyro. This can be done, firstly, by looking into any real servo-actuators to be used according to the basic control requirements that were previously set, such as the response bandwidth, the damping ratio and overshoots. Secondly, once the suitable servo-actuator has been chosen, the dynamic actuation of the actuator can be modelled to obtain the

transfer functions.

Finally, the transfer functions of the real actuator can be put into the autogyro model, and the whole flight performance can be evaluated and adjusted.

Another important aspect of the control mechanism that has to be accounted for, is the mechanical control linkage of the vehicle. An autogyro is a unique flying vehicle, of which, every mechanical actuation from the pilot stick involves a series of axial and rotational translations of control linkages. Each component has to be considered as a rigid body having mass and dimension, and therefore, the dynamic model of this control links must also be obtained and included in the control system to ensure proper accuracy in the mechanical displacement, thus the flight performance.

Therefore, the strategies of this chapter are to model both, the servo-actuator control, and the mechanical control link for the G-UNIV autogyro. It is expected that a full order transfer functions that involve both dynamic models will be obtained and implemented into the G-UNIV automatic flight control system.

5.1.1 Electrically-Driven Actuator

In early days of flights, the manoeuvre of an aircraft was done through a purely mechanical actuation from the pilot control yoke or stick to the control surfaces. As aircraft systems are becoming more and more complex, with the increase in aircraft size, having a full mechanically powered controls, correspondingly increase the liability of the aircraft in terms of the reliability and cost effective. As such, the requirements of having powered flight control with power actuators have become more apparent [122].

There have been several electrically driven power actuators introduced in aviation industry such as the Electro-hydrostatic Actuators (EHAs) and the Electro-mechanical Actuators (EMAs). The development of these actuators have been made, as early as the days since powered actuation was first introduced [123]. For the EMAs, the early implementation was very much hindered due to some issues with mechanical jamming and heating, which eventually affecting flight safety [122].

More studies and improvement have been done in the past decades to implement EMAs for power actuation, especially in modern aircraft. Boeing and Rockwell, for instance, have conducted a feasibility study of implementing EMAs in wide-body commercial aircraft [124]. This is then followed by some studies on the same objective, until Norton

[125] have successfully tested the advanced electro-mechanical actuation system on a modified U.S. Air Force C-141A aircraft in 1986. The overall results were testified the reliability of the EMAs being used, similar to the normal hydraulic powered actuator.

The EMAs was initially introduced on aircraft as part of the effort to reduce the cost of maintaining hydraulic powered aircraft. There have been factors that lead to more demand of employing EMA as the main actuator in flight, which also lead to more studies were done in perfecting the design and acceptance to be used as the main actuator on board. One of the factors is the new aircraft concept called 'More Electric Aircraft' (MEA), which introduced more electrical functions on board rather than mechanical, including the flight actuation system [122, 126–131]. In fact, studies have also been made in the positive effect of employing EMA actuators in the MEA aircraft. Employing the EMA manage to reduce the total weight of the aircraft and increase its efficiency, compared to the EHAs [130].

For a light aircraft, the control hardware mechanism is less complex and more simple compared to bigger or wide-body aircraft, which is due to weight limitation. If a powered actuator is required to be used on a small aircraft, the weight limitation will become part of the priority for the design requirements. This weight limitation is essential especially for a light autogyro as the implementation of power actuator must not violate the underlying attributes the aircraft was built for, in terms of simplicity and the cost of maintenance. Hence, EMA is found suitable for light autogyros power actuator due to the weight advantage as mentioned above.

5.1.2 Design Limitations

It is important to note that the actual G-UNIV autogyro was no longer exists in the premise when this study is conducted. As such, the actual geometrical locations and dimensions of the mechanical control links, including the type of material being used were not known. For this reason, in order to establish the dynamic model of the control linkages, assumptions were made for all variables that require geometrical positions and dimensions.

Moreover, other significant hardware data, such as the battery and alternator's capacity, the geometrical location of the battery and other electrical hardware were also not available. This situation also contributes to another limitation, which is the CG changes of the vehicle if modifications are being made. For this reason, the CG changes due to modifications will not be accounted for the vehicle's dynamic behaviour. Thus,

in any circumstances, the vehicle will always fly with the default values. It is also worth mentioning that any hardware would be expected to be of low cost “off-the-shelf" and not at the“high-tech" end of the spectrum.

5.2 Assumed Design of the Control Hardware

5.2.1 Load Estimation of the G-UNIV Linkages

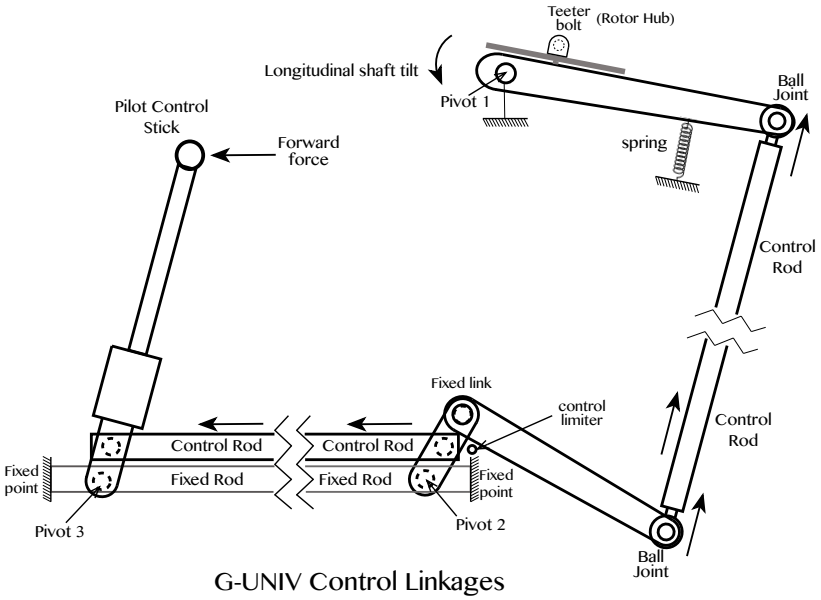

Figure 5.1: Mechanical control linkages of G-UNIV autogyro

Figure 5.1 shows the approximate mechanical control linkages diagram of the bare airframe G-UNIV light autogyro in longitudinal flight mode. The linkages consist of at least three mechanical links including the pilot control stick. The arrow shows the direction of the force applied on the pilot control stick and the effect of the stick control to the longitudinal shaft tilt (θ_s), which directly contribute to the pitch manoeuvre of the vehicle. A forward push of the control stick will cause the horizontal control rod to move forward and produces a negative longitudinal shaft tilt as shown by the arrows. Conversely, a backward pull of the control stick causes a positive rotor disc tilt for a nose-up condition. The tensioner spring attached to the rotor shaft link as seen in the figure is an adjustable spring which has two proposes: To continuously hold the longitudinal shaft link backwards for a positive airflow through the rotor-disc, and as a trim setting mechanism in the forward trimmed flight of the vehicle. Currently, the trim setting is made by adjusting the spring tension to allow for a certain extension to be

applied on the spring in specific flight speed. This also affects the control stick condition in trimmed flight where less pilot force is needed to hold the stick in trim position. Since the spring is attached to the longitudinal shaft link, the trim adjustment has to be done manually on the ground, and the correct trim setting can only be confirmed through flight tests.

The stability and control enhancement through automatic flight control system for this autogyro can be done by having the correct hardware for the control mechanism. The most important hardware item is the servo mechanism that acts as the control actuator for the augmentation system. The correct requirement in terms of force or torque of the servo-actuator has to be known, depending on the location where the servo will be installed along the mechanical linkages. Hence, it is then important to estimate the forces exerted along the control linkages due to the rotor hub forces during flight.

Since the control linkages illustrated in Figure 5.1 consist of several links with different lengths and translations, rigid-body analysis can be made to estimate the forces and moments applied to the linkages. The instantaneous forces at trim flight conditions are considered for the calculation where forces and moments exerted along the linkages are in equilibrium. Considering a 2-dimensional system for the longitudinal mode, the sum of forces and moment in equilibrium flight are given by

$$\begin{aligned} \sum F_x &= 0 \\ \sum F_z &= 0 \\ \sum M &= 0 \end{aligned} \tag{5.2.1}$$

The rigid-body analysis can be done for each control link through the free body diagram approach, in which, each rigid body translates and rotates under the influence of the individual force connected within the link.

For the G-UNIV control link, Link 1 is the first to be considered where the force F_{12} is estimated due to the rotor hub forces F_{hub}, as shown in Figure 5.2.

In equilibrium flight, the moment about point O_A is given by

$$M_{O_A} = -M_{F_{hub}} + M_{F_s} + M_{F_{12}} = 0 \tag{5.2.2}$$

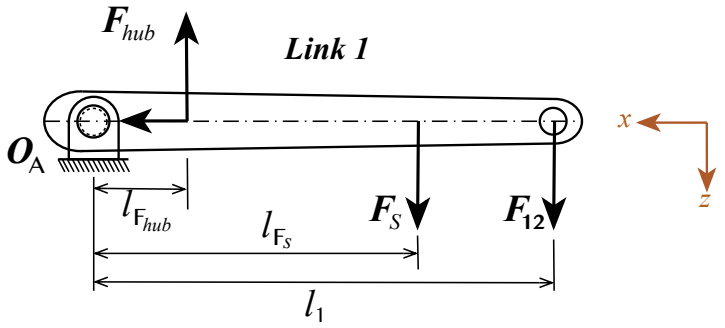

Figure 5.2: Free body diagram of control link 1

For consistency, the (+ve) and (−ve) sign used in the moment calculations are based on the same standard convention used for the autogyro model. In equation (5.2.2), M_{F_s} is the moment due to the spring force F_s, and $M_{F_{hub}}$ is the moment due to the rotor hub forces F_{hub}, which was previously obtained from the rotor model. Since there is no exact data of the G-UNIV autogyro's tensioner spring, the amount of spring force F_s is based on the estimation of spring stiffness (k) and the extension length of the spring (Δl_s) for an estimated amount of pilot control force F_p at trim condition. The spring force can be written by

$$F_s = k\,\Delta l_s \tag{5.2.3}$$

Hence, the instantaneous force F_{12} of Link 1 can then be obtained by the summation of the scalar multiplication of each force member and its length according to equation (5.2.2).

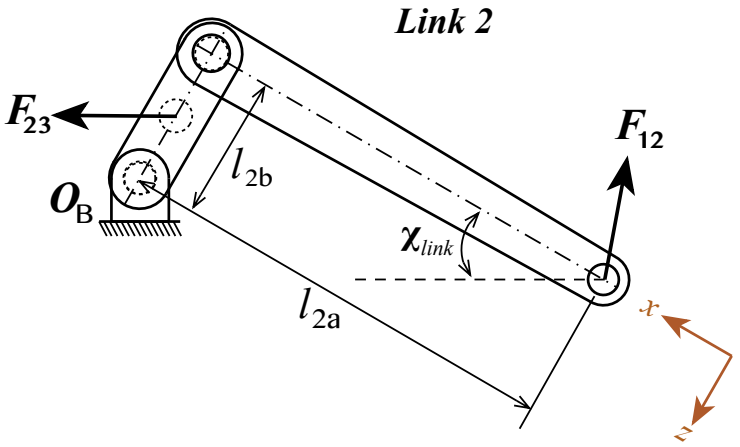

Figure 5.3: Free body diagram of control link 2

The estimated force F_{12} of Link 1 is translated into Link 2 through a 2-force member

with a certain angle of translation. The forces exerted within Link 2 can also be estimated by considering a free body diagram of Link 2 as shown in Figure 5.3. As such, the instantaneous value of the angle χ_{link} has become part of the estimation for the force F_{23} exerted at the other end. Hence, from the free body diagram of Link 2, the moment about point O_B in equilibrium flight is given by

$$M_{O_B} = -M_{F_{12}} - M_{F_{23}} = 0 \tag{5.2.4}$$

where the moment $M_{F_{12}}$ is already known from the previously obtained force F_{12} of Link 1. The horizontal force F_{23} of Link 2 can then be obtained through the same scalar multiplication of force and length according to (5.2.4).

Finally, the control stick force estimation can be done similarly, since Link 3 is attached to Link 2 through another 2-force member as shown in Figure 5.1. Considering the free body diagram of Link 3 as shown in Figure 5.4, the moment about point O_C of Link 3 in equilibrium flight is given by

$$M_{O_C} = -M_{F_{23}} - M_{F_P} = 0 \tag{5.2.5}$$

Applying the same method for the previous two links, the instantaneous force exerted at the control stick (F_P) due to the rotor hub forces in equilibrium flight can be estimated from equation (5.2.5).

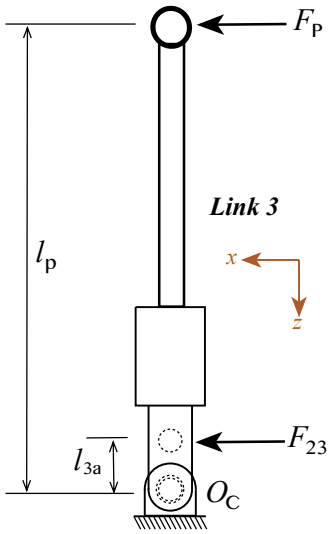

Figure 5.4: Free body diagram of control link 3

Table 5.2.1 shows the estimated value of forces for all three links in equilibrium flight condition for different trim airspeeds. Note that the spring stiffness (k) is fixed in a way that the spring will be expanded to a specific length according to the longitudinal

shaft tilt (θ_s) in trim flight.

Table 5.2.1: G-UNIV mechanical linkage forces (estimated)

Forces	40 mph	50 mph	55 mph	65 mph	75 mph
Spring Expansion [m]*	0.015	0.020	0.025	0.035	0.040
F_{12} [N]	212.1	207.6	203.2	194.3	189.3
F_{23} [N]	1179.9	1157.3	1134.1	1087.6	1061.6
F_P [N]	59.0	57.9	56.7	54.4	53.1

*Spring Stiffness, $k = 1000$ N/m

Table 5.2.1 also reveals the biggest force were exerted between Link 2 and Link 3. This is due to the short moment length for the forces being applied between the horizontal two-force members. If the servo-actuator is to be employed between these horizontal two-force members, the output force requirement of servo-actuator would also be high. It is also important to note that these force values were estimated according to the equilibrium flight condition where the sum of forces and moment within the linkages are zero. As such, these estimated forces can be considered as the minimum force required for the servo-actuator, as the value would definitely be higher in other flight circumstances especially in abrupt manoeuvres.

The table also suggests that the forces along all three links are bigger at lower flight speeds and smaller at higher flight speeds. This can be seen as the force exerted throughout the linkages relatively changes with the change of longitudinal shaft tilt, θ_s. At lower flight velocity, more aft tilt of θ_s to create more lift to maintain the vehicle in airborne condition, thus creating bigger rotor hub forces.

It can be seen that the force applied to the control stick causes 20 times bigger force at the horizontal two-force member, and denoted with a ratio of 1 : 20. This force is then reduced to 5.6 times smaller at the longitudinal shaft link, before being transferred to the rotor hub to compensate the hub forces. Hence, it can be concluded that the mechanical linkage of the G-UNIV autogyro is estimated to have the stick-to-hub force ratio of 1 : 3.6. This also means that a 1-Newton pilot stick force will cause a 3.6 Newton force at the rotor hub, and conversely from the rotor hub to the pilot control stick.

5.2.2 Modelling the G-UNIV Control Link

It is important to understand how the fundamental control linkage of the G-UNIV works to determine or estimate the value of forces and moments exerted at each control link for each control input. The dynamics of the G-UNIV control linkages in Figure 5.1 can be modelled using the common rigid-body dynamics with their differential equations. Since the whole mechanical linkages consist of many inter-related moving parts and joints, the system is then considered as a multi-body dynamics system. This type of dynamics can be modelled with the common Matlab and Simulink environment, but the derivation of the equations of motion is somewhat tedious with many stages of rigid-body dynamics and prone to error.

The multibody modelling task has now become simpler with the Simscape™ Multibody™ Link environment without the need to derive any of the multi-link dynamic equations. Formally known as 'SimMechanics', the 'Simscape Multibody' is a special tool used for physical modelling simulation. This tool runs under the Simulink™ environment and commonly used in mechanical systems modelling of multibody systems [132–136].

The only drawback of the Simscape Multibody model is the longer simulation run-time, compared to Matlab and Simulink. This is because, Simscape block-sets are governed by the "higher index" Differential Algebraic Equations (DAEs) rather than the Ordinary Differential Equations (ODEs) used in Simulink. For a multibody simulation, DAEs calculations are reduced to ODEs within the computing environment to enable the calculation to be performed through Simulink [133]. This CPU run-time delay, however, is becoming less significant when considering the time required to model a multibody dynamics with the conventional way.

5.2.2.1 Simscape Multibody Modelling of the G-UNIV Control Link

The Simscape™ Multibody™ Link (SML) is a specialised tool within the Simscape Multibody that enables a CAD model to be exported and translated into Simscape physical model and then calculated under the Simulink environment [137]. This important tool enables any multibody dynamics to be visualised in its actual form and dimension in the CAD drawing and then exported into Simscape™ physical model so that the dynamic behaviour can be quantified and further analysed. The SML tool will first generate an XML file of the CAD drawing with all the detail geometry and material properties of each part of the multibody structure, which is later translated

into Simulink environment. The final output of this translation tool is the equivalent model of the CAD model in the form of block-sets. Each one of the block-set represents a single solid and rigid part of the CAD model, which includes the geometry and rigid transformation of the solid parts.

For the G-UNIV mechanical control links, the CAD model of the basic control links has been developed based on the static analysis diagram in Figure 5.1. A free educational license cloud-based CAD application called *Onshape*® (www.onshape.com) is used to develop the CAD model of the control linkages as shown in Figure 5.5.

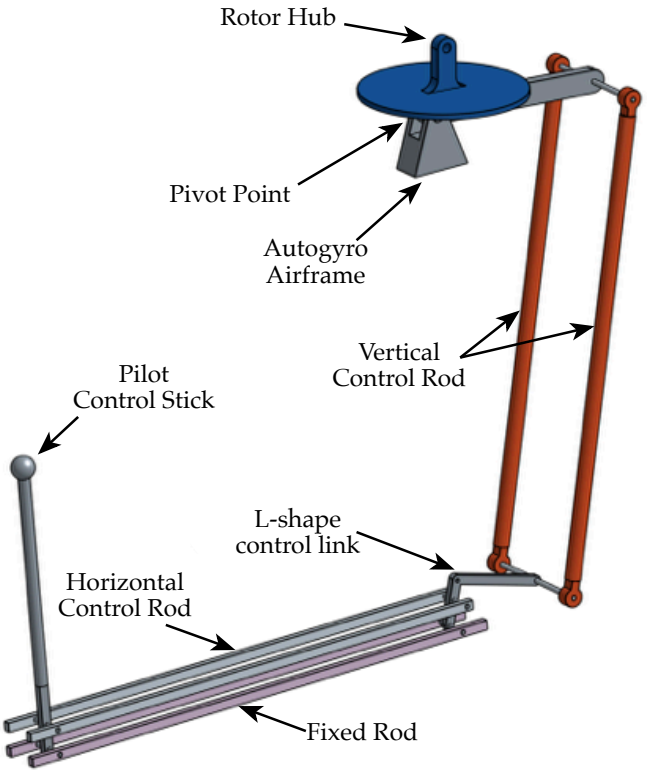

Figure 5.5: Assembly drawing of G-UNIV BASIC control linkages

The Simscape Multibody blockset of the basic control link model are shown in Figure 5.6. Each one of the blocks represents a rigid part and joint that involved in the model where the transformation from one axis to another is also included. The material properties data and the geometry of each part are also carried within the block. The 'Solver Configuration' block is used to specify the local solver configuration of the multibody system. The global Simulink solver is always set as the default solver which can be used in the Simscape physical model simulation.

In some circumstances, a local solver can be specified depending on the nature of the dynamic response of the particular system, whether to have fixed-step or variable-step

solver. The system's gravity is specified in the 'Mechanism Configuration' block. For the G-UNIV control linkage application, the gravity is set to [0 0 -9.81] ms^{-2}. The orientation between two different elements or frames is defined as a fixed 3-D rigid transformation in the 'Transformation' block. Here, the different orientations can be in the form of rotational or translational transformation. The 'World' frame is set as a fixed frame outside of the particular multibody system and used as the reference frame for all multibody orientations. Further detail functionalities of the Simscape Multibody can be referred to the product's User's Guide [137].

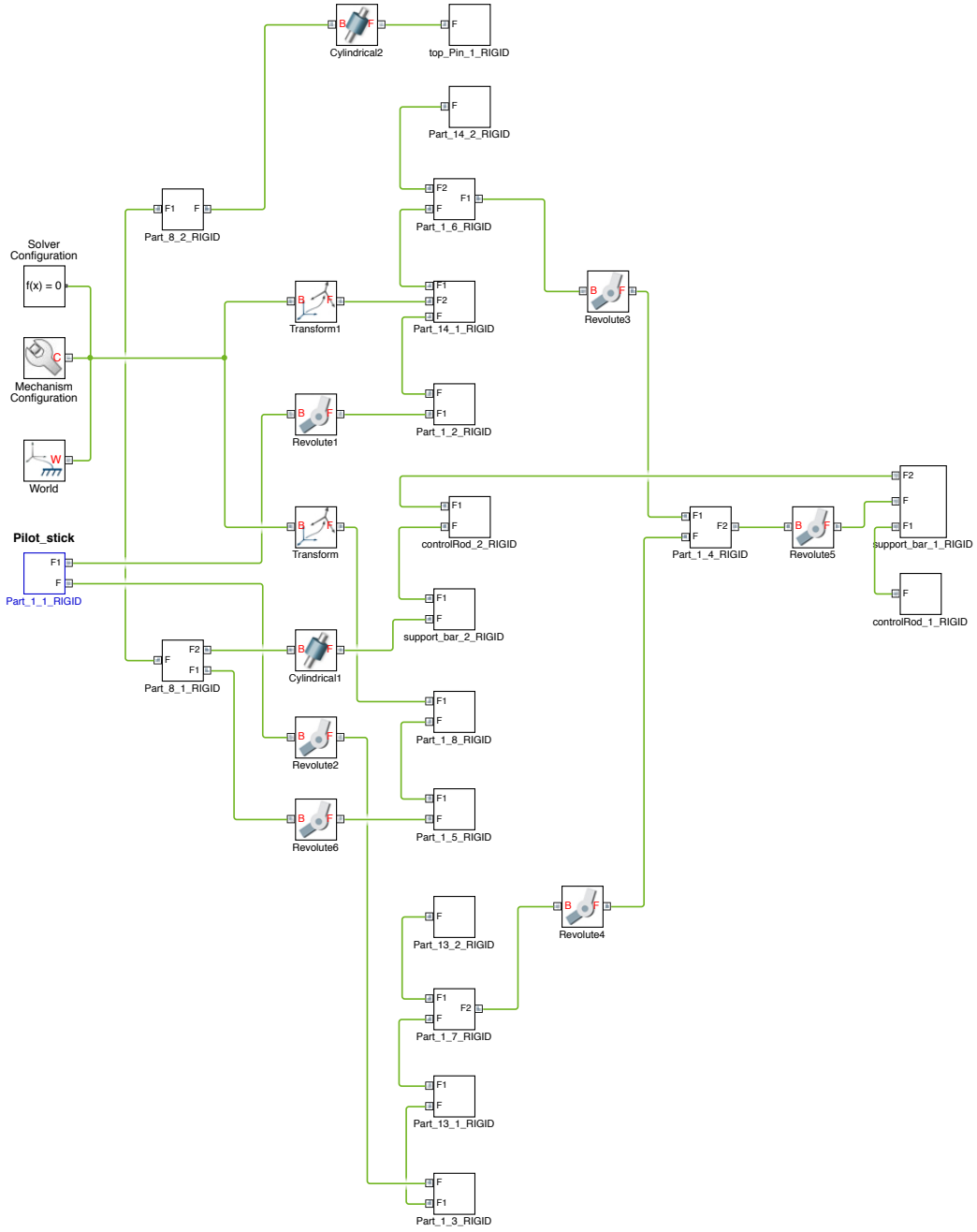

Figure 5.6: Simscape Multibody model of G-UNIV mechanical control linkages

The full physical model blockset in Figure 5.6 can be grouped and simplified into several sets of blocks according to their physical location within the linkage to ease in further analysis. The simplified blockset is shown in Figure 5.7.

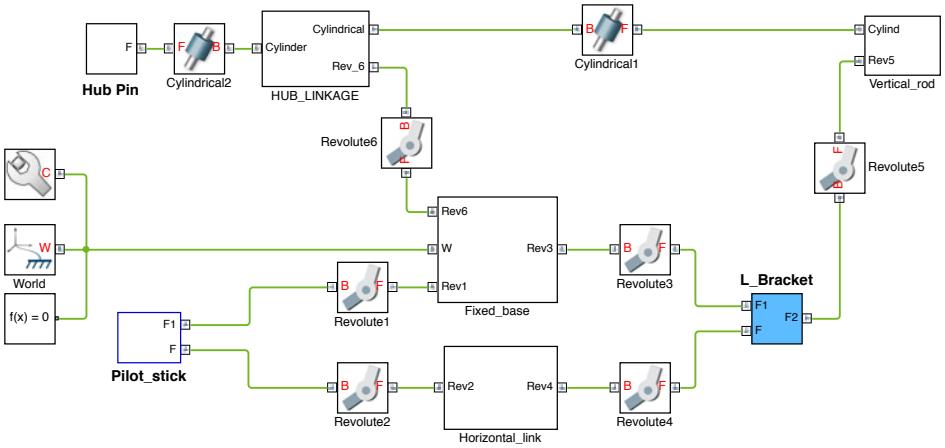

Figure 5.7: G-UNIV basic control schematic in simplified form

The simulation result of the physical multibody model is run and displayed in the 'Mechanics Explorer' in the form of a visual 3-D. Figure 5.8 shows the visual result of the G-UNIV basic control links simulation. Without external force or moment acting on the physical multibody model, the rigid parts of the model will be seen swinging freely around their revolute and cylindrical joints, unless certain damping coefficients are set to represent frictions within the joints.

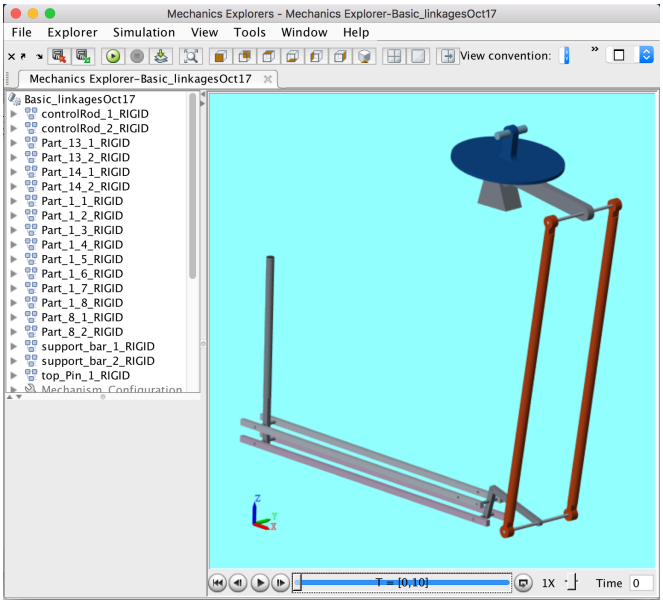

Figure 5.8: 3-D simulation result of the G-UNIV basic control link

The next step is to develop the servo-actuation model to be implemented into the physical model of the G-UNIV control linkages so that the control enhancement that was developed in Chapter 4 can be performed.

5.2.3 Locating the Servo-actuator Unit

There are at least two possible locations where the servo-actuator can be placed within the control linkage (see Figure 5.1); To place horizontally along the horizontal control rod, or to place vertically along the vertical control rod.

The only advantage of choosing the second option is the smaller force required to move or to deflect the control shaft, compared to the first option (see Table 5.2.1).

However, for this option, two servo-actuator units are needed, which is due to the space restriction on the vehicle's airframe and the shaft tilting mechanism that requires two servo-actuators to be used, as shown in Figure 5.9. Having two servo-actuators in this vertical height will obviously contribute to more restrictions such as weight and changes of CG location during flight manoeuvre.

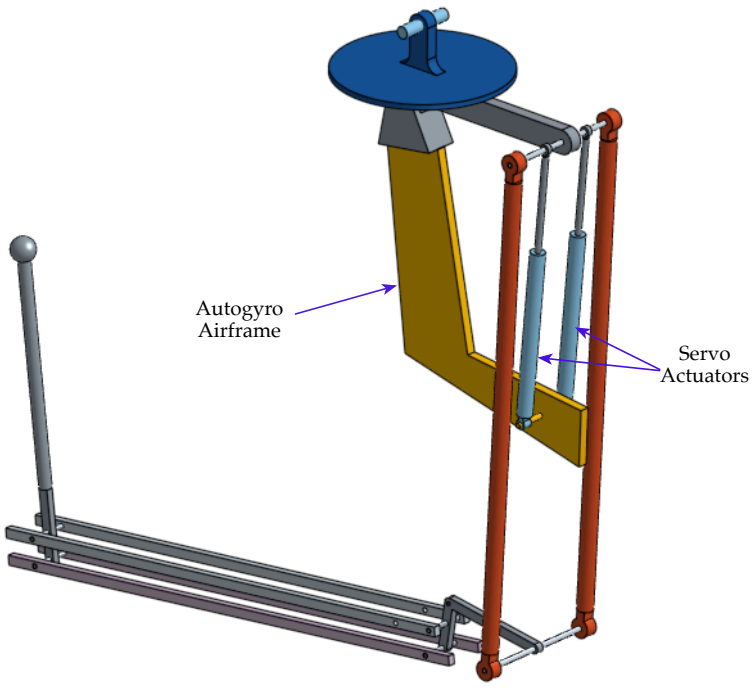

Figure 5.9: Two unit servo-actuator vertically positioned at vertical airframe

According to the estimated forces at equilibrium flight condition listed in Table 5.2.1, the highest force is required at the horizontal control rod compared to other control links. Should a linear servo-actuator is to be installed in horizontal position, the only challenge is to find a suitable linear actuator that could deliver the significant amount of linear force for the actuation. This, however, is still manageable as the G-UNIV autogyro is an experimental type aircraft that allows for any necessary modification to be made according to the research objective. Therefore, having the linear actuator located within the horizontal control link is now considered as the best option.

The CAD model developed for this new actuator configuration is shown in Figure 5.10. It is expected that there will be a slight change in the overall CG location with the new configuration.

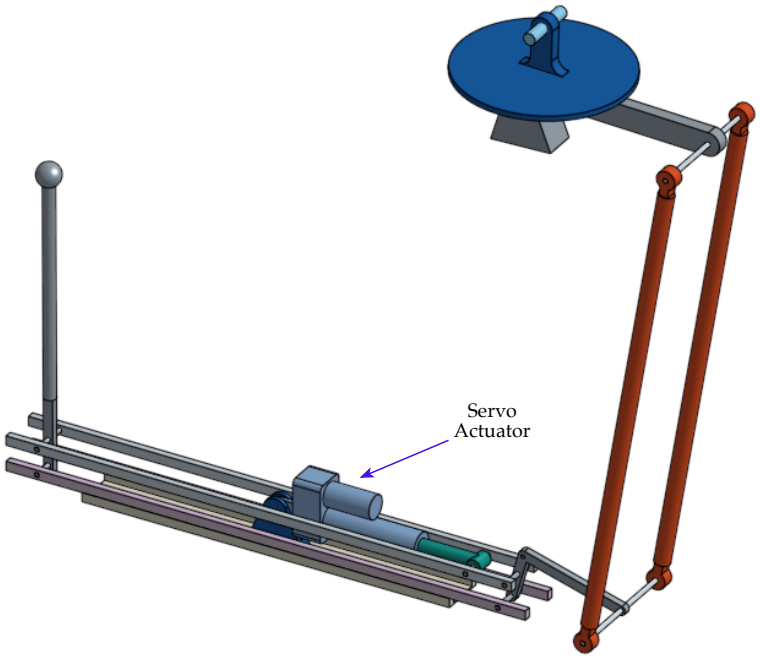

Figure 5.10: A servo-actuator horizontally positioned at the airframe base

5.2.4 Electro-Mechanical Actuation Model

The following section describes the modelling of the servo-actuation model. The EMA system in the research is modelled in two separate modules: The DC Motor module and the Linear Actuator module. In reality, these hardware modules are combined to form a linear actuator. The DC motor acts as the source of torque, which is electrically

driven according to the amount of input voltage and current. The linear actuator acts as the slave according to the torque action of the DC motor.

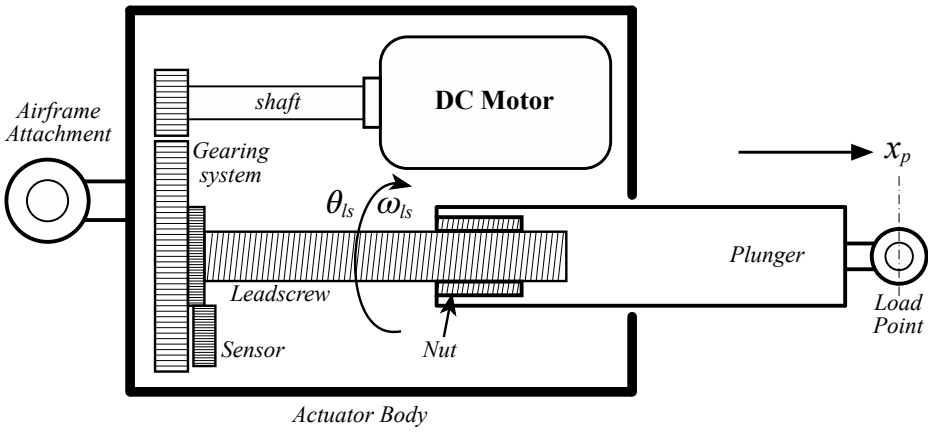

Figure 5.11: General construction of a typical linear EMA

Figure 5.11 illustrates a typical linear EMA which consists of the DC motor (usually a BLDC motor) and linear actuator built in one housing. The shaft torque produced by the DC motor is translated into linear force action through a direct link between the gearing system and the leadscrew. Consequently, the linear force applied through the plunger is caused by the screw action between the leadscrew and the plunger nut.

5.2.4.1 DC Motor Modelling

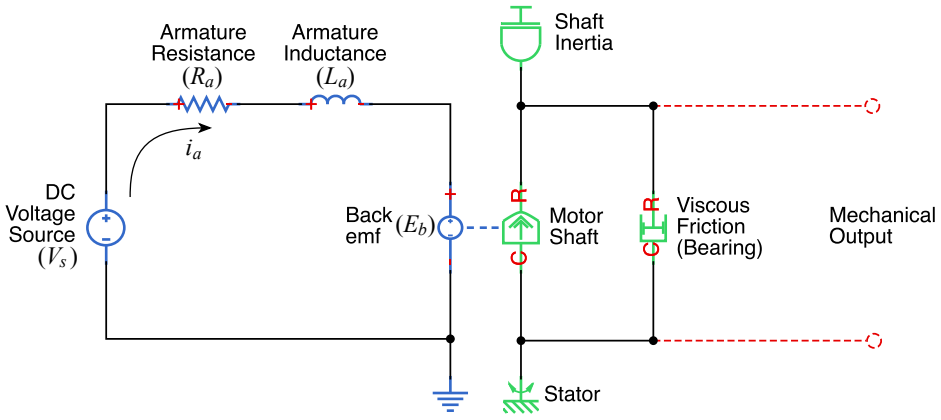

Figure 5.12: DC motor schematic with Simscape

Figure 5.12 shows a simple schematic diagram of a typical DC motor, which consists of two different elements: The electrical element (shown on the left), and the mechanical element (on the right). A full description of the DC motor principle and mathematical modelling is described in Appendix D.1.

The DC motor blockset used in the Simscape™ physical modelling package (Figure 5.12) is assumed to be an ideal system with maximum power transfer between the two elements without power loss. This assumption was set as a default for the Simscape blockset to ease in the calculations, where the derivation of the DC motor model is described in Appendix D.1. Thus, the power dissipation of both electrical and mechanical elements are equal and can be written as

$$P_e = P_m \tag{5.2.6}$$

which can be solved according to equation (D-10) and (D-8) of Appendix D.1 as

$$\begin{aligned} E_b\, I_a &= T_m\, \omega_m \\ K_e\, \omega_m\, I_a &= K_t\, I_a\, \omega_m \\ K_e &= K_t \end{aligned} \tag{5.2.7}$$

Hence, with this 'no power loss' assumption between the electrical and the mechanical element, the *back-emf constant*, K_e and the *torque constant*, K_t are assumed to have the same value if these units are normalised into SI units. It is important to note that the standard unit for K_e is $Volts/(rad/s)$, while K_t is given by $Nm/Ampere$. These are simply understood as the size of angular speed achieved with the input voltage, and the size of torque created with the amount of armature current (input current).

The Exlar GSM20 in Table 5.2.2, for instance, is one of the 'of-the-shelf' DC motor product used in this study with the given $K_e = 35.5\, V/krpm$, which is equivalent to $0.59\, V/(rad/s)$ in SI unit. On the other hand, the K_t of the same motor is given by $K_t = 5.2\ lb\, in/A$, which is equivalent to $0.59\, Nm/A$ in SI unit. Since the transition between the electrical and the mechanical element is assumed to happen without power loss, the numerical figure is expected to be the same.

Therefore, from Appendix D.1, the transfer functions of the DC motor's shaft angular velocity and position due to the amount of input voltage are given by

$$\frac{\omega_m(s)}{V_s(s)} = \frac{K_t}{(L_a s + R_a)(J_m s + B_m) + K_t K_e} \tag{5.2.8}$$

$$\frac{\theta_r(s)}{V_s(s)} = \frac{K_t}{s\big[(L_a s + R_a)(J_m s + B_m) + K_t K_e\big]} \tag{5.2.9}$$

5.2.4.2 DC Motor Model Simulation

The initial goal of the chapter is to choose a suitable real aircraft servo-actuator model to be implemented in the G-UNIV control enhancement. However, this is not possible as the manufacturer datasheet of a real aircraft servo-actuator is not accessible over the public domain, which is due to propriety restriction.

Alternatively, three industrial-type servo-actuators of different manufacturers have been selected to be modelled, of which the manufacturer's datasheets are available over the public repositories; the *Exlar-GSM20* from Exlar Corporation [138, 139], the *Lo-Cog 9234S004* from Pittman Inc. [140], and the *M1453L* from Parker Inc [141]. The basic parameters of the three motors according to their manufacturer's datasheet are listed in Table 5.2.2.

Table 5.2.2: Servo motor parameters of different manufacturers

Motor Parameter	Unit	Model		
		GSM20	9234S004	M1453L
Torque Const., K_t	$lbf\,in/A$	5.2	0.59	–
	Nm/A	0.59	1.82×10^{-2}	0.775
Back-emf Const., K_e	$V/krpm$	35.5	1.91	81.16
	$V/(rad/s)$	0.59	1.82×10^{-2}	0.775
Rotor Inertia, J_m	$kg\,m^2$	8.77×10^{-7}	4.2×10^{-6}	1.6×10^{-3}
Viscous Damping, B_m	$Nm/(rad/s)$	–	2.6×10^{-6}	2.02×10^{-4}
Resistance, R_a	Ω	6.25	0.83	0.22
Inductance, L_a	mH	10.7	0.63	1.94
Max. Current, I_a	A	9.7	–	86.3
Cont. Current, I_a	A	3.4	–	28.78
Max. Rot. Speed, θ_m	RPM	5000	6151	3000

A uniform random voltage input of $\pm 12V$ is applied to the Simscape model of Figure 5.12 and then simulated, with all data from Table 5.2.2 being fitted. The instantaneous results of all important elements are quantified from the simulation and recorded in Table 5.2.3.

Figure 5.13 shows the simulation results of the Exlar GSM20 servo motor with the given input voltage V_{in}. Simulation results for the other two motors are put in Appendix D.2 for reference.

Table 5.2.3: Exlar GSM20 parameters at $t = 0.15\,sec$ (from simulation)

Instantaneous Values	Model		
	GSM20	9234S004	M1453L
V_s @ V_{in} (V)	10.1	10.1	10.1
V_{R_a} (mV)	36.242	215.313	59.985
V_{L_a} (mV)	28.676	−11.809	−941.714
E_b @ V_{emf} (V)	10.038	9.900	10.985
I_a (mA)	5.799	259.414	272.659
ω_m (rad/s)	17.014	543.940	14.174
θ_m (deg)	−61.3	-2.31×10^3	−47.3

The simulation results can easily be verified by using the steady-state values stated in the DC motor modelling in Appendix D.1. Instantaneous conditions at simulation time $t = 0.15\,sec$ is chosen as the steady-state condition to be verified as listed in Table 5.2.3. The Kirchhoff's Voltage Law (KVL) of the circuit in Figure 5.12 is verified by plugging the values of V_{R_a}, V_{L_a} and V_{emf} into equation (D-1). The result also shows that a small amount of resultant current I_a is used to drive the motor, which is due to the back-emf produced as the rotor shaft starts rotating. The faster the shaft rotates, the bigger will be the back-emf, thus smaller amount of armature current (I_a) is used to drive the motor in the steady-state condition. The shaft speed ω_m for all three motors are verified by plugging their corresponding back-emf E_b values into equation (D-10). Hence, the transfer functions of the Simscape simulation model are then obtained through the linear analysis tool of Simulink and written by

$$\begin{aligned} \frac{\omega_m(s)}{V_s(s)} &= \frac{6.287 \times 10^7\, s}{s^2 + 812.2s + 3.723 \times 10^7} \left[\frac{(rad/s)}{Volt}\right] \\ \frac{\theta_r(s)}{V_s(s)} &= \frac{3.602 \times 10^9}{s^2 + 812.2s + 3.723 \times 10^7} \left[\frac{deg}{Volt}\right] \end{aligned} \tag{5.2.10}$$

A comparison is also made to verify the Simscape Servo-motor model against manufacturer's data, as shown in Figure 5.14 [140]. The Pittman 9234S004 servo-motor was chosen since the manufacturer's plot of the angular speed and current versus the torque is available to be compared with the simulation model than the other two motors. Figure 5.14 also shows a good correlation between the manufacturer's plot and the plot produced by the Simscape simulation, which gives better confidence on the

newly developed Simscape physical model.

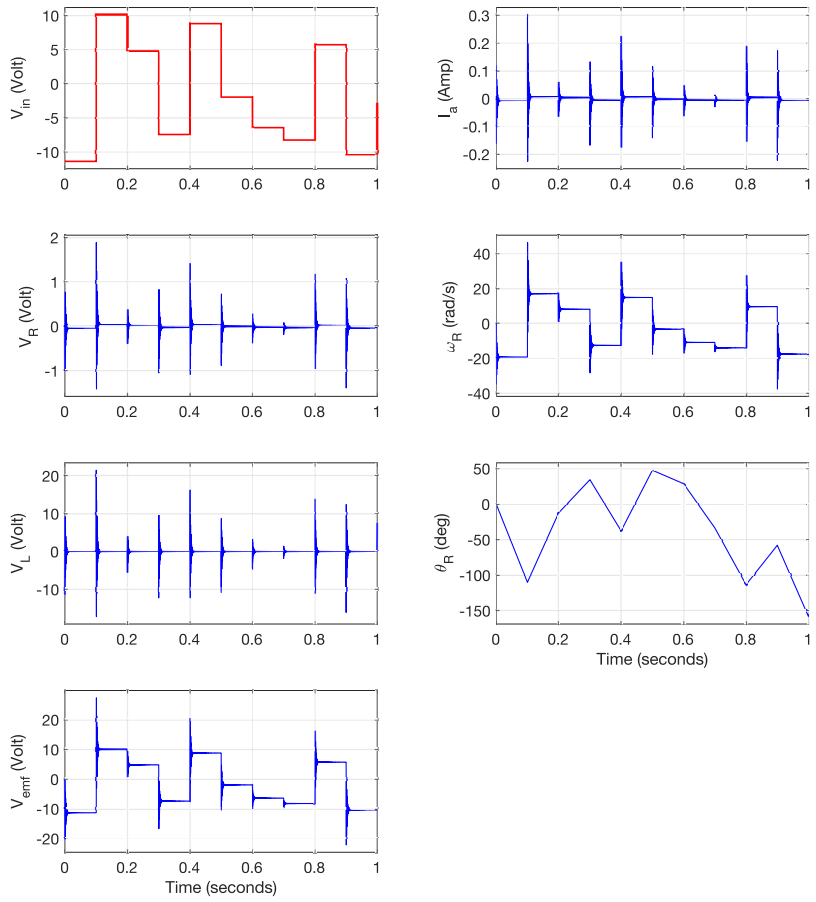

Figure 5.13: Exlar-GSM20 Simscape model simulation

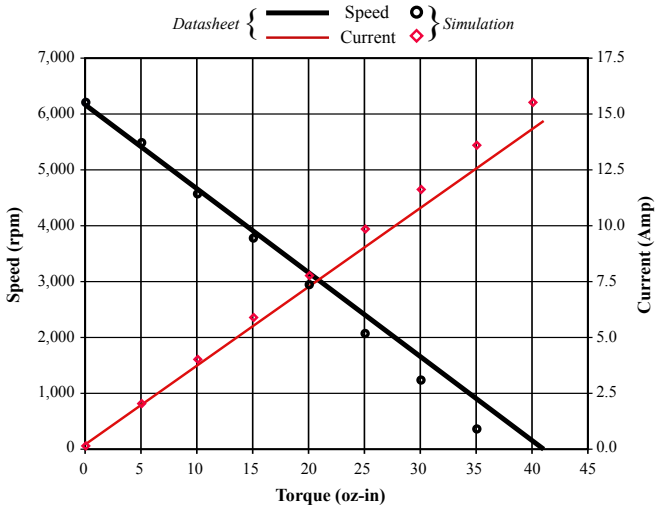

Figure 5.14: Manufacturer's Vs simulation plot of the Lo-Cog9234S004 DC motor

5.2.4.3 The Linear Actuation Model

The actuator shown in Figure 5.11 is a typical linear EMA used in most mechanical actuation applications. The linear speed and force of the plunger are transmitted from the angular speed and torque of the motor shaft through at least two stages of transmission; The gearbox transmission, and the lead screw mechanism. The gearbox changes the amount of speed and torque of the motor shaft according to the loading demand. The lead screw mechanism then translates this rotor speed and torque into a translational transmission to operate the load. For an autogyro case, the load is the aerodynamic force from the rotor hub, which is transmitted through control links. If the linear actuator is installed as a longitudinal control actuation in the G-UNIV autogyro, the plunger stroke of the actuator will directly produce the longitudinal shaft tilt (longitudinal control angle θ_s) of the autogyro.

Most linear actuators come with a transducer that acts as a position sensor that determines the linear extension of the plunger according to the screw rotations (see Figure 5.11). The feedback signal is fed back to the position control mechanism of the servo system so that the required linear position of the plunger can be achieved. The same feedback mechanism is also used to achieve the desired extension rate of the linear system, based on the motor shaft angular rate. It will be shown later that PID controllers are used for this purpose.

One common method used to model the dynamic behaviour of a linear actuator is by obtaining the equations of motion of the actuator in the rigid body form. The differential equations obtained for the model are then transferred into the Simulink environment and simulated. Du et al. [142] and Previdi et al. [143] have demonstrated the modelling of linear EMA with free-body diagrams, where the linear actuator is separated into individual parts according to their masses. The free-body diagram was used to study how individual parts interacted with each other with the existence of spring damping and stiffness between them. This method produces better accuracy in the dynamic behaviour estimation of the linear actuator but increasing the degree of freedom in the model.

Figure 5.15 shows the schematic of the rigid body diagram of the linear actuator dynamics. The free-body diagram of the screw mechanism is also shown. The θ_m represents the motor shaft rotation. The gearbox consist of a speed reduction gear with a gear ratio n_g, followed by a leadscrew or ball screw with a pitch ratio n_p, which represents the amount of linear extension per unit radian of rotation. The x_0 in the figure represents the linear position of the leadscrew, while x_p is the point where the load is attached

to, which also represents the linear extension of the plunger relative to x_0 according to the leadscrew rotation.

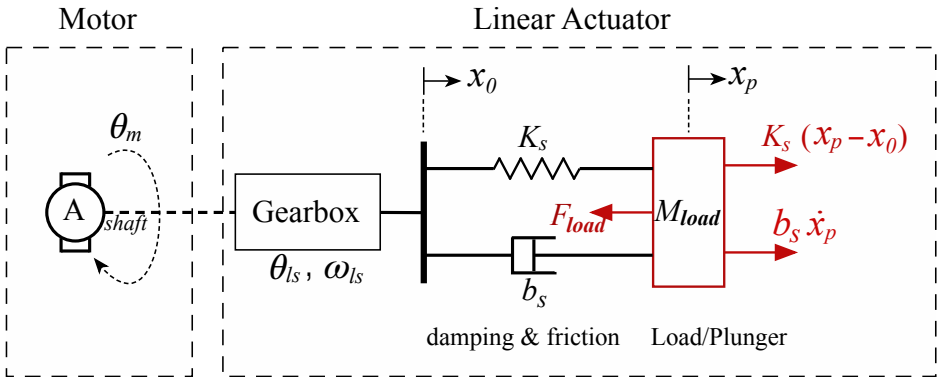

Figure 5.15: Simplified rigid body diagram of a linear actuator

The stiffness of the leadscrew is modelled as a spring with the coefficient K_s, and the viscous damping b_s gives the leadscrew friction. If a ball screw is to be used in this model, the viscous damping is then considered to be small compared to a normal leadscrew mechanism. The screw is made of a highly stiff material that whatever rotational changes of θ_m through the gearing system is then translated to an opposite reaction force of the screw that moves the plunger (load) in a linear form.

Hence, the dynamic behaviour of the load mass M_{load} that attached to the linear actuator can be defined by a second order differential equations and written as

$$M_{load}\frac{d^2x_0}{dt^2} - b_s\frac{d\,x_0}{dt} - K_s(x_p - x_0) + F_{load} = 0 \tag{5.2.11}$$

It is important to note that the viscous damping b_s in equation (5.2.11) is solely based on the given viscous friction of the actuator and does not include other types of friction such as Coulomb friction, as those values were not given in the manufacturer's product datasheet. These assumptions are made due to the non-linearities characteristics of those frictions, of which, to include into the modelling of the DC motor would be difficult [144, 145]. In fact, viscous friction is used in the model due to its linearity and easily to be modelled. Hence, excluding other frictions from the DC motor model would not significantly affecting the overall simulation results since the difference is small. Finally, equation (5.2.11) can then be implemented into Simulink, and the transfer functions can be obtained.

5.2.4.4 Physical Modelling of a Linear EMA

Another approach to model the dynamic behaviour of a linear actuator is through physical modelling. This approach has been shown by Khan et al. [146] where the Matlab's Simscape package SimPowerSystem™ is used for the electrical servo-actuator model in their study.

Figure 5.16 shows the schematic diagram of a DC motor using the Simscape physical modelling package that exposes the electrical and mechanical elements of the DC motor. Each block of the schematic will be translated into ODEs and numerically calculated by Matlab, of which are similar to equation (D-1) in Appendix D.1.

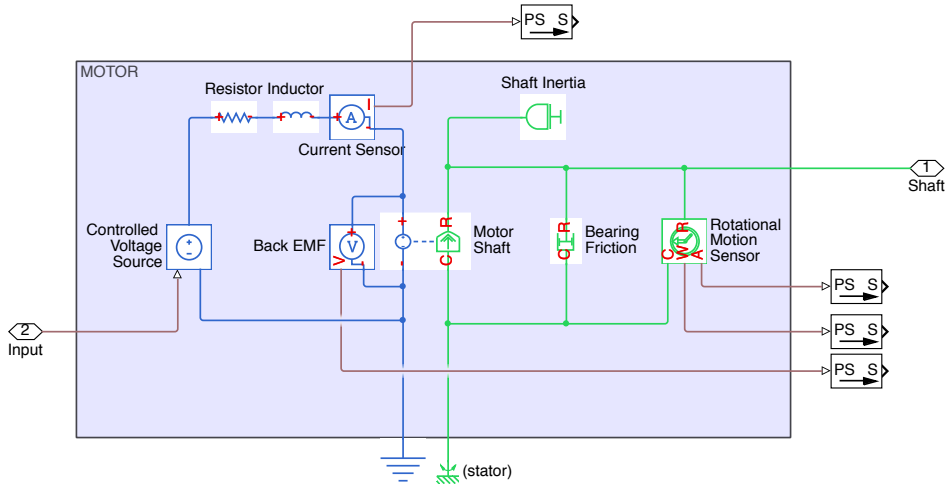

Figure 5.16: Physical model schematic of the DC motor with Simscape

For the Simscape modelling of the gearbox in Figure 5.15, the gear ratio n_{gear} is defined as the ratio of the motor shaft angular speed ω_m to the output angular speed (the leadscrew) ω_{ls}, and written by

$$n_{gear} = \frac{\omega_m}{\omega_{ls}} \tag{5.2.12}$$

If the gearbox is used to achieve a mechanical advantage in the form of higher output torque, the angular speed is then reduced according to the same gear ratio. Normally, spur gears are used, since the motor shaft and the output shaft (the leadscrew) rotations are in parallel (see Figure 5.11). A higher output torque can be achieved by turning the spur gear into a reduction gear, which can be done by having an output gear with a bigger diameter, thus, reducing the angular speed of the output shaft.

It has been understood that the linear translation of the plunger in Figure 5.11 is delivered by the angular velocity of the motor shaft through the leadscrew mechanism. How fast the plunger moves depends on the screw-lead size (S_{lead}) and how fast the screw rotates (ω_{ls}), and this is given by

$$\dot{x}_p = \frac{\omega_{ls}\, S_{lead}}{2\pi} \tag{5.2.13}$$

For a linear actuator with a leadscrew unit, the size of the screw-lead S_{lead} is provided in most manufacturer's datasheet. The screw-lead size S_{lead} is defined as the linear distance where the leadscrew nut (or plunger) travels per screw revolution and is given in the unit $^{mm}/_{rev}$ [147]. Generally, it takes about one revolution for the nut to move from one thread to the adjacent one, which can also be approximated as the circumference of the leadscrew.

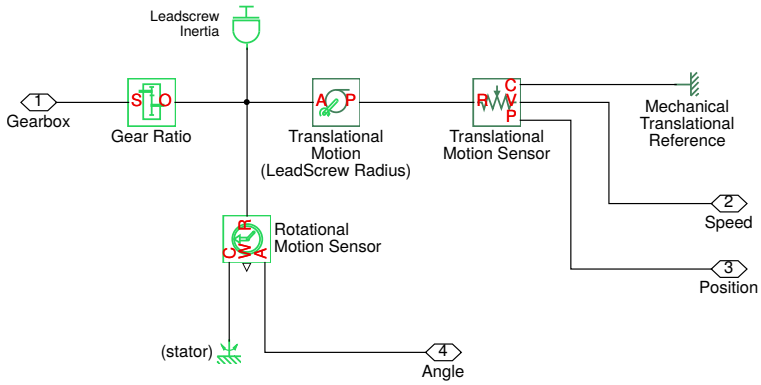

Figure 5.17: Simscape schematic diagram of the linear actuator model

Figure 5.17 shows the schematic diagram of the Simscape physical modelling of the gearing and linear actuator module that also shows related sensors to be used as feedback measurements. Since the Simscape block requires the value of the leadscrew radius (R_{lead}) rather than the screw-lead size (S_{lead}), then the above approximation can be used. Hence, equation (5.2.13) can be re-written as

$$\dot{x}_p = \omega_{ls}\, R_{lead} \tag{5.2.14}$$

Integrating the linear speed of equation (5.2.14) also yields the linear length or position where the plunger travels, which is written as

$$x_p = \theta_{ls}\, R_{lead} \tag{5.2.15}$$

The DC motor module (Figure 5.12) are then combined with the linear actuator module (Figure 5.17) to form a complete linear EMA. The simplified Simscape block of the linear actuator module is shown in Figure 5.18.

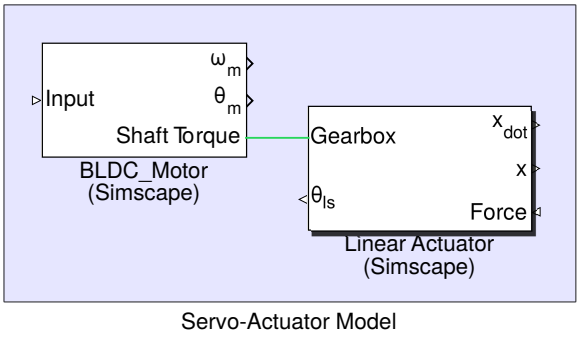

Figure 5.18: Servo-actuator block with Simscape

5.2.5 Linear Position and Speed Control

In order to serve the purpose of having a real servo-actuator for autogyro's flight stability and controls, the effectiveness of the servo-actuator in delivering sufficient amount of force for the control requirement is crucial. Nevertheless, the effectiveness of the actuation system needs to be assessed based on the accuracy of output response for a given input command, which is known as tracking. As such, a closed-loop system with an appropriate controller is introduced within the servo-actuator unit with certain requirements that are mentioned below.

Fast transient response and small steady-state error are considered as important requirements that have to be met for a good control actuation system. The time to achieve a transient response is closely related to the bandwidth of the system response. The faster the transient response time, the bigger will be the bandwidth. On the other hand, the steady-state error is closely related to the servo's accuracy to track the command signal. A small steady-state error also means good damping and less overshoot on the output response while tracking the input command.

However, the process of acquiring and tuning the controller parameters is time-consuming, since there are other smaller or subdivision requirements to comply with, as real servo-actuators are being used. For a linear actuation system, the controller dealt with axial length and speed of the actuator for a given amount of force applied for the load. For this type of actuation, not only a bigger bandwidth with the least steady-state error is to be achieved. A real servo-actuator has its own limitations such as the maximum

allowable armature current, the maximum motor rpm, and other limitations specified by the manufacturer. All of these limiting parameters subdivide the basic requirements to ensure the practicality of the specific servo-actuators, which eventually contribute to the difficulty of the controller tuning processes.

Parker Hannifin Inc., as one of the leading servo-actuator manufacturer, had demonstrated a more practical and easy-to-be-tuned controller. Instead of using a purely tuned PID, the controller was manipulated to be a PIV (Proportional + Integral + Velocity) controller for high-performance servo-actuator [148]. In this method, controller gains were formulated in such a way that only two control parameter requirements are needed; The *Bandwidth* (BW) and the *Damping Ratio* (ζ) of the actuator response.

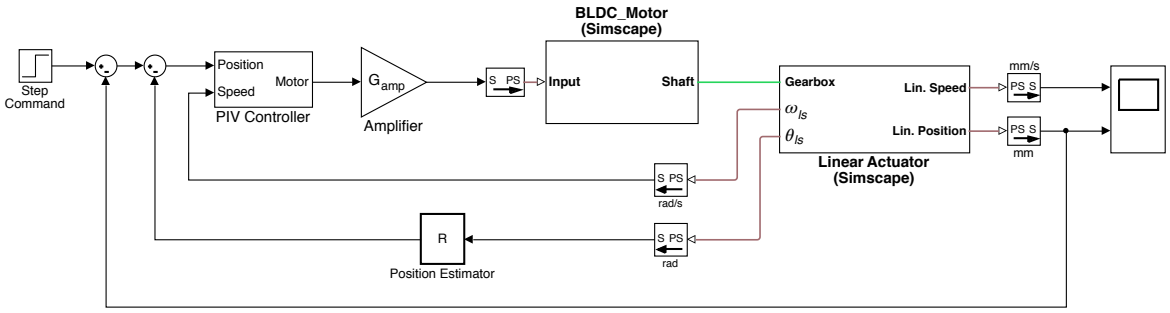

Figure 5.19: Linear servo-actuator schematic diagram with the PIV controller

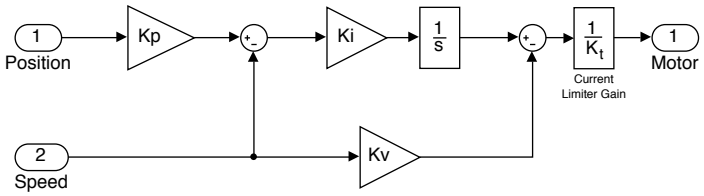

Figure 5.20: The PIV controller

Figure 5.19 shows the overall schematic of a PIV controller implemented on a linear servo-actuator model adapted from Ref. [148], with the PIV controller diagram shown in Figure 5.20. Note that the angular velocity control loop is formed as the most inner feedback loop, which is also known as the fastest loop to be calculated or controlled. In this case, the rotational speed of the leadscrew is given the most priority to be controlled to ensure a fast transient response by the control requirement. The manipulation of the velocity error in this configuration enables the overshoot and the rise-time to be independently controlled and tuned so that faster steady-state response can be achieved with minimum overshoots. This response characteristic is impossible to achieve with a normal PID tuner, due to the strong coupling between the rise-time

and the overshoot. In a normal differential gain, increasing the rise-time also causes an increase in overshoot, thus making the process of gain tuning to be more difficult.

The servo-actuator chosen to be used in this control model is the Exlar-GSM20 Linear Actuator with related parameters as mentioned in the previous Table 5.2.2.

All gain parameters used for the controller are based on Parker's recommendation of the same reference source [148]. Since a linear servo-actuator is used for the flight control actuation, the axial position control is formed as the outermost feedback loop. This axial actuator movement will later turn into the longitudinal shaft tilt (θ_s) of the autogyro, once the actuator is connected to the control link.

In order to understand the behaviour of the GSM20 linear actuator for different control conditions, the controlled linear actuator model is simulated with different damping ratios (ζ) and bandwidths (BW). The performance of the linear actuation responses is evaluated with a $+12V$ step input starting at 0.1 sec of the simulation time. Step input is typically used in this simulation to demonstrate a fast input command so that a damped response is fully excited. The simulation results of the two different conditions are shown in Figure 5.21 and 5.22 and the performance parameters such as the overshoots, rise-time, peak current and RPM are furnished in Table 5.2.4.

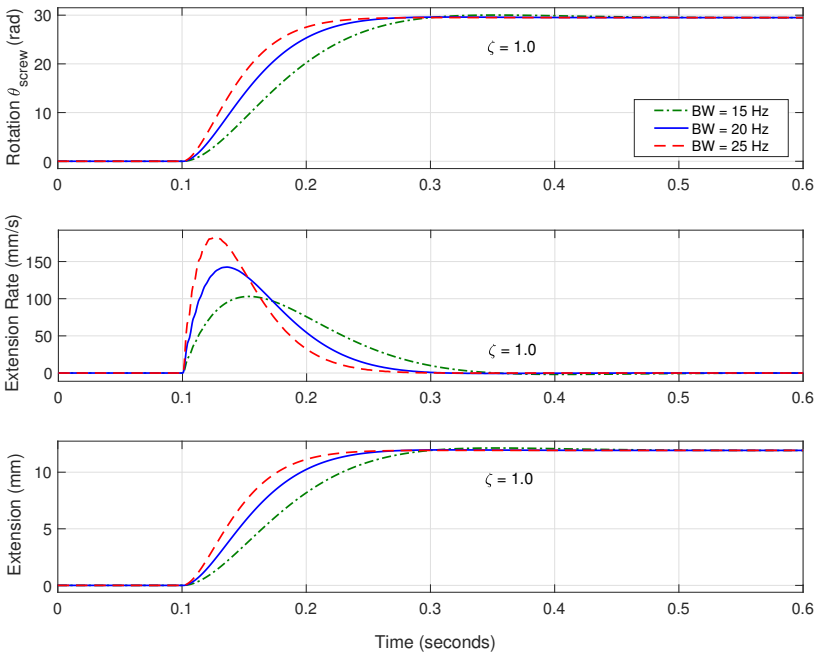

Figure 5.21: GSM20 linear actuator response at fixed ζ and different BW

Figure 5.21 shows simulation results of the actuator at a fixed damping ratio ($\zeta = 1.0$), with the changing in bandwidths (BW = 15Hz, 20Hz, 25Hz). In general, the rise-times are seen to correspond to the bandwidth directly. The bigger the bandwidth, the quicker the rise-time of the response but the overshoots are seen to be less affected by the rise-time for this controller, or even with changes in bandwidth. The extension rate of the plunger is also seen to reach the highest value at the biggest bandwidth (25 Hz) where the rise-time is the quickest (75.35 ms). This can be understood as the condition where the leadscrew rotation is accelerated at the beginning of the excitation until the plunger reaches the peak value at the fastest rate (183 mm/s) compared to the other two conditions.

At this particular bandwidth (25 Hz), the rotation of the motor shaft is stated to have a rotation rate of 4320 RPM. This value is almost double the speed of rotation at 15 Hz bandwidth where the shaft rotates at the rate of 2440 RPM. Hence, in the condition where the damping is fixed, the bigger bandwidth will result in a quicker rise-time, thus, faster settling time.

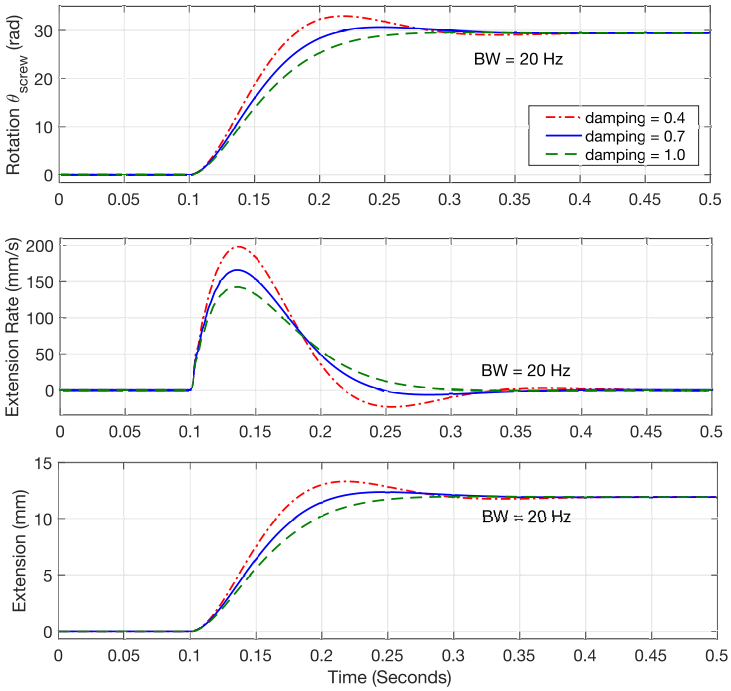

Figure 5.22: GSM20 linear actuator response at fixed BW and different ζ

On the other hand, Figure 5.22 shows simulation results of the actuator at a fixed bandwidth ($BW = 20$Hz), but with changes in damping ratios ($\zeta = 0.4, 0.7, 1.0$). In general, overshoots are seen to correspond to the damping directly. At the condition where the actuator is underdamped ($\zeta = 0.4$), the overshoot is seen to be significantly high (11.8%), and this condition is practically unacceptable for a linear actuator. The

settling time for the underdamped condition is also seen to be the slowest, compared to the other two damping conditions. In fact, it can be seen that both, overshoot and rise-time are significantly affected by the damping. Less damping corresponds to higher overshoot but quicker rise-time. Hence, to have a good linear actuation control, the damping ratio must be at least 0.7 or critically damped.

In conclusion of the two simulation results, it is found that the damping of $\zeta = 1.0$, in a 20 Hz bandwidth is the best choice of requirements for the Exlar GSM20 linear actuator. The PIV control tuning values quantified from the GSM20 simulation results for the two tuning conditions (fixed BW and fixed ζ) are summarised in Table 5.2.4. The simulation results also show none of the values exceeding the maximum rating stated in the manufacturer's datasheet [138, 139]. Therefore, it is considered that the controller has achieved the desired control characteristics, without violating the linear actuator's physical restrictions given by the manufacturer (see Table 5.2.2).

Table 5.2.4: PIV tuning values for fixed BW and fixed ζ

Parameter		Bandwidth [Hz] (Fixed $\zeta = 1.0$)			Damping (Fixed BW=20Hz)		
		BW=15	BW=20	BW=25	$\zeta = 0.4$	$\zeta = 0.7$	$\zeta = 1.0$
Controller Gains	K_p	31.4159	41.8879	52.3599	69.8132	52.3599	41.8879
	K_i	0.3831	0.6811	1.0642	0.4087	0.5449	0.6811
	K_v	0.0040	0.0054	0.0068	0.0032	0.0043	0.0054
Performance	Overshoot (%)	1.531	0.505	0.505	11.798	3.65	0.505
	Rise-time (ms)	120.7	92.42	75.35	53.64	71.18	92.42
Steady-state values	θ_{ls} (rad)	29.7	29.7	29.7	29.7	29.7	29.7
	x_p (mm)	11.987	11.988	11.988	11.988	11.988	11.988
Peak values	ω_{ls} (RPM)	2440	3370	4320	4680	3920	3370
	$\dot{x}_p$ (mm/s)	103.2	142.6	183.1	198.23	165.85	142.6
	I_a (A)	1.00	2.15	3.78	2.48	2.30	2.15

Hence, it is decided the actuator model to be set according to these response characteristics;

* Minimum response bandwidth, $BW_{min} = 20$ Hz
* Minimum damping ratio, $\zeta_{min} = 1.0$
* The maximum overshoot must not exceed 3%

The GSM20 linear actuation model of Figure 5.19 with the same control settings is then

simulated with a constant random input signal for 10 seconds, and the result is shown in Figure 5.23. The simulation result shows a proper tracking of the command input. Therefore, using the linear analysis tool in the Simulink environment, the transfer function of the dynamic system for the linear actuator can be obtained in the form of 4^{th} order function.

$$\frac{\dot{x}(s)}{V_{in}(s)} = \frac{1.575\,e^9\,s}{s^4 + 566.5s^3 + 1.855\,e^6\,s^2 + 9.299\,e^7\,s + 1.576\,e^9} \left[\frac{\text{mm/s}}{\text{V}}\right]$$
$$\frac{x(s)}{V_{in}(s)} = \frac{1.575\,e^9}{s^4 + 566.5s^3 + 1.855^{\,6}\,s^2 + 9.299\,e^7\,s + 1.576^{\,9}} \left[\frac{\text{mm}}{\text{V}}\right] \tag{5.2.16}$$

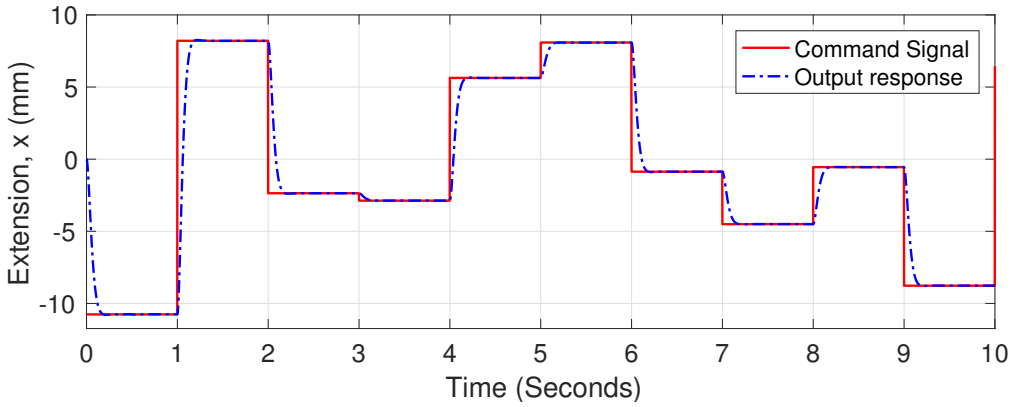

Figure 5.23: GSM20 actuator response to input command (BW=20Hz, $\zeta = 1.0$)

5.3 G-UNIV Control Linkage with Actuator Model

The physical model of the basic mechanical control links of the G-UNIV autogyro has been developed and presented in Section 5.2.2 in this chapter. The basic concept of the Simscape™ Multibody™ physical modelling has also been described in the same section. This was then followed by the development of the actuation control system in Section 5.2.4 which was embedded together with the physical model of the electromechanical actuation according to the design and control requirements.

5.3.1 Deployment of the Complete Model

The next step is to look into the deployment of the full actuation system into the existing G-UNIV mechanical control linkage model. A new simulation will be established on the complete actuator and control link deployment and the analysis will be presented at the end of the section, including the establishment of complete transfer function of the full dynamic system. Since the dynamic model of the mechanical control link and the control actuation system were done in separate modules, the deployment will be done according to Figure 5.24.

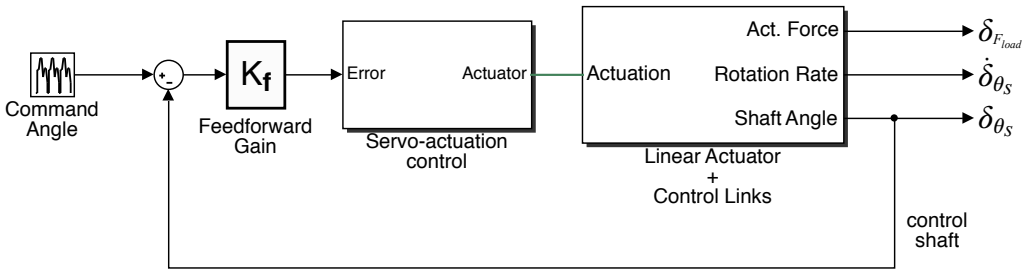

Figure 5.24: G-UNIV mechanical control link with actuation control in Simulink

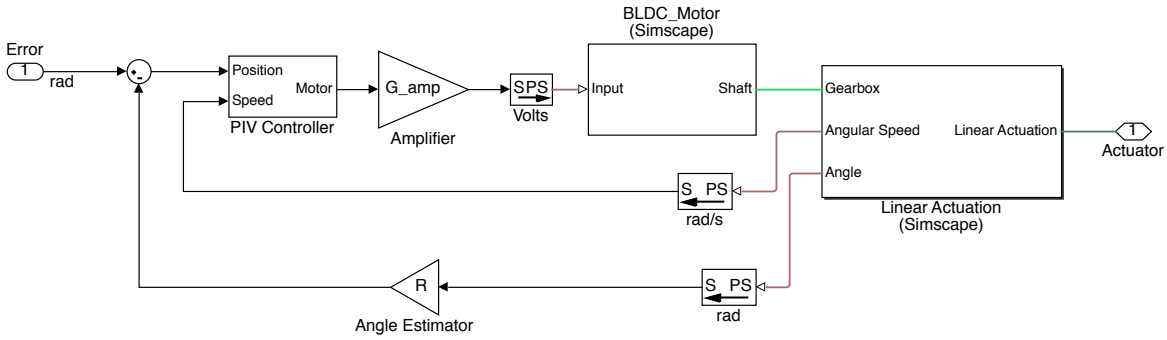

Figure 5.25: The 'Servo-actuation' control schematic in Simscape

The control actuation is used to produce the correct amount of linear actuation according to the servo-actuator requirements as described in Section 5.2.5. In order to produce the proper longitudinal rotor shaft tilt, the longitudinal shaft angle (θ_s) is fed back into the 'Servo-actuation Control' module (as detailed in Figure 5.25), so that the correct linear actuation is produced accordingly. Note that the 'Servo-actuation Control' in Figure 5.25 employed the same control actuator from Figure 5.19, with a small modification, where the linear position control loop for the 'plunger' is replaced with the longitudinal shaft control loop (θ_s angle). In this case, the θ_s angle is the most important parameter to be controlled, as it is the actual feedback parameter of the G-UNIV control enhancement. Moreover, the 'Feedforward Gain' K_f is used to produce a zero steady-state error signal, so that the command signal can be tracked

properly by the controller. The value of K_f is established through a trial and error process according to the expected output. From the same 'Servo-actuation Control' blockset, the linear actuator will then extends and contracts the mechanical control linkage of the vehicle according to the desired θ_s angle. In this case, the physical actuation force of the 'Linear Actuation' blockset is transferred to the linear actuator through the physical output point 'Actuator'.

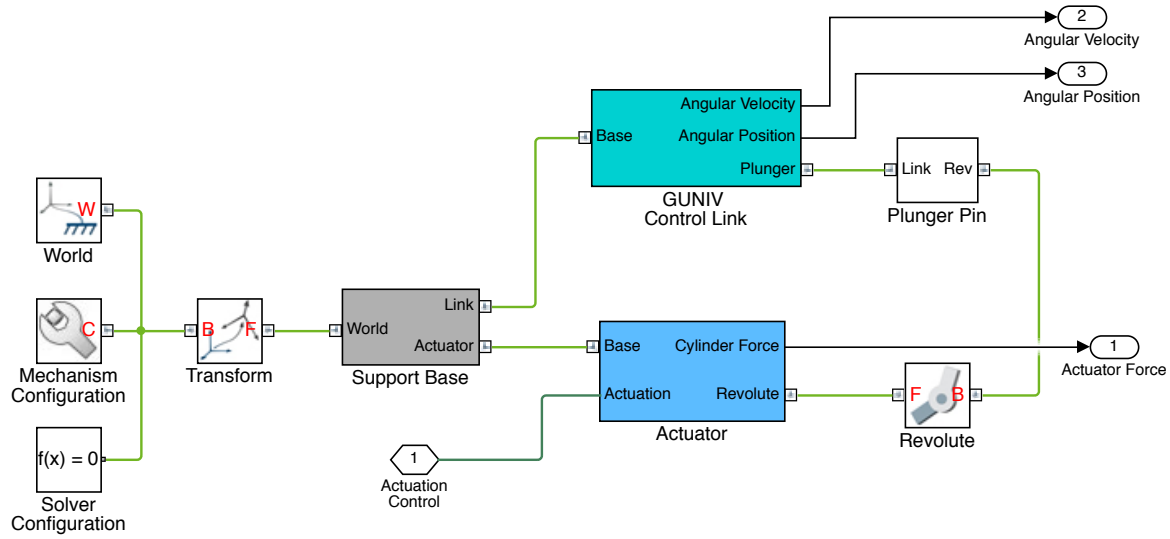

Figure 5.26: Linear Actuator + Control Links block (Simscape Multibody)

The Simscape multibody blockset of the 'Linear Actuator + Control Links' of Figure 5.24 is detailed in Figure 5.26, which also represents the whole mechanical hardware linkages shown in Figure 5.10. The 'G-UNIV Control Link' blockset in Figure 5.26 was actually the simplified schematic of the full mechanical link blockset of Figure 5.6, while the 'Actuator' blockset represents the Simscape multibody of the actuator hardware, as detailed in Figure 5.27.

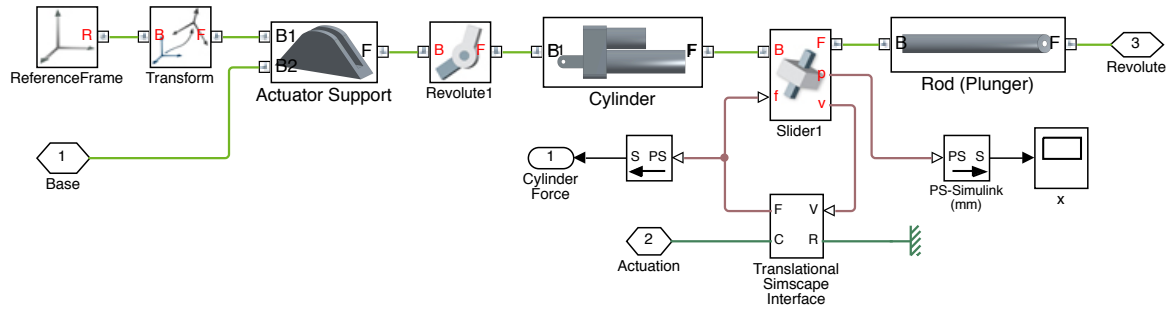

Figure 5.27: Actuator block (Simscape Multibody)

The 'Actuator' blockset demonstrates the actuation process of the linear actuator

through the 'Translational Simscape Interface' sensor within the two multibody parts (see Figure 5.27). This sensor changes the physical translational movement of the rod (plunger) into Simulink signals in the form of the axial position (x_p), axial speed ($\dot{x}_p$), and the force required to move the G-UNIV mechanical control link (F_{load}). This is one of the examples where the dynamics between two or more physical parts are being translated into ODEs and then numerically evaluated into Simulink values. In this case, the sensors are assumed to be placed at the prismatic joint (slider). Since the actuator's cylinder is fixed, the movement of the plunger is evaluated relative to the cylinder position. The same method is used for other physical joints within the blockset such as the Revolute joint and Cylindrical joint.

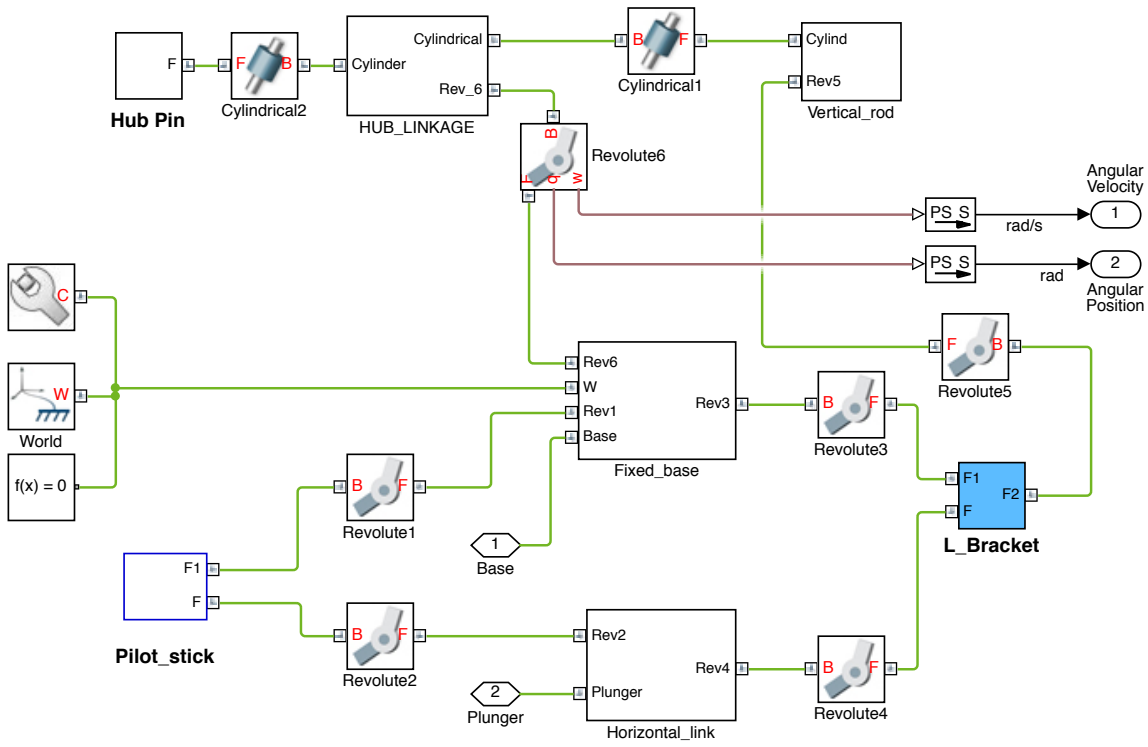

Figure 5.28: G-UNIV Control Link block (Simscape Multibody)

The extended or contracted plunger will then move the mechanical control link within the 'G-UNIV Control Link' blockset through the physical connecting point 'Plunger' as shown in Figure 5.28. The figure also shows different links between joints and rigid parts within the mechanical link. The axial movement of the plunger contribute to translations in different degree of freedom from the horizontal link to the vertical through several revolute joints, and finally to the pivot point of the rotor hub. According to the multibody links in the same figure, 'Revolute6' is assumed to be the pivot joint of the rotor hub. Thus, the rotation of the Hub Linkage yields the angular speed and position of the longitudinal shaft control relative to the actuator's translational control link. Therefore, the rotational sensors embedded in the Revolute6 are used

as the Rotational Simscape Interface module, which translates the rotational physical dynamics into numerical values in the Simulink environment. These Simulink signals are then fed back to the controller module as the longitudinal shaft control angle (δ_{θ_s}) to match with the desired command input.

5.3.2 Simulation Results

Note that in the development stage of the actuation control, steps input is commonly used to evaluate the maximum actuator response according to the actuator requirements. This is because, steps command always excites the response behaviour of the system, particularly the damping at the maximum level. However, step inputs are not suitable for evaluation of the control surface deflection due to the practicality of the response rate in real flight. As such, it is known that the normal response rate for an actuator control deflection is close to a trapezoidal profile. Therefore, the simulation study for the complete actuator linkage control system will be done using a trapezoidal profiled command input with an input signal setting of not exceeding $\pm 12V$.

According to the actuator control schematic in Figure 5.24, the changes in angular position of the control link δ_{θ_s} also reflects the same longitudinal shaft tilt described in previous chapters. The input signal replicates the actual pilot control stick deflection with a built-in rotational transducer that translates the degree of control stick rotation to voltage signals. Note also that the rate of longitudinal shaft control tilt is defined as

$$\delta_{\omega_s} = \delta_{\dot{\theta}_s} = \frac{d}{dt}(\delta_{\theta_s}) \tag{5.3.1}$$

Figure 5.29 shows simulation results of the longitudinal shaft tilt response of the G-UNIV due to the pilot input command. The simulation is based on the same Exlar GSM20 linear EMA, complying with the minimum actuator requirements, concerning the minimum damping and bandwidth. Three important response parameters are shown in the figure; the longitudinal shaft tilt (δ_{θ_s}), the angular rate of change of the shaft tilt ($\delta_{\dot{\theta}_s}$), and the actuator force exerted due to the control response.

The longitudinal tilt angle δ_{θ_s} shows a good tracking response to the pilot command input with a small delay and less overshoot, which is due to the $BW = 20$Hz and $\zeta = 1.0$. The δ_{θ_s} began at -6 deg and deflected to $+6$ deg in a time duration of 1 sec, which means that δ_{θ_s} rotate at the rate of $+12$ deg/s as shown in the δ_{θ_s} plot. It is also important to re-emphasise that the '+' sign of the δ_{θ_s} magnitude represents a rearward or back tilt of the longitudinal control angle for an autogyro. During the

same transition period, the plunger of the linear actuator extends about +18 mm with the maximum transition rate of approximately +18 mm/s. Hence, the axial-to-radial transition ratio in this particular case is assumed to be about 1.5:1, which means every 1 mm axial translation contributes to a 0.67 degree of change in the δ_{θ_s} position.

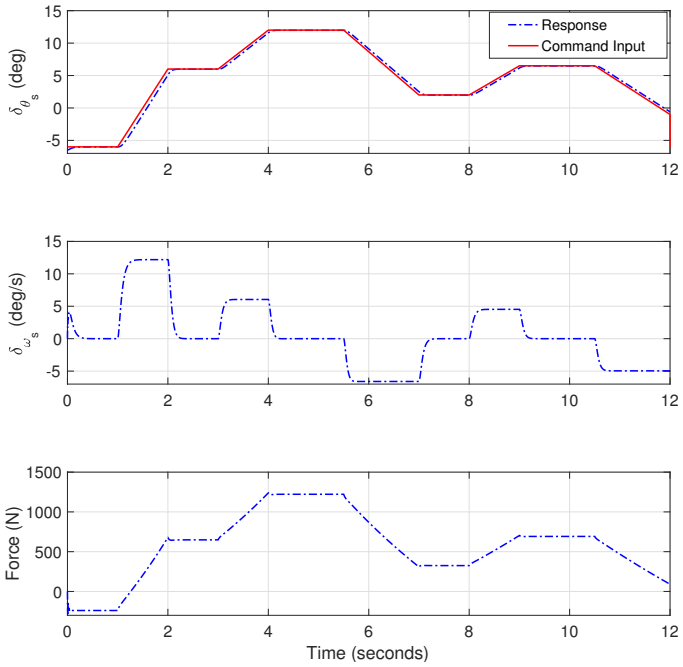

Figure 5.29: Longitudinal shaft tilt response of the G-UNIV physical model

The changes of the actuator force in Figure 5.29 only represents the amount of force exerted or applied when the actuator plunger moves. It is important to understand that this force is applied only to the total mass of the mechanical control linkages where the plunger is attached to, as the type of material including the inertia properties of the control links were already assigned in the CAD model. Thus, this force does not represent the aerodynamic load of the rotor hub as the actuator links are not currently attached to the real autogyro model. Note that the Pivot Point of the rotor hub (named 'Revolute6') in the multibody model was assigned with a certain value of spring stiffness and damping. This setting represents the real spring damper that is originally installed at the hub bar of the pivot point of the real G-UNIV autogyro. All these are variables that contribute to the amount of actuator force presented in the plot.

In order to deploy the actuator control links into the aircraft model, the physical model of the whole actuator control link must first be linearised to obtain the transfer functions of the system.. Then, the dynamic behaviour of the system can be analytically evaluated and manipulated further in the flight control system. In this case, the linear analysis tool of the Simulink environment was used to linearised the physical model

of the actuator-linkage system. The linearisation was done according to the initial conditions of the model and produces a linear state-space matrix of, 1 input, 2 outputs with 10 states (10 × 10 state matrix). All matrices including their transfer functions are furnished in Appendix D.3 for further reference. To verify the linear model, the model is simulated and compared with the physical model as shown in Figure 5.30. The comparison plots show a close correlation between the linearised and the physical model, which is expected.

It can be seen from the 10×10 state-space matrix in (D-1) of Appendix D.3 that not all of the 10 state derivatives are significant, in terms of values. Hence, the 10×10 matrix is then reduced to a 6×6 by omitting those less significant derivative terms (written as equation (D-4)), with new transfer functions that produce the same simulation results, written below

$$\frac{\delta_{\dot{\theta}_s}}{V_{in}} = \frac{5.3e^8\, s^3 + 5.3e^{11}\, s^2}{s^6 + 2111\, s^5 + 9.1e^5\, s^4 + 9.8e^8\, s^3 + 4.9e^{10}\, s^2 + 5.3e^{11}\, s}$$
$$\frac{\delta_{\theta_s}}{V_{in}} = \frac{5.3e^8\, s^2 + 5.3e^{11}\, s}{s^6 + 2111\, s^5 + 9.1e^5\, s^4 + 9.8e^8\, s^3 + 4.9e^{10}\, s^2 + 5.3e^{11}\, s} \tag{5.3.2}$$

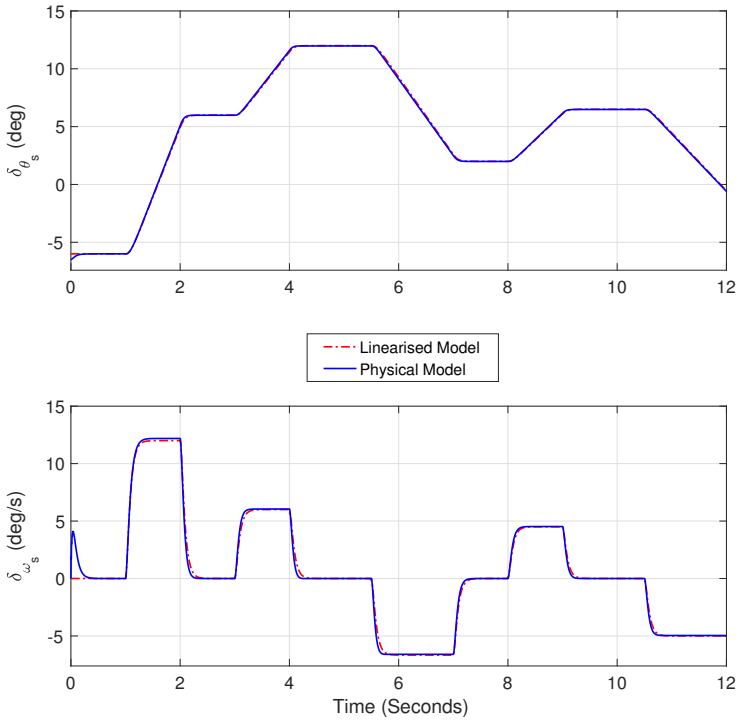

Figure 5.30: Physical Vs linearised model response of rotor shaft tilt

The complete transfer functions in (5.3.2) will be applied as part of the linear pilot

model for the autogyro's control enhancement that will be described in Chapter 6.

5.4 Chapter Summary

The objective of the chapter is to model the control linkage of an autogyro with the servo-actuator being employed so that the dynamic model of the servo-actuation control can be implemented in the vehicle's control enhancement. This is because a close-to-real dynamic control actuation model based on real hardware is vital to accurately address the pilot-vehicle time delay into the flight controller for better flight qualities performance.

The modelling started with a rigid-body evaluation of the autogyro's basic mechanical control linkage to estimate the amount of force required at the control linkage. For the G-UNIV autogyro, the amount of force has been estimated at different locations along the control link, based on the equilibrium flight data. This force estimation then became one of the basic requirements for the servo-actuator to be employed in the vehicle.

Technically, the modelling of the real hardware control linkage with actuation control in the chapter was divided into two main modules before being deployed together, which is summarised in the following.

(a) *The Mechanical Control Links.*

i) A 3D representation of the G-UNIV mechanical control links including the actuator was modelled in a 3D CAD software, before being translated into a physical model representation using the Simscape™ Multibody™ modelling tool. This method significantly simplifies the modelling process that involves multibody dynamics for complicated rigid mechanical links.

ii) The dynamic behaviour of the physical model can then be evaluated through normal simulations and linearisations within the normal Simulink environment. For the G-UNIV autogyro, this multibody model is then deployed together with the actuation control where the full simulation of the whole mechanical control linkages are quantified and verified.

(b) *The Actuation Control.*

i) In this part, the dynamics of the servo-actuation is modelled according to the real industrial-type servo-actuator with the manufacturer's hardware datasheet is available in the public domain. The physical model of the servo-actuation was developed with the Simscape™ Physical Modelling tool within the Simulink environment to ease the modelling process.

ii) Other dynamic response requirements for the actuator have also been ascertained in the development process such as the bandwidth, the damping ratio and the maximum percentage of overshoot. As such, the actuation controller was also being set according to these requirements, and the recommendations from the manufacturer were used for the controller settings.

Both modules were successfully evaluated and verified with the newly obtained transfer functions of both dynamic models. Finally, the deployment of the two modules to form a full actuation control linkage model were made and the full model was again verified through simulations. The transfer functions of the complete control actuation model were finally obtained. These transfer functions are assumed to represent the pilot-actuator dynamics model and will be put into the vehicle's automatic flight control system in Chapter 6 for further testing.

Chapter 6

Evaluation of Control Enhancements

6.1 Introduction

In Chapter 4, enhancement of the flight control system of a light autogyro was developed and tested against the proposed autogyro flying qualities requirements described in Chapter 2. However, the automatic flight control enhancement in Chapter 4 was considered as a preliminary model since the real hardware of the control mechanism was not determined and tested on the G-UNIV autogyro. One of the most important hardware mechanisms used in aircraft flight control system (AFCS) is the servo-actuator, of which was initially implemented on the G-UNIV as a simple first-order dynamic model. To ensure the effectiveness of the automatic flight control enhancement for the autogyro, real actuation control hardware mechanism has to be modelled and later implemented into the new control systems. This was explained in Chapter 5 where the servo-actuator control linkage was modelled according to the estimated amount of force required for the G-UNIV autogyro to operate its mechanical control linkages during flight. The servo-actuator chosen to be used was a brushless-type DC-powered linear electromechanical actuator (EMA), and the complete electrical and hardware modelling were made according to specific requirements. These models include the mechanical control linkages of the G-UNIV that provide the longitudinal shaft tilt action for the rotor hub.

Therefore, the objective of this Chapter is two-fold: Firstly, to implement a more realistic servo-actuation dynamic model that was previously developed into the G-UNIV autogyro model. Secondly, to evaluate the longitudinal flying qualities performance

of the G-UNIV autogyro with the control enhancement and the new servo-actuation model in place.

Evaluations will be done according to the same approaches that have been implemented in Chapter 4, and generally described in the following;

* Evaluation of the unaugmented or open loop dynamic response of the vehicle.

  This evaluation is meant to understand the direct effects of the new hardware configuration to the vehicle's dynamic response, without the control enhancement in place.

* Evaluation of the augmented or closed-loop dynamic response of the vehicle.

  Evaluations are made for both, the autogyro equipped with the Stability Augmentation System (SAS), and the autogyro equipped with the Rate-Command Attitude Hold System (RCAH). It is expected that all controller gain values would require fine tuning with the new hardware model to ensure the effectiveness of the control enhancement.

For those evaluations, the dynamic characteristic of the autogyro such as bandwidth and time response parameters in short-term and phugoid mode are quantified based on the linear model of the vehicle and its new servo-actuator. Finally, the effectiveness of the newly developed control enhancement is confirmed through nonlinear simulation for the longitudinal full order dynamic model. Consequently, the load factor or g-force that affecting the rotorspeed is also evaluated in the nonlinear simulation. Atmospheric disturbances are also included in the nonlinear simulation for better realisation of the autogyro control enhancement.

6.1.1 Limitations

It is important to note that the flying qualities evaluations in this chapter are made within the following limitations:

a) Flight envelope protection is not implemented in the automatic flight control model. Since the G-UNIV autogyro being used in this research was registered under the experimental category, a lot of hardware configuration changes have been made in the past 15 years the vehicle was in research studies. Hence, there was no limitation involving the attitude and altitude of the vehicle available or

recorded during the time. Therefore, it can be understood that the real flight envelope for the G-UNIV was not directly defined in previous studies. In fact, most light autogyros are operated in lower flight speed regime and lower altitude, of which the atmospheric effects are less significant, compared to fixed-wing aircraft and helicopters.

b) The new servo-actuation model which include its mechanical linkage has been comprehensively modelled in the previous chapter. This new servo-actuation model with its degree of complexities is then considered as the main control hardware for the AFCS in this chapter. Hence, other hardware used in the AFCS such as rate-gyros and other sensors are not modelled and assumed to function with high level of accuracy.

6.2 Evaluation of the Unaugmented Model

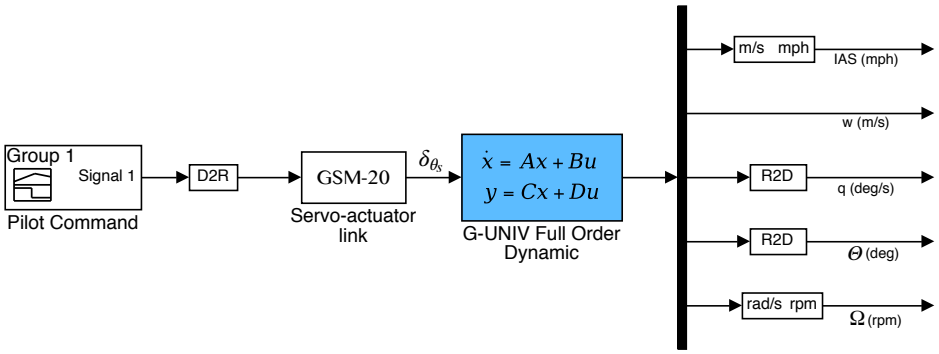

Figure 6.1: Schematic of G-UNIV linear model with servo-actuator link

To quantify the flying qualities characteristics of the vehicle, the linearised model of the G-UNIV and servo-actuator is used and shown in Figure 6.1. The linearised G-UNIV basic airframe model was taken from Chapter 3, while the linearised model of the GSM20 servo-actuator link was obtained in Chapter 5. The unaugmented response of the linearised G-UNIV with the GSM20 servo-actuator dynamic model similar to Figure 6.1 is evaluated according to the proposed flying qualities criteria discussed in Chapter 2 (refer to Table 2.5.1). For consistency, the same flight condition at 75 mph is taken into consideration to be analysed and evaluated. Figure 6.2 shows the unaugmented dynamic response of the G-UNIV linearised model with and without the GSM20 control actuator link for comparison. Note that, a trapezoidal input profile is being used to closely represents a more practical pilot input profile for ease of clarity. The Figure obviously shows the dynamic model of the control actuator links, which

contributes to an approximate 0.1 second delay on the vehicle's dynamic response, with no significant changes in overshoot for the state responses.

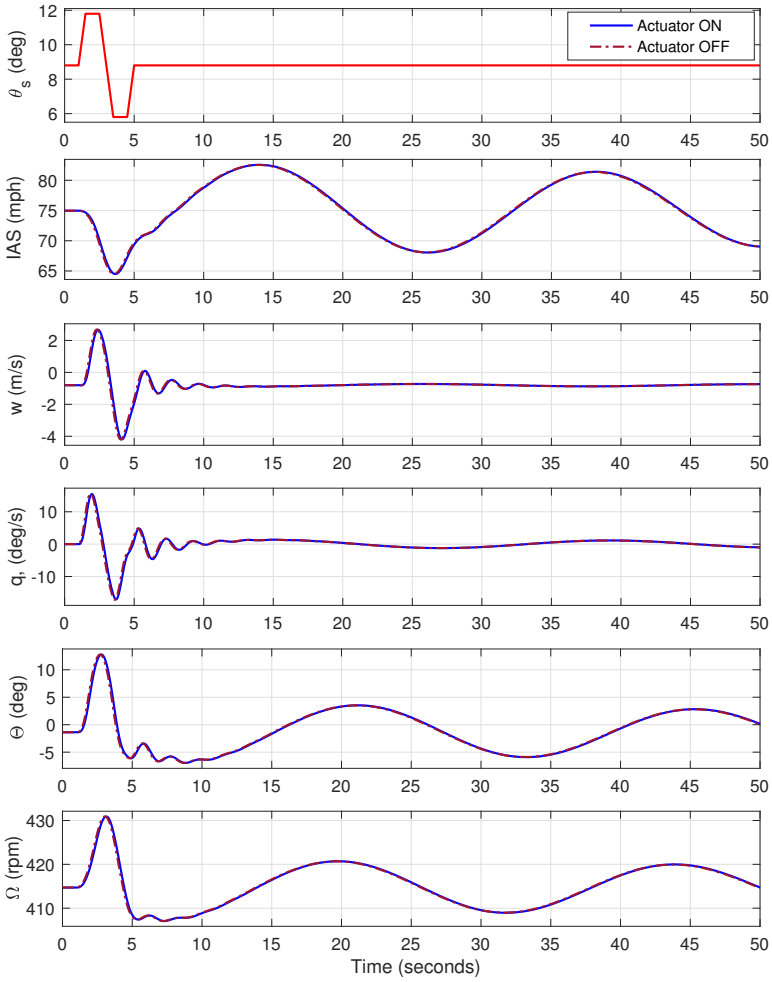

Figure 6.2: Dynamic response of G-UNIV with the GSM20 servo-actuator

The evaluation will be more worthwhile if the effect of the GSM20 servo-actuator link can be compared with the basic (default) actuator model in Chapter 4. The basic actuator implemented in Chapter 4 was modelled as a simple first-order system with a time-lag of $\tau_a = 0.05$ sec (20 Hz), where the transfer function is given by

$$G_{act} = \frac{1}{1 + \tau_a\, s} = \frac{1}{1 + 0.05\, s} = \frac{20}{s + 20} \tag{6.2.1}$$

while, for the GSM-20 servo-actuator link in Chapter 5, the transfer function is more complex

$$G_{\text{GSM20}} = \frac{5.3e^8\, s^2 + 5.3e^{11}\, s}{s^6 + 2111\, s^5 + 9.1e^5\, s^4 + 9.8e^8\, s^3 + 4.9e^{10}\, s^2 + 5.3e^{11}\, s} \tag{6.2.2}$$

It is important to note that the transfer function in (6.2.2) includes the dynamics of the electrical components of the actuator motor and all mechanical links to the longitudinal shaft tilt (δ_{θ_s}) of the G-UNIV.

Further evaluation of the unaugmented model with different actuator configurations are made according to the proposed flying qualities criteria in the short-period and phugoid mode and the results are described in the following.

6.2.1 Unaugmented Short-period Mode

This evaluation is made by quantifying the effect of the new GSM20 actuator linkage hardware on the unaugmented short-period response compared to the basic actuator dynamic according to the proposed criteria (see Table 2.5.1). The evaluation covered both flight categories of the criteria; the lower-speed flight (IAS 40 mph and 50 mph) and high-speed flight (IAS 55 mph, 65 mph and 75 mph). According to the criteria, the short-period mode evaluation consists of two; *Pitch attitude changes to small-amplitude input* and *Pitch attitude changes to moderate-amplitude input.*

Table 6.2.1 shows the bandwidth characteristics, including the phase-delay τ_θ for both actuator-linkage configurations for the unaugmented short-period response across the airspeed. Implementing the new actuator-linkage dynamic model does not significantly change the amplitude of the response, but changes the phase response of the vehicle. This phase difference is shown by the bode plot of the pitch attitude response for the G-UNIV in Figure 6.3. Referring to the same plot, at lower frequency oscillation, the phase of the pitch response is seen to have a small phase lead of approximately 5° for approximately −20 dB/decade of gain changes in the control input. This is an indication that the short-period mode oscillation at this flight speed (75 mph) is very lightly damped, and a small change in the pilot input could lead the dynamic of the vehicle to move towards an unstable condition. At the flight speed of 75 mph, the short-period damping is just 0.15 at the frequency of 3.27 rad/s, and this is where the peak of the gain response is maximum.

Another fact from the bode plot figure is that, at lower frequency region, the pitch response of the vehicle with the new servo-actuator are seen to be equal and coincides with the basic actuator model. This situation can be understood as the actuator-linkage

Table 6.2.1: Bandwidth response of unaugmented short-period flight mode

Flight Speed	**Parameter**	**Short-period Mode**	
		Basic Actuator	GSM20 Actuator
40 mph $\lambda_{sp} = -0.493 \pm 1.26i$ $\zeta_{sp} = 0.37$	$\omega_{BW(phase)}$ (rad/s)	1.38	1.34
	$\omega_{BW(gain)}$ (rad/s)	1.85	1.65
	τ_θ (msec)	50.7	89.3
50 mph $\lambda_{sp} = -0.492 \pm 1.79i$ $\zeta_{sp} = 0.27$	$\omega_{BW(phase)}$ (rad/s)	1.93	1.88
	$\omega_{BW(gain)}$ (rad/s)	2.33	2.09
	τ_θ (msec)	51.0	90.6
55 mph $\lambda_{sp} = -0.491 \pm 2.06i$ $\zeta_{sp} = 0.23$	$\omega_{BW(phase)}$ (rad/s)	2.20	2.15
	$\omega_{BW(gain)}$ (rad/s)	2.52	2.26
	τ_θ (msec)	53.5	93.2
65 mph $\lambda_{sp} = -0.487 \pm 2.60i$ $\zeta_{sp} = 0.18$	$\omega_{BW(phase)}$ (rad/s)	2.72	2.66
	$\omega_{BW(gain)}$ (rad/s)	2.93	2.35
	τ_θ (msec)	54.7	94.0
75 mph $\lambda_{sp} = -0.483 \pm 3.23i$ $\zeta_{sp} = 0.15$	$\omega_{BW(phase)}$ (rad/s)	3.32	3.26
	$\omega_{BW(gain)}$ (rad/s)	0.58	0.44
	τ_θ (msec)	58.6	96.4

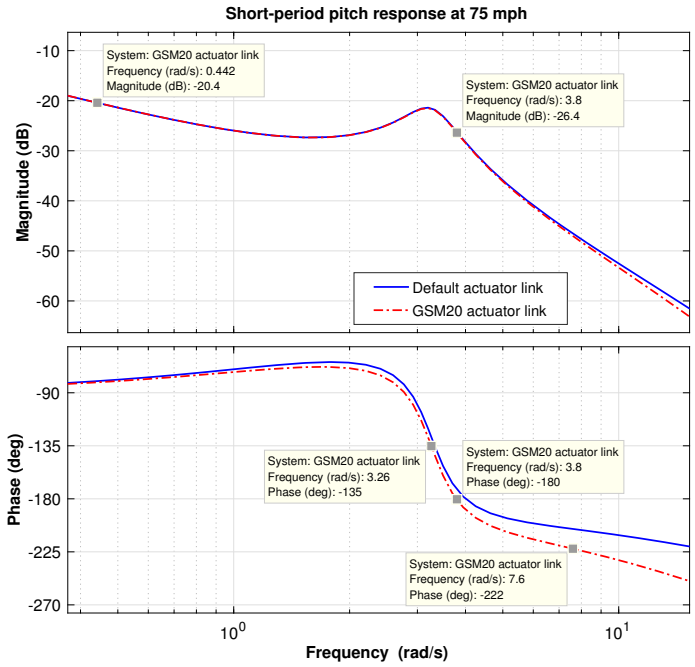

Figure 6.3: Freq. response of unaugmented short-period mode at 75 mph

dynamics do not significantly affect the vehicle's overall response at input frequencies lower than the phase bandwidth frequency. However, more significant changes can be seen as the frequency and input gain increases, causing the vehicle to experience a rapid phase lag in the pitch response. For the short-period oscillation of the G-UNIV at 75 mph, the same gain peak can be seen for both actuator configurations. From this particular point, the phase lag between the two actuator dynamics starts to deviate from each other where the GSM20 actuator linkage is seen to have more steeper phase lag, causing more phase delay compared to the vehicle with the basic actuator model. This situation is expected to happen due to the additional dynamic complexities from the GSM20 servo-actuator linkages compared to the basic first-order actuator dynamic. Hence, at the flight speed of 75 mph, the time lag contributed by the phase delay of the G-UNIV autogyro deviated between the two different actuator dynamics from 58.6 msec. to 96.4 msec., as mentioned in Table 6.2.1.

The same bandwidth plot in Figure 6.3 also shows that the steeper or sharper peak gain curve causes the 6 dB gain margin to deflect the gain bandwidth further to the left at the lower frequency compared to the phase bandwidth. This exhibits a PIO prone condition where the damping of the unaugmented autogyro is relatively reduced in higher airspeed, which also contributes to higher overshoots and more short-period oscillations, even with a small control input. This result is also found to be consistent regardless of the type of actuator dynamics being implemented for the unaugmented case.

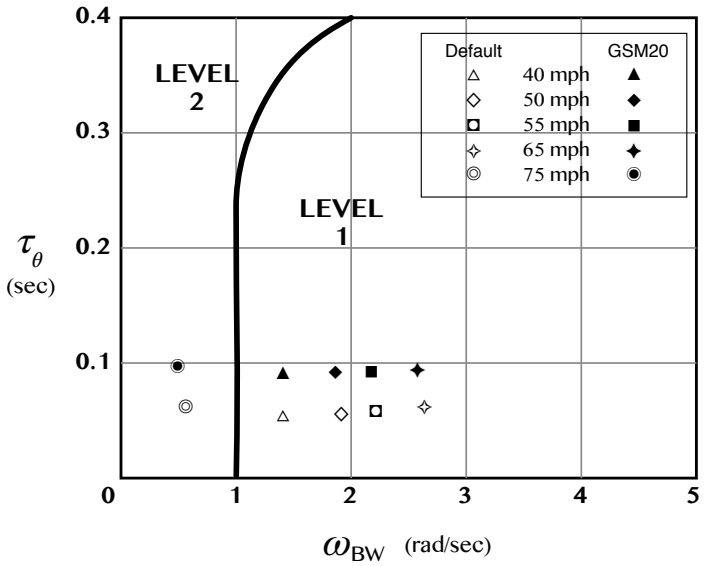

Figure 6.4: Short-term response to small-amp. input (all speed)

The bandwidth (ω_{BW}) and phase delay (τ_θ) of the two different vehicle configurations are then mapped into the proposed criteria limit in Figure 6.4 for the whole flight regime. The limits also revealed a level 2 flying qualities for the autogyro at higher speed regime, which also corresponds to the same trend for the vehicle with the basic actuation linkage in Chapter 4.

Figure 6.5 shows the time response of the unaugmented short-period mode of the G-UNIV with the new GSM20 servo-actuator model, which exhibits an approximate 0.04 seconds delay in the dynamic response compared to the basic actuator dynamics. The amplitude, however, does not significantly changed and almost remain the same with the basic actuator model. This is due to the damping parameters which remain the same for both actuator configurations in an unaugmented flight, and the only thing that has changed is the time constant. These conditions are again mentioned in Table 6.2.1, which revealed the same short-period eigenvalues obtained for both actuator configurations throughout the flight regime.

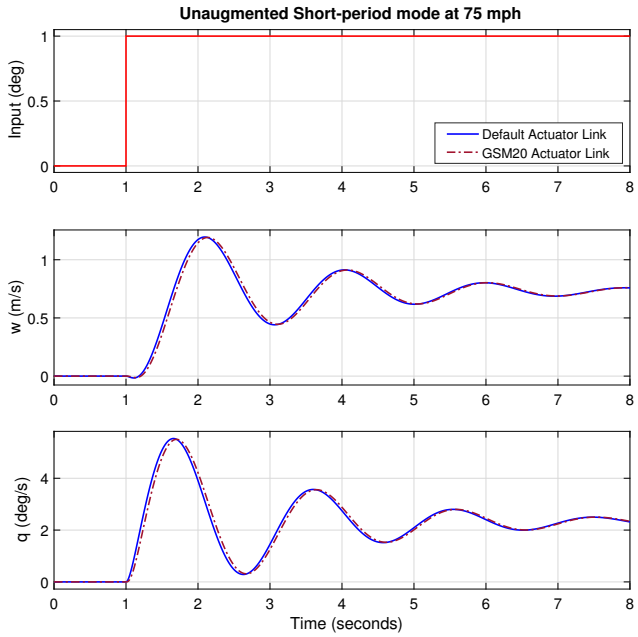

Figure 6.5: Unaugmented short-period response at 75mph

Evaluations of the *Pitch attitude changes to moderate-amplitude input* or the so-called 'Pitch Quickness' evaluations are shown in Table 6.2.2 and Figure 6.6. These evaluations represent the pitch response of the vehicle at lower flight speed regime (at 40 mph and 50 mph) due to moderate amplitude input being applied in steady-state flight condition. The same table also revealed the difference in pitch attitude response between the two servo-actuator dynamic models, which is less significant. As such, the flying qualities performance of the two actuators is seen almost coincides with each other

within the pitch quickness limits as shown in Table 6.2.2. This result also exhibits the same damping parameters of the two actuator dynamics for the short-term oscillation, which corresponds to the previous results listed in the Table 6.2.1.

Table 6.2.2: Pitch Quickness evaluation of G-UNIV basic configuration

Parameter	**Flight Speed**			
	40 mph		50 mph	
	Basic	*GSM20*	*Basic*	*GSM20*
q_{pk} (deg/s)	31.0	30.6	30.4	29.8
$\Delta\theta_{pk}$ (deg)	29.7	29.7	21.0	21.0
$\Delta\theta_{min}$ (deg)	15.5	15.5	6.5	6.5
$\frac{q_{pk}}{\Delta\theta_{pk}}$ (s^{-1})	1.04	1.03	1.45	1.42

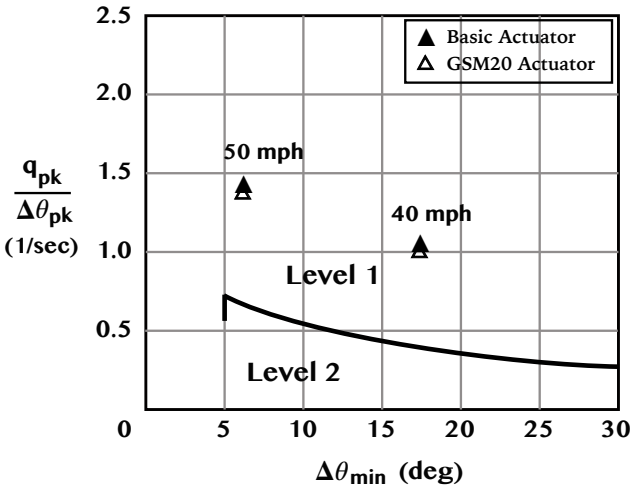

Figure 6.6: Pitch-quickness comparison for different actuation

In conclusion for the unaugmented short-period flight mode, the deployment of the GSM20 servo-actuator link model directly contributes to the phase-lag of the pitch response, thus, affecting the phase delay of the vehicle's dynamic response. This small degradation in the dynamic response is due to the increase in the dynamic complexities of the electro-mechanical linkage mechanism within the GSM20 servo-actuator, including the mechanical control links. This change, however, does not significantly affect other parameters such as the period and damping of the short-period oscillation. In general, the bandwidth characteristics listed in Table 6.2.1 revealed that the dynamic of the basic airframe of the G-UNIV is more likely of a rate-response type, as the bandwidth (ω_{BW}) exhibits the lesser of $\omega_{BW(gain)}$ and $\omega_{BW(phase)}$.

6.2.2 Unaugmented Phugoid Mode

Similar to the short-period evaluation, the phugoid dynamic stability parameters were quantified from the full order linear model as shown in Figure 6.1. For the unaugmented autogyro model, the phugoid mode was found to be consistent between the two different actuator models. It is well understood that the servo-actuator has relatively fast dynamics and usually operates at higher frequency region relative to the rigid body dynamics of an aircraft. Due to the huge difference between the two operating frequencies, the servo-actuator dynamics will not affect the mid-term response (phugoid mode) of the vehicle. Hence, the phugoid dynamic stability parameters quantified from the unaugmented simulation are same for both servo-actuator models as listed in Table 6.2.3.

Table 6.2.3: Unaugmented full-order time response parameters

Speed (IAS)	**Basic G-UNIV with GSM20 Actuator**	
	Eigenvalues (λ_{ph})	Phugoid Parameter
40 mph	$0.0692 \pm 0.455i$ (unstable phugoid)	$\zeta_{ph} = -0.150$ $\omega_n = 0.46$ rad/s $T_{ph} = 13.8$ sec $T_2 = 10.0$ sec
50 mph	$0.0148 \pm 0.394i$ (unstable phugoid)	$\zeta_{ph} = -0.0376$ $\omega_n = 0.39$ rad/s $T_{ph} = 15.9$ sec $T_2 = 46.8$ sec
55 mph	$0.0045 \pm 0.365i$ (unstable phugoid)	$\zeta_{ph} = -0.0124$ $\omega_n = 0.37$ rad/s $T_{ph} = 17.2$ sec $T_2 = 153.8$ sec
65 mph	$-0.0119 \pm 0.316i$ (Level 2)	$\zeta_{ph} = 0.038$ $\omega_n = 0.32$ rad/s $T_{ph} = 19.9$ sec $T_{1/2} = 58.2$ sec
75 mph	$-0.0063 \pm 0.260i$ (Level 2)	$\zeta_{ph} = 0.024$ $\omega_n = 0.26$ rad/s $T_{ph} = 24.2$ sec $T_{1/2} = 109.3$ sec

6.3 Stability Augmentation System Evaluation

Figure 6.7 shows the schematic block diagram of the G-UNIV SAS. Due to the dynamic changes caused by the inclusion of the new servo-actuator, the SAS controller obtained in Chapter 4 is fine-tuned to achieve the desired flying qualities criteria for the G-UNIV autogyro. The process of fine-tuning the SAS controller gains was time-consuming since the implementation of the new servo-actuator hardware model causes a degradation in the phase-lag of the vehicle. The evaluations of the vehicle's flying qualities in the short-period and phugoid modes with the SAS control enhancement are discussed in the following sections. As mentioned in Section 6.1.1, the vertical speed sensor and pitch-rate gyro are assumed to be highly accurate. As such, the transfer functions of both sensors are defined by a constant value of 1 and written by

$$G_{ws}(s) = 1 \tag{6.3.1}$$

$$G_{qs}(s) = 1 \tag{6.3.2}$$

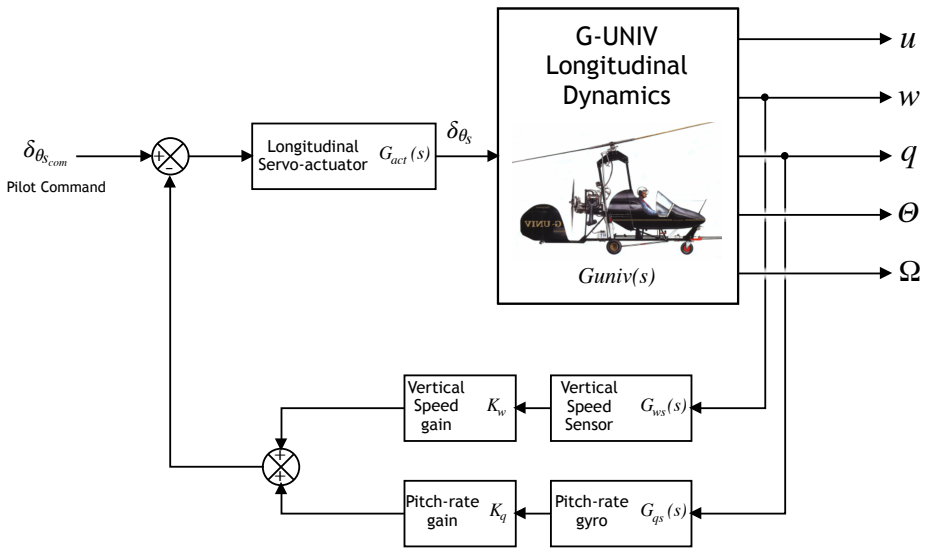

Figure 6.7: Schematic of G-UNIV SAS system

6.3.1 Evaluation of SAS in Short-period Mode

The same approach in Chapter 4 was carried out to fine-tune the SAS controller of the G-UNIV dynamic model with the GSM20 actuator in place. For the short-period mode response, the reduced-order version of Figure 6.7 was used to quantify the dynamic response parameters. The SAS state feedback gain $\mathbf{K} = \begin{bmatrix} K_w & K_q \end{bmatrix}$ for the whole flight spectrum was fine-tuned through the same pole-placement iteration process of choosing the correct eigenvalues that would give the best bandwidth and damping performance. The new set of poles with the new bandwidth characteristics and feedback gains for each flight state are listed in Table 6.3.1. For the short-period bandwidth characteristics, the table shows compliance with the bandwidth requirements of the proposed autogyro flying qualities criteria.

Figure 6.8 shows the example of bandwidth parameter changes with the SAS augmentation in place for the G-UNIV autogyro at 75 mph. With the correct placement of poles for the augmented model, the gain peak or overshoot in the previous bandwidth response managed to be minimised or eliminated. This process ended in an increase of the damping ratio where $\zeta_{sp} > 0.5$ across the flight regime. In fact, the phase-lag of the pitch response has also improved in the augmented model, as revealed in Table 6.3.1.

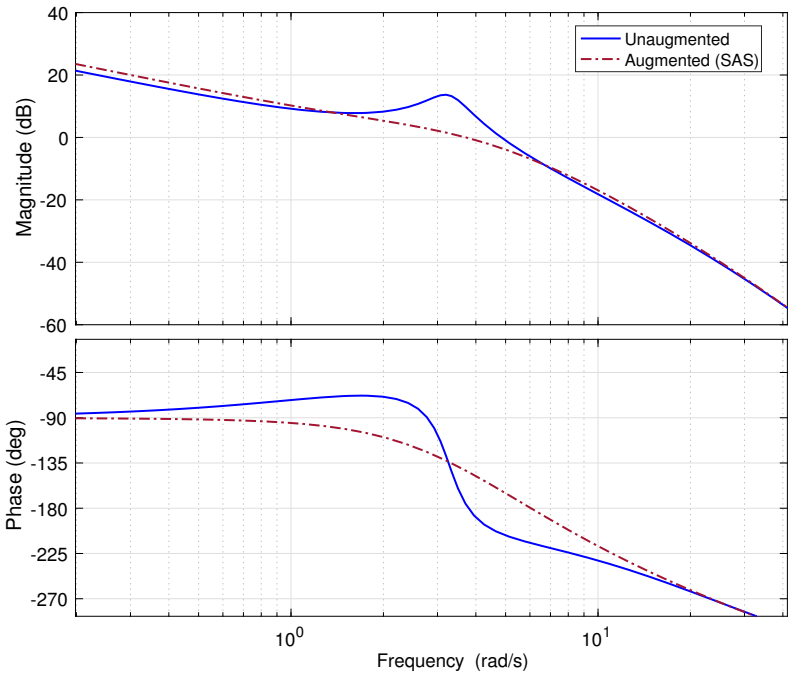

Figure 6.8: Bandwidth plot of short-period mode with SAS at 75 mph

Table 6.3.1: Bandwidth comparison of short-period SAS with GSM20 actuation

Flight Speed	**Parameter**	**Unaugmented**	**Augmented**
40 mph	Gain, $[K_w \ K_q]$	–	$[-0.0023 \quad 0.0615]$
	Eigenvalues, λ_{sp}	$-0.493 \pm 1.26i$	$-1.09 \pm 1.13i$
	Damping, ζ_{sp}	0.37	0.69
	$\omega_{BW(gain)}$ (rad/s)	2.25	2.57
	$\omega_{BW(phase)}$ (rad/s)	1.47	1.62
	τ_θ (msec)	73.0	70.3
50 mph	Gain, $[K_w \ K_q]$	–	$[-0.0047 \quad 0.0843]$
	Eigenvalues, λ_{sp}	$-0.492 \pm 1.79i$	$-1.40 \pm 1.44i$
	Damping, ζ_{sp}	0.27	0.70
	$\omega_{BW(gain)}$ (rad/s)	2.81	3.01
	$\omega_{BW(phase)}$ (rad/s)	2.02	2.07
	τ_θ (msec)	73.8	71.9
55 mph	Gain, $[K_w \ K_q]$	–	$[-0.0052 \quad 0.0969]$
	Eigenvalues, λ_{sp}	$-0.491 \pm 2.06i$	$-1.56 \pm 1.73i$
	Damping, ζ_{sp}	0.23	0.67
	$\omega_{BW(gain)}$ (rad/s)	2.27	3.26
	$\omega_{BW(phase)}$ (rad/s)	2.15	2.40
	τ_θ (msec)	92.8	72.1
65 mph	Gain, $[K_w \ K_q]$	–	$[-0.0076 \quad 0.1620]$
	Eigenvalues, λ_{sp}	$-0.487 \pm 2.60i$	$-2.52 \pm 2.16i$
	Damping, ζ_{sp}	0.18	0.76
	$\omega_{BW(gain)}$ (rad/s)	2.56	3.90
	$\omega_{BW(phase)}$ (rad/s)	2.66	3.20
	τ_θ (msec)	94.0	72.0
75 mph	Gain, $[K_w \ K_q]$	–	$[-0.0137 \quad 0.1918]$
	Eigenvalues, λ_{sp}	$-0.483 \pm 3.23i$	$-3.34 \pm 2.50i$
	Damping, ζ_{sp}	0.15	0.80
	$\omega_{BW(gain)}$ (rad/s)	0.44	4.13
	$\omega_{BW(phase)}$ (rad/s)	3.26	3.52
	τ_θ (msec)	96.4	73.2

The short-period bandwidth and phase delay for both dynamic responses of the G-UNIV (with and without the SAS) for the whole flight regime is mapped into the proposed short-period limit criteria as shown in Figure 6.9. The figure also revealed compliance with Level 1 flying qualities for the G-UNIV equipped with the SAS compared to the one without the SAS. Note that these results are based on the SAS controller that has been fine-tuned with the GSM20 servo-actuator hardware in place. Similar results of the basic actuator model as reported in Chapter 4 can be referred to for comparison. It can be seen from the limit that the two higher flight speed conditions (65 mph and 75 mph) that previously exhibit a PIO-prone condition were obviously improved through this control enhancement.

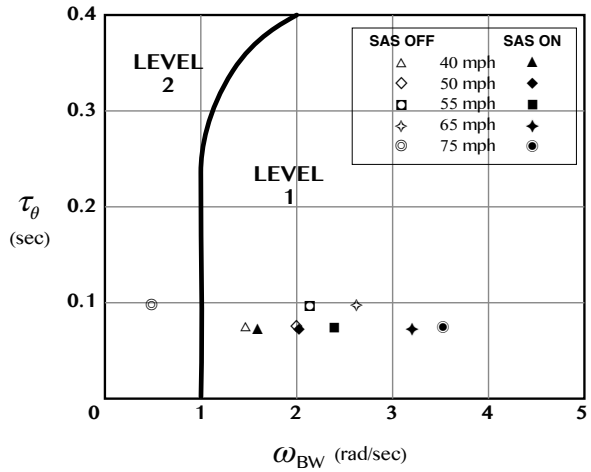

Figure 6.9: Bandwidth response limit to small-amp. input for the SAS

The 'Pitch-Quickness' response of the short-period SAS is now considered and compared with the unaugmented response. The parameters are listed in Table 6.3.2, and the limit is shown in Figure 6.10. The same evaluation has been done for the basic actuator model in Chapter 4, which can be used as a reference.

Table 6.3.2: Pitch-Quickness evaluation of SAS with the GSM20 actuator

Parameter	**Flight Speed**			
	40 mph		**50 mph**	
	Unaugmented	Augmented	Unaugmented	Augmented
q_{pk} (deg/s)	30.6	27.9	29.8	26.9
$\Delta\theta_{pk}$ (deg)	29.7	19.1	21.0	14.3
$\Delta\theta_{min}$ (deg)	15.5	15.2	6.5	10.9
$\frac{q_{pk}}{\Delta\theta_{pk}}$ (s^{-1})	1.03	1.46	1.42	1.88

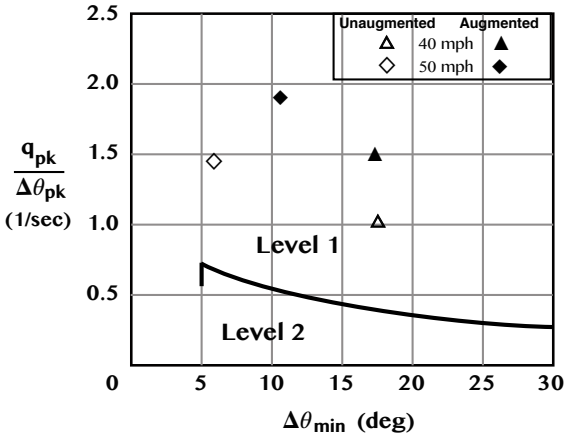

Figure 6.10: Pitch-quickness limit for medium-amp. input of the SAS

Note that the pitch-quickness results represent the pitch response of the vehicle at the lower flight speed regime (at 40 mph and 50 mph) due to a moderate-amplitude input being applied in steady-state flight condition. The values listed in Table 6.3.2 exhibit an improvement in the rate of change in pitch attitude, in which, the values of the quickness for both flight conditions are moved further away from the level 2 region, as shown in Figure 6.10. This is interpreted as an improvement in the pitch attitude responsiveness of the augmented autogyro model for every moderate-amplitude input changes. Autogyros with a lightly damped short-period pitch behaviour will produce a bigger pitch amplitude deflection ($\Delta\theta$) in response to a moderate-amplitude input. This higher amplitude oscillation would cause the vehicle to be less controllable and could lead to catastrophe especially at lower flight speeds if the oscillation is not sufficiently damped.

In this case, the short-period pitch damping function is effectively implemented by the SAS. For the G-UNIV autogyro, the pitch-quickness of the unaugmented response was already within the Level 1 flying qualities. However, the SAS augmentation produces a better result as the pitch quickness parameters for both flight conditions were moved further away from the Level 2 boundary.

6.3.2 Evaluation of SAS in Phugoid Mode

For the phugoid mode evaluation of the G-UNIV autogyro, the feedback gain obtained from the short-period SAS is implemented into the full order dynamic model as

$$K = \begin{bmatrix} 0 & K_w & K_q & 0 & 0 \end{bmatrix} \tag{6.3.3}$$

Hence, the new full order state feedback of the SAS for all flight conditions are written as

$$\begin{aligned}
&40 \text{ mph:} \quad K = \begin{bmatrix} 0 & -0.0023 & 0.0615 & 0 & 0 \end{bmatrix} \\
&50 \text{ mph:} \quad K = \begin{bmatrix} 0 & -0.0047 & 0.0843 & 0 & 0 \end{bmatrix} \\
&55 \text{ mph:} \quad K = \begin{bmatrix} 0 & -0.0052 & 0.0969 & 0 & 0 \end{bmatrix} \\
&65 \text{ mph:} \quad K = \begin{bmatrix} 0 & -0.0076 & 0.1620 & 0 & 0 \end{bmatrix} \\
&75 \text{ mph:} \quad K = \begin{bmatrix} 0 & -0.0137 & 0.1918 & 0 & 0 \end{bmatrix}
\end{aligned} \tag{6.3.4}$$

From the feedback gain K in (6.3.4), the phugoid mode parameters are then quantified from the simulation and listed in Table 6.3.3 for the flying qualities evaluation.

Table 6.3.3: Full order time response evaluation of SAS with the GSM20 actuator

Speed (IAS)	**Unaugmented**		**Augmented** $K = [0\ K_w\ K_q\ 0\ 0]$	
	Eigenvalues (λ_{ph})	Parameter	Eigenvalues (λ_{ph})	Parameter
40 mph	$0.0692 \pm 0.455i$ (undefined phugoid)	$\zeta_{ph} = -0.150$ $\omega_n = 0.46$ rad/s $T_{ph} = 13.8$ sec $T_2 = 10.0$ sec	$0.0424 \pm 0.328i$ (undefined phugoid)	$\zeta_{ph} = -0.128$ $\omega_n = 0.33$ rad/s $T_{ph} = 19.2$ sec $T_2 = 16.4$ sec
50 mph	$0.0148 \pm 0.394i$ (undefined phugoid)	$\zeta_{ph} = -0.0376$ $\omega_n = 0.39$ rad/s $T_{ph} = 15.9$ sec $T_2 = 46.8$ sec	$0.0182 \pm 0.291i$ (undefined phugoid)	$\zeta_{ph} = -0.063$ $\omega_n = 0.29$ rad/s $T_{ph} = 21.6$ sec $T_2 = 38.2$ sec
55 mph	$0.0045 \pm 0.365i$ (undefined phugoid)	$\zeta_{ph} = -0.0124$ $\omega_n = 0.37$ rad/s $T_{ph} = 17.2$ sec $T_2 = 153.8$ sec	$0.0098 \pm 0.279i$ (Level 3)	$\zeta_{ph} = -0.0351$ $\omega_n = 0.28$ rad/s $T_{ph} = 22.5$ sec $T_2 = 70.5$ sec
65 mph	$-0.0119 \pm 0.316i$ (Level 2)	$\zeta_{ph} = 0.038$ $\omega_n = 0.32$ rad/s $T_{ph} = 19.9$ sec $T_{1/2} = 58.2$ sec	$-0.0089 \pm 0.227i$ (Level 1)	$\zeta_{ph} = 0.039$ $\omega_n = 0.23$ rad/s $T_{ph} = 27.7$ sec $T_{1/2} = 77.9$ sec
75 mph	$-0.0063 \pm 0.260i$ (Level 2)	$\zeta_{ph} = 0.024$ $\omega_n = 0.26$ rad/s $T_{ph} = 24.2$ sec $T_{1/2} = 109.3$ sec	$-0.0111 \pm 0.154i$ (Level 1)	$\zeta_{ph} = 0.072$ $\omega_n = 0.16$ rad/s $T_{ph} = 40.8$ sec $T_{1/2} = 62.4$ sec

Table 6.3.3 revealed a small improvement in the phugoid mode parameters at higher speed regime, but degraded at the lower speed regime. Similar results were obtained and previously discussed, where the blended-feedback SAS only improve the short-period mode, but not the phugoid mode (see section 4.2.1.3 in Chapter 4). It is believed that the increased in short-period damping might contribute to a sluggish dynamic response specifically affecting the phugoid mode. One way to directly improve the phugoid oscillation is by having a speed-damper, which is out of the context of this study as to maintain the simplistic configuration of light autogyros.

Figure 6.11 shows the time response example of the full order dynamic response of the augmented G-UNIV autogyro at 75 mph with the new GSM20 servo-actuator link being applied. Note that, the full order simulation was based on a $\pm 2^{\circ}$ doublet input applied in 4 seconds with a fixed engine throttle setting. The dynamic response shows better short-period damping for the augmented model which also lead to a better phugoid oscillation.

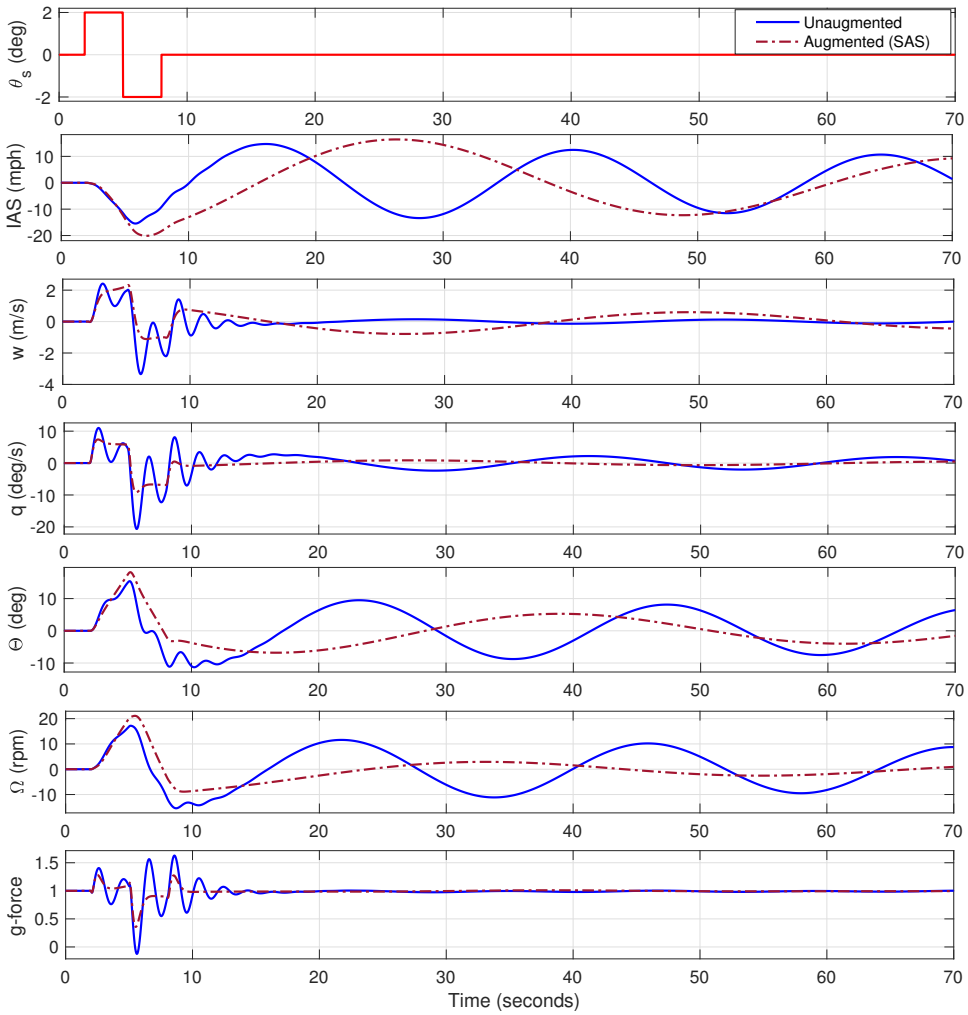

Figure 6.11: Full order mid-term response of G-UNIV with SAS at 75 mph

Nevertheless, the 'load factor' or the so-called 'g-force' were also given attention of affecting the stability of the rotorspeed degree of freedom. It was previously proposed in section 2.5.3 based on the recommendation by Gallup [60] that the g-force must not more than $1.2g$ in any circumstances or flight manoeuvre. In Figure 6.11, the maximum g-force acted on the vehicle is about $1.25g$ for an abrupt 2° input, which is a bit higher than the maximum g-force limit being proposed. However, whether or not violating the maximum $1.2g$ would lead to an unstable rotorspeed condition is still questionable, since the detailed study on this matter for an autogyro is not available in the public domain. The figure also shows that the same doublet input caused the rotorspeed to increase from 0 to 20 rpm before decaying abruptly about 26 rpm at the end of the command input, with the vehicle remaining in airborne according to the vertical speed (w). Another concern about this situation is whether or not the structural strength of the rotor blade would be able to withstand this amount of g-force without exceeding its structural integrity and breaking up. Therefore, it is important for the autogyro to comply with the proposed flying qualities requirements in short-period and phugoid mode, of which are considered as the main criteria to comply with.

6.4 The Rate-Command Attitude Hold System

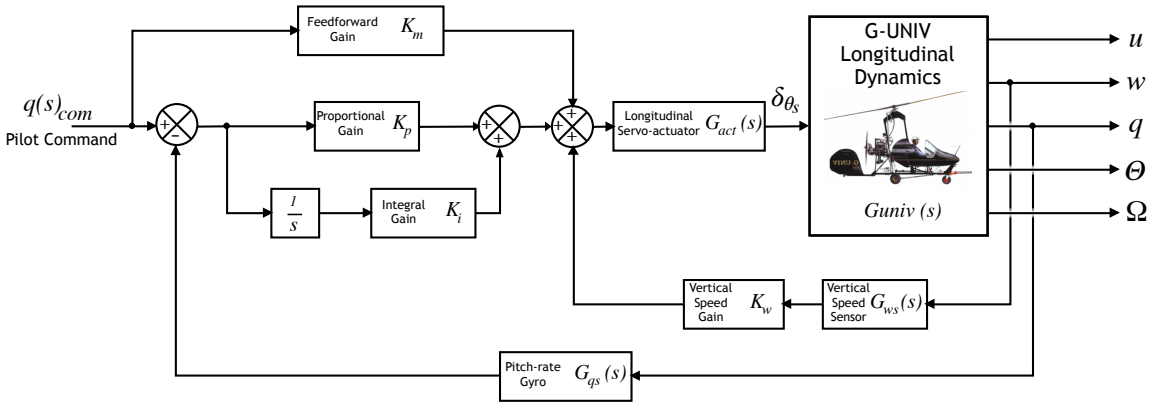

Figure 6.12: Full order Schematic of the G-UNIV RCAH

With the stability augmentation system in place, the manoeuvrability of the autogyro is upgraded through the implementation of RCAH, as shown in Figure 6.12. The RCAH enables a precise manoeuvre to be applied to the vehicle for every degree of stick deflection. Note that the RCAH controller implemented in this chapter is based on the same approach in Chapter 4, except that the new RCAH system in this chapter is based on the newly fine-tuned state feedback gain with the GSM20 servo-actuator being employed. In this section, only the short-period mode evaluations are carried out

for the RCAH system, as the phugoid evaluation is not applicable due to the attitude hold function provided by the RCAH system. As such, the linearised model of the short-period mode is used where the short-period oscillation parameters with RCAH can be quantified and analysed against the proposed flying qualities criteria.

6.4.1 Short-Period Mode Evaluation of the RCAH

The short-period mode evaluations were made based on the linearised reduced order model of Figure 6.12 with the RCAH controller being engaged. The short-period evaluations of the RCAH are divided into three different criteria or requirements (see Table 2.5.1); The *Bandwidth* requirement, *Time response* requirement, and *Pitch-quickness* requirement.

The *bandwidth* and *time-response* parameters (including the damping) were quantified from the simulation and listed in Table 6.4.1. Note that, employing the GSM20 servo-actuator into the G-UNIV model causes some changes in the short-period eigenvalues of the RCAH model. Hence, the RCAH controller was then fine-tuned through the same method as discussed in Chapter 4, and new gain values are listed in Table 6.4.1. Referring to the RCAH controller schematic in Figure 6.12, the integral gain $K_i = K_{q_e}$, the proportional gain $K_p = K_q$, and the feed-forward gain $K_m = (m - K_q)$. The 'm' is known as the feed-forward factor of the gain K_m that is used to reduce the integrator lag time in the RCAH controller and to have a faster response time. Detailed development of the RCAH controller has been discussed in Chapter 4.

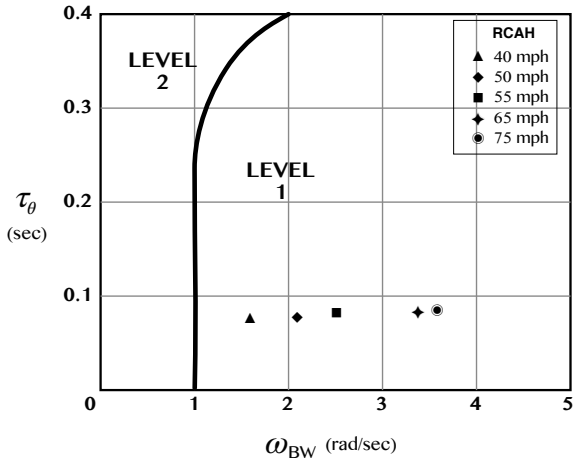

Figure 6.13: Bandwidth limit for short-term response with RCAH

Table 6.4.1: Bandwidth parameters of the short-period RCAH

Flight Speed	**RCAH Parameter**	
40 mph	Gain, $K_{sp} = [K_w \ K_q \ K_{q_e}]$	$[-0.0065 \quad 0.1267 \quad 0.1430]$
	Eigenvalues, λ_{sp}	$-1.10 \pm 0.994i$
	Damping, ζ_{sp}	0.74
	$\omega_{BW(gain)}$ (rad/s)	2.67
	$\omega_{BW(phase)}$ (rad/s)	1.68
	τ_θ (msec)	76.4
50 mph	Gain, $K_{sp} = [K_w \ K_q \ K_{q_e}]$	$[-0.0108 \quad 0.1656 \quad 0.2549]$
	Eigenvalues, λ_{sp}	$-1.32 \pm 1.12i$
	Damping, ζ_{sp}	0.76
	$\omega_{BW(gain)}$ (rad/s)	3.11
	$\omega_{BW(phase)}$ (rad/s)	2.15
	τ_θ (msec)	78.4
55 mph	Gain, $K_{sp} = [K_w \ K_q \ K_{q_e}]$	$[-0.0139 \quad 0.1907 \quad 0.3703]$
	Eigenvalues, λ_{sp}	$-1.43 \pm 1.31i$
	Damping, ζ_{sp}	0.77
	$\omega_{BW(gain)}$ (rad/s)	3.34
	$\omega_{BW(phase)}$ (rad/s)	2.48
	τ_θ (msec)	79.2
65 mph	Gain, $K_{sp} = [K_w \ K_q \ K_{q_e}]$	$[-0.0194 \quad 0.2739 \quad 0.6615]$
	Eigenvalues, λ_{sp}	$-1.75 \pm 1.29i$
	Damping, ζ_{sp}	0.81
	$\omega_{BW(gain)}$ (rad/s)	3.96
	$\omega_{BW(phase)}$ (rad/s)	3.35
	τ_θ (msec)	80.8
75 mph	Gain, $K_{sp} = [K_w \ K_q \ K_{q_e}]$	$[-0.0267 \quad 0.3306 \quad 0.8662]$
	Eigenvalues, λ_{sp}	$-1.78 \pm 1.47i$
	Damping, ζ_{sp}	0.77
	$\omega_{BW(gain)}$ (rad/s)	4.11
	$\omega_{BW(phase)}$ (rad/s)	3.66
	τ_θ (msec)	81.3

Table 6.4.1 shows a slight increase in the short-period damping across the flight regime albeit the slower response time from the phase-lag compared to the short-period SAS. The slower response time is understood as the result of increased in damping which

causes a slower rise time. All these effects can be seen through the changes on the RCAH bandwidth characteristics in the Table 6.4.1. These small effects, however, did not cause the bandwidth and time-response characteristics to deviate away from the proposed flying qualities bandwidth criteria. The new RCAH effect is also revealed in the bandwidth limit diagram in Figure 6.13. The bandwidth diagram also exhibits a Level 1 flying qualities for the G-UNIV autogyro equipped with the RCAH across the flight regime.

Table 6.4.2: Pitch-Quickness parameters of G-UNIV with RCAH

Parameter	**Flight Speed**	
	40 mph	**50 mph**
q_{pk} (deg/s)	11.7	16.1
$\Delta\theta_{pk}$ (deg)	7.58	8.05
$\frac{q_{pk}}{\Delta\theta_{pk}}$ (s^{-1})	1.54	2.0
$\Delta\theta_{min}$ (deg)	5.94	5.93

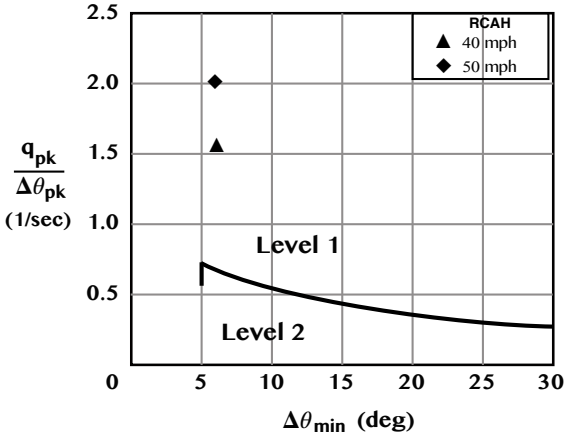

Figure 6.14: Pitch-quickness limit of the G-UNIV with RCAH

The 'Pitch-Quickness' of the vehicle with RCAH is also quantified where a moderate amplitude input that excites a pitch amplitude of 6° (more than 5°) is applied. The quickness parameters for the RCAH are shown in Table 6.4.2 and also mapped into the pitch-quickness flying qualities limit in Figure 6.14 for reference. It is found that the pitch-quickness of the G-UNIV with the RCAH augmentation obviously comply with the Level 1 flying qualities limit. The implementation of the RCAH augmentation changed the position of the pitch-quickness parameters in the limit compared to the previous SAS augmentation (see Figure 6.10), but none of the two configurations degrading the quickness level.

6.4.2 Full Order Evaluation of the RCAH

Figure 6.15 shows a full-order time response of the G-UNIV autogyro at flight speed of 75 mph with the RCAH in place. The vehicle is given a pitch-rate command $q_{com} = \pm 2$ (deg/s) in the form of doublet input for a duration of 12 seconds. The q_{com} is seen to be well tracked by the pitch-rate response (q) to zero steady-state error with the rise-time of approximately 185 msec. The first +2 deg/s of the command input q_{com} represents a pull-back stick deflection that directly causes the vehicle to pitch up at the rate of 2 deg/s in the first 6 seconds. This is then followed by a -2 deg/s push-forward stick which causes a nose-down pitch attitude back to the original pitch for the rest of the 6 seconds duration. Theoretically, a +2 deg/s q_{com} input is expected to produce a 12° pitch attitude (Θ) for the 6 seconds duration. In reality, the simulation produced the maximum pitch attitude of about 12.7° for the same time duration. The overshoot is considered as contributed by the attitude response delay with the same given rise-time. Since the engine throttle was set to the trim setting to produce a constant airspeed of 75 mph, the nose-up attitude obviously causes a 25 mph decreased in the forward airspeed before being restored with a nose-down manoeuvre of the -2 (deg/s) forward stick. The simulation was made without the throttle control to accurately quantify the dynamic response of the vehicle with the RCAH control. In fact, it is expected that the throttle control is manually performed by the pilot.

The rotorspeed Ω also shows the same amount of changes with the pitch attitude within the same time duration. These changes in the rotorspeed are expected since the rotorspeed is known to be closely coupled with the pitch attitude of the autogyro. Consequently, the load factor or the g-force of the vehicle revealed a $1.1G$ at the point where the abrupt manoeuvre of ± 2 (deg/s) was taken place. This is considered as an improvement compared to the SAS augmentation in Figure 6.11.

For this full-order G-UNIV response with RCAH in place, the 'rate-attitude hold' function of the controller actually holds the rate changes in pitch, thus, turn all dynamic response modes into non-oscillatory mode except for the short-period mode. As such, the phugoid oscillation parameters are then impossible to be quantified and defined according to the proposed flying qualities criteria in the RCAH mode. In fact, there will be no issue regarding the dynamic stability of the vehicle in phugoid mode with the RCAH control in place.

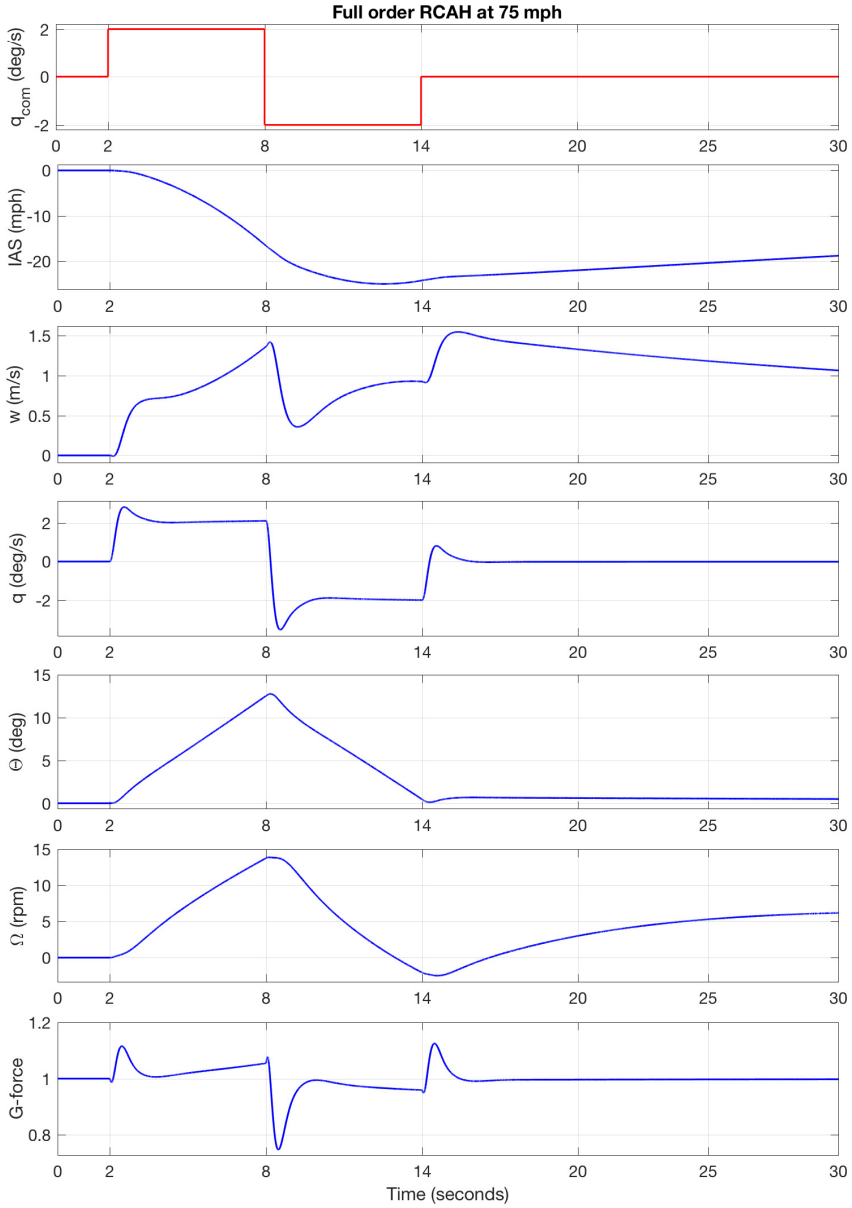

Figure 6.15: Full-order response of G-UNIV with RCAH at 75 mph

6.5 Evaluation Using the Nonlinear Model

The nonlinear simulation of the autogyro is made to give a complete picture of the vehicle's behaviour according to its mathematical model. In the research, the nonlinear mathematical model of the autogyro was initially modelled and run in the Matlab environment. The same nonlinear model can also be implemented in a graphical way with Simulink blocks, so that analysis, testing and model manipulation can be done easily.

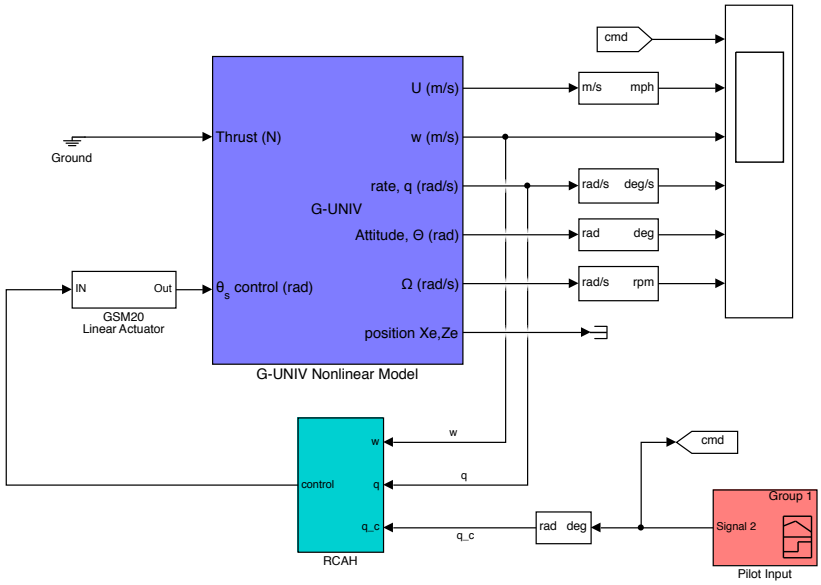

Figure 6.16: Schematic of Nonlinear G-UNIV model with RCAH controller

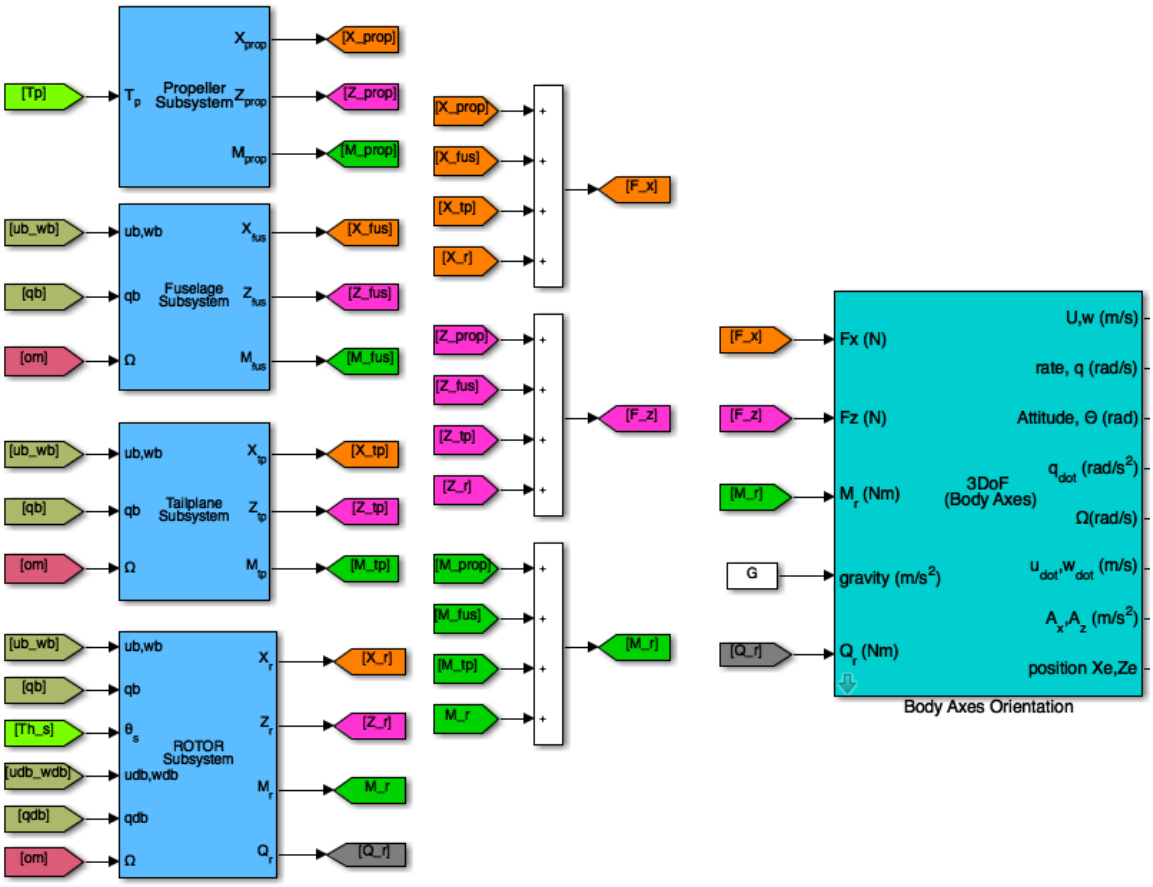

Figure 6.17: G-UNIV nonlinear equations of motion in Simulink environment

For the G-UNIV autogyro, the nonlinear mathematical model that was developed in Chapter 3 is translated to Simulink block diagrams, of which the nonlinear simulation of the vehicle can be done. Figure 6.16 shows the Simulink block diagram of the nonlinear G-UNIV model with the RCAH controller and the new linear EMA in place.

Figure 6.17 shows the breakdown of the nonlinear G-UNIV model, which clearly indicate the force and moment calculations from all subsystems in Simulink blocks. The longitudinal flight attitudes of the autogyro are consequently calculated in the 'Body Axes Orientation' block, of which the dynamic behaviour of the vehicle can be quantified and evaluated. Note that the simulation of Simulink block diagrams cannot be done without the initial conditions being set. For the G-UNIV autogyro, the trim values at specific flight condition are used as the initial condition of the Simulink blocks.

6.5.1 RCAH Performance with Atmospheric Disturbance

Stability evaluations of the augmented nonlinear model will be more realistic by considering the responsiveness of the model against atmospheric disturbances. A working RCAH controller will try to maintain the attitude-hold character of the controller even under atmospheric disturbances.

MIL-F-8785C [27] specifies standardised turbulence deviations in three different classifications based on its severity; light, moderate or severe [149]. For example, *light* turbulence was standardised to have velocity of 1.524 m/s (5 ft/s), *moderate* turbulence with velocity of 3.048 m/s (10 ft/s), and 4.572 m/s (15 ft/s) for *severe* turbulence. According to the references, these standard deviations are only applicable for flight altitude of more than 609 m (2000 ft), as the turbulence deviations may change significantly as the altitude goes further away from the sea level. However, for the sake of evaluating the RCAH control, those standard deviations can be used with the assumption that the maximum flight altitude of a light autogyro is more than 2000 ft. Hence, a discrete gust model is used to replicate the wind gust, which generally represents the linear turbulence model in simple square or step signals. Furthermore, the amplitude of wind gust being set for the simulation was higher than the standard, just to see how does an autogyro that is equipped with RCAH augmentation responded.

Figure 6.18 and 6.19 show the disturbance model (discrete gust) developed from Simulink's Aerospace blockset, as part of the G-UNIV nonlinear block diagram. The discrete gust model was originally presented by a 3-dimensional wind gust: The horizontal wind gust (u_g), the lateral wind gust (v_g), and the vertical wind gust (w_g). All wind gust

values were given in standard SI unit (m/s). Since the simulation was meant for the longitudinal mode of the autogyro, only u_g and w_g were used in the evaluation.

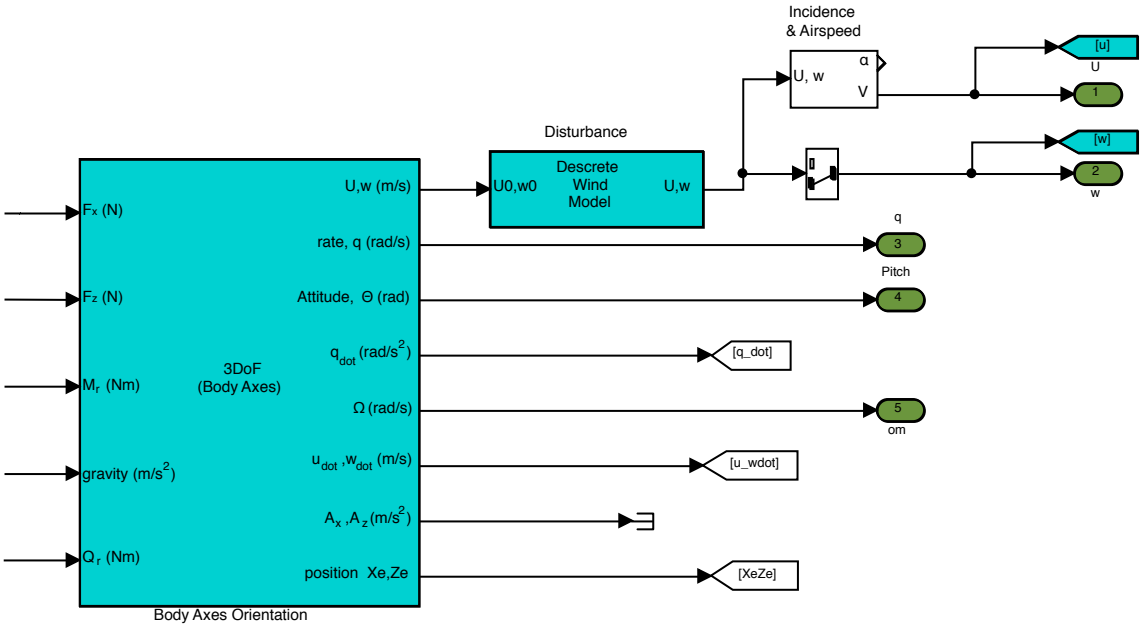

Figure 6.18: G-UNIV nonlinear model with the 'Disturbance' block

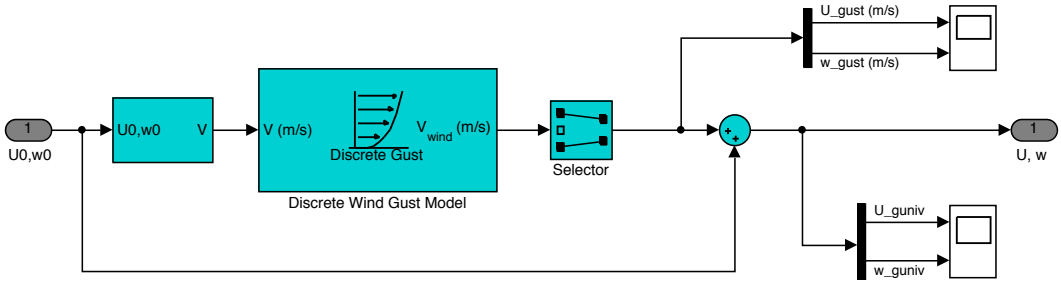

Figure 6.19: Details of the 'Disturbance' block diagram (discrete gust)

Figure 6.20 shows a headwind gust with a given amplitude of $u_g = 4$ m/s applied to the G-UNIV equipped with RCAH controller at the flight speed of 75 mph. The length of the gust was set to $dx = 50$ m, with the engine throttle setting at its constant trim. To evaluate the functionality of the RCAH controller, the control stick was given an abrupt input pulse of 1 deg/s for 6 seconds (from $t = 4$ s to $t = 10$ s) as seen in the figure. The headwind gust was then applied on the G-UNIV in the form of a negative step input (at $t = 15$ s) with a slope that represents the length of the gust (dx). In this case, since the autogyro flies with a forward speed of 75 mph (33.5 m/s), the slope settled at $t = 16.5$ s due to the gust length of $dx = 50$ m. That was about 1.5 s of time duration for the autogyro to pass through the 50m length headwind gust.

The attitude responses of the G-UNIV are also predicted according to the functionality of the RCAH controller. The 1 deg/s control input was well captured by the attitude hold controller, which is clearly shown by nonlinear attitude responses in Figure 6.20. The simulation results can be seen corresponding to what would be expected for an attitude-hold controller. For example, the pitch-rate captures the 1 deg/s command input with a rise-time of 199 msec. The pitch angle also shows more or less, the same compliance with a 6.1° pitch angle in approximately 6 sec. The rotorspeed also revealed the same response as of the pitch attitude response. Nevertheless, the RCAH was seen to respond well to the headwind disturbance. The effect of the headwind can be seen as a small bump on most of the attitude responses. The pitch-rate, for instance, is seen to have a small bump of about 0.4 deg/s and a small pitch up attitude due to the headwind, before recovery and settling back to the commanded pitch rate, q_{com}.

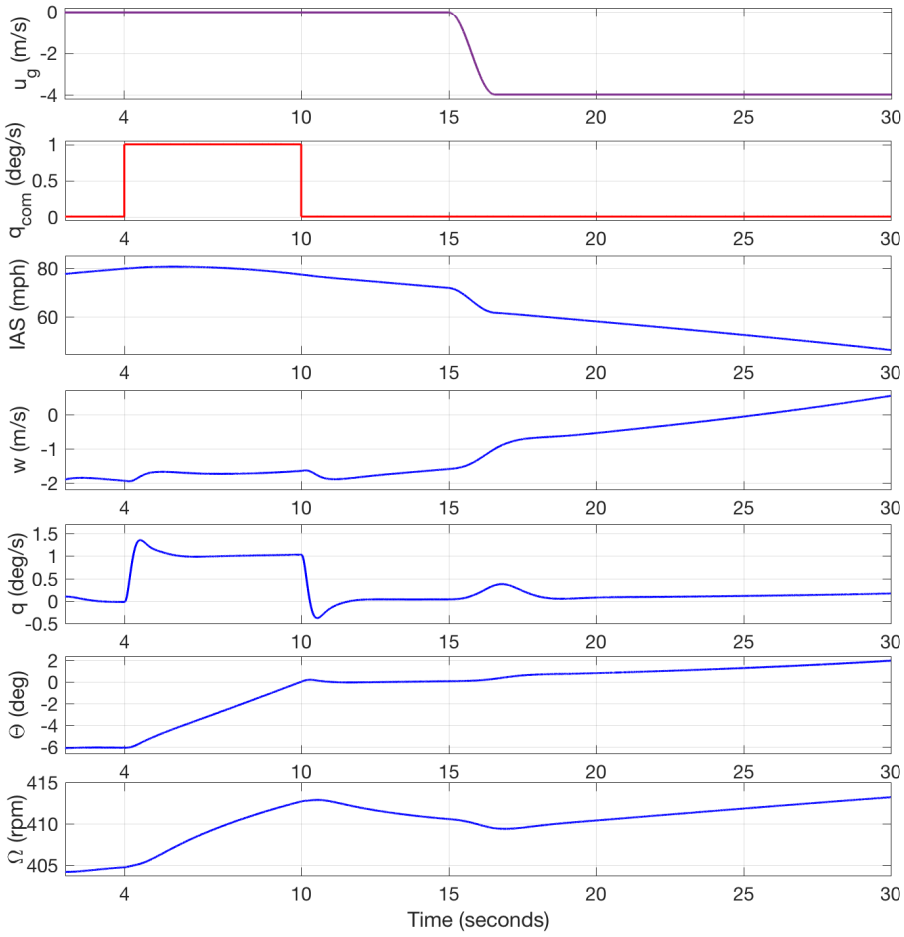

Figure 6.20: Nonlinear response of RCAH with headwind gust at 75 mph

The effect of an upwind gust disturbance w_g to the attitude response of the G-UNIV is shown in Figure 6.21. In this case, the gust was set to an amplitude of 2 m/s, with the gust length (dz) of 20 m. This can be seen in the figure as a negative step with a steeper slope compared to the previous headwind disturbance. Due to the forward

speed of the autogyro, it requires about a time duration of 0.6 sec for the aircraft to pass through the 20 m length gust. Since the disturbance is in the normal direction of the aircraft, the most affected attitude response are the aircraft's vertical speed (w) and the pitch-rate (q). The figure revealed that the autogyro climbs with a vertical rate of 2.7 m/s in 0.6 sec, before being restored back by the attitude hold system. Simultaneously, the pitch-rate of the autogyro shows a +1.2 deg/s deflection due to the upwind gust, before immediately being restored by the attitude-hold system. The corrective action of the attitude-hold system also causes a counter pitch-rate deflection about −1.3 deg/s due to the short-period damping, before settling at zero steady-state error to the command input. Figure 6.21 also shows a small effect on the autogyro pitch attitude, but the rotorspeed significantly affected by the upwind gust with an approximate 5 rpm reduction before being recovered back to its normal speed.

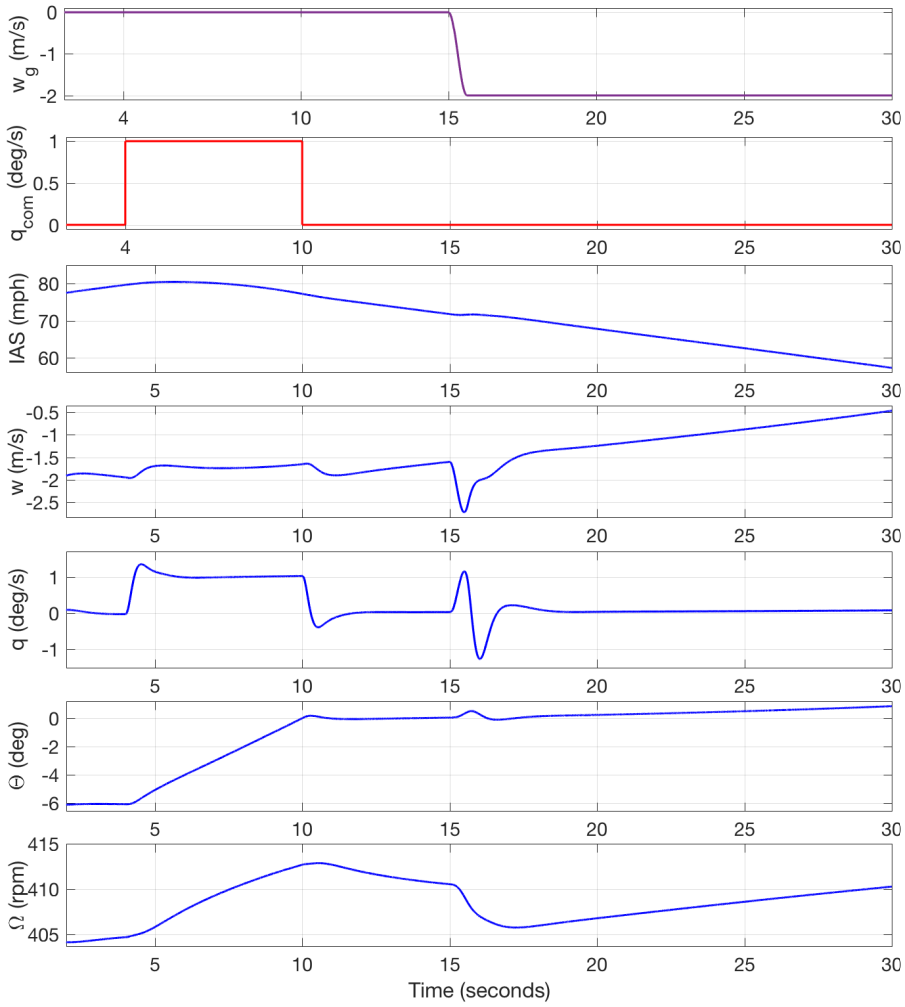

Figure 6.21: Nonlinear response of RCAH with upwind gust at 75 mph

It can be concluded from the simulation results that the RCAH has successfully employed and functional for the nonlinear G-UNIV model with the GSM20 linear actuator

hardware model in place. The G-UNIV attitude response of the result shows that the rate-command function of the controller tracks the pilot command signal quite well. It is then assumed that the G-UNIV light autogyro flies with an improved flying qualities performance with the aid of a simple automatic control enhancement.

6.6 Chapter Summary

The main objective of this chapter is to evaluate the longitudinal control enhancement of a light autogyro equipped with the actual servo-actuator dynamic model according to a specific longitudinal flying qualities criteria.

In general, the longitudinal flying qualities requirements for light autogyros were divided into three different criteria: The short-period mode criteria, the phugoid mode criteria, and the load factor or g-force criteria.

To maximise the possibility that the control enhancement will be working on a real autogyro in the future, three different strategies have been used in the evaluations:

a) *Evaluation of the unaugmented model.*

   This evaluation was meant to understand the direct effects of the new hardware configuration (the servo-actuator model) on the autogyro's dynamic response, without the control enhancement in place.

   – The deployment of the new GSM20 servo-actuator dynamic model directly contributes to a small phase-lag in the short-period oscillation of the whole vehicle. This effect was well understood due to the complexity of the GSM20 servo-actuator dynamics compared to the basic actuator model. The phugoid oscillation, however, was not affected by the servo-actuator configuration.

b) *Evaluation of the augmented model.*

   Evaluations were made for both, the autogyro equipped with the Stability Augmentation System (SAS), and then the autogyro equipped with the Rate-Command Attitude Hold System (RCAH).

   – For the Stability Augmentation System (SAS), the short-period mode of the autogyro was improved. The bandwidth and time response parameters of the short-period mode criteria revealed a Level 1 flying qualities for the

SAS control enhancement. However, the SAS control evaluation revealed a less significant improvement on the phugoid criteria especially on the lower flight speed regime of the vehicle, which remains unstable. Furthermore, the compliance of the g-force requirement was not met throughout the flight regime.

- For the Rate-Command Attitude Hold System (RCAH), the bandwidth and time response parameters of the short-period mode criteria also revealed Level 1 flying qualities. The pitch-rate input command was found to track the vehicle's pitch-rate response for the whole flight regime well. For this type of control system, the phugoid mode was turned into a non-oscillatory motion due to the attitude-hold function of the RCAH control. Since the attitude-hold function of the RCAH was working well for the whole speed regime, the phugoid oscillation is then considered as stable, thus, complying with the Level 1 flying qualities of the phugoid mode criteria. Nonetheless, the g-force criteria were fully met for the RCAH control throughout the flight regime.

c) *Evaluation using the nonlinear model.*

The Rate-Command Attitude Hold System (RCAH) was then employed into the nonlinear dynamic model of the G-UNIV autogyro and the flying qualities were re-evaluated.

- It was found that the dynamic response of the vehicle works well with the attitude hold function of the RCAH controller. Nevertheless, the longitudinal atmospheric disturbance was also applied to the nonlinear simulation for better realisation of the control enhancement. The RCAH controlled autogyro correctly managed the longitudinal atmospheric disturbance in the form of headwind and upwind gust.

According to the evaluation results, the Rate-Command Attitude Hold System (RCAH) was found to be the most suitable option to be implemented for the autogyro's control enhancement. The RCAH results have shown good compliance with all longitudinal flying qualities requirements for the light autogyro. It is assumed that with this control enhancement in place, piloting this vehicle should be easier and enjoyable.

On the other hand, the Stability Augmentation System alone was found to be unsuitable for autogyro control enhancement, especially for the phugoid mode. The unstable phugoid oscillation of the vehicle requires another damping mechanism to be implemented, which is the speed damper. This, however, would result in a more complicated control hardware, thus, almost impossible to be implemented on 'light autogyros'.

Chapter 7

Conclusion and Recommendation

7.1 Research Goal

The main goal of the research was stated in Chapter 1, i.e to demonstrate that the flying qualities of light autogyros can be significantly improved using conventional control techniques and hardware, making them safer and a more attractive vehicle to operators.

To achieve the main goal, several objectives were set, as stated in the following:

(i) *Development of a Nonlinear Light Autogyro Mathematical Model*,

(ii) *Propose a Suitable Flying Qualities Requirements for Light Autogyros*,

(iii) *Development of Control Enhancement Methods for Light Autogyros*,

(iv) *Development of a Nonlinear Hardware Model for the Control Enhancement*,

(v) *Evaluations of the Effectiveness of Control Enhancement on Autogyro Flying Qualities Performance.*

In this chapter, how much or to what extent the main goal and objectives have been met will be discussed.

7.2 Research Conclusion

(i) *Development of a Nonlinear Light Autogyro Mathematical Model*

The development of a nonlinear mathematical model of a light autogyro were successfully conducted. It is important to mention in this concluding remark that the mathematical model being developed was a full order nonlinear model. However, the mathematical model was later reduced to a longitudinal mode so that the focus of the research is narrowed down to the main stability issues experienced by most light autogyros, which is the longitudinal instability. The mathematical model, known as 'Autogyro Rotor-Disc Simulation Model' (ARDiS) was extensively modified from the conventional 'rotor-disc' Helicopter Generic Simulation package (HGS) that was originally made for helicopter simulation [22].

In the ARDiS model, the rotorspeed degree of freedom was successfully included in the model to account for the nature of autorotating flight for light autogyros. From this important feature, the strong coupling between the rotorspeed and the pitch attitude of the vehicle were managed to be quantified and evaluated. Other important modifications include the kinematics of the rotor subsystem that was modified to suit for multiple axes transformations including the 'shaft-offset' which is quite common but significant for most light autogyros. The specific lift curve characteristics of the NACA 8-H-12 aerofoil was also embedded into the rotor subsystem. This modification has caused significant changes in the rotor-disc forces and moments calculation, which also contributed to a better correlation with the real autogyro flight data. Another significant achievement in this model is the 'flapping dynamics' modification that includes the 'teetering' effect of the rotor blades, as part of the essential attributes of light autogyros. One last modification that was successfully carried out on the ARDiS model was the rotor-disc dynamic inflow model, which is opposite compared to a conventional helicopter.

Validation of the ARDiS model was successfully made between the model and the flight data for the G-UNIV autogyro in longitudinal trim flight. The good agreements regarding magnitude and trend with the flight data, especially on the pitch attitude and control parameter gives more confidence for the ARDiS model. Additionally, verification of the effect of longitudinal CG position with the control margin of the vehicle proves the effectiveness of the model in the simulation. Most importantly, simulation results prove that the simplicity of the rotor-disc calculation approach in the ARDiS enables the model to run on a basic machine with minimum computational effort.

(ii) *Propose a Suitable Flying Qualities Requirements for Light Autogyros*

New flying qualities requirements for light autogyros were proposed. It was found that the dynamic flight characteristics of light autogyros are a mix of conventional fixed-wing aircraft and helicopters. Surveys on the safety track records of light autogyro in the UK also found some intriguing facts about the longitudinal instability of most typical autogyros. In more detail, for a typical light autogyro, the phugoid oscillation was either lightly damped or unstable while the short-period mode was also found to be lightly damped. Investigations also found at least two unique parameters that influence the longitudinal stability of light autogyros, which also affect each other in the event of rapid manoeuvres as follows;

- the vertical distance of the propeller thrust line relative to the vehicle's CG, and
- the instantaneous distance of the rotor thrust line relative to the vehicle's CG,

Managing these two parameters in the event of rapid manoeuvres in flight was also found to be quite challenging for an inexperienced pilot and could lead to catastrophe. Additionally, it was also found on most old-generation or typical light autogyros that their tailplane is less effective and does not significantly contribute to pitch stability.

From all of those above-mentioned unique dynamic stability attributes, the flying qualities requirements to be proposed for light autogyros were carefully made. The process started by investigating the existing flying qualities standards for conventional aeroplanes and helicopters. In this particular stage, the existing airworthiness standards, the BCAR Section T [21] was included as the underlying guidelines for the new flying qualities attributes. Finally, the flying qualities criteria were then chosen by looking at the most sensible among the existing aeroplane and helicopter criteria, according to the unique dynamic stability attributes of typical light autogyros. Note that the proposed flying qualities requirements also include the evaluation method to be used. The flying qualities criteria were segregated in three parts; the short-period mode, the phugoid mode and the rotorspeed criteria.

The proposed flying qualities requirements in this part are considered as a preliminary. It is an iterative process as it involves thorough quantitative and qualitative investigations with flight testing and subsequent refinement until it is mature enough to be established and to be included in regulatory criteria.

(iii) *Development of Control Enhancement Methods for Light Autogyros*

The control enhancement for light autogyros was developed based on the proposed autogyro flying qualities requirements. The basic premise that was set as part of the objective for the control enhancement was to have a low cost and simple controller, which is crucial for a typical light autogyro. Initially, the nonlinear ARDiS model was linearised into a fifth order longitudinal mode state-space model. The flying qualities evaluations of the vehicle were made according to the proposed flying qualities requirements. The use of linear model enables the short-period and the phugoid mode of the vehicle to be quantified and evaluated accordingly.

To justify the necessity of having a flight control enhancement for the autogyro, the bare airframe (open loop) model was first evaluated according to the proposed flying qualities requirements. It was found that the bare airframe model of the G-UNIV autogyro failed the compliance test. The bandwidth response of the vehicle's short-period mode showed a PIO-prone condition at higher forward airspeed. The same non-compliance condition was also found on the phugoid evaluation, which indicated an unstable dynamic condition, especially at lower airspeeds. Identification of poor open loop longitudinal flying qualities also justified the necessity to have enhancement control for the vehicle as the most effective solution.

The design of the control enhancement was broken into two parts to suit for the flying qualities requirements; the rate-response control, and the rate-command attitude control. The rate-response control in the form Stability Augmentation System (SAS) was used in the research to augment the short-period oscillation. This was implemented by first, reducing the full order longitudinal model into a second-order short-period mode. Blended feedback through pole-placement approach was used for the SAS, with feedback gain settings that resulted in an improved damping and response bandwidth. In contrast, the short-period augmentation did not significantly improve the phugoid oscillation, as what is needed for the phugoid mode is additional speed damping. However, to introducing a speed damping on a simple light autogyro will increase the complexity of the controller hardware, and thus, defeating the objective to have a simple, low-cost control enhancement. This is also crucial to maintain the simplicity of a light autogyro, concerning the operating cost and systems complexity. As such, no design on the additional speed control was attempted in this research, and the throttle setting was assumed to be manually controlled by the pilot.

Alternatively, the Rate-Command Attitude Response (RCAH) control was introduced to give the pilot a better control of the aircraft manoeuvres. The simulation results generated from the RCAH were quite promising, with a convincing zero steady-state pitch-rate tracking response. In specific, the evaluation of both, short-period and

phugoid mode resulted in a flying qualities improvement of the G-UNIV autogyro following the proposed criteria.

The implementation of the flight control enhancement according to the proposed flying qualities objectives was achieved, with the default actuator dynamics being introduced as part of the autogyro's basic configuration.

(iv) *Development of a Nonlinear Hardware Model for the Control Enhancement*

The basic premise that was initially set was to employ simple low cost hardware to serve the purpose of a control actuation medium between the pilot, the controller and the vehicle response. An actual 'of-the-shelf' electromechanical linear actuator (EMA) was chosen to be implemented as part of the autogyro's hardware configurations. Initially, the maximum force exerted at the control linkages were estimated with a rigid-body calculations with trim values being used. The suitable EMA servo-actuator was then chosen according the load requirement that was previously estimated.

In this part of the research, the nonlinear mathematical model of the servo-actuator hardware including the basic control linkages of the G-UNIV autogyro was formed and successfully used in the control enhancement. The servo-actuator hardware itself contains two main parts; A 'Brushless-type' DC motor with internal sensors to provide the servo-actuation controls, and the linear actuator in the form of a plunger to implement the actuation force to the control linkage. A mathematical model of the whole servo-actuator and the G-UNIV mechanical control linkages was developed using the Simscape™ Physical Modelling package with the help of a 3D CAD software called Onshape®. Later in this part, the complete nonlinear model of the servo-actuator, together with the autgoyro control linkages were then linearised to ease the control enhancement simulation. Prior to this, both, the linear and nonlinear servo-actuator models were successfully evaluated and verified.

(v) *Evaluations of the Effectiveness of Control Enhancement on Autogyro Flying Qualities Performance*

Final evaluations of the G-UNIV autogyro with the control enhancement were made, with the new servo-actuator dynamic model being deployed. Initially, an open loop (unaugmented) simulation was used to understand the effect of the new servo-actuator model on the dynamic response of the G-UNIV autogyro. The phase-delay of the unaugmented pitch response was found to be significantly increased with the new servo-actuator model, which consequently degrades the effectiveness of the control enhancement. Therefore, all control enhancements were fine-tuned with new feedback

gains and re-evaluated against the proposed flying qualities criteria. According to the new evaluations, there was a small change in flying qualities of the augmented model, but it still complies with the proposed flying qualities requirements. In fact, the time-response simulation of the nonlinear G-UNIV model was successfully made for the RCAH controller with the servo-actuator hardware model in place. Atmospheric turbulence in terms of discrete wind gusts in the longitudinal mode was also imposed into the nonlinear simulation and managed to be controlled by the flight controller.

As a final concluding remark, the control enhancement of the light autogyro was successfully implemented, with the longitudinal flying qualities performance of the G-UNIV were significantly improved. These flying qualities performance include the short-period and the phugoid mode, and consequently, the rotorspeed mode.

7.3 Recommendation for Future Work

(a) Extension of the ARDiS Simulation Package

- The ARDiS was designed as a generic package for autogyros simulation. It is recommended that the ARDiS to be applied on different types of autogyros in the future to build more confidence on the simulation package.
- As the only 'rotor-disc' or 'multiblade' simulation package available for autogyros simulation, it is also recommended that thorough investigation be carried out to solve for the uncertainties on the rotor blade's aerodynamic forces and moments calculations. Small modifications were made on the ARDiS to include the zero angle of attack coefficient that represents the non-symmetrical shape of the NACA 8-H-12 aerofoil. However, it is believed that the modification was not good enough to improve the degree of fidelity of the simulation package, as good as the individual-blade approach. Hence, the future investigation is justified and worthwhile to be carried out to improve the simulation package.
- In the ARDiS simulation package, the forces and moments of the G-UNIV's fuselage and empennage (which include the rudder and tailplane) were calculated through lift and drag approximations from the VPM-M16 autogyro. Therefore, it is recommended for the G-UNIV autogyro to be wind-tunnel tested, so that the forces and moments calculation will be more accurate according to its own lift and drag coefficients.

(b) Issues Relating to the Proposed Flying Qualities Requirements

- It is important to understand that in order to create a good flying qualities requirements and criteria for any flying vehicle, extensive investigations and flight tests are required. Hence, the process to produce a good and promising flying qualities requirements for light autogyros may take time, cost and efforts to be completed. However, the process has to be started at some point with a proposed flying qualities requirements, such as those presented in Chapter 3. Therefore, it is strongly recommended that the process to be continued with thorough investigations, simulations and flight tests so that the currently proposed flying qualities requirements can be improved consequently, for the benefits of all.

(c) Issues Relating to the Control Enhancement

- It is important to mention that when the study is conducted, the G-UNIV autogyro was already being donated to the Flying Museum in Edinburgh, thus, the actual airframe was no longer available to be accessed. This included the geometrical locations and dimensions of the mechanical control links, electrical hardware, such as the alternator, battery pack, and other electrical equipments that were installed permanently on the vehicle. All these are called the 'minimum equipment list' that must be available on board the vehicle prior to fly. Keeping track the history of these equipments are essential if a modification to be carried out in the future. Since all these information were not available during the study, the hardware modifications were also difficult. Hence, for the control hardware requirements, all hardware dimensions were based on estimated values. However, since the objective of the controller part was to demonstrate that the control enhancement can be implemented on light autogyros, the results produced were accepted. Therefore, it is recommended that the study on the same particular subject to be continued in the future with a complete actual hardware, whether or not with the same vehicle (the G-UNIV), so that the results will be more realistic.

Appendix A

Rotor-disc Inflow Model

For a typical rotorcraft, understanding the dynamic of airflow that passes through the rotor disc is essential. The modelling of dynamic inflow of a rotor is done according to the objective of what the rotor model is designed for. For an autogyro that operates at lower speed flying region with relatively low operating rotorspeed, the rotor-disc induced velocity model is based on Glauert's inflow model, which is more simple and fundamental, and typically being used in conventional rotor-disc or multiblade helicopter modelling approach. In this approach, the induced airflow passes through the rotor-disc (denoted as v_i) is represented by variations of inflow in a linear form by three different inflow terms or components over the whole disc; the uniform term (v_0), the longitudinal inflow term (v_{1_s}), and the lateral inflow term (v_{1_c}), written by

$$v_i = v_0 + \frac{r_b}{R}(v_{1_c}\cos\psi + v_{1_s}\sin\psi) \tag{A-1}$$

which is normalised with the term (ΩR) to ease the calculation, and written by

$$\lambda_i = \lambda_0 + \bar{r}_b(\lambda_{1_c}\cos\psi + \lambda_{1_s}\sin\psi) \tag{A-2}$$

From the momentum theory, the uniform term (λ_0) is then written in the function of rotor disc velocity components

$$\lambda_0 = \frac{C_T}{2\sqrt{\mu^2 + (\mu_z - \lambda_0)^2}} \tag{A-3}$$

where $\mu = \sqrt{\mu_x^2 + \mu_y^2}$, is the normalised rotor-disc in-plane velocity component with the hub as the origin (shown in Figure A.1), C_T is the rotor thrust coefficient obtained from analytical solution of the rotor blade forces in Section (3.4.2), and μ_z is non-dimensional normal velocity component of the rotor-disc at the hub. In the rotor-disc model, the value of induced velocity λ_0 is obtained by solving the non-linear equation (A-3) numerically.

The harmonic components λ_{1_c} and λ_{1_s} of the induced velocity is determined by considering another set of axes orientation called the *wind axes*, which is aligned with the plane of rotation around the *z-disc* axis. The axes orientation also determined as the function of rotor-disc side-slip angle ψ_w, where

$$\psi_w = \tan^{-1}\left(\frac{\mu_x}{\mu_y}\right)$$

The transformation from the disc axes to the wind axes is given by

$$\begin{bmatrix} \lambda_{1_c} \\ \lambda_{1_s} \end{bmatrix}_{\text{wind}} = T_{\text{disc}\to\text{wind}} \begin{bmatrix} \lambda_{1_c} \\ \lambda_{1_s} \end{bmatrix}_{\text{disc}} \tag{A-4}$$

where the transformation matrix $T_{\text{disc}\to\text{wind}}$ is written as

$$T_{\text{disc}\to\text{wind}} = \begin{bmatrix} \cos\psi_w & \sin\psi_w \\ -\sin\psi_w & \cos\psi_w \end{bmatrix} \tag{A-5}$$

The lateral term of the induced velocity in the rotor-wind axes can be neglected ($\lambda_{1_{s_{\text{wind}}}} = 0$), while the longitudinal term of the induced velocity χ_w in the rotor-wind axes can be written in the form

$$\lambda_{1_{c_{\text{wind}}}} = \begin{cases} \lambda_0 \tan\dfrac{\chi_w}{2} & \chi_w < \dfrac{\pi}{2} \quad \text{(normal operation)} \\ \lambda_0 \cot\dfrac{\chi_w}{2} & \chi_w > \dfrac{\pi}{2} \quad \text{(windmill state)} \end{cases} \tag{A-6}$$

where χ_w is the rotor wake angle shown in Figure 3.15, which is defined for an autogyro as

$$\tan \chi_w = \frac{\mu}{-(\mu_z - \lambda_0)} \tag{A-7}$$

It is important to note that the normal flight condition of an autogyro is in windmill state as referred to equation (A-6).

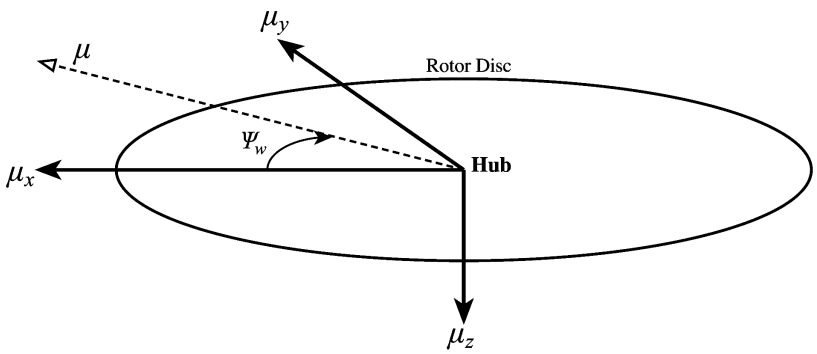

Figure A.1: Rotor-disc sideslip angle

Appendix B

Trim Calculation

The first step to evaluate the dynamic behaviour of a newly designed aircraft mathematical model is to determine the trim values for a defined flight state of the model. Trim is a condition where the aircraft is in steady flight, with all forces and moments are in equilibrium. These trim values will then be used as the point of references to calculate and analyse the dynamic response of the nonlinear model of the aircraft from a small perturbation. The autogyro is trimmed by setting the vehicle to fly in a straight and level condition at constant airspeed, by which all translational and angular accelerations of the vehicle are set to zero [150]. As such, for the longitudinal model of an autogyro, equations (3.3.1a) through (3.3.1d) are then re-written as

$$\frac{\sum X}{m} - g\sin\Theta = 0 \tag{B-1a}$$

$$\frac{\sum Z}{m} + g\cos\Theta = 0 \tag{B-1b}$$

$$\sum M = 0 \tag{B-1c}$$

$$Q_R = 0 \tag{B-1d}$$

There are four *unknown* parameters to be calculated for the trim conditions of the G-UNIV at a given forward airspeed V_f. The four unknowns are; the required propeller thrust (T_{prop}), the pitch attitude (Θ), the longitudinal rotor hub tilt (θ_s), and the rotorspeed (Ω).

The trim calculations for the nonlinear equations are implemented through the *Newton-*

Raphson iterative method. One special condition that has to be met is the number of unknowns must equal to the number of nonlinear equations [151,152], generally written as

$$\begin{aligned} f_1(x_1, x_2, x_3, \ldots, x_n) &= 0 \\ f_2(x_1, x_2, x_3, \ldots, x_n) &= 0 \\ &\vdots \\ f_n(x_1, x_2, x_3, \ldots, x_n) &= 0 \end{aligned} \tag{B-2}$$

where n is the number of unknown. Hence, the unknown variables for the equilibrium equations in (B-1) can be defined as vectors of the following

$$\mathbf{x} = \begin{bmatrix} T_{prop} \\ \Theta \\ \theta_s \\ \Omega \end{bmatrix}, \qquad \mathbf{f}(\mathbf{x}) = \begin{bmatrix} f_1(T_{prop}, \Theta, \theta_s, \Omega) \\ f_2(T_{prop}, \Theta, \theta_s, \Omega) \\ f_3(T_{prop}, \Theta, \theta_s, \Omega) \\ f_4(T_{prop}, \Theta, \theta_s, \Omega) \end{bmatrix} = \begin{bmatrix} f_1(\mathbf{x}) \\ f_2(\mathbf{x}) \\ f_3(\mathbf{x}) \\ f_4(\mathbf{x}) \end{bmatrix} \tag{B-3}$$

The functions $f_1, \ldots, f_4$ from (B-1) are then evaluated in the form of partial derivatives matrix, known as the *Jacobian* matrix, which is defined by

$$\mathbf{J} = \frac{\partial(f_1, f_2, \ldots f_n)}{\partial(x_1, x_2, \ldots x_n)} = \begin{bmatrix} \frac{\partial f_1}{\partial x_1} & \frac{\partial f_1}{\partial x_2} & \cdots & \frac{\partial f_1}{\partial x_n} \\ \frac{\partial f_2}{\partial x_1} & \frac{\partial f_2}{\partial x_2} & \cdots & \frac{\partial f_2}{\partial x_n} \\ \vdots & \vdots & \ddots & \vdots \\ \frac{\partial f_n}{\partial x_1} & \frac{\partial f_n}{\partial x_2} & \cdots & \frac{\partial f_n}{\partial x_n} \end{bmatrix} \tag{B-4}$$

Since the partial derivatives are complex to be solved analytically, the Jacobian is best evaluated numerically. To solve for the unknown ($\mathbf{x}$), a small deviation of the unknown variables is introduced and denoted as $\delta\mathbf{x}$. Based on the Jacobian matrix, the new succession functions according to the small deviation can then be given by

$$\mathbf{f}(\mathbf{x} + \delta\mathbf{x}) = \mathbf{f}(\mathbf{x}) + \mathbf{J}.\delta\mathbf{x} \tag{B-5}$$

where, the $\delta\mathbf{x}$ in equation (B-5) for the G-UNIV becomes

$$\delta\mathbf{x} = \begin{bmatrix} \delta T_{prop} \\ \delta\Theta \\ \delta\theta_s \\ \delta\Omega \end{bmatrix} \tag{B-6}$$

In the Newton-Raphson iterative process, the converging solution of the unknown is achieved when $\mathbf{f}(\mathbf{x} + \delta\mathbf{x})$ if close to zero. Hence, the expression in (B-5) can be re-arranged to solve for the new deviation of the unknown, given by

$$\mathbf{x}_{n+1} = \mathbf{x}_n - \mathbf{J}^{-1}.\mathbf{f}(\mathbf{x}_n) = \mathbf{x}_n - \delta\mathbf{x}_n \tag{B-7}$$

where

$$\delta\mathbf{x}_n = \mathbf{x}_{n+1} - \mathbf{x}_n \tag{B-8}$$

For the G-UNIV in longitudinal mode, the solutions for the unknowns are set according to the criteria given by

$$|\delta\mathbf{x}_n| = |\mathbf{x}_{n+1} - \mathbf{x}_n| < \varepsilon \tag{B-9}$$

where ε is the tolerance set for the numerical iterations to converge, usually $< 10^{-9}$.

Appendix C

Pole-Placement Technique

For a system of n^{th} order, the transfer function can be written in a general form as

$$Y(s) = \frac{poly(num)}{poly(den)} = \frac{b_{n-1}s^{n-1} + \cdots + b_1 s + b_0}{s^n + a_{n-1}s^{n-1} + \cdots + a_2 s^2 + a_1 s + a_0}\, U(s) \tag{C-1}$$

The pole-placement calculation can be simple, if the **A**, **B** and **C** matrices of the state-space equation of the system is in the control canonical form given by

$$\dot{x} = \begin{bmatrix} -a_{n-1} & -a_{n-2} & \dots & -a_1 & -a_0 \\ 1 & 0 & \dots & 0 & 0 \\ \vdots & \vdots & \ddots & \vdots & \vdots \\ 0 & 0 & \dots & 1 & 0 \end{bmatrix} x + \begin{bmatrix} 1 \\ 0 \\ \vdots \\ 0 \end{bmatrix} u \quad ; \tag{C-2a}$$

$$y = \begin{bmatrix} b_{n-1} & b_{n-2} & \dots & b_0 \end{bmatrix} z \tag{C-2b}$$

where the values of the top row of the state matrix (C-2a) is the *poly(den)* of (C-1). Similarly, the values of the control vector in C-2b is the *poly(num)* of (C-1). In this form, the top row values of **A** matrix actually determine the eigenvalues of the system,

$$|\lambda \mathbf{I} - \mathbf{A}| = \lambda^n + a_{n-1}\lambda^{n-1} + \cdots + a_0 \tag{C-3}$$

For a linear state feedback of a general form ($u = -\boldsymbol{K}x$), is considered in control

canonical form if the **B** matrix complies with (C-2a), thus the canonical form of **BK** can be written as

$$\mathbf{BK} = \begin{bmatrix} K_1 & K_2 & \dots & K_n \\ 0 & 0 & \dots & 0 \\ \vdots & \vdots & \ddots & \vdots \\ 0 & 0 & \dots & 0 \end{bmatrix} \tag{C-4}$$

where $\mathbf{K} = \begin{bmatrix} K_1 & K_2 & \dots & K_n \end{bmatrix}$.

To solve for the **K** matrix of the control canonical form, the closed-loop feedback $(\mathbf{A} - \mathbf{BK})$ is solved with any preassigned poles of $s^n + a_{n-1}s^{n-1} + \cdots + a_0$.

However, it is very unlikely to have one particular real system in control canonical form. Therefore, a transformation (T) can be created to form an equivalent canonical form system so that the pole-placement can be done accordingly from a non-canonical system. To create this transformation, the AB matrices of the system must be controllable according to Davison [107]. If not, the transformation of the equivalent canonical form system will not be possible.

Then, a new feedback state z is introduced, where

$$z = \boldsymbol{T}x \quad \text{so that,} \quad x = \boldsymbol{T}^{-1}z \tag{C-5}$$

From this transformation $\boldsymbol{T}$, the non-canonical form system can be transformed into canonical form where the newly transformed state-space equations are expressed by

$$\dot{z} = \hat{\boldsymbol{A}}z + \hat{\boldsymbol{B}}u \tag{C-6}$$

$$u = -\hat{\boldsymbol{K}}z \tag{C-7}$$

where $\hat{\boldsymbol{A}} = \boldsymbol{T}\boldsymbol{A}\boldsymbol{T}^{-1}$, $\hat{\boldsymbol{B}} = \boldsymbol{T}\boldsymbol{B}$ and $\hat{\boldsymbol{K}} = \boldsymbol{K}\boldsymbol{T}^{-1}$. Hence, the closed-loop state feedback of the transformed matrices can be written as

$$\dot{z} = (\hat{\boldsymbol{A}} - \hat{\boldsymbol{B}}\hat{\boldsymbol{K}})z \tag{C-8}$$

The controllable matrices of the original non-canonical system are given by

$$\boldsymbol{C_x} = \begin{bmatrix} \boldsymbol{B}, \boldsymbol{A}\boldsymbol{B}, \boldsymbol{A}^2\boldsymbol{B}, \dots, \boldsymbol{A}^{n-1}\boldsymbol{B} \end{bmatrix} \tag{C-9}$$

Similarly, the controllable matrices of the transformed system yield

$$\boldsymbol{C_z} = \left[\hat{\boldsymbol{B}}, \hat{\boldsymbol{A}}\hat{\boldsymbol{B}}, \hat{\boldsymbol{A}}^2\hat{\boldsymbol{B}}, \ldots, \hat{\boldsymbol{A}}^{n-1}\hat{\boldsymbol{B}}\right] \tag{C-10}$$

Therefore, from the above relationship, the controllable matrices of the transformed system in (C-10) can be re-written as

$$\boldsymbol{C_z} = \boldsymbol{T}\left[\boldsymbol{B}, \boldsymbol{AB}, \boldsymbol{A}^2\boldsymbol{B}, \ldots, \boldsymbol{A}^{n-1}\boldsymbol{B}\right] = \boldsymbol{TC_x} \tag{C-11}$$

which can be seen as a strong relationship between $\boldsymbol{C_x}$ and $\boldsymbol{C_z}$.

Therefore, the pole-placement technique to find the state feedback matrix $\boldsymbol{K}$ at pre-determined closed-loop poles can be summarised in simple algorithm as follows;

- Starting with the original state-space linear system of $\dot{x} = \boldsymbol{A}x + \boldsymbol{B}u$ and $y = \boldsymbol{C}x$ where $u = -\boldsymbol{K}x$, the transfer function can be obtained through $\boldsymbol{C}(s\boldsymbol{I} - \boldsymbol{A})^{-1}\boldsymbol{B}$.
- From the transfer function, the control canonical form of the system matrices $\dot{z} = \hat{\boldsymbol{A}}z + \hat{\boldsymbol{B}}u$ can be obtained.
- The transformation matrix $\boldsymbol{T}$ can be found by observing the similarity between $\dot{x} = \boldsymbol{A}x + \boldsymbol{B}u$ and $\dot{z} = \hat{\boldsymbol{A}}z + \hat{\boldsymbol{B}}u$ where $z = \boldsymbol{T}x$. The similarity is actually given by the controllability matrices $\boldsymbol{C_x}$ and $\boldsymbol{C_z}$. The transformation matrix can then be obtained by $\boldsymbol{T} = \boldsymbol{C_z}\left[\boldsymbol{C_x}\right]^{-1}$.
- From the desired pole locations and the control conanical feedback $(\hat{\boldsymbol{A}} - \hat{\boldsymbol{B}}\hat{\boldsymbol{K}})$, the values of conanical matrix $\hat{\boldsymbol{K}} = \left[\hat{K_1}\ \hat{K_2}\ \ldots\ \hat{K_n}\right]$ can be obtained.
- Finally, the closed-loop state feedback $\boldsymbol{K} = \left[K_1\ K_2\ \ldots\ K_n\right]$ of the original system can be determined by $\boldsymbol{K} = \hat{\boldsymbol{K}}\boldsymbol{T}$.

Appendix D

Hardware Model

D.1 DC Motor Modelling

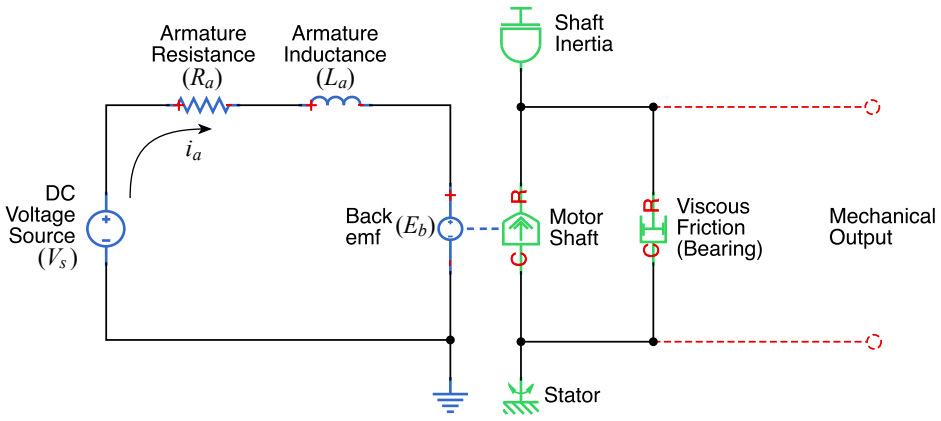

Figure D.1: DC motor schematic with Simscape

According to the DC motor schematic, the armature is a rotating conductor in the form of coil or winding. This armature winding produces a certain amount of inductance L_a with an internal resistance denoted by R_a when the armature is connected to the voltage source V_s. Interaction between the current that flows through the armature winding and the main magnetic flux will generate a rotational force that turns the armature (rotor) based on the Lorentz's principle. This rotating armature will then interact with the main magnetic flux that generates an induced electromotive force (emf), which always opposes the supply current. Due to this opposing reaction, the electromotive force is then called the 'back-emf' (E_b). The faster the rotor rotates, the higher the electromagnetic induction, thus the higher the back-emf will be. Hence, it

can be understood that the amount of back-emf is directly proportional to the rotational speed of the rotor ($E_b \propto N_{rotor}$).

The voltage changes in the time domain for the electrical elements of the motor in Figure D.1 can be summarised with the Kirchhoff's Voltage Law (KVL) and written as

$$V_s(t) = R_a\, i_a(t) + E_b(t) + L_a \frac{d}{dt} i_a(t) \tag{D-1}$$

The resultant current from the interaction between the supply and the back-emf is called armature current I_a and is the one that drives the DC motor which is then given in the s-domain form as

$$I_a(s) = \frac{V_s(s) - E_b(s)}{L_a s + R_a} \tag{D-2}$$

On the other hand, modelling of the mechanical element of the motor begins by considering at least two different physical phenomena acting on the rotating armature shaft; the resistive torque by viscous damping and the torque contributed by the mass of inertia of the rotor shaft. The viscous damping is a generic term used to represents a physical effect causing the rotation of a mechanical element to be damped or slowed down. For a rotating shaft, the viscous damping are contributed by a small air friction and bearing friction and producing a resistive torque which is directly proportional to the rotational speed of the shaft. The torque is given by

$$T_b(t) = B_m \frac{d\theta_r(t)}{dt} \tag{D-3}$$

where B_m is the viscous damping coefficient of the rotor shaft, which is normally included in the product datasheet.

Another resistive torque is produced when the rotor mass of inertia is accelerated around the shaft axis and given by

$$T_j(t) = J_m \frac{d^2\theta_r(t)}{dt^2} \tag{D-4}$$

where J_m is the rotor inertia which is also included in the manufacturer's datasheet.

Hence, the total resistive torque acting on the rotating mechanical element of the motor can then be obtained by summing equations (D-3) and (D-4) as,

$$T_t(t) = J_m \frac{d^2\theta_r(t)}{dt^2} + B_m \frac{d\theta_r(t)}{dt} \tag{D-5}$$

which can be written in the s-domain form as

$$T_t(s) = [J_m\, s^2 + B_m\, s]\, \theta_r(s) \tag{D-6}$$

The angular velocity of a rotating mechanical element (rotor shaft) is also defined as

$$\omega_r(t) = \frac{d\theta_r(t)}{dt}$$

and therefore, equation (D-6) yields

$$T_t(s) = [J_m\, s + B_m]\, \omega_r(s) \tag{D-7}$$

The torque generated by the motor is actually driven by the armature current with a motor torque constant K_t and written by

$$T_m(s) = K_t\, I_a(s) \tag{D-8}$$

where the armature current I_a is the resultant current between the back-emf and the supply that was mentioned previously in equation (D-2).

Hence, the net torque of the motor in equilibrium condition can then be obtained by summing the generated torque of (D-8) and the reaction (resistive) torque in (D-7) that yields

$$T_m - T_t = 0 \tag{D-9}$$

Due to the electro-mechanical coupling of the motor, the back-emf (E_b) is also known to be the function of the rotor angular speed (ω_r) which can be written as

$$E_b(s) = K_e\, \dot{\theta}_r(s) = K_e\, \omega_r(s) \tag{D-10}$$

where K_e is the voltage constant and also known as the back-emf constant of the DC motor.

Hence, substituting equation (D-10) into (D-2) also yields

$$I_a(s) = \frac{V_s(s) - K_e\, \omega_r(s)}{L_a s + R_a} \tag{D-11}$$

The transfer function of the EMA's rotating element can then be obtained by rearranging equations (D-7) to (D-11). The transfer function of the rotating shaft velocity and position due to the amount of input voltage is then given by

$$\frac{\omega_m(s)}{V_s(s)} = \frac{K_t}{(L_a s + R_a)(J_m s + B_m) + K_t K_e} \tag{D-12}$$

$$\frac{\theta_r(s)}{V_s(s)} = \frac{K_t}{s\big[(L_a s + R_a)(J_m s + B_m) + K_t K_e\big]} \tag{D-13}$$

D.2 DC Motor Simulation Results

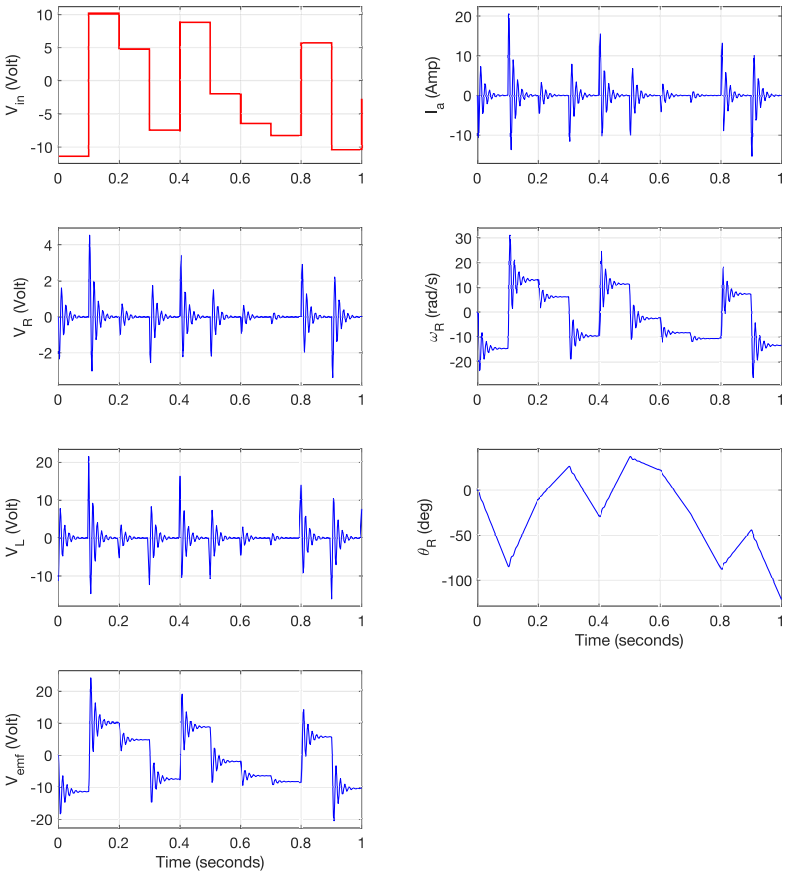

Figure D.2: Physical model simulation of Parker-M1453L DC Motor

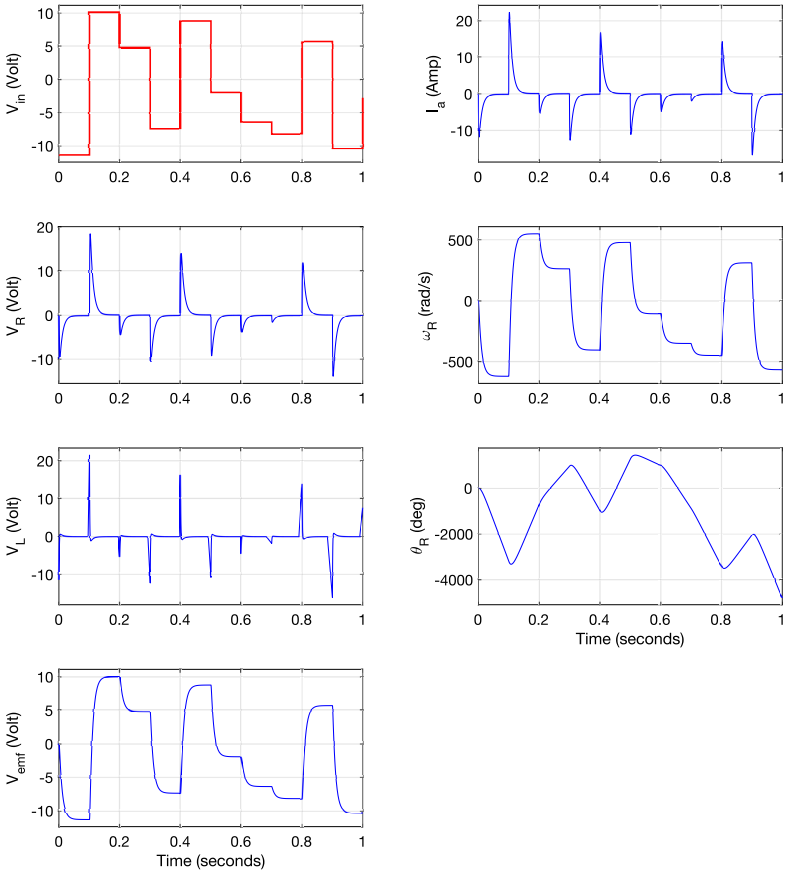

Figure D.3: Physical model simulation of Pittman-9234S004 DC Motor

D.3 State-Space Matrices of Actuator + Linkage

Refer to the next page.

$$A = \begin{bmatrix} -1000 & 0 & 0 & 0 & 0 & 0 & -50.95 & 0 & 0 & 0 \\ 0 & 0 & 0 & 1 & 0 & 0 & 0 & 0 & 0 & 0 \\ 0 & 0 & 0 & 0 & 1 & 0 & 0 & 0 & 0 & 0 \\ -5599 & 1.78e^{-11} & -1.78e^{-12} & 0 & 0 & -125.6 & -301.6 & 0 & 41.6 & 0 \\ 0 & -1.74e^{-15} & 0 & 0 & 0 & 1.74e^{-15} & -1.74e^{-15} & 0 & 0 & 0 \\ 0 & 0 & 0 & 0 & 0 & 0 & 1 & 0 & 0 & 0 \\ -1.0e^{4} & -1.78e^{-12} & 1.78e^{-12} & 0 & 0 & -237.9 & -546.2 & 0 & 75.3 & 0 \\ 1685 & 0 & 0 & 0 & 0 & -945.3 & 0 & 0 & 0 & -0.01153 \\ 2.5e^{5} & 0 & 0 & 0 & 0 & 0 & 0 & 7438 & -565.2 & 0 \\ -2474 & 0 & 0 & 0 & 0 & 0 & 0 & 0 & 0 & 0 \end{bmatrix}, \quad B = \begin{bmatrix} 0 \\ 0 \\ 0 \\ 0 \\ 0 \\ 0 \\ 0 \\ -1712 \\ 0 \\ 0 \end{bmatrix} \tag{D-1}$$

while

$$C = \begin{bmatrix} 0 & 0 & 0 & 0 & 0 & 0 & -0.5522 & 0 & 0 & 0 \\ 0 & 0 & 0 & 0 & 0 & -0.5522 & 0 & 0 & 0 & 0 \end{bmatrix}, \quad D = \begin{bmatrix} 0 \\ 0 \end{bmatrix} \tag{D-2}$$

with transfer functions written by

$$\frac{\delta_{\dot{\theta}_S}}{V_{in}} = \frac{5.3e^{8}s^{7} + 5.3e^{11}s^{6} - 0.01s^{5} - 9.928s^{4} - 2.5e^{-18}s^{3} - 2.5e^{-15}s^{2} + 1.65e^{-44}s}{s^{10} + 2111s^{9} + 9.0e^{5}s^{8} + 9.76e^{8}s^{7} + 4.88e^{10}s^{6} + 5.3e^{11}s^{5} - 0.91s^{4} - 9.94s^{3} - 1.85e^{-13}s^{2} - 2.54e^{-15}s - 7.7e^{-28}} \tag{D-3}$$

$$\frac{\delta_{\theta_S}}{V_{in}} = \frac{5.3e^{8}s^{6} + 5.3e^{11}s^{5} - 0.01s^{4} - 9.928s^{3} - 2.5e^{-18}s^{2} - 2.5e^{-15}s + 1.65e^{-44}}{s^{10} + 2111s^{9} + 9.0e^{5}s^{8} + 9.76e^{8}s^{7} + 4.88e^{10}s^{6} + 5.3e^{11}s^{5} - 0.91s^{4} - 9.94s^{3} - 1.85e^{-13}s^{2} - 2.54e^{-15}s - 7.7e^{-28}}$$

The 10×10 matrix is then reduced to a 6×6 by removing those less significant derivatives which yields

$$A = \begin{bmatrix} -2111 & -9.1e^5 & -9.8e^8 & -4.9e^{10} & -5.3e^{11} & 0 \\ 1 & 0 & 0 & 0 & 0 & 0 \\ 0 & 1 & 0 & 0 & 0 & 0 \\ 0 & 0 & 1 & 0 & 0 & 0 \\ 0 & 0 & 0 & 1 & 0 & 0 \\ 0 & 0 & 0 & 0 & 1 & 0 \end{bmatrix}, \quad B = \begin{bmatrix} 1 \\ 0 \\ 0 \\ 0 \\ 0 \\ 0 \end{bmatrix} \tag{D-4}$$

while

$$C = \begin{bmatrix} 0 & 0 & 5.3e^8 & 5.3e^{11} & 0 & 0 \\ 0 & 0 & 0 & 5.3e^8 & 5.3e^{11} & 0 \end{bmatrix}, \qquad D = \begin{bmatrix} 0 \\ 0 \end{bmatrix} \tag{D-5}$$

with transfer functions written by

$$\begin{aligned} \frac{\delta_{\omega_s}}{V_{in}} &= \frac{5.3e^8\, s^3 + 5.3e^{11}\, s^2}{s^6 + 2111\, s^5 + 9.1e^5\, s^4 + 9.8e^8\, s^3 + 4.9e^{10}\, s^2 + 5.3e^{11}\, s} \\ \frac{\delta_{\theta_s}}{V_{in}} &= \frac{5.3e^8\, s^2 + 5.3e^{11}\, s}{s^6 + 2111\, s^5 + 9.1e^5\, s^4 + 9.8e^8\, s^3 + 4.9e^{10}\, s^2 + 5.3e^{11}\, s} \end{aligned} \tag{D-6}$$

References

[1] H. Glauert, "A GENERAL THEORY OF THE AUTOGYRO," tech. rep., Scientific Research, Air Ministry, 1926.

[2] J. De La Cierva, "The Development of the Autogiro," *Journal of the Royal Aeronautical Society*, vol. 30, no. 181, pp. 8–29, 1926.

[3] M. A. Lock, "Further Development of Autogyro Theory - Part 1," tech. rep., Scientific Research, Air Ministry, 1927.

[4] J. G. Leishman, "Development of the Autogiro: A Technical Perspective," *Journal of Aircraft*, vol. 41, pp. 765–781, Jul 2004.

[5] R. Ford, *Germany's Secret Weapons in World War II*. Staplehurst: Spellmount, 2000.

[6] J. Lopez-Diez, C. Cuerno-Rejado, and J. Lopez-Ruiz, "Study of Competitive Missions for Autogyros," in *25th European Rotorcraft Forum*, (Madrid, Spain), ERF, 1999.

[7] Anon., "The Aerodynamics of Gyroplanes," tech. rep., CAA UK, 2010.

[8] Anon., "CAP 735 Aviation Safety Review 1992 - 2001," tech. rep., Safety Regulation Group, CAA UK, 2002.

[9] Anon., "CAP 780 Aviation Safety Review 2008," tech. rep., Safety Regulation Group, CAA UK, 2008.

[10] M. Bagiev and D. G. Thomson, "Handling Qualities Evaluation of an Autogiro Against the Existing Rotorcraft Criteria," *Journal of Aircraft*, vol. 46, no. 1, pp. 168–174, 2009.

[11] M. Bagiev, D. G. Thomson, and S. S. Houston, "Autogyro Inverse Simulation for Handling Qualities Assessment," in *European Rotorcraft Forum 2003*, (Friedrichshafen, Germany), Confederation of European Aerospace Societies, 2003.

[12] F. N. Coton, L. Smrcek, and Z. Patek, "Aerodynamic Characteristics of a Gyroplane Configuration," *Journal of Aircraft*, vol. 35, no. 2, pp. 274–279, 1998.

[13] S. S. Houston, "Longitudinal stability of gyroplanes," *Aeronautical Journal*, vol. 100, no. 991, pp. 1–6, 1996.

[14] S. S. Houston, "Identification of autogyro longitudinal stability and control characteristics," *Journal of Guidance Control and Dynamics*, vol. 21, no. 3, pp. 391–399, 1998.

[15] S. S. Houston, "Identification of gyroplane lateral/directional stability and control characteristics from flight test," *Proceedings of the Institution of Mechanical Engineers, Part G: Journal of Aerospace Engineering*, vol. 212, pp. 271–285, Jan 1998.

[16] S. Houston and D. G. Thomson, "Identification of Gyroplane Stability and Control Characteristics," *RTO Systems Concepts and Integration Panel (SCI) Symposium*, vol. 11, June 1999.

[17] V. M. Spathopoulos, S. S. Houston, and D. G. Thomson, "Flight dynamics issues relating to autogyro airworthiness and flight safety," in *AHS 54th Annual Forum*, (Washington, USA), Enlighton-Glasgow, 1998.

[18] M. Bagiev, D. Thomson, and S. Houston, "Autogiro Handing Qualities Assessment," *AHS 60th Annual Forum*, pp. 787–799, January 2004 2004.

[19] S. S. Houston, D. G. Thomson, and V. M. Spathopoulos, "Experiments in Autogyro Airworthiness for Improved Handling Qualities," *American Helicopter Society*, vol. 50, no. 4, pp. 295–301, 2005.

[20] Anon., "CAP 643 British Civil Airworthiness Requirements - Section T: Light Gyroplanes, Issue 3," tech. rep., CAA UK, 2005.

[21] Anon., "CAP 643 British Civil Airworthiness Requirements Section T - Light Gyroplanes, Issue 5," tech. rep., CAA UK, 2013.

[22] D. G. Thomson, "Development of a Generic Helicopter Model for Application to Inverse Simulation," Tech. Rep. 9216, University of Glasgow, Glasgow, 1992.

[23] R. R. Gilruth, "NACA Report No. 755: Requirements for Satisfactory Flying Qualities of Airplanes," Tech. Rep. 755, National Advisory Committee for Aeronautics, Langley Field, 1943.

[24] W. H. Phillips, "NACA Report 927: Appreciation and Prediction of Flying Qualities," tech. rep., National Advisory Committee for Aeronautics, Springfield, 1949.

[25] Anon., "AGARD-R-577-70: V/STOL Handling Qualities Criteria," tech. rep., NATO, London, 1970.

[26] Anon., "MIL-F-83300: Flying Qualities of Piloted V/STOL Aircraft," tech. rep., US Military, 1970.

[27] Anon., "MIL-F-8785C: Flying Qualities of Piloted Airplanes," tech. rep., U. S. Military, 1980.

[28] Anon., "MIL-HDBK-1797: Flying Qualities of Piloted Aircraft," tech. rep., Department of Defence, Washington, 1997.

[29] Anon., "DEF STAN 00-970: DESIGN AND AIRWORTHINESS REQUIREMENTS FOR SERVICE AIRCRAFT: VOLUME 2 - ROTORCRAFT," Tech. Rep. 1, Ministry of Defense, Bristol, 1984.

[30] Anon., "ADS-33E-PRF: Handling Qualities Requirements for Military Rotorcraft," tech. rep., US Army, March 2000.

[31] H. Andrews, "Report No. 311: Flight Mechanics Panel Symposium on Flying Qualities," tech. rep., AGARD, Neuilly Sur Seine, France, 1992.

[32] G. D. Padfield, "Rotorcraft Handling Qualities Engineering: Managing the Tension between Safety and Performance," *32nd Alexander A. Nikolsky Honorary Lecture - Journal of the American Helicopter Society*, vol. 58, no. 1, pp. 1–27, 2013.

[33] M. Cook, *Flight Dynamics Principles*. Oxford, UK: Elsevier Ltd, 2nd ed., 2007.

[34] S. S. Houston, "Validation of a Nonlinear Individual Blade Rotorcraft Flight Dynamics Model Using a Perturbation Method," *Aeronautical Journal*, vol. 98, no. 977, pp. 260–266, 1994.

[35] S. Houston and D. Thomson, "A Study of Gyroplane Flight Dynamics," in *21st European Rotorcraft Forum*, no. VII-6, (St. Petersburg, Russia), ERF1995, 1995.

[36] V. M. Spathopoulos, "Validation of a rotorcraft mathematical model in autorotation by use of gyroplane flight tests," *The Aeronautical Journal*, vol. 108, no. 1079, pp. 51–58, 2004.

[37] V. M. Spathopoulos, S. S. Houston, and D. G. Thomson, "Flight dynamics issues relating to autogyro airworthiness and flight safety," in *AHS 54th Annual Forum*, (Washington, USA), Enlighton-Glasgow, 1998.

[38] D. G. Thomson and S. S. Houston, "Experimental and Theoretical Studies of Autogyro Flight Dynamics," in *24th Congress of International Council of the Aeronautical Sciences*, (Yokohama), ICAS2004, 2004.

[39] D. Thomson and S. Houston, "Advances in Understanding Autogyro Flight Dynamics," in *64th American Helicopter Society Annual Forum*, (Montreal, Canada), pp. 391–403, AHS International, Inc., April 2008.

[40] S. S. Houston, "Light gyroplane empennage design considerations," *The Aeronautical Journal*, vol. 115, no. 1170, pp. 505–511, 2011.

[41] S. Laine, "EFFECT OF HORIZONTAL TAIL ON THE STABILITY OF THE VPM M16 AUTOGYRO," tech. rep., Department of Applied Mechanics, Aalto University, 2010.

[42] H. Duda, I. Pruter, C. Deiler, H. Oertel, and A. Zach, "Gyroplane Longitudinal Flight Dynamics," in *CEAS 2011 - The International Conference of the European Aerospace Societies*, 2011.

[43] EASA, "Annual Safety Review 2013," tech. rep., European Aviation Safety Agency, Luxembourg, 2014.

[44] AAIB, "AAIB Bulletin No: 2/94 Ref: EW/C93/12/1," tech. rep., Air Accidents Investigation Branch, UK, 1994.

[45] AAIB, "AAIB Bulletin No: 7/96 Ref: EW/C96/4/7," tech. rep., Air Accidents Investigation Branch, UK, 1996.

[46] AAIB, "AAIB Bulletin No: 1/2001 Ref: EW/C2000/04/03," tech. rep., Air Accidents Investigation Branch, UK, 2001.

[47] AAIB, "AAIB Bulletin No: 5/2002 Ref: EW/C2001/6/01," tech. rep., Air Accidents Investigation Branch, UK, 2002.

[48] AAIB, "AAIB Bulletin No: 9/2003 Ref: EW/C2002/05/05," tech. rep., Air Accidents Investigation Branch, UK, 2003.

[49] AAIB, "AAIB Bulletin No: 9/2004 Ref:EW/C2003/06/05," tech. rep., Air Accidents Investigation Branch, UK, 2004.

[50] AAIB, "AAIB Bulletin No: 9/2007 Ref: EW/C2006/06/01," tech. rep., Air Accidents Investigation Branch, UK, 2007.

[51] AAIB, "AAIB Bulletin No: 12/2010 Ref: G-CEYX EW/G2010/09/21," tech. rep., Air Accidents Investigation Branch, UK, Hampshire, UK, 2010.

[52] NTSB, "NTSB - Aviation Accidents Final Report: WPR13FA074," tech. rep., National Transportation Safety Board, USA, Scottsdale, AZ, 2014.

[53] NTSB, "NTSB - Aviation Accidents Final Report: ERA13FA219," tech. rep., National Transportation Safety Board, USA, Orlando, FL, 2015.

[54] NTSB, "NTSB - Aviation Accidents Final Report: CEN16LA347," tech. rep., National Transportation Safety Board, USA, Little Rock, AR, 2017.

[55] I. L. Ashkenas, H. R. Jex, and D. T. McRuer, "Norair Report NCR-64-143: Pilot-Induced Oscillations - Their cause and analysis," tech. rep., Norair Division, Northrop Corporation, Springfield, June 1964.

[56] D. T. McRuer, "Pilot-Induced Oscillations and Human Dynamic Behavior," tech. rep., NASA, Hawthorne, CA, July 1995.

[57] T. D. McRuer, C. S. Droste, R. A. Hess, D. P. LeMaster, S. Mathhews, J. McDonnel, J. McWhae, W. W. Melvin, and R. W. Pew, *Aviation Safety and Pilot Control: Understanding and Preventing Unfavorable Pilot-Vehicle Interactions*. Washinton, D.C.: National Academy Press, 1997.

[58] C. Beaty, "Gyroplane Stability - Understanding PIO, Buntover, and How Gyroplane Rotors Work," *RotorTech*, pp. 18 – 23, Aug 1995.

[59] Anon., *FAA-H-8083-21: Rotorcraft Flying Handbook - For Gyroplane Used Only*. Oklahoma City: Federal Aviation Administration, 2000.

[60] M. Gallup, *Inverse Simulation of Autogyros*. M.sc., University of Glasgow, 2014.

[61] D. G. Mitchell, D. B. Doman, D. L. Key, D. H. Klyde, D. B. Leggett, D. J. Moorhouse, D. H. Mason, D. L. Raney, and D. K. Schmidt, "Evolution, Revolution, and Challenges of Handling Qualities," *Journal of Guidance, Control, and Dynamics*, vol. 27, pp. 12–28, Jan 2004.

[62] Anon., "MIL-STD-1797A: Flying Qualities of Piloted Aircraft - Notice of Cancellation (Notice 2)," tech. rep., Department of Defence, Interface Standard, 1997.

[63] Anon., "MIL-HDBK-1797: Flying Qualities of Piloted Aircraft - Notice of Cancellation (Notice 1)," tech. rep., Department of Defence, Handbook, August 2004.

[64] Anon., "Flying Qualities of Piloted Aircraft - Notice of Reinstatement (Notice 3)," tech. rep., Department of Defence, Interface Standard, August 2004.

[65] Anon., "DEF STAN 00-970-Part 1, Section 2, Issue 2: Design and Airworthiness Requirements for Service Aircraft - Flight," tech. rep., Ministry of Defence, 1999.

[66] W. Bihrle, "AFFDL-TR-65-198: A Handling Qualities Theory for Precise Flight Path Control," tech. rep., US Air Force, New York, 1966.

[67] Anon., "MIL-H-8501A: HELICOPTER FLYING AND GROUND HANDLING QUALITIES; GENERAL REQUIREMENTS," tech. rep., Systems Engineering Group, Ohio, 1961.

[68] MIL-H-8501A, "MIL-H-8501A - Notice 2 - Notice of Cancellation," tech. rep., Systems Engineering Group, Ohio, 1995.

[69] Anon., "DEF STAN 00-970: Design and Airworthiness Requirements for Service Aircraft: Part 7, Issue 6 - Rotorcraft (Subpart B)," tech. rep., UK Ministry of Defence, Glasgow, 2015.

[70] J. N. Willims, J. A. Ham, and M. B. Tischler, "Flight Test Manual-Rotorcraft Frequency Domain Flight Testing," tech. rep., Ames Research Center, Moffett Field, CA, Sep 1995.

[71] M. Bagiev, D. Thomson, and S. Houston, "Autogiro Handing Qualities Assessment," in *AHS 60th Annual Forum*, (Baltimore), pp. 787–799, American Helicopter Society, June 2004.

[72] M. Bagiev and D. G. Thomson, "Handling Qualities Assessment of an Autogiro," *Journal of the American Helicopter Society*, vol. 55, no. 3, 2010.

[73] J. G. Leishman, *Principles of Helicopter Aerodynamics*. Cambridge University Press, 2006.

[74] G. D. Padfield, *Helicopter Flight Dynamics: The Theory and Application of Flying Qualities and Simulation Modelling*. John Wiley & Sons, 2nd ed., 2007.

[75] G. D. Padfield, *Helicopter Flight Dynamics (Google eBook)*. John Wiley & Sons, 2nd ed., 2008.

[76] W. Johnson, "A History of Rotorcraft Comprehensive Analyses," tech. rep., NASA, Moffett Field, CA, 2012.

[77] R. Du Val and C. He, "FLIGHTLAB modeling for real-time simulation applications," *International Journal of Modeling, Simulation, and Scientific Computing*, vol. 8, no. 4, pp. 1–18, 2017.

[78] R. W. Du Val and C. He, "Validation of the FLIGHTLAB virtual engineering toolset," *Aeronautical Journal*, vol. 122, no. 1250, pp. 519–555, 2018.

[79] S. Robinson and M. Jump, "Progress in the Development of Handling Qualities Critical Design Guidelines for an Autogyro," in *American Helicopter Society 67th Annual Forum*, (Virginia), AHS International Inc., 2011.

[80] S. Rutherford, *Simulation Techniques for the Study of the Manoeuvring of Advanced Rotorcraft Configurations*. PhD thesis, University of Glasgow, 1997.

[81] S. Rutherford and D. G. Thomson, "Helicopter Inverse Simulation Incorporating an Individual Blade Rotor Model," *Journal of Aircraft*, vol. 34, pp. 627–634, Sep 1997.

[82] S. S. Houston, "Analysis of Rotorcraft Flight Dynamics in Autorotation," *Journal of Guidance Control, and Dynamics*, vol. 25, no. 1, pp. 33–39, 2002.

[83] S. S. Houston, "Validation of a rotorcraft mathematical model for autogyro simulation," *Journal of Aircraft*, vol. 37, no. 3, pp. 403–409, 2000.

[84] V. M. Spathopoulos, *The assessment of a rotorcraft simulation model in autorotation by means of flight testing a light gyroplane.* PhD thesis, University of Glasgow, 2001.

[85] V. M. Spathopoulos, "Validation of a rotorcraft mathematical model in autorotation by use of gyroplane flight tests," *The Aeronautical Journal*, vol. 108, no. 1079, pp. 51–58, 2004.

[86] M. Bagiev, *Gyroplane Handling Qualities Assessment Using Flight Testing and Simulation Techniques.* PhD thesis, University of Glasgow, 2005.

[87] G. R. Leacock, *Helicopter inverse simulation for workload and handling qualities estimation.* PhD thesis, University of Glasgow, 2000.

[88] D. G. Thomson and S. S. Houston, "Investigation of Gyroplane Teeter Margin Limits," tech. rep., University of Glasgow, Glasgow, June 2006.

[89] S. S. Houston and D. G. Thomson, "Flight Investigation of Gyroplane Longitudinal Flight Dynamics," tech. rep., University of Glasgow, Glasgow, 1997.

[90] S. S. Houston, "Identification of autogyro longitudinal stability and control characteristics," *Journal of Guidance Control and Dynamics*, vol. 21, no. 3, pp. 391–399, 1998.

[91] J. Trchalik, *Aeroelastic modelling of gyroplane rotors.* Phd thesis, University of Glasgow, 2009.

[92] P. Harwood, "Top Gear for Gyros 2 - Gyroplane Explained." `https://www.youtube.com/watch?v=o9o30tvFeGg{&}t=107s`, 2017. Accessed: 15 March 2017.

[93] D. A. Peters and N. HaQuang, "Dynamic inflow for practical applications," *American Helicopter Society*, vol. 33, pp. 64–68, Oct 1988.

[94] R. F. Schaefer and H. A. Smith, "Aerodynamic Characteristics of the NACA 8-H-12 Airfoil Section at Six Reynolds Numbers," tech. rep., National Advisory Committee for Aeronautics (NACA), Langley, VA, 1998.

[95] S. Wolfram, *An Elementary Introduction to the Wolfram Language.* Wolfram Media, Inc., 2015.

[96] F. Szabo, *The Linear Algebra Survival Guide: Illustrated with Mathematica*. Montreal, Canada: Elsevier Inc., 2015.

[97] L. V. Schmidt, *Introduction to Aircraft Flight Dynamics*. Reston, Virginia: AIAA, 1998.

[98] R. C. Nelson, *Flight Stability and Automatic Control*. Boston, MA: McGraw-Hill, 2nd ed., 1998.

[99] Y. Qian, G. Ou, A. Maghareh, and S. J. Dyke, "Parametric identification of a servo-hydraulic actuator for real-time hybrid simulation," *Mechanical Systems and Signal Processing*, vol. 48, no. 1-2, pp. 260–273, 2014.

[100] Z. Yao, J. Tang, T. Rui, and J. Duan, "A time-frequency analysis based internal leakage detection method for hydraulic actuators," *Advances in Mechanical Engineering*, vol. 9, no. 1, pp. 1–8, 2016.

[101] W. R. Evans, "Graphical Analysis of Control Systems," *Transactions of the American Institute of Electrical Engineers*, vol. 67, pp. 547–551, Jan 1948.

[102] W. R. Evans, "Control System Synthesis by Root Locus Method," *Transactions of the American Institute of Electrical Engineers*, vol. 69, no. 1, pp. 66–69, 1950.

[103] B. Stojiljković, L. Vasov, Č. Mitrović, and D. Cvetković, "The application of the root locus method for the design of pitch controller of an F-104A aircraft," *Journal of Mechanical Engineering*, vol. 55, no. 9, pp. 555–560, 2009.

[104] B. J. Wellman and J. B. Hoagg, "Quadratically Parameterized Root Locus Analysis," *IEEE Transactions on Automatic Control*, vol. 59, pp. 1803–1817, Jul 2014.

[105] D. Antunes and W. P. M. H. Heemels, "Root locus analysis for randomly sampled systems," in *2014 European Control Conference (ECC)*, (Strasbourg, France), pp. 1619–1624, IEEE, Jun 2014.

[106] T. B. Sekara and M. R. Rapaic, "A revision of root locus method with applications," *Journal of Process Control*, vol. 34, pp. 26–34, Oct 2015.

[107] E. J. Davison, "On Pole Assignment in Linear Systems with Incomplete State Feedback," *IEEE Transactions on Automatic Control*, vol. 15, no. 3, 1970.

[108] O. Bachelier, J. Bosche, and D. Mehdi, "On Pole Placement via Eigenstructure Assignment Approach," *IEEE Transactions on Automatic Control*, vol. 51, pp. 1554–1558, Sep 2006.

[109] K. Yang and R. Orsi, "Static Output Feedback Pole Placement via a Trust Region Approach," *IEEE Transactions on Automatic Control*, vol. 52, pp. 2146–2150, Nov 2007.

[110] S. Das, K. Halder, I. Pan, S. Ghosh, and A. Gupta, "Inverse optimal control formulation for guaranteed dominant pole placement with PI/PID controllers," in *2012 International Conference on Computer Communication and Informatics*, no. 1, pp. 1–6, IEEE, Jan 2012.

[111] H. R. Mokadam, B. M. Patre, and D. K. Maghade, "Tuning of multivariable PI/PID controllers for TITO processes using dominant pole placement approach," *International Journal of Automation and Control*, vol. 7, no. 1 of 2, p. 21, 2013.

[112] D. Maghade and B. Patre, "Pole placement by PID controllers to achieve time domain specifications for TITO systems," *Transactions of the Institute of Measurement and Control*, vol. 36, no. 4, pp. 506–522, 2014.

[113] R. Ding, B. Xu, J. Zhang, and M. Cheng, "Self-tuning pressure-feedback control by pole placement for vibration reduction of excavator with independent metering fluid power system," *Mechanical Systems and Signal Processing*, vol. 92, no. 38, pp. 86–106, 2017.

[114] H. Duda, "Flight control system design considering rate saturation," *Aerospace Science and Technology*, vol. 2, pp. 265–275, May 1998.

[115] N. U. Rahman, J. F. Whidborne, and A. K. Cooke, "Longitudinal Control System Design and Handling Qualities Assessment of a Blended Wing Body Aircraft," in *International Bhurban Conference and Applied Sciences & Technology*, (Islamabad), pp. 177–186, IEEE, 2009.

[116] S. Mansor, Y. A. M. Nogoud, and R. Alamin, "Longitudinal command stability augmentation system design for unstable aircraft using flying and handling qualities specifications," in *2015 International Conference on Computing, Control, Networking, Electronics and Embedded Systems Engineering (ICCNEEE)*, pp. 136–142, IEEE, Sep 2015.

[117] S. Raj and M. S. Mohan, "Performance Evaluation of Stability Augmentation System by various Flight Control Laws," in *IEEE ICCSP 2015*, (Kakinada, India), pp. 694–701, IEEE, 2015.

[118] MathWorks, *Control System Toolbox - Reference R2017a.* Natick, MA: MathWorks Inc., 2017.

[119] B. Stevens, F. Lewis, and E. Johnson, *Aircraft Control and Simulation.* New Jersey: Wiley-Blackwell, 3rd ed., 2015.

[120] R. T. Perera, "Design of a Flight Control System in Compliance with Fling and Handling Quality Requirements," *Journal of Engineering and Technology of The Open University of Sri Lanka (JET-OUSL)*, vol. 1, no. 1, pp. 35–50, 2013.

[121] W. Guo, *Gain Scheduling for a Passenger Aircraft Control System to Satisfy Handling Qualities*. Msc thesis, Cranfield University, 2010.

[122] A. Boglietti, A. Cavagnino, A. Tenconi, S. Vaschetto, and P. di Torino, "The safety critical electric machines and drives in the more electric aircraft: A survey," in *2009 35th Annual Conference of IEEE Industrial Electronics*, pp. 2587–2594, IEEE, Nov 2009.

[123] W. P. Lear, "Remote and automatic electric controls for aircraft," *Journal of the Franklin Institute*, vol. 238, pp. 9–35, Jul 1944.

[124] D. Rubertus, L. Hunter, and G. Cecere, "Electromechanical Actuation Technology for the All-Electric Aircraft," *IEEE Transactions on Aerospace and Electronic Systems*, vol. AES-20, pp. 243–249, May 1984.

[125] W. J. Norton, "AD-A176 148: Advanced Electromechanical Actuation System (EMAS) Flight Test," tech. rep., U. S. Air Force Systems Command, Wright-Patterson AFB, 1987.

[126] R. I. Jones, "The more electric aircraft - assessing the benefits," *IMechE*, vol. 216, pp. 259–269, 2002.

[127] J. Rosero, J. Ortega, E. Aldabas, and L. Romeral, "Moving Towards a More Electric Aircraft," *IEEE Aerospace and Electronic Systems Magazine*, vol. 22, pp. 3–9, Mar 2007.

[128] A. Garcia, J. Cusido, J. Rosero, J. Ortega, and L. Romeral, "Reliable Electro-Mechanical Actuators in Aircraft," *IEEE Aerospace and Electronic Systems Magazine*, vol. 23, pp. 19–25, Aug 2008.

[129] J. C. Shaw, S. D. A. Fletcher, P. J. Norman, and S. J. Galloway, "More Electric Power System Concepts for an Environmentally Responsible Aircraft (N+2)," in *2012 47th International Universities Power Engineering Conference (UPEC)*, pp. 1–6, IEEE, Sep 2012.

[130] H. QI, Y. FU, X. QI, and Y. LANG, "Architecture Optimization of More Electric Aircraft Actuation System," *Chinese Journal of Aeronautics*, vol. 24, pp. 506–513, Aug 2011.

[131] J. Fu, J.-C. Maré, and Y. Fu, "Modelling and simulation of flight control electromechanical actuators with special focus on model architecting, multidisciplinary effects and power flows," *Chinese Journal of Aeronautics*, vol. 30, pp. 47–65, Feb 2017.

[132] M. Schlotter, "Multibody System Simulation with SimMechanics," tech. rep., 2003.

[133] G. D. Wood and D. C. Kennedy, "Simulating Mechanical Systems in Simulink with SimMechanics," 2003.

[134] P. Frankovský, D. Hroncová, I. Delyová, and I. Virgala, "Modeling of Dynamic Systems in Simulation Environment MATLAB/Simulink âĂŞ SimMechanics," *American Journal of Mechanical Engineering*, vol. 1, no. 7, pp. 282–288, 2013.

[135] D. Hroncova and M. Pastor, "Mechanical System and SimMechanics Simulation," *American Journal of Mechanical Engineering*, vol. 1, no. 7, pp. 251–255, 2013.

[136] F. J. Alvarez and J. Fern, "SIMULADORES BASADOS EN HERRAMIENTAS DE MODELADO FISICO PARA EL APOYO A LA ENSENANZA DE CONTROL AUTOMATICO (II): PENDULO ROTATORIO," in *Actas de las XXXVI Jornadas de Automatica*, (Bilbao), pp. 667 – 673, Comite Espanol de Automatica de la IFAC (CEA-IFAC), 2015.

[137] Mathworks, "Simscape Multibody Link - User's Guide R2017a," 2016.

[138] Exlar, "GSM-20 Electric Linear Actuator - Electrical Data," 2016.

[139] Exlar, "GSM-20 Electric Linear Actuator - Mechanical Data," 2016.

[140] Pittman, "Lo-Cog® DC Motor - 9234S004," 2001.

[141] Parker, "Electromechanical Actuator Products," 2003.

[142] X. Du, R. Dixon, R. Goodall, and A. Zolotas, "Modelling and control of a high redundancy actuator," *Mechatronics*, vol. 20, pp. 102–112, Feb 2010.

[143] F. Previdi, A. Cologni, M. Madaschi, N. Matteuzzi, M. Nardeschi, S. Toro, and S. Savaresi, "Modeling and control of an electro-mechanical ballscrew actuator for vibration active damping," in *2014 IEEE Conference on Control Applications (CCA)*, pp. 177–182, IEEE, Oct 2014.

[144] I. Virgala, P. Frankovský, and M. Kenderová, "Friction Effect Analysis of a DC Motor," *American Journal of Mechanical Engineering*, vol. 1, no. 1, pp. 1–5, 2013.

[145] I. Virgala and M. Kelemen, "Experimental Friction Identification of a DC Motor," *International Journal of Mechanics and Applications*, vol. 3, no. 1, pp. 26–30, 2013.

[146] M. A. Khan, I. Todić, M. MILOŠ, Z. STEFANOVIĆ, and Ä. BLAGOJEVIĆ, "Control of Electro-Mechanical Actuator for Aerospace Applications," *Strojarstvo*, vol. 52, no. 3, pp. 303–313, 2010.

[147] J. Kasberg, "The Fundamentals of Ball Screws," *MachineDesign.com*, Aug 2015.

[148] Parker, "Fundametals of Servo Motion Control," tech. rep., Parker Hannifin Corporation, Ohio, 2005.

[149] N. Kannan and M. S. Bhat, "Longitudinal Hinfinity Stability Augmentation System for a Thrust Vectored Unmanned Aircraft," *Journal of Guidance, Control, and Dynamics*, vol. 28, no. 6, pp. 1240–1250, 2005.

[150] W. H. Press, S. A. Teukolsky, W. T. Vetterling, and B. P. Flannery, *Numerical Recipes: The Art of Scientific Computing - 3rd edition.* New York: Cambridge University Press, 3rd editio ed., 2007.

[151] G. E. Urroz, "Solution of non-linear equations," Tech. Rep. September, 2004.

[152] T. Young and M. J. Mohlenkamp, "Introduction to Numerical Methods and Matlab Programming for Engineers," tech. rep., Ohio University, Athens, Ohio, 2011.